University of Sheffield
Department of Civil and Structural Engineering
Sheffield Water Centre

Numerical and experimental study on remote sensing of turbulent free-surface flows

Yun-Hang Cho
曹潤鏗

The University Of Sheffield.

Agency for Science, Technology and Research
SINGAPORE

In collaboration with the Singapore Agency of Science, Technology and Research.
Submitted in part fulfilment of the requirements for the degree of
Doctor of Philosophy,
Original submission: 31 January 2023
Viva Voce: 18 July 2023
Minor Corrections: 07 September 2023

Abstract

In water flows, understanding pollutant mixing helps to predict the spread of diseases and/or harmful chemicals whilst understanding sediment transportation helps to predict where blockages may occur within the water transportation infrastructure. Both are important turbulence-driven properties that are exacerbated during floods. Past studies have shown that the surface of water flow can give information regarding the turbulent water flow underneath (although the exact relationship is still not clear). It has been hypothesised that this could also be used to deduce overall flow properties such as flow rate and turbulence level.

However, in many published open channel computational fluid dynamics (CFD) simulations, the dynamic water-air surface boundary is modelled as a 'rigid lid' to reduce computational load. In essence, the small vertical fluctuations at the water surface are assumed to not exist; with only transverse and streamwise velocities permitted (slip condition). This is done even in shallow water flows where a rough bed may influence the water surface. The purpose of this research is to investigate the impact of the rigid lid assumption (if any).

To achieve this, a suite of shallow water experimental tests was designed and conducted to replicate natural flows over rough beds. A range of sensing techniques was used to measure the flow and the water surface. For the flow, stereo Particle Imaging Velocimetry (PIV) and Acoustic Doppler Velocimetry (ADV) were deployed. To mitigate the typical dynamic distortion of a vertical PIV laser plane by the fluctuating water surface, the laser plane here was projected from beneath a bed of hexagonal-packed, translucent spheres. To measure the water surface, novel 3D infrared mapping sensors from the gaming industry (Microsoft Kinect) were tested and used alongside traditional conductance wave probes.

The results obtained from these physical experiments were used to validate various CFD models developed in an open-source code called OpenFOAM®. In rigid lid simulations, the flow turbulence was modelled using the Wall Adapting Large Eddy (WALE) method. The normalised velocity profiles and turbulence profiles were in good general agreement with the experiments and published literature. However, the Reynolds' shear stresses from the CFD was forced to zero at the rigid lid. This is despite turbulent structures being identified immediately beneath the free-surface through U-level, Proper Orthogonal Decomposition

(POD), Quadrant analysis, Q-criteron and Lambda-2.

This suggests that the sub-surface turbulence has an important impact on the water surface behaviour and that the rigid lid may not be suitable, especially at relative submergence <3. The CFD model forms one of the first OpenFOAM publications on Open Channel flows over rough beds and drastically reduces the barriers to using OpenFOAM in this research field.

Acknowledgements

I would like to express my gratitude to:

- My academic supervisors, Dr Andrew Nichols and Dr Po Yang.
- My industry supervisor, Dr Dao My Ha and his colleagues Dr Ba Te and Dr Tuyen from the Institute of High Performance Computing at the Agency of Science Technology and Research in Singapore.
- My colleagues, Arthur Hajaali and QianYu Li at the University of College London.
- Professor Simon Tait, Dr Melika Gül, Dr Nidiana Rosado Hau for their fluid dynamics and CFD feedback during 2023 when I was preparing for my thesis submission and viva.
- Drs Songdong Shao, Viktor Fedun, Wendy Wu Jiayi, Fred Sonnenwald, Katya Zossimova, Demetris Bates and Gianluca Pironti who helped to review and give feedback on my work.
- Holly Harris, Laura Wright, Professor Luca Susmel, Professor Steve Thornton and the PGR Civil Engineering team.
- Other staff at the University of Sheffield; Alan Grundy, Bez Khan and Paul Bentley from the IT team for assisting me with all my IT problems over the years. To Paul Osborne who showed me the ropes when I first arrived and made sure I didn't flood the laboratory too many times! George Turner from the English Language Teaching Centre who provided viva preparation training and feedback.
- Professor Horoshenkov and Dr Shucksmith for testing me during my confirmation review.
- My family and friends in the UK and Asia who supported me as I travelled this journey of research.

Nomenclature

$\bar{u}$	Mean local streamwise velocity
$\bar{v}$	Mean local vertical velocity
$\bar{w}$	Mean local spanwise (transverse) velocity
ϵ	Turbulent Dissipation rate
μ_t	Turbulent eddy viscosity
ν	Kinematic viscosity of water
ω	Turbulent Dissipation rate with shear stress transport
τ_{bed}	Bed stress, see eq. 2.2.1
a	Polynomial term used in eq. 8.1.1
A_i,A_j	Face normal vector used to calculate OQ_x in eq. 6.2.2
b	Polynomial term used in eq. 8.1.1
c	Polynomial term used in eq. 8.1.1
c_i	Vector from the center of cell to adjacent cell centroid in eq. 6.2.2
D	Fixed constant using Combes et al. (2011) notation. Distance between camera and bed used in eq. 8.1.2

D	Flow depth (mm)
d	Polynomial term used in eq. 8.1.1
D_{CFD}	Height of the computational domain, see Figure 6.31
D_{EXP}	Depth of flow from free surface to bed, see Figure 6.31
D_H	Hydraulic diameter
e	Polynomial constants used in eq. 8.1.3
e_i	Vector from centroid of face to centroid of edge in eq. 6.2.2
f	Polynomial constants used in eq. 8.1.3
f_0	Temporal frequency of oscillation of the free surface pattern
f_c	Cut-off frequency
f_D	Darcy-Weisbach friction factor, see eq.2.4.1
f_i	Vector from centroid of cell to face see Figure 6.17
f_{shm}	Frequency of simple harmonic motion
f_s	Sampling frequency
g	Acceleration due to gravity
k	Turbulent Kinetic Energy (TKE)
k_s	Hydraulic Roughness
L	Characteristic length scale representing the flow
L_1	CFD residual equal normalisation technique, see section 7.2.2
L_2	CFD residual Euclidean normalisation technique, see section 7.2.2
L_∞	CFD residual maximum normalisation technique, see section 7.2.2

L_0	Characteristic spatial period
OQ_x	Orthogonal Quality, where x is face or cell
Q	Flow rate
q	Turbulent velocity as defined by Muraro et al. (2021)
r	Raw sensor output value used in eq. 8.1.1
R_H	Hydraulic radius
RS_x	Reynolds shear stress where the subscript x denotes the directions uv, uw and vw
t	Time in seconds
u	Instantaneous streamwise velocity
$u^{'}$	Instantaneous streamwise velocity fluctuation
U^{+}	Normalised depth-local mean streamwise velocity
U_{*}	Shear (friction) velocity
U_B	Bulk flow velocity (mean velocity)
U_{max}	Maximum streamwise velocity
v	Instantaneous vertical velocity
$v^{'}$	Instantaneous vertical velocity fluctuation
w	Instantaneous spanwise velocity
$w^{'}$	Instantaneous spanwise velocity fluctuation
X	Streamwise direction coordinate axis
Y	Vertical direction coordinate axis

y^+	Normalised depth-wise location
y_0	Zero-velocity position
Z	Spanwise direction coordinate axis
z	Distance between camera and free-surface, see eq. 8.1.1
δ	Boundary layer of a flow (see Figure 2.4a)
δ_s	Laminar sub-layer of a flow (see Figure 2.4a)
Fr	Froude number, see eq. 2.5.1
N	Manning's Number, see eq. 2.1.1
Re	Reynolds' number, see eq. 2.2.9
S	Slope of the bed
A	Cross sectional area of the flow

κ	Von Kármán constant
μ	Dynamic viscosity
ρ_{lag}	Spatial lag in 2D space
ρ_f	Density of the fluid
υ	Kinematic viscosity

Organisations

ASTAR	Agency for Science Technology and Research, Singapore
EA	Environment Agency
IHPC	Institute of High Performance Computing (within ASTAR)

NI	National Instruments
NSCC	Singapore's National Supercomputing Center
UCL	University College London

Acronyms

ADV	Acoustic Doppler Velocimetry
CFD	Computational Fluid Dynamics
IBM	Immersed Boundary Method
LDA	Laser Doppler Anemometry
LDV	Laser Doppler Velocimetry
LES	Large Eddy Simulation, turbulence model
PDF	Probability Density Function
PIV	Particle Image Velocimetry
PTV	Particle Tracking Velocimetry
RANS	Reynolds Averaged Navier Stokes, turbulence model
SNR	Signal to Noise Ratio
SPH	Smoothed Particle Hydrodynamics
TiO_2	Titanium Dioxide, white colourant
TKE	Turbulent Kinetic Energy
VoF	Volume of Fluid, free-surface modelling approach
WALE	Wall Adapting Local Eddy-viscosity, type of LES model
WP	Conductance wave probe

‘Observing the motions of a water surface, they are similar to curls of hair. Water flows consist of two kinds of vortices; one vortex motion is promoted by mainstream, whereas the other is generated intermittently by separated reverse flow.’

Fasso (1987) Birth of Hydraulics in the Renaissance

Contents

List of Tables

List of Figures

Chapter 1

Introduction

1.1 Background and Motivation

1.1.1 Diseases through water

Human civilisation over the past century has been generally unsustainable. Post the COVID pandemic of 2019-2022, it is imperative that our water infrastructure remains resilient since sewer overflows have a big impact on disease vectors (e.g. London's open sewers of the 1800s). In the UK, a combined sewage system is often used, where rain and wastewater are transported in the same pipes to wastewater treatment plants. During periods of heavy rain, this untreated combined waste is directly discharged to rivers and seas. Hence, it is vital to have an accurate understanding of how pollutants are mixed inside water channel flows (Tudor, 2022). At the same time, in many high-rise residential units such as those in Hong Kong and Singapore, airborne diseases have been known to spread vertically through the waste (soil) pipe (Yu et al., 2004). Thus, one of the detection strategies is monitoring and testing sewage water. The mixing of such disease vectors into sewer flows is a big concern because, across the globe, population growth, climate change, urbanisation and consumerism are increasing the peak flows in rivers and urban drainage systems (Brown et al., 2011).

1.1.2 Pollutant mixing and sediment transportation

Key reports such as the UK's 2008 Climate Change Act (UK Government, 2008), the EU's Water Framework Directive (European Commission, 2000), and Singapore's 2012 National Climate Change Strategy (National Climate Change Secretariat, 2012) have highlighted the risks of climate change both at a national and international policy level. According to Fowler and Kilsby (2003), extreme rainfall events have approximately doubled over parts of the UK since 1960. Across Europe, Asia and many parts of the world, the high-intensity rainfall in recent years has led to numerous floods and landslides (Guardian, 2022; Osborn and Hulme, 2002; Presse, 2022). The typical detrimental effects such as flash flooding and sewer overflows will be further exacerbated by the increased risk of diseases that follow untreated wastewater.

However, real-time remote monitoring and future prediction of flow rates, turbulence, and flood propensity, are challenging to accomplish. Two key problems exist:

1. River systems and water modelling rely on information provided by sensors. Depth measurements are routinely taken in rivers and sewers, and velocity measurements (velocimetry) at the water surface are becoming increasingly reliable and popular, but they cannot provide details about the turbulent flow conditions or sediment transport beneath the water surface.

2. Detailed hydrodynamic computational fluid dynamics (CFD) simulations require months of computer resources so use many simplifications such as a rigid lid to assume the water surface as a flat solid surface. This may not necessarily be justifiable as the water surface is dynamically linked to the underlying turbulence. A fixed water surface could cause turbulence to be improperly modelled.

Within open channel simulations, the water surface is known as the free-surface. This is due to the difference between the densities of gas and liquid at the interface between the two phases. The inertia of the gas is effectively negligible compared to the liquid so the liquid can move 'freely' relative to the gas.

Turbulent structures are generated near the rough channel bed (Kline et al., 1967), they are shaped and influenced by the flow conditions (Komori et al., 1989). Such information can be used to learn more about the flow properties (Nichols and Rubinato, 2016). Patterns of the free-surface of turbulent open channel flows have also been shown by Horoshenkov et al., 2013a to contain information regarding the underlying hydraulic conditions (e.g. turbulent intensity, flow depth) and boundary conditions (e.g. bed roughness and sediment transport). Hence, it has been postulated that a remote measurement of surface dynamics can allow remote assessment of flow conditions (Dolcetti et al., 2016; Fujita, 2011; Nichols and Rubinato, 2016). Experimentally, these linkages have not been fully investigated. One of the most difficult problems for certain low turbulence flows, is the small size of the features on the surface (see region 0 in Figure 1.1). Hence, they cannot be reliably used to infer flow properties. From a practical perspective, measuring the turbulence immediately beneath the free-surface is challenging as the fluctuating free-surface often leads to noisy data. Thus CFD simulations are an important tool to study this region.

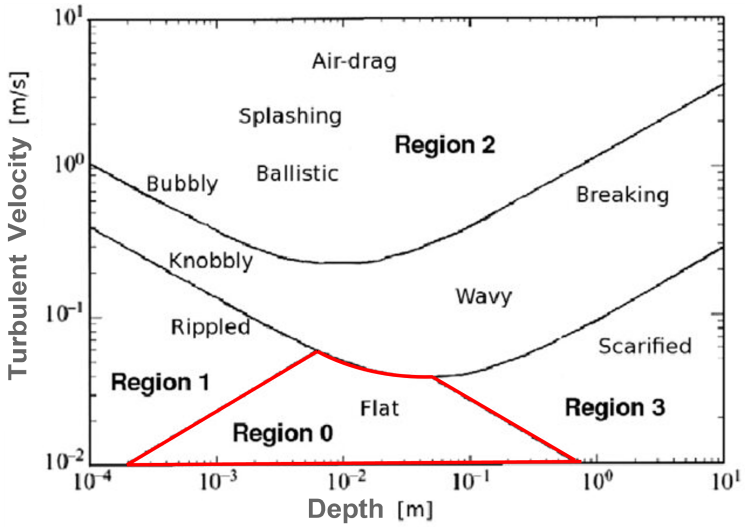

Figure 1.1: Brocchini and Peregrine (2001) suggested free-surface patterns can be split into four regimes based on turbulent velocity and flow depth (Wacławczyk and Oberlack, 2011).

However, many CFD simulations of open channel hydraulics use a rigid lid approximation assuming that the small surface fluctuations mean there is little effect of the free-surface on the flow (Bomminayuni and Stoesser, 2011; Stoesser et al., 2003). This is problematic because if the free-surface is capable of providing information on the flow condition, then the rigid lid removes the availability of such information. Furthermore, a rigid lid could change the way that near-surface turbulence behaves. This in turn affects simulations around pollutant mixing and sediment transportation.

1.2 Research Question

The above evidence has shown that the reliability of rigid-lid CFD simulations may be questioned due to a limited understanding of the relationship between free-surface and sub-surface dynamics. This is particularly the case in shallow flows where the horizontal length scale of the flow is significantly larger than the flow depth. Additionally, there is a lack of sensors which can accurately measure the free-surface fluctuations in 3D over time. Therefore, the research questions that this thesis aims to address are:

1. Can low-cost, off-the-shelf 3D infrared sensors be used in measuring smaller turbulent free-surfaces? What are the challenges?

2. Does a rigid lid boundary in shallow rough bed open channel simulations affect the accuracy of the flow characteristics for flows with small free-surface fluctuations?

The outcomes of this research will likely enable future development of better tools to forecast or nowcast the pollutant mixing and sediment transportation.

In Rogati, 2017's 'A Beginner's Guide to Data Engineering', a data science Hierarchy of Needs concept is introduced (see Figure 1.2). This is very important because the insufficient or incorrect type of data, in the wrong format, can significantly influence the performance of a model. A model can only be as good as the data that it is given. Thus, at the basic level,

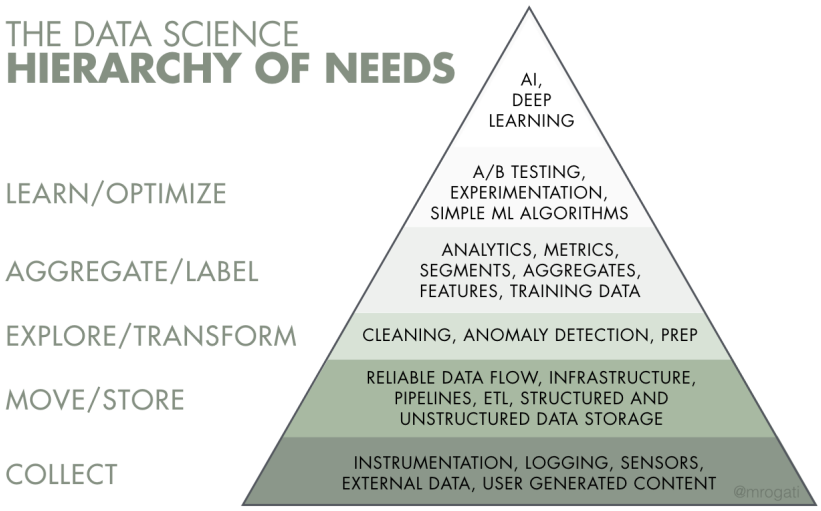

Figure 1.2: Data Science Hierarchy of Needs. At the base, the right instrumentation and sensing techniques must be used to collect the necessary data before calibration, cleaning of the data, and detailed analysis or more advanced learning. (Rogati, 2017)

the right kind of data needs to be collected. This may lead to a high storage demand for large data sets. The data may also need to be filtered to remove erroneous data or re-arranged into another format. Information has to be extracted from the data and only then can more advanced data analysis begin to produce useful information. This thesis covers the first 4 to 5 levels of the pyramid with the aim of extracting features and learning from them. The fundamental hierarchy drives the objectives and the order in which tasks are performed in this project.

The experimental work presented in this thesis adopts a technology transfer approach by using instrumentation from other fields and adapting it to collect novel 3D flow data. The novelty and high demands on the sensors require careful assessment of the data post-processing to allow the validation of any CFD simulations. The following section will state the aims, objectives and scope of this thesis research.

1.3 Aims and Objectives

1.3.1 Aim:

Establish the effect of the free-surface on the flow field and its implications for rigid lid simulations on shallow open channel flows. In particular, where the small-scale free-surface patterns are heavily influenced by flow turbulence. There is currently a limited understanding partly due to the limited ability to measure dynamic 3D surfaces. This project will aim to study how 3D sensors could be used to detect the dynamic shape of the free-surface pattern.

1.3.2 Objectives:

1. Establish a new set of flow conditions over a rough bed with different relative submergence.
2. Test novel 3D infrared sensors to understand its ability to measure small dynamic free-surface patterns.
3. Develop a computational fluid dynamics model with a physical bed roughness capable of simulating the aforementioned flow conditions.
4. Compare the velocity, turbulence intensity, and Reynolds' shear stress profiles from a rigid-lid CFD simulation with the experimental results (with a real free-surface).
5. Use visualisation techniques to identify turbulent coherent structures and assess how they interact with the rigid lid/free-surface.

The research presented in this thesis is the result of a collaboration between the University of Sheffield (UK) and the Institute of High Performance Computing (IHPC) at the Agency of Science, Technology and Research (ASTAR) in Singapore. The project involved two main phases covering experimental flows at the University of Sheffield's hydrodynamic re-circulating flume and through the collaboration with ASTAR, access to the National Supercomputer Centre in Singapore (NSCC) for numerical simulations.

1.3.3 Scope:

To design and test a range of flow conditions representative of natural flows in the real world, and to develop a rigid lid CFD model that can match the flow properties. If such a simulation can fully match the experimental flows, then the free-surface clearly does not have much influence on the flow underneath.

1.4 Related Paper Publications

- **Cho, YH.**; M. Gul, A. Nichols (2023). Turbulent structures identification using flow reconstruction from quadrant analysis. Journal of Hydraulic Research (submission in progress)

- **Cho, YH.**; A. Nichols (2024). Novel Approach to PIV in Open Channel flows Using Illumination from Beneath the Bed. the Journal of Flow Measurement and Instrumentation (submission in progress)

- **Cho, YH.**; M. H. Dao, A. Nichols (2022). Computational Fluid Dynamics Simulation of Rough Bed Open Channels Using OpenFOAM. Frontiers Environmental Science. 10:981680.
  Retrieved from doi.org/10.3389/fenvs.2022.981680

- Nichols, A., M. Rubinato, **YH. Cho** and J. Wu (2020) Optimal Use of Titanium Dioxide Colourant to Enable Water Surfaces to Be Measured by Kinect Sensors. MDPI Sensors 2020, 20, 3507. Retrieved from doi.org/10.3390/s20123507

- **Cho, YH.**, M. Rubinato, and A. Nichols (2017). The Kinect sensor as a tool for remote flow characterisation. *In Proceeding of the 37th IAHR World Congress, Kuala Lumpur, Malaysia, 13-18 August, 2017* (pp. 5600-5607). IAHR.
  Retrieved from www.iahr.org/site/cms/contentCategoryView.asp?category=341

- Rubinato, M., **YH. Cho,**, and A. Nichols (2017). Sensing of free-surface patterns in opaque flows using Kinect. *In Proceeding of HydroSenSoft, International Symposium and Exhibition on Hydro-Environment Sensors and Software 2017*, Spain. IAHR.
  Retrieved from www.ifema.es/hydrosensoft_06

ORCID: 0000-0001-9035-4395. Other works: researchgate.net/profile/Yun-Hang-Cho/research

1.5 Thesis Structure

Chapter 2 introduces some core concepts of open channel flows central to this study whilst chapter 3 presents a literature review of relevant experimental free-surface and flow dynamics. This includes an assessment of existing sensing technologies. Chapter 4 presents an introduction to computational fluid simulations with a review of relevant parameters such as turbulence models and the rigid lid assumption.

Chapter 5 details the approach towards the experimental testing whilst chapter 6 of the thesis presents the development of various CFD models. It contains the methods used to create the CFD model including the meshing, boundary conditions, solvers, initial conditions and other optimisations for high performance parallel computing. Chapter 7 outlines the post-processing steps that were taken prior to deeper analysis of the flow. These include processing the experimental ADV and PIV data as well as checking the stabilisation of the experimental tests and CFD simulations.

Chapter 8 presents the results and discussion of the CFD simulation and a comparison with the experimental data and published literature. It will discuss the findings of the thesis as a whole and relate these to previous work in the context of the two main research questions presented in this thesis.

Lastly, chapter 9 summarises the work, provides a conclusion to the research questions, highlights key achievements and poses questions and suggestions for future work.

Chapter 2

Introduction to Open Channel Flows

This chapter introduces the essential knowledge for open channel flows and tools used for experimental fluid dynamics. The fundamentals of open-channel hydraulics is well established. For example, Chadwick and Morfett (2002)'s book, 'Hydraulics in Civil Engineering' gives an excellent account by combining fundamental theories with modern applications.

An open channel flow is constrained by solid boundaries at the channel bed and sides of the flow (wetted perimeter). If the centerline of the flow is sufficiently far away from the sides of the channel (relative to the flow depth), the sides of the channel do not affect the behaviour of the water at the center. This type of behaviour is known as shallow water.

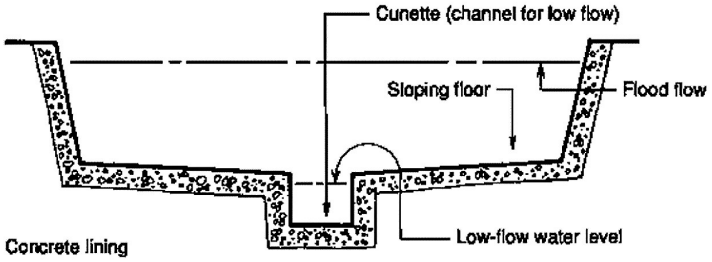

Figure 2.1: Schematic of a typical drainage open channel. A cunette is a small open channel within a larger open channel. During dry weather or moderate rain, the cunette carries the water whilst during heavy rainfall, the larger channel is filled (Stauffer and Spuhler, 1991).

A typical open channel used in real-world drainage systems is shown in Figure 2.1. During dry weather and low to moderate rainfall, the smaller central channel (known as a cunette) is designed to carry the flow whilst the larger wider channel is used when there is heavy rainfall and the water-carrying capacity needs to be increased. Figure 2.2 shows an image of such a channel in Singapore. The width of a cunette can be less than a metre wide making it possible to construct a 1:1 model replica in a water laboratory without too many practical difficulties. One of the most important issues in open channel drainage is preventing overflow, so sediment transportation and the causes of blockages are key considerations. To understand these effects, turbulence and the role of the channel bed's surface roughness must be analysed.

Figure 2.2: Typical open channel drainage with the cunette visible. Image of Ulu Pandan 'Canal' in Singapore (Tan and Yeo, 2009).

2.1 Manning's Equation

Manning (1895), gives an empirical measure of the roughness experienced by uniform open channel flows (see eq. 2.1.1). Manning's number helps engineers understand how the velocity of an open channel flow changes as the depth of the flow increases. This is used to compare the experimental flow conditions and ensure that laboratory scale conditions are comparable to the real world.

$$N = \frac{1}{U_B} R_H^{\frac{2}{3}} \sqrt{S}, \tag{2.1.1}$$

where U_B is a velocity representing the flow in m/s, R_H is the hydraulic radius in metres and S is the gradient (aka slope) of the bed. For wide channels, the hydraulic radius can be approximated as the flow depth.

2.2 Mean Velocity Profiles

Within the flow, the behaviour of the flow changes near solid boundaries such as the bed. This region of change is known as the boundary layer and causes the velocity to decrease.

In deeper flow where the velocity is constant over a majority of the depth (U_∞), the boundary layer is defined as beginning at the bed and ending when the velocity reaches 99% of U_∞. This velocity value is often used as a reference to normalise the flow and allow the shape of the profile to be compared with other flows. In shallower flow, the velocity is not constant over a majority of the depth, so it simply increases until the water surface. In this case, the reference velocity value is taken as the average velocity of the bulk flow (U_B).

At the ideal, smooth, channel wall, the velocity is reduced to zero due to the flow's viscosity causing fluid friction. This completely halts the flow of the fluid at the wall (known as the no-slip condition). As the distance from the boundary wall increases (y), the velocity also increases (Figure 2.3).

2.2.1 Source of Turbulence

The variation of velocity across the boundary layer is called shear. Shear is also what produces turbulence. Since the layer of water further away from the wall experiences less friction, a rotational motion is induced which gains energy and leads to the formation of

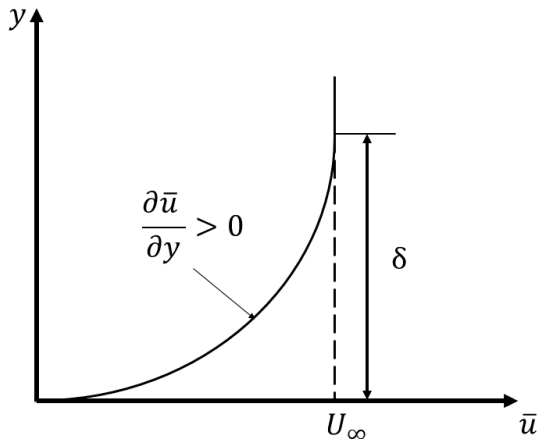

Figure 2.3: Turbulent boundary layer within a flow. y is the vertical distance away from a solid boundary. $\overline{u}$ is the time-averaged mean velocity parallel to the wall. δ is the thickness of the boundary layer.

turbulent eddies and structures. As the shear in the boundary layer decreases moving away from the boundary, the turbulence strength and intensity also decreases.

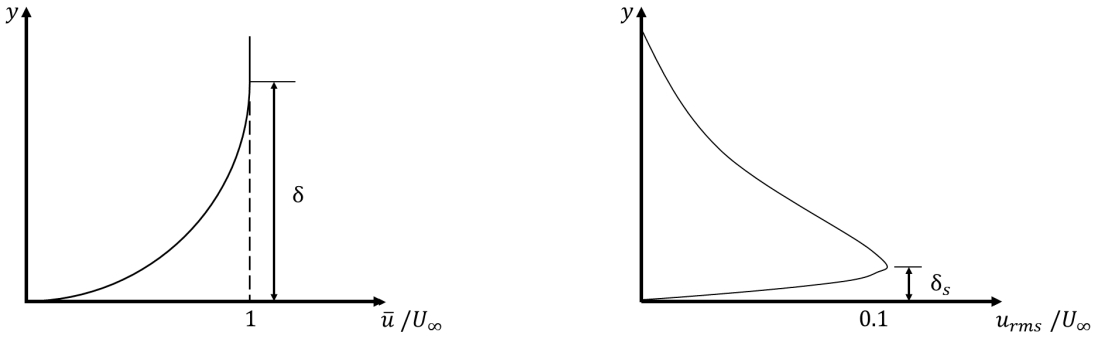

(a) Time averaged velocity profile normalised by the free stream velocity

(b) Representation of the turbulence intensity profile, normalised by the free stream velocity

Figure 2.4: Velocity and turbulence profile of a boundary layer normalised by the free stream velocity. Near the bed, the turbulence intensity increases.

Due to the no-slip condition, as the velocity reduces to zero near the wall (Figure 2.4a), the turbulence must also be zero so within the boundary layer (δ) is another layer known as the laminar sub-layer (δ_s). This is illustrated in Figure 2.4b.

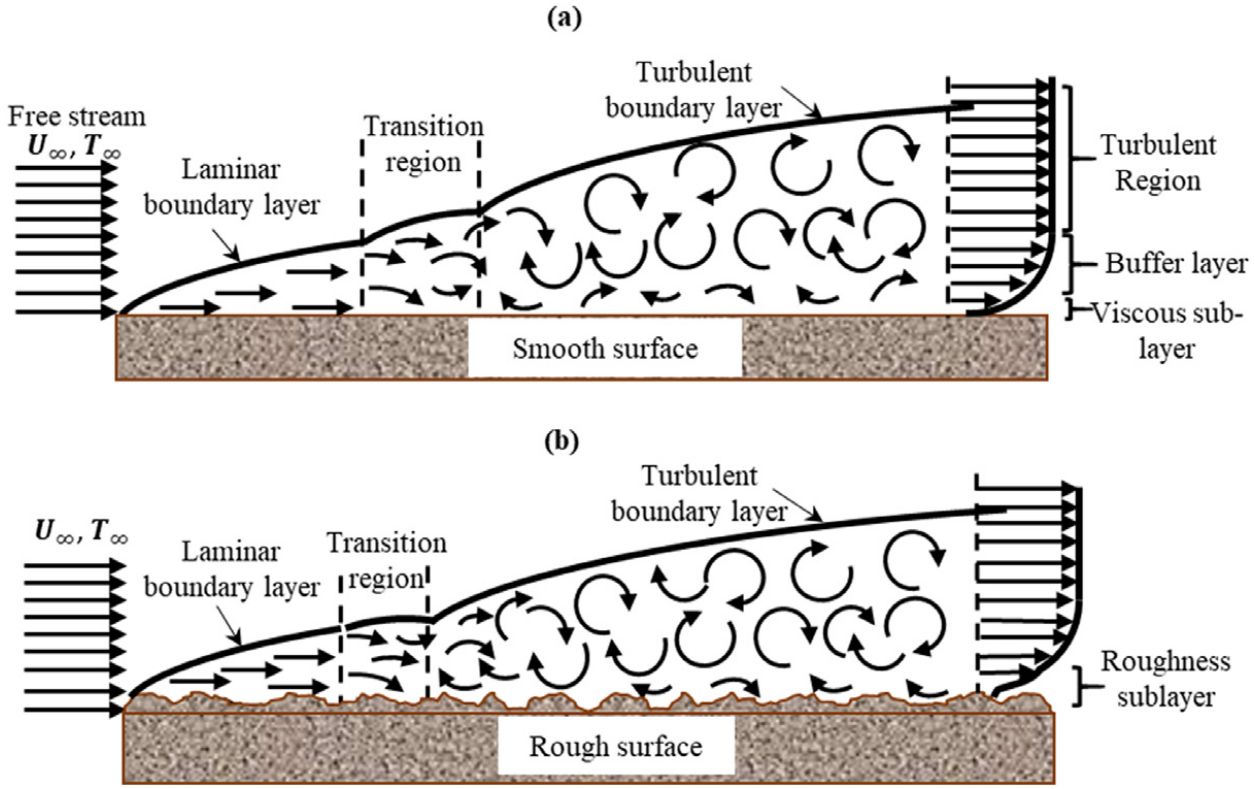

Figure 2.5: Boundary layer flows over from left to right over: (a) smooth and (b) rough surfaces (Kadivar et al., 2021). For flow over a rough surface, a roughness sublayer exists in the near wall region which does not exist in flow over a smooth surface.

For the same flow over a rough surface, this roughness causes flow instability close to the wall which leads to increased turbulence disrupting the sublayer and creating an additional roughness sub-layer. Kadivar et al. (2021) provides a good representation of this in Figure 2.5 by comparing turbulent flow over smooth surfaces with turbulent flow over rough surfaces.

Since turbulence is strongly related to shear, a velocity scale (u_*) is used to represent the shear strength τ_{bed}, at the boundary using Equation 2.2.1:

$$\tau_{bed} = \rho u_*^2. \tag{2.2.1}$$

where ρ is the fluid density.

The bed stress, τ_{bed} can also be expressed as a function of the distance from the wall (y), the mean velocity ($\overline{u}$) and the fluid kinematic viscosity (v). The shear velocity, u_* can then be re-arranged to depend on $\frac{\partial \overline{u}}{\partial y}\Big|_{y=0}$ as shown in Equation 2.2.3.

Since:

$$\tau_{bed} = \rho v \left.\frac{\partial \bar{u}}{\partial y}\right|_{y=0}. \tag{2.2.2}$$

$$u_* = \sqrt{\tau_{bed}/\rho} = \sqrt{v\left(\left.\frac{\partial \bar{u}}{\partial y}\right|_{y=0}\right)} \tag{2.2.3}$$

Near the wall, the shear velocity relates to the turbulence strength and the laminar sub-layer thickness through $U_{rms} \approx u_*$ and:

$$\delta_s = 5\frac{\nu}{u_*}. \tag{2.2.4}$$

In a steady, wide and uniform open channel flow with bed slope S, the momentum equation for a length of channel (dx) with width (b), height (h) and volume (dV), can be represented as:

$$\rho(dV)gS - \tau_{bed}(dx)b \equiv \rho g(dxhb)S - \tau_{bed}(dx)b = 0. \tag{2.2.5}$$

Thus, rearranging to solve for τ_{bed} and then substituting Equation 2.2.1 yields the equation for the friction shear velocity,

$$u_* = \sqrt{ghS}. \tag{2.2.6}$$

The shape of velocity profiles within the different regions of the boundary layer is well known. In particular, close to the bed within the laminar sub-layer, the viscosity dominates the vertical transport mechanism of momentum and suppresses the turbulence. Substituting Equation 2.2.1 into 2.2.2 and using the approximation $\frac{\partial u}{\partial y} \approx \frac{u}{y}$, the velocity profile within the laminar sub-layer can be solved:

$$\bar{u}(y) = \frac{u_*^2 y}{\nu}. \tag{2.2.7}$$

Above the laminar sub-layer, the velocity profile is logarithmic and its shape is dependent on the bed stress (with u_*) and the bed texture (described by the characteristics roughness, y_0). The profile can be described by:

$$\bar{u}(y) = \frac{2.3u_*}{\kappa} \log_{10}(y/y_0), \tag{2.2.8}$$

where κ is the Von Kármán constant, experimentally determined to be 0.41 (Hughes, 2010).

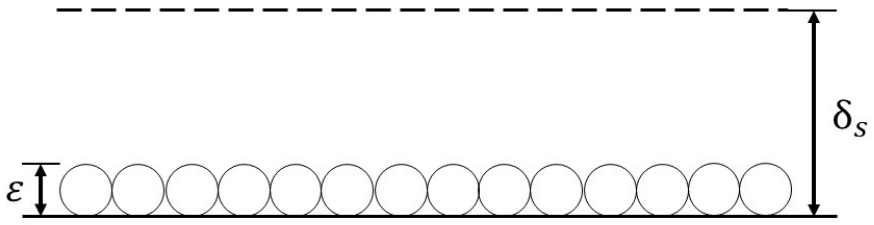

(a) Smooth turbulent flow, defined as: $\frac{u_*\varepsilon}{\nu} < 5$ and $y_0 = \frac{\nu}{9u_*}$.

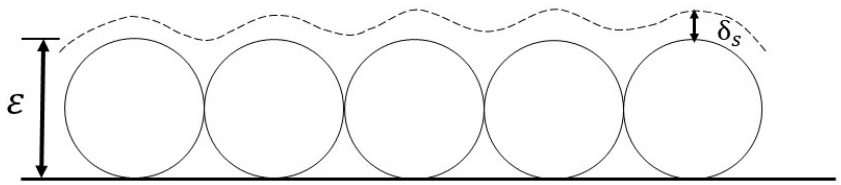

(b) Rough turbulent flow, defined as: $\frac{u_*\varepsilon}{\nu} > 70$ and $y_0 = \frac{\varepsilon}{30}$.

Figure 2.6: Illustration of turbulent flow over rough spheres with different relative submergence. u_* is the shear velocity of the flow, ν is the kinematic viscosity of water, and ε is the diameter of the bed roughness element.

Nikuradse investigated the effect of bed geometry and roughness on the shape of the velocity profile by gluing uniform sand grains of diameter ε, to the bed of a flume and measuring the velocity profile at different flow rates (Nikuradse, 1933; Thakkar et al., 2017). It was

discovered that two different behaviours appeared based on two variables: their roughness Reynolds number, $\frac{u_*\varepsilon}{\nu}$ and the characteristic roughness, y_0. Nikuradse's findings state that when the surface roughness is smaller than the laminar sub-layer ($\varepsilon < 5\frac{\nu}{u_*}$), then the flow above the laminar sub-layer effectively does not 'feel' the bed surface roughness. This is known as 'smooth turbulent flow'. When the roughness becomes larger than the laminar sub-layer, specifically $\varepsilon > \frac{70\nu}{u_*}$ or substituting Equation 2.2.4 $\varepsilon > (14 - 20)\delta_s$, then the flow above the laminar sub-layer 'feels' the bed surface roughness. Under these conditions $y_0 = \varepsilon/30$, meaning the characteristic roughness is a function of the real roughness scale, and the logarithmic profile is altered by the bed surface roughness. This is known as rough turbulent flow (Figure 2.6b).

If the velocity profile is plotted using a semi-logarithmic scale on the y axis, the flow outside the laminar sub-layer will follow a logarithmic pattern and therefore appear as a straight line. The shear velocity can be estimated from the gradient of the logarithmic line multiplied by a factor of κ /2.3. The characteristic roughness, y_0 can be estimated based on the y-intercept as shown in Figure 2.7. Figure 2.8 shows the different layers as the flow approaches the wall. The buffer region is hard to capture mathematically and although there are many proposed equations to model the shape of the entire profile (e.g. Colebrook White in section 2.4), these have not been proven to be consistent and capable of being generalised.

Most flows fall into the categories of turbulent or laminar flows. In turbulent flow, many eddies of different sizes exist within the flow and create a fluctuating velocity appearing seemingly at random (Figure 2.9). The majority of flows in sewers and rivers are turbulent flows. Experimentally, similar turbulent flows need to be recreated in the laboratory.

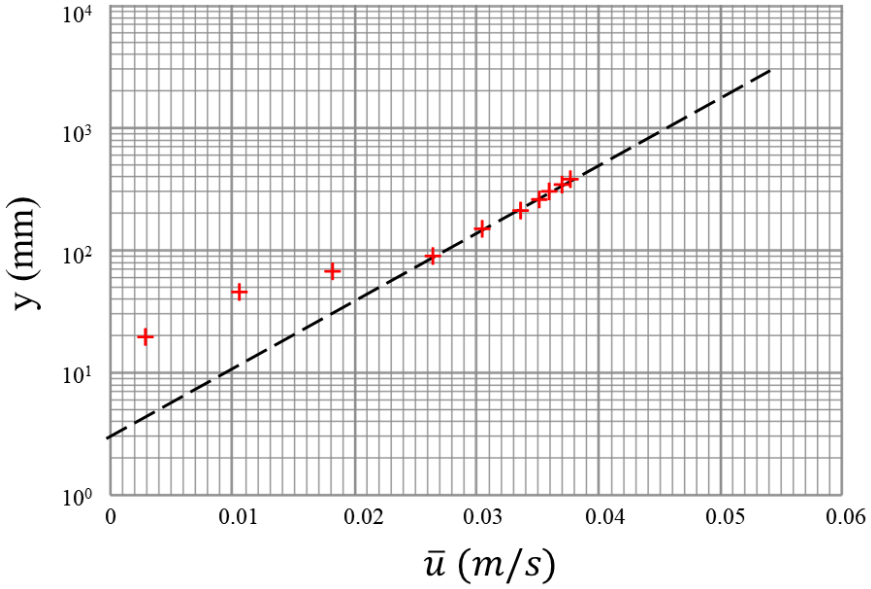

Figure 2.7: Theoretical logarithmic velocity profile of a flow plotted on a semi-log y axis. The red crosses indicate sensor readings and the dashed line is the linear log law which is able to approximate the outer region of the boundary layer.

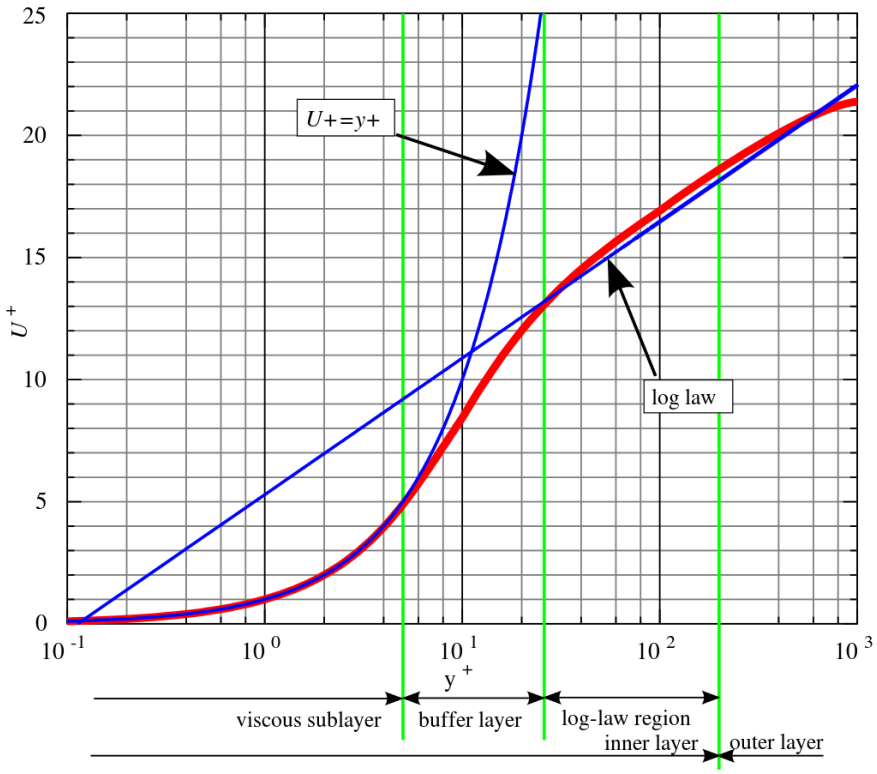

Figure 2.8: Logarithmic velocity profile of a flow near the wall. As the flow approaches the wall (inner layer), the velocity decreases following certain behaviours depending on the region (Nezu and Rodi, 1986). U^+ is the velocity normalised by the shear velocity (u_*). y^+ is the vertical coordinate, y multiplied by $\frac{\rho U_*}{\mu}$.

2.2.2 Measure of Turbulence, Reynolds' number

A ratio proposed by Sir Osborne Reynolds (1842 - 1912) provides an indication of the level of turbulence through the Reynolds' number. in essence, it is the ratio of inertial to viscous forces as shown in Equation 2.2.9 (Reynolds, 1883):

$$Re = \frac{UL}{\nu}, \tag{2.2.9}$$

where U is a velocity representing the flow in m/s, L is a length scale representing the flow (in metres) and ν is the kinematic viscosity of the fluid (m^2/s).

For open channels, the length scale representing the flow is often defined as the hydraulic radius (R_H, also measured in metres). For wide channels, this approximates to the flow depth. Reynolds' numbers calculated using the depth are referred to as depth-based Reynolds' numbers.

Generally, open channel flows with a Reynolds' number (based on hydraulic diameter) of less than 500 are laminar and flows with a Reynolds' number over 2000 are fully turbulent (Reynolds, 1883). Flows between these numbers are generally a mix of laminar flow with occasional and unpredictable bursts of turbulence.

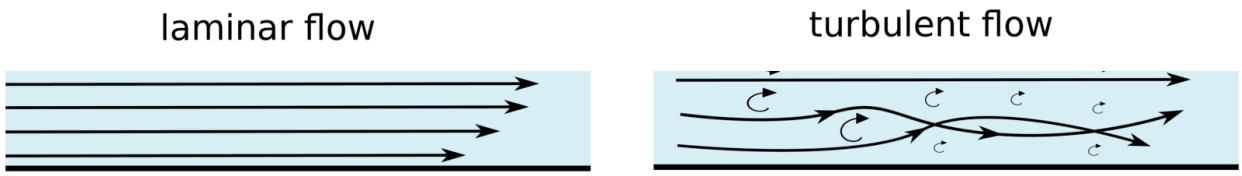

Figure 2.9: Comparison of turbulent and laminar flow comparison. The turbulent flow contains many eddies of different sizes and energies (CFD support, 2020).

2.3 Representing Turbulence Mathematically

Within the velocity field, turbulent eddies appear as fluctuations in velocity readings. Where flows are laminar, it is expected that the instantaneous velocity at any point in a stabilised flow would be the same as the mean velocity, $\overline{u}$, over time. However, turbulence introduces fluctuations away from this mean value. Thus an instantaneous velocity value $u'(t)$ can be broken down into two components using Equation 2.3.1. This is known as the Reynolds decomposition and is illustrated in Figure 2.10.

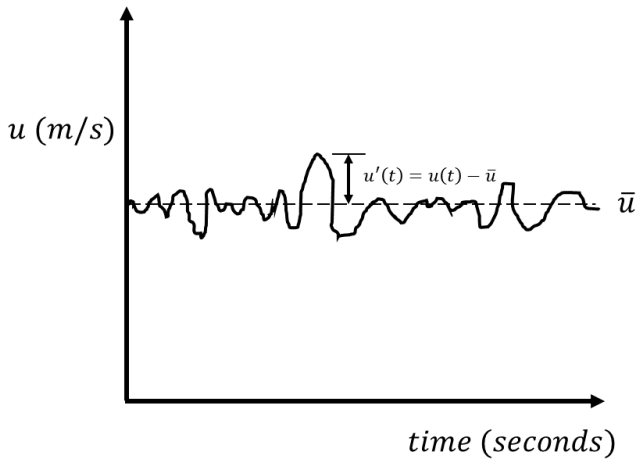

Figure 2.10: Reynolds' decomposition of a turbulent flow by describing the instantaneous fluctuation as a deviation from the mean velocity (see eq. 2.3.1).

$$u(t) = \overline{u} + u'(t). \tag{2.3.1}$$

Rearranging Equation 2.3.1, the turbulence fluctuation can be obtained:

$$u'(t) = u(t) - \overline{u}. \tag{2.3.2}$$

The turbulence strength (U_{rms}) can then be calculated using the root mean square:

$$U_{rms} = \sqrt{\overline{u'(t)^2}}. \tag{2.3.3}$$

Lastly, dividing the turbulence strength by a reference velocity gives the turbulence intensity, $U_{intensity}$. The reference velocity is commonly taken as the shear velocity or the mean bulk flow velocity, U_B. Using turbulence intensity in Equation 2.3.4, the turbulence within different flows with different velocity profiles can be normalised for comparison.

$$U_{intensity} = U_{rms}/U_B. \tag{2.3.4}$$

Likewise, the Reynolds' shear stress can also be mathematically defined using Equation 2.3.5 to 2.3.7 where RS_i is the Reynolds' shear stresses with subscript i being the different cross products. The density of water is denoted with ρ whilst v' and w' represent the vertical and transverse velocity fluctuations respectively.

$$RS_{uv} = \rho\overline{u'(t)v'(t)}/U_{shear}, \tag{2.3.5}$$

$$RS_{uw} = \rho\overline{u'(t)w'(t)}/U_{shear}, \tag{2.3.6}$$

$$RS_{vw} = \rho\overline{v'(t)w'(t)}/U_{shear}. \tag{2.3.7}$$

2.4 Colebrook-White Equation

The Colebrook-White equation expands on the work of Nikuradse and Manning by generalising the relationship which allows it to be applied to different types of flows (Colebrook, 1939). The Colebrook-White equation defines a relationship between the Darcy-Weisbach friction factor, f_D and the hydraulic roughness coefficient, k_s. This is important because knowledge about the hydraulic roughness will also provide more information regarding the general flow capacity. The Colebrook-White equation is given as:

$$\frac{1}{\sqrt{f_D}} = -2log\left(\frac{k_s}{3.71D_H} + \frac{2.51}{Re\sqrt{f_D}}\right), \tag{2.4.1}$$

where f_D is defined as:

$$f_D = \frac{8gD_HS}{4u^2},$$

where D_H is the hydraulic diameter, Re is the Reynolds number, S is the gradient of the bed, u is the velocity and g is the acceleration due to gravity. This can be rearranged to solve for the hydraulic roughness coefficient, k_s:

$$k_s = 3.71D_H\left(10^{-\frac{1}{2\sqrt{f_D}}} - \frac{2.52}{Re\sqrt{f_D}}\right). \tag{2.4.2}$$

Once the value of k_s is obtained, it can be used to calculate the theoretical U^+. This is an important dimensionless velocity used to compare different flows using the logarithmic law of the wall through self-similarity. The equation for U^+ is:

$$U^+ = \frac{1}{\kappa}ln\left(\frac{y}{k_s}\right) + A_r, \tag{2.4.3}$$

where A_r is an adjustable empirical constant that varies depending on the roughness of the flow (Schlichting and Gersten, 2016).

2.5 Froude Number

Named after William Froude (1810 - 1897), the Froude number (Fr) is an indicator of critical/sub-critical flows in shallow water. In supercritical flows, disturbances in the flow only influence the behaviour of the water downstream whilst in subcritical flows, the disturbance influences both upstream and downstream.

$$Fr = \frac{U_B}{\sqrt{g\frac{A}{B}}}, \tag{2.5.1}$$

where U_B is the bulk average flow velocity, g is gravitational acceleration, A is cross sectional area of the flow and B is the width of the free-surface. For open channels with a rectangular cross-section (i.e. the width of the free-surface is the same width as the bed and channel walls), A/B simplifies to the flow depth. A Froude number less than 1 represents sub-critical flow. Above 1, the flow is a supercritical flow.

2.6 Weber Number

The Moritz Weber number (We) is the ratio of inertia and the surface tension (Peakall and Warburton, 1996). This is useful for open channel multi-phase flows which have a free-surface interface and will be used later to assess whether the surface features generated are modulated by the surface tension or dominated by gravity. Small-scale laboratory studies must ensure that any tested flows have a similar Weber range to be comparable to field experiments.

$$We = \frac{\overline{U_B}^2 \rho D}{\sigma}, \tag{2.6.1}$$

where U_B is the time-averaged velocity, ρ is the density, D is the average depth and σ is the surface tension.

2.7 Summary of Open Channel Flow Concepts

The past chapter summarised some fundamental concepts of open channel flows.

The geometry of a typical open channel flow is presented with some real-life examples. It was shown that compared to experimental flumes, cunettes (the central channel within a wider channel) used in urban drainage systems are of similar width and bed roughness.

The difference in the flow behaviour and turbulence generation between flow over smooth and rough beds were explained with reference to literature. Ways to quantify turbulence mathematically using the Reynolds' decomposition were discussed. Methods used to normalise flow velocity and depth were presented, these enable a more robust comparison between flow conditions with different velocities and depths.

Common non-dimensional hydraulic parameters such as the depth-based Reynolds number (a measure of turbulence), Manning's number (effect of bed roughness on the flow), Weber number (effect of surface tension on free-surface mechanics) and the Froude number (a measure of flow criticality) are introduced.

These form the fundamental knowledge necessary to begin an investigation into open channel flows and their complex nature.

The following two chapters will present a review of open-channel free-surface flows. Chapter 3 will focus on the experimental work whilst Chapter 4 will review computational fluid dynamics modelling.

Chapter 3

Experimental Channel Flow Review

Whilst the academic field of free-surface dynamics has been relatively new, the free-surface and its captivating, seemingly magical pattern have been the source of curiosity for decades. For example, Fasso even tried to note down the different vortex patterns observed in 1987.

Da Vinci was one of the first to visually describe vortices in water channels based on their influence on the free-surface (Nezu and Nakagawa, 1991). Figure 3.1 shows a digital replica of his sketch with wisps representing the motion of currents and eddies. However, the relationship between flow turbulence and free-surface dynamics has not been investigated until more recently.

Figure 3.1: Da Vinci's art work, the 'Deluge'. An attempt to visualise large and small eddies was made. (Nezu and Nakagawa, 1991; Vinci, 1517).

In the 1930-1960s, statistical theories of turbulence, coherent structures (Taylor, 1935), bursting phenomena in boundary layers and vortex pair phenomena in mixing layers were established (Kolmogorov, 1941). Studies on turbulence in open channel flows soon followed.

In the 1970s, the measurement of turbulence in water was made possible through the invention of hot film anemometers. Flow visualisation techniques such as the hydrogen bubble method also came into use (Kline et al., 1967). In the 1980s, Laser Doppler Velocimetry (LDV) superseded hot film anemometers with improved accuracy and reliability utilising a laser's Doppler shift to measure velocity. Using such tools, researchers began to investigate the potential to link flow properties to the free-surface behaviour, and the possibility of measuring this behaviour remotely (Fujita, 2011).

Muraro et al. (2021) presents a detailed review of the research on understanding the free-surface dynamics of open channel flows. Within their work, a turbulence vs length scale diagram is adapted from Brocchini and Peregrine (2001) to compare the turbulence and the flow depth from different laboratory and field studies (see Figure 3.2). This will be useful later when comparing the flow conditions tested in this study. This chapter will review the work conducted so far in the field of free-surface dynamics and explore the latest technologies used to discover free-surface features.

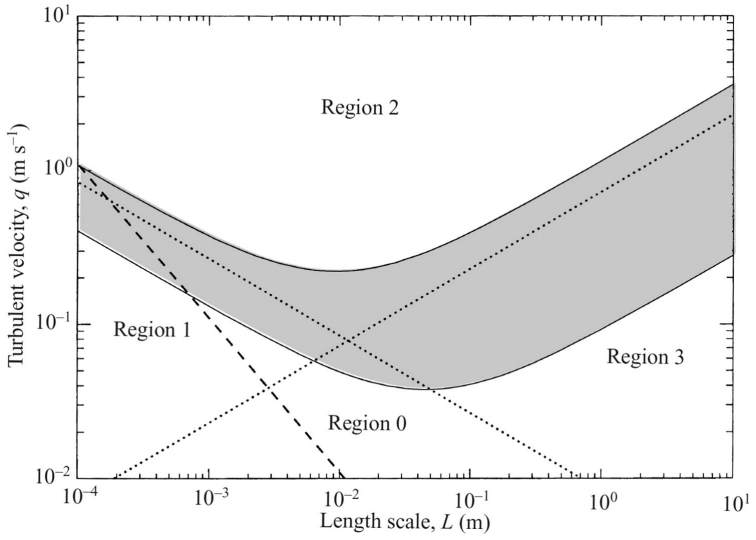

Figure 3.2: Classification of free-surface flows into different regions with distinct free-surface behaviours. Turbulence velocity, q is a function of free-surface characteristic length scale, L (Brocchini and Peregrine, 2001; Muraro et al., 2021). The dotted lines are a simplified division of the plane whilst the dashed line represents Re = 100.

3.1 Free-surface Dynamics

Technically, open channel flows are multi-phase fluid flows consisting of a water phase and an air phase. The two phases are separated by the free-surface which has a dynamic pattern. In ocean water, this pattern has been shown to be caused by a combination of external elements such as wind shear from the air phase, and movement of liquid from the water phase. Therefore, in the absence of any external effects from the air phase, the free-surface roughness can only be caused by the water flow beneath. Many studies have already attempted to establish a link between the free-surface and the underlying flow characteristics. For example, Lamb's classic text on hydrodynamics contains examples of research on this area (Lamb, 1993).

3.1.1 Creation of Turbulent Structures

Some of the earliest work investigating the creation of turbulence in open channel flows came from Kline et al. (1967). This work focused on visualising the turbulent boundary layer through hydrogen bubbles to reveal the existence of well-organised turbulent structures moving through the laminar sub-layer. As shown in Figure 3.5, these near-wall structures were stretched into streaks by the flow before breaking up and interacting with the main flow.

Grass (1971) showed the presence of large turbulent structures even in the absence of dominant spatial bed features (see Figure 3.3). This is important because it suggests that turbulent structures observed by Kline et al. (1967) exist in a range of bed roughness conditions. The study also confirmed that turbulence production is largely caused by 'in-rush' and 'ejection' events in the boundary layer of the flow near the bed.

Turbulent open channel flows always exhibit a complex rough free-surface composed of boils, vortices and dynamic features (Nezu and Nakagawa, 1991). The dynamic free-surface patterns are composed of:

- Turbulent structures features below the surface (Dolcetti et al., 2016),
- The dynamic oscillation of these features (Nichols et al., 2016),
- Resulting gravity/capillary waves (Dolcetti et al., 2016).

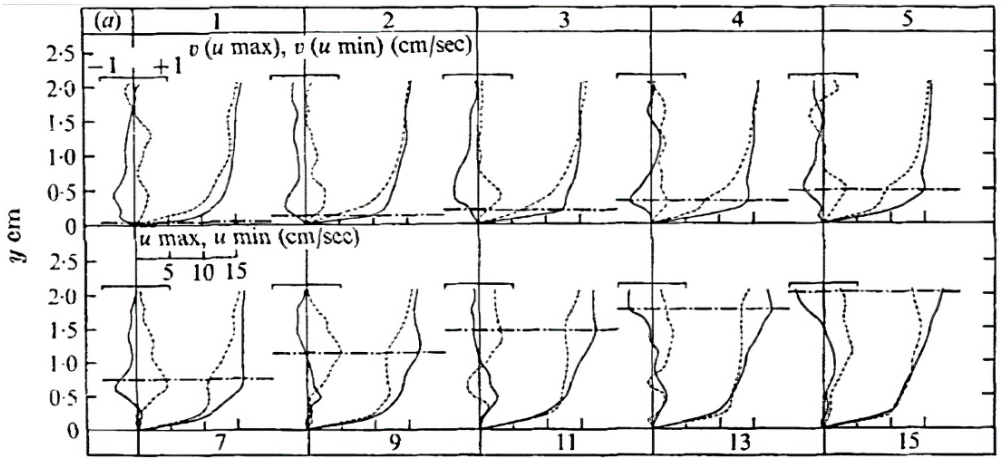

Figure 3.3: Large turbulent structures even in the absence of dominant spatial bed features (Grass, 1971). y is the vertical distance (in cm) from the bed, and u is the streamwise velocity (in cm/s).

Illustrated in Figure 3.4, Nezu and Nakagawa (1991) postulated that three types of turbulent boil structures are present:

- The first type is 'kolk-boils', vortices that form behind obstacles/dips in the flow bed.
- The second type is boils generated because of secondary currents' cellular movement.
- The third and last type of turbulent boil structures are those which occur with strong, bursting motions from the wall region, these continue to the free-surface to create free-surface vorticity boils (Kline et al., 1967).

In addition to being observed experimentally, Handler and Zhang (2013) were able to simulate this directly in using computational fluid dynamics. It was also witnessed that rapid expansion of near-wall vortices occurred as they moved towards the free-surface. These are illustrated in Figure 3.5.

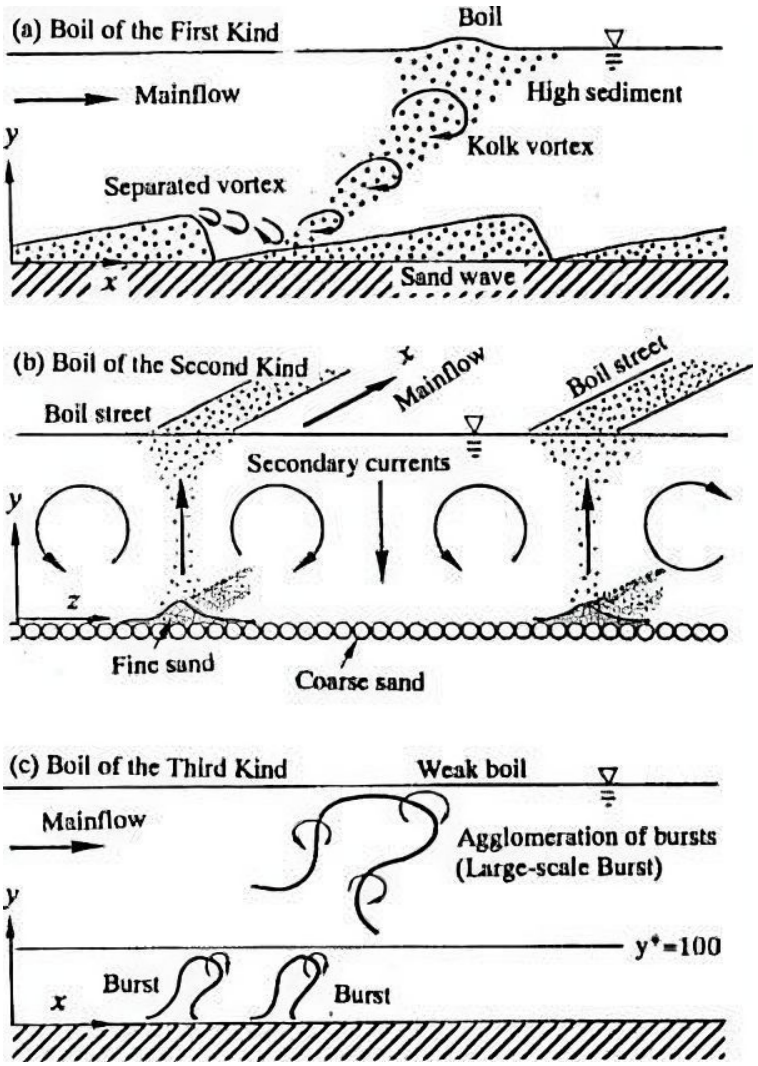

Figure 3.4: The three types of free-surface features (known as 'boils') and their generation mechanism (Nezu, 2005).

Colombini and Parker (1995) adapted previous flow models linking streamwise flow to transverse variations via second-order turbulence. Whilst the previous models were only able to predict flow streaks and boils with high sediment transportation, this new model was able to predict streaks even at low Shields' numbers. The Shields' number is a dimensionless number providing information on the ability of a sediment particle to be forced into motion (Ouriemi et al., 2007). Since the motion is cellular, the boils were automatically simulated in the process. Gulliver and Halverson (1987) were able to replicate this motion in the laboratory using hydrogen bubbles illuminated with a laser light sheet. Meanwhile, Savelsberg and van de Water (2008) noticed surface indentations above vortices when turbulence is generated from flow around a cylinder. This is a strong indication of type two boils. The

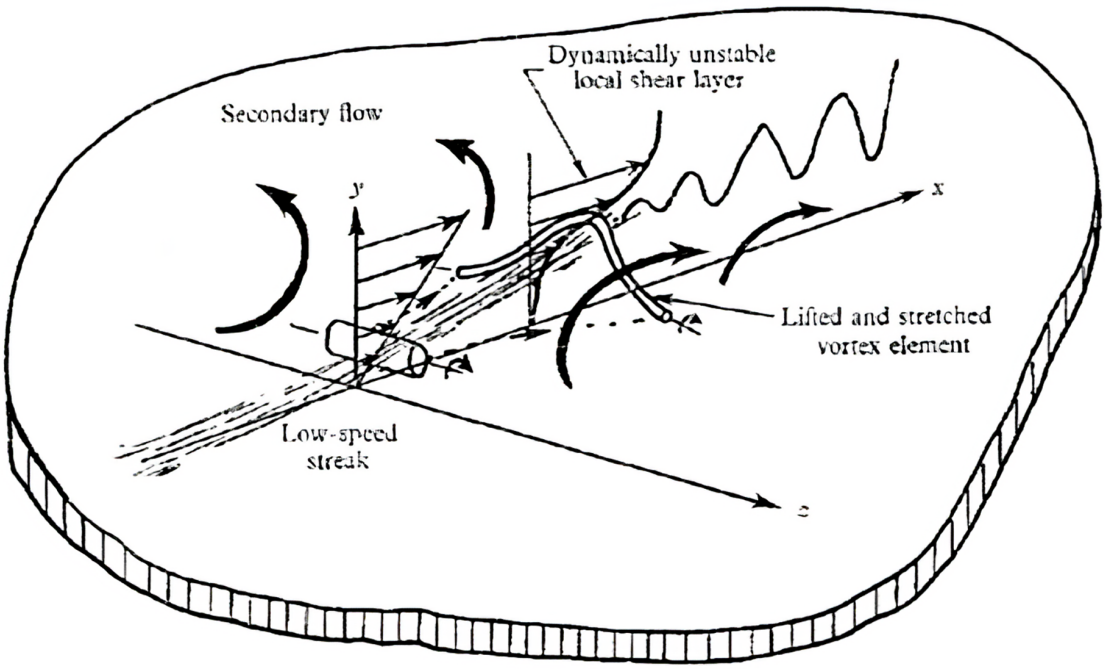

Figure 3.5: Bursting phenomena generating turbulence structures (Kline et al., 1967). Streaks are generated at the bed and create an unstable local shear layer. This causes vortex elements to be lifted and stretched. In deeper flows, the extra space may enable counter-rotating secondary circulation zones as indicated by the arrows.

existence of secondary current boils is now generally accepted.

Teixeira (2006) extended on Phillip's resonant interaction theory to develop an analytical model for simulating surface wave generation from subsurface turbulence. They suggest that this requires a match of length and time scales between turbulence and the presence of free waves. Since air forcing is not within the scope of this study, the question extends to whether existing surface patterns created from imperfect flume geometry can distort into wave patterns, through resonance with the underlying turbulent flow (Dolcetti, 2016a). Since the discovery of the type three boil, the question becomes how do these get transported to the free-surface and what causes their bursting?

3.1.2 Propagation of Structures to Free-surface

Komori et al. (1989) built upon this work by discovering that the mass of water beneath a bursting motion is directly lifted to renew the free-surface. It was found that the mass transfer coefficient of the liquid is proportional to the square root of the free-surface renewal frequency. Importantly, their work demonstrated visually that the surface-renewal motions originate with the bursting motions in the buffer region although it is still not clear why bursting motions are triggered.

In 2011, Fujita (2011) discovered a relation between advection features of the free-surface profile and a rough bed. Using a turbulent open-channel flow with hemispherical bed roughness elements, the free-surface and the underlying flow were sensed using high frame rate cameras. Comparisons of the free-surface profile and the near-surface flow showed that the speed of the free-surface features was strongly linked to the flow velocity and that there is a correlation between the fluctuation of the free-surface and the vertical velocity of the underlying vortical structure. This is direct evidence that under certain flow conditions (40mm deep 0.4 m/s flow over a bed of 30mm diameter hemispheres), the behaviour of the free-surface reflects changes in the flow field. More experimentation under different conditions should be established to investigate the nature of this relationship.

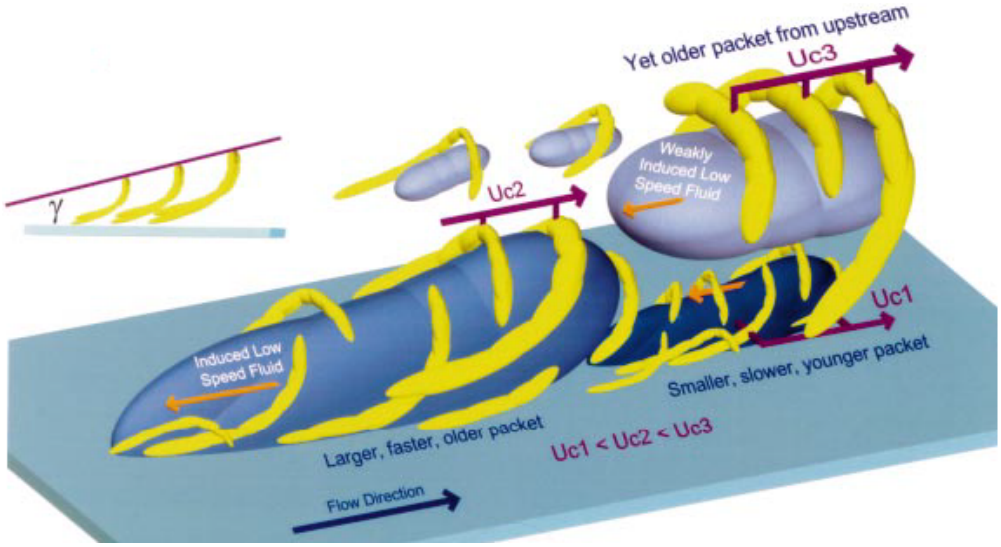

Figure 3.6: Propagation of structures from the bed to the free-surface (Adrian et al., 2000). Induced structures exhibit low speed relative to the bulk flow. The size of the structures increases and rises over time (as shown in the structures labelled Uc1 to Uc3).

Adrian et al. (2000) presents a summary of the different turbulent structures observed and evidence that suggests they are the same structure at different stages in their life (Figure 3.6) whilst Roy et al. (2004) showed that these turbulent structures are inclined in the direction of flow.

3.1.3 Response of Free-surface

There are some who claim that large structures cause the bursting, however, the inter-dependency between the bed and structures is still unknown. Findings by Falco (1977) and Yalin (1992) show turbulence structures hitting the surface and decaying into small eddies.

Through the use of ink droplets in a shallow, turbulent, hydraulic jump flow, Brocchini and Peregrine (2001) hypothesised the propagation of turbulent structures to travel at the same velocity as the fluid flow. Brocchini and Peregrine (2001) also present an in-depth explanation of the gravity-capillary wave model. These are dispersive in nature so the speed of their advection depends on the length scale of the wave. The model previously shown in Figure 3.2 contains four distinct regions where waves disperse and act differently. The diagram compares the length scale to the turbulent velocity where the shaded area represents the region of marginal breaking. This was obtained by using two estimated values for the critical Weber number $[(\pi - 2)/5 < We_c < \pi/4]$ and the critical Froude number $[(5/2 - \pi/2)/250 < Fr_c < \pi/24]$. The two straight dotted lines represent a simplified division of the plane whilst the dashed line represents Re = 100. However, surface patterns are often further distorted by the geometry and turbulence structures so there are some limitations to the model.

Moreover, Brown and Roshko (1974) discovered vortex pair phenomena in turbulent mixing layers. This is important since these discoveries were made by qualitative observations using flow visualisations and not hot wire anemometers. Prior to this, the accepted theory was that turbulence is completely random and chaotic. This highlights the need for 3D free-surface sensing which is capable of visualising the flow and providing depth measurements throughout a 2D area of the free-surface.

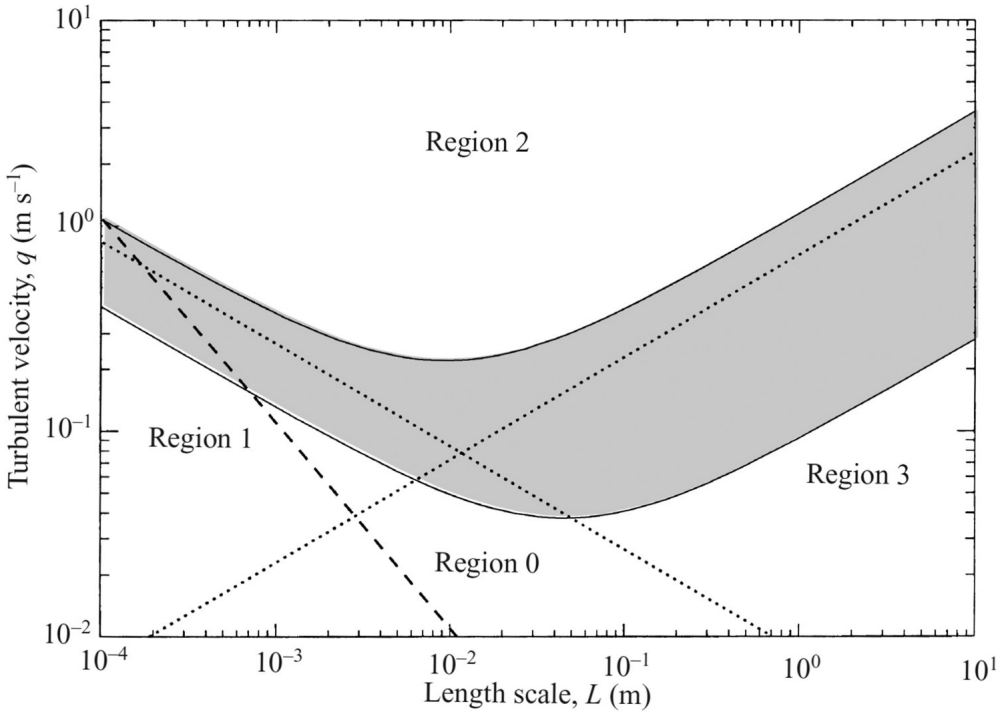

Figure 3.7: A figure to classify free-surface flows into different regions with distinct free-surface behaviours. Turbulence velocity, q as a function of free-surface characteristic length scale, L (Brocchini and Peregrine, 2001; Muraro et al., 2021). The dotted lines are a simplified division of the plane whilst the dashed line represents Re = 100.

Horoshenkov et al. (2013b) proposed new approximations for describing the free-surface of shallow flows. In addition to the features explained above, they discovered the presence of additional free-surface waves (not due to gravity or capillary waves). This is presented as Equation 3.1.1:

$$W(\rho_{lag}) = e^{-\rho^2/\sigma_w^2} \cos(2\pi/L_0\rho_{lag}), \tag{3.1.1}$$

where ρ_{lag} is the spatial lag, σ_w is the spatial radius of correlation and the L_0 characteristic period of the free-surface. More recently, Nichols et al. (2014) suggested that these additional features found by Horoshenkov et al. (2013b) were actually a combination of separate but overlapping oscillating features that decay with an exponential term:

$$f_{shm} = \frac{1}{2\pi}\sqrt{\frac{g}{(1.5N+1)\sigma}}, \tag{3.1.2}$$

where f_{shm} is the frequency of simple harmonic motion, g is the gravitational acceleration, N is the number of free-surface roughness heights and σ is the disturbance height.

Smith et al. (1999) and Kumar et al. (1998) tried to relate the flow surface characteristics to the energy dissipation mechanisms within the flow with some success. Savelsberg and van de Water (2009; 2008) proposed that the turbulence effects on the free-surface are obscured by gravity-capillary waves which propagate away from turbulent disturbances. Interestingly, they were able to measure the free-surface with a scanning laser whilst simultaneously measuring the near-surface flow field using flow visualisation techniques (Figure 3.8). However, Fujita (2011) suggested the turbulent effects on the free-surface could still be seen and found that the "boils" on the free-surface looked very similar to those suggested by Adrian et al. (2000) and Gakhar et al. (2020). What is clear is that flow visualisation tools are essential towards studying the true nature of turbulence impacting free-surface dynamics. The following section presents some of the tools used by the previous hydraulics research and how they can be used to measure the flow and/or free-surface.

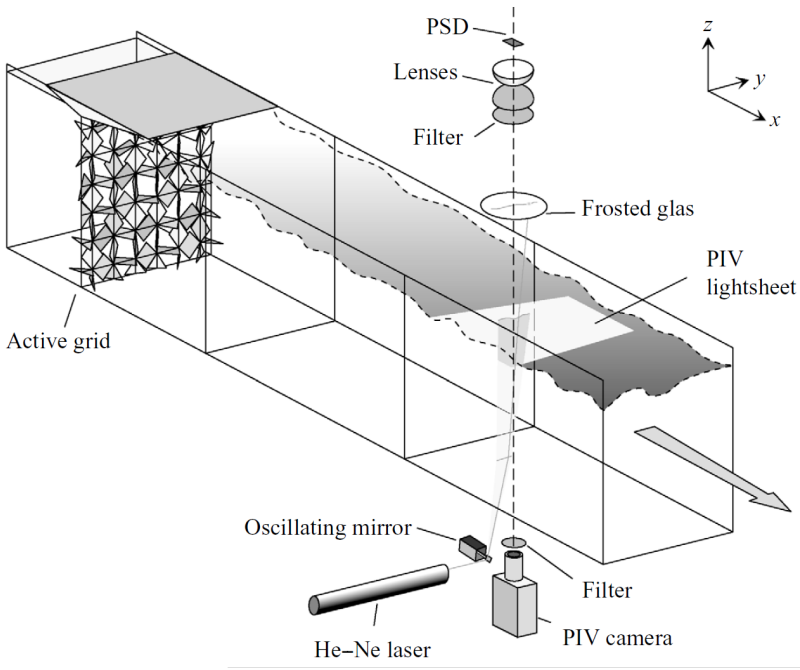

Figure 3.8: Example PIV setup within a flume (Savelsberg and van de Water, 2008). An active grid at the inlet reduces the size of any turbulent features to stabilise the flow, A Helium-Neon laser light sheet is projected into the flow. A camera with an optical filter observes the particles illuminated by the laser light.

3.2 Sensing Technologies

In the past, various technologies have been developed to measure turbulence in water flows. Turbulent measurements in water flow with hot film probes are much more difficult to make than hot wire measurements in air flows. This made it difficult to compare turbulence in air with turbulence in water so whilst research in aerodynamics progressed very quickly in the early 70s, it was only with the development of new devices such as Laser Doppler Velocimetry by Yeh and Cummins (1964) that measuring turbulence in water flows have become possible.

Doppler Velocimetry is a method to measure the velocity of fluids. Objects moving towards a sensor reflect a signal with a higher frequency whilst objects moving away reflect a signal with a lower frequency. This effect is known as the Doppler shift (named after Physicist Christian Doppler). By measuring the change in this frequency, the velocity can be deduced. This can be used in many different applications from the movement of stars and galaxies to the flow of blood inside blood vessels.

To measure position, a time-of-flight (ToF) technique can be used. If the speed of an emitted signal is known (e.g. EM wave travelling at the speed of light in air), and the time between the emitted signal and the received signal is recorded, then the distance to the surface that reflected the signal can be calculated.

The selection of instrumentation depends on the purpose and its use in the laboratory or field. Key performance indicators of instruments include their stability, compactness and sensitivity. Many methods of detecting water flows are available, these can be broadly categorised into intrusive and non-intrusive approaches:

1. Intrusive techniques must penetrate into the flow/free-surface and may cause disruption to the flow/free-surface itself by virtue of its presence.

2. Non-intrusive detection techniques remain in the air and are able to remotely sense flow properties without contact.

Due to the low density of air compared to water, the disturbance to the natural convection

of air by the presence of the remote sensing instrument in laboratory conditions usually does not significantly affect the behaviour of the water and free-surface. Hence, this can be seen as a more desirable approach. This is especially true when considering the potentially high maintenance required for intrusive techniques (for example, due to corrosion).

Lastly, the ability of a sensor to measure a wide area or only a single point location is also an important consideration. The next section will discuss some common and new techniques used to measure water position and velocity.

3.2.1 Intrusive Methods

3.2.1.1 Hot Wire/Film Probe

A hot wire/film probe (or anemometer) is constructed of two vertical probes with a wire/film connected between the tips. A current is supplied through the circuit and heats the wire/film. As the flow passes the probe, heat is transferred from the probe affecting the resistance of the wire. This change is measured and calibrated against a particular flow property such as depth or velocity (Dantec Dynamics, 2017). Two types of hot wire probes exist: constant current and constant temperature.

In constant current, if the water flow is too low, the wire may overheat and burn. If the flow is too high, the current may not be high enough to provide sufficient heat transfer for accurate determination of the flow velocity. Furthermore, when used in water over time, a film will form on the wire. This affects the calibration of the system.

For constant temperature probes, this problem is less severe as only the smaller scales of turbulence will be affected. Patterson (1958) presents a summary of water-based hot-wire probes and the use of electromagnetic and pressure measuring systems for delivering accurate measurements of the flow velocity. The work presented by Kline et al. (1967) covered in chapter 3 used temperature linearised hot-wire anemometers to make mean velocity measurements.

3.2.1.2 Acoustic Doppler Velocimetry (ADV)

Acoustic Doppler Velocimetry (ADV) uses the Doppler Effect to measure the change in wavelength of a signal after it is reflected back from particles travelling in the remote sampling volume. Based on this change, the velocity of these particles can be deduced. A transducer sends out an ultrasonic signal towards the sampling volume. Three or more receivers measure the return signal and convert this into velocities in three directions (see Figure 3.9). The ADV can detect velocities across a range of water qualities and is hence quite versatile. ADVs are often used in the field as well as laboratory experiments due to their reliability and ability to operate in water with high amounts of dirty particles (Cea et al., 2007; Clark and Kehler, 2011; Garcia Novo et al., 2019).

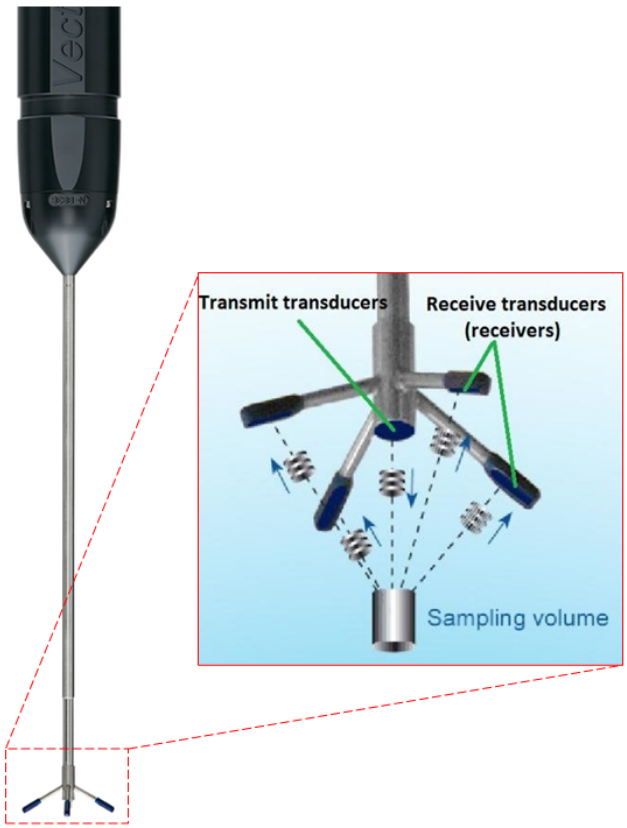

Figure 3.9: Downwards facing 'Vectrino' ADV probe from Nortek (2017). Closeup shows the ADV probe and schematic of the sampling volume (Nortek, 2018).

3.2.1.3 Conductance Probe

A conductance probe detects the free-surface boundary using the changes in conductivity as the water level rises. Conductance is the inverse of resistance and a measure of how easily current flows through a material. The probe is connected to a 'wave monitor' that gives a proportional voltage output (see Figure 3.10). A calibration process links the voltage readings to the depth of water at that voltage. During the test, as the voltage fluctuates, the depth of water can be deduced (Churchill Controls, 2011).

Figure 3.10: Churchill wave monitor for three conductance probes. The gain and datum can be adjusted to change the sensitivity and adjust the zero position of the signal from the probes (plugs into the front of the machine). These modified signals are then output from the rear of the machine to an analogue to digital converter for data capture and storage on a computer. Image taken by the author.

3.2.2 Non-intrusive Methods

Non-intrusive remote sensing methods use a variety of different techniques along the entire electromagnetic and acoustic spectrum to measure the flow. This section presents some common techniques used to measure experimental open channel flows.

3.2.2.1 Laser Doppler Velocimetry

Using a similar principle as the Acoustic Doppler Velocimetry (ADV) in section 3.2.1.2, Laser Doppler Velocimetry (LDV) uses the Doppler effect from a laser signal to gauge the velocity of the flow particles. Instead of an acoustic transducer and receiver, a photo-sensor is used. These do not require any velocity calibration and if a two-colour system or three-beam polarization system is used, they can independently measure the longitudinal and vertical velocity components with great accuracy. However, like ADVs they are point source sensors only able to collect flow information at a single point.

In 2003, Hyun et al. presented a comparison of LDV and a new 'Particle Image Velocimetry' (PIV) technique in open channel turbulent flows. It found similar results in both sets of data, even in regions of flow reversal and high shear indicating that both were suitable sensors for measuring open channel flows.

3.2.2.2 Particle Image Velocimetry (PIV)

Particle Image Velocimetry is used to achieve 2D or even 3D instantaneous velocity maps in fluids. To do this, seeding particles must be used in the flume. A laser illuminates the particles using a plane of light whilst a nearby camera captures to position of the particles. Double frame techniques can be used to capture pairs of image frames and identify the change in position to calculate the velocity field. Ruonan et al. (2016) compared the performance of ADV and PIV techniques finding that the sampling frequency of the ADV device does not influence the time-averaged velocity but has a significant influence on the turbulence detected. The paper recommends a sampling rate of 100Hz in order to measure the turbulence.

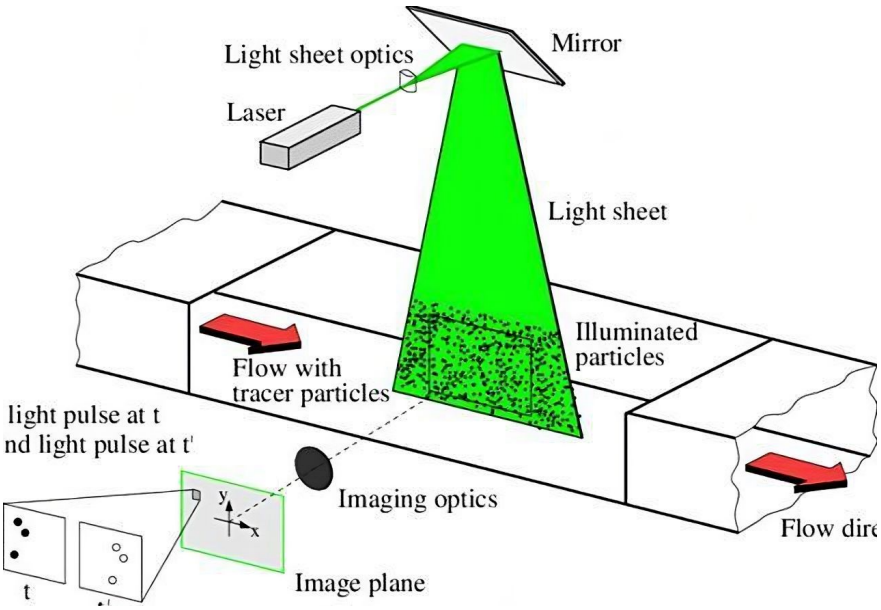

Figure 3.11: Single camera PIV system with a vertical laser plane projected from above the free-surface (Kompenhans et al., 2000). Laser light illuminates the particles within the flow whilst a camera captures their movements over time.

3.2.2.3 Laser Induced Florescence (LIF)

A similar principle is used in Laser Induced Florescence (LIF). A laser excites a fluorescent solute in the flow. After excitation, the energy level of the solute drops, emitting light at a different wavelength. This is recorded by a charge-coupled device (CCD) camera and allows the free-surface to be seen (Lommer, 2002).

When selecting seeding particles for PIV or LIF which do not have neutral buoyancy, it becomes essential to minimise sediment fall or rise to ensure the particles follow flow paths in a representative manner. In reference to Fick's law (COMSOL, 2015), the diffusion of sediment from higher concentration regions to lower concentration regions should balance the sediment settlement, therefore a sufficient flow rate is needed to ensure the turbulent water is able to keep the particles suspended and representative of the vortex structures.

Nezu and Sanjou (2011) presents a combined PIV/LIF technique for synchronous measurement of turbulent coherent structures in a variety of flows from open channels to vegetated and wind-induced flows. Using these techniques the fluid/particle interaction and the relationship between coherent structures and sediment transport could be studied.

3.2.3 Free-surface Sensing

Horoshenkov et al. (2013b) have shown that the flow conditions may be inferred from the measured free-surface dynamics. For example, Nichols (2015) was able to relate the scale of surface features to the scale of turbulent structures. This section will discuss methods for measuring free-surfaces.

3.2.3.1 Acoustic Methods

Ultrasonic probes have been used to measure free-surfaces of turbulence flows. For example, ADS.ltd manufacture probes that use the back-scatter of ultrasonic waves to detect the Doppler shift and obtain a streamwise surface velocity measurement (*ADS* 2020). An image of the ADS Echo is shown in Figure 3.12. The mean surface level can also be calculated based on the time of flight.

Attempts have also been made to directly infer the local surface fluctuation from the scatter of an airborne ultrasonic field. Based on the phase shift of the ultrasonic signal, Nichols (2015) was able to rebuild the features of a rough free-surface, akin to a wave monitor. Dolcetti (2016a) was able to use similar acoustic techniques to collect data and compare it to linear models using the Kirchhoff approximation. However, the limited resolution of the conductance probes affected the accuracy of the numerical model.

Figure 3.12: Example of an acoustic device used to measure the free-surface, the Echo device from *ADS* (2020). This sensor can measure in depths of up to 20 feet (6.1 m).

3.2.3.2 Infrared Sensing

The Microsoft infrared sensors known as 'Kinect' is a group of two 3D motion sensing products originally developed by Microsoft intended for gaming purposes (Microsoft, 2014). These products provide a low cost, low maintenance, 3D imaging capability and have attracted interest from industry and academics alike.

The first generation of the Kinect utilised hardware developed by a company called PrimeSense (Figure 3.13a). It is a 'structured light' approach whereby an infrared projector emits a unique pattern of dots. Based on the distortion of the pattern, the 640 x 480 pixel depth sensor is able to calculate the distance of the object/surface to the camera for each pixel. An RGB optical colour camera of the same resolution is also present. Because the system relies on infrared technology, it also functions in low light/dark environments. It has a horizontal field of view of 57 degrees and a vertical field of view of 43 degrees. The entire system samples at a rate of 30Hz.

(a) First generation (b) Second Generation

Figure 3.13: Different generations of Microsoft Kinect infrared sensors used to capture a 3D depth field. Originally designed for gaming purposes but later tested for research in many different fields (Nichols et al., 2020).

The second generation of the Kinect uses a Time of Flight approach with a 1920 x 1080 pixel colour camera and a 512 x 424 pixel depth camera (Figure 3.13b). This calculates the distance to the object by measuring the amount of time needed for the light to return. The increase in resolution has been possible due to the USB 3.0 connection upgrade allowing higher data transfer capability. It has an improved field of view at 70 degrees horizontal (Kinect 1 = 57 degrees) and 60 degrees vertical (Kinect 1 = 43 degrees). Like the previous

Table 3.1: From Sarbolandi et al., 2015. Kinect device failure ratios: 1 = equal behaviour between the devices. 0 for Kinect 1 and infinity for Kinect 2 indicate high failures respectively. Shades of red intensity show deviations from 1.

	Failure ratio (KinectSL / KinectTOF)	
Ambient Background Light	Below 1μW/cm2	Above 1μW/cm2
	0,55	**INF. ∞**
Depth Inhomogeneity and Dynamic Scenery	Static	Dynamic>40 pixel/s
	4,00	**INF. ∞**
Semitransparent Media & Scattering	Light penetration<80%	Light penetration>80%
	0,16	**INF. ∞**
Multipath Effect	15<Angle<25	25<Angle
	0,00	**1,00**
Linearity Error	< 2.5 m	> 2.5 m
	7,00	**5,50**
Systematic Error: Planarity	< 2.5 m	> 2.5 m
	5,45	**12,12**
Temperature Drift	Before 10'	After 10'
	0,87	**1,52**

generation, the second-generation Kinect is also able to function in the dark.

To date, these infrared sensors have been used in a range of research applications such as medical (to detect heart attacks (Patel and Chauhan, 2014)), robotics and surveillance (Boulos et al., 2011). Its use in 3D real-time modelling is encouraging as this could be adapted to remote sensing of waterways. Through testing of the depth capabilities over seven different types of tests, Sarbolandi et al. (2015) showed the limitations of both the Kinect 1 device and the Kinect 2 device. These findings are summarised in Table 3.1. It appears from the literature that each device shows weaknesses in different areas. The temperature drift performance of both devices also varies compared to each other. This makes their utilisation in side-by-side scenarios difficult.

3.2.3.3 Applications in Research

Corti et al. (2016) further investigated the link between temperature variation and accuracy. The use of a fan to cool the Kinect seemed to reduce the error and increase stability. Furthermore, they discovered multipath errors caused errors of up to 80mm. Multipath errors occur when data from a pixel travels a different path than expected and hence provides an incorrect distance. Examples of multipath errors include reflections off nearby objects

or refraction when it enters different mediums at an angle leading to a different time of flight. Wasenmüller and Stricker (2017) reinforced the findings of Corti et al. (2016). They recommend running the Kinect 2 device for at least 25 minutes to reach a steady state temperature; this was in comparison to the Kinect 1, which appeared to reach a steady state after just a few seconds. Corner pixels in Kinect 2 appeared to deviate with a significant amount of flying pixels. Flying pixels are erroneous depth readings in areas of a sudden depth change. In this respect, the Kinect 1 demonstrated better precision for both smooth and rough surfaces.

This led to the conclusion that Kinect 2 needed extra post-processing to compensate for random noise, flying pixels and multi-path interference. Otherwise, Kinect 1 may be a better option despite the lower resolution.

For Kinect 2, Hansard (2012) presented an attempt to merge depth and colour information together in time-of-flight devices. Here, they demonstrate a 3D projective transformation that could be used to cross-calibrate colour and depth cameras. They also specify the difference between calibration error (due to the imperfect camera and image models) and total error (which includes specific noise and biases). A similar approach should be used in this study.

3.2.3.4 Use in sensing water

In the field of fluids study, Combés et al. (2015) were the first to reconstruct a free-surface using the Kinect camera. However, the use of the Kinect in turbulent flows remained unexplored until Nichols and Rubinato (2016) presented an initial assessment of the Kinect 1 for use in detecting flow surfaces. Martínez-Aranda et al. (2018) compared the Kinect 1 to CFD models identifying some potential limitations such as the limited field of view and the need for an opaque free-surface. This author presented an initial study into the potential for Kinect sensors to be used for mapping clear water surfaces from turbulent open channel flows and gravity waves (Cho et al., 2017).

Based on the root mean squared free-surface roughness height measured on flows over a spherical bed by Nichols (2015), similar to the conditions examined in this thesis, measurements of the surface roughness ranged between 0.2mm to 1mm. Hence, a sensor would need to be accurate to within 0.1mm tolerance. Work described in the methodology development section of Chapter 5 compares the performance of Kinect 1 against Kinect 2 in this application. This was presented at the International Association for Hydro-Environment Engineering and Research (IAHR) World Congress (Cho et al., 2017).

3.3 Summary

Some historical background on the study of water flows has been presented. It was shown that the turbulent eddies have been captured visually as early as 1452 during the Renaissance era. The development of new sensing capabilities enabled more scientific studies on the behaviour of water flow in the 1970s.

Literature on the classification of different free-surface behaviours in open-channel flows has been introduced. Research on the generation and propagation of coherent structures as well as their influence on the free-surface have been reviewed.

Previous attempts to mathematically quantify the relationship between the free-surface dynamics and the flow have had some success but still require further investigation. The need for flow visualisation was highlighted since many discoveries are made that way.

A review of sensor technologies was also presented with a focus on the new possibilities for non-intrusive remote flow and free-surface sensing. Such methods minimise disturbance to the flow and its phenomena, require less maintenance and could gather new data near the free-surface which was previously difficult to achieve. Additionally, wide-area sensors such as cameras are also good tools for flow visualisation. It should be noted that the water surface of most open-channel flows has small vertical features so measurements using infrared wavelengths should give better resolution than methods such as acoustic sensors (which has longer wavelengths).

The following chapter focuses on how open channel flows have been modelled and computationally simulated, the software used, the challenges in modelling the flow turbulence and the free-surface; and their advantages in the digital age.

Chapter 4

Literature Review of CFD Simulations of Open Channel Flows

Computational Fluid Dynamics (CFD) is the process of using the power of computers to calculate and predict the behaviour of fluid motion. This has the benefit of not requiring physical laboratories, simulating flows that may otherwise be very difficult/impossible to set up, and providing a new tool for engineers to explore designs before committing to construction. To increase the speed of the simulation, the work is often split between multiple computer nodes running in parallel (at the same time) or in the case of 'High Performance Computing (HPC)', split between hundreds of computers/nodes. This reduces the workload significantly and can turn year-long simulations into mere weeks. Unfortunately, turbulent flow simulations are still very computationally intensive with high-resolution simulations taking months to run (Shahriari et al., 2020).

The fundamental application of using computational power to solve the Navier-Stokes (NS) equation is well established with much literature providing derivations and explanations. Versteeg (2007) give an introduction on applying computational modelling techniques to fluid physics. In addition, Chapter 9 of *'Computational Methods for Fluid Dynamics'* by Ferziger (2002) gives a comparison between different computational methods for fluid dynamics.

This literature review will cover the most relevant research conducted on open channel

flow simulations. Section 4.1 covers free-surface modelling in CFD, section 4.2 reviews CFD simulations on flow over rough beds, section 4.3 covers the fundamentals in turbulence models and their capabilities, finally section 4.4 introduces CFD software.

4.1 Free-surface Modelling in CFD

Chapter 6 on free-surface flows in the book 'Computational Techniques for Multiphase Flows 2nd edition' by Yeoh et al. (2019) is a good contemporary introduction to surface modelling. In fluid dynamics, there are two main frames of reference: Eulerian and Langrangian. The Eulerian view of the flow focuses on specific fixed locations in the 3D space through which fluid flow through (e.g. speed camera approach). However, Lagrangian view follows an individual fluid parcel as it moves through space and time (e.g. dash cam footage). Within the subset of Eulerian surface modelling, two main types of models exists: Surface and Volume methods. This section will introduce them.

4.1.1 Surface Models

Surface models assume the free-surface as a sharp interface. The following section briefly describes some popular surface models and assesses their suitability. In terms of surface modelling, these include the 'Particles on Interface' method which requires sequential numbering of mass-less particles on the surface and fits a cubic spline using these points (Daly, 1969). Unfortunately, the method does not function if the fluid detaches from the main body. Nichols and Hirt (1973) extends this further using the 'Height' function. As the name suggests, the height of any point in a 2D flow is specified to a reference line such as the fluid bed. This method requires single values describing the free-surface so breaking waves where the free-surface exists in two locations above the bed can cause problems. Lastly, level set methods, first introduced by Sethian and Smereka (2003), are also a good way to model fluid-interface problems.

4.1.2 Volume Models

Volume methods such as Marker and Cell (MAC) present a more versatile approach than surface models. With the use of mass-less markers, the position of the markers are tracked throughout the fluid. A cell is recognised as full if a marker is present, empty if there is no marker and surface if it is a full cell adjacent to an empty cell (Harlow and Welch, 1965). This allows the modelling of detached and merging fluids at the expense of additional computational resources.

Volume of Fluid (VoF) is a similar approach using Eulerian grid methods. Whilst the MAC method utilises marker particles to track the free-surface, the VoF method calculates the volume fraction of the fluid via a transport equation (updated with local velocities). This fraction is then reassembled using different techniques to obtain the free-surface (Hirt and Nichols, 1979).

4.1.3 Other Methods

Whilst these approaches are all using the Eulerian frame of reference, Lagrangian approaches have also been showing promising results such as smooth particle hydrodynamics (SPH). First proposed as a tool to model free-surface flows by Monaghan (1994), SPH is a mesh-less particle-based method first developed by Belytschko et al. (1996) for tackling astrophysics challenges. In open channel simulations, Kazemi et al. (2017) used SPH to model the free-surface but was unable to achieve a good accuracy potentially due to the inability of SPH to model turbulence properly. For more information on SPH and other Lagrangian techniques, the reader is referred to Mansilla (2018)'s thesis on 'Numerical Modelling of Hydraulic Free Surface Flows and Scale Effects Associated with Physical Modelling'.

Due to the computational requirements needed to model the free-surface, many open channel studies actually neglect it all together, instead choosing to apply a rigid lid approximation.

4.2 Use of Rigid Lid Approximation

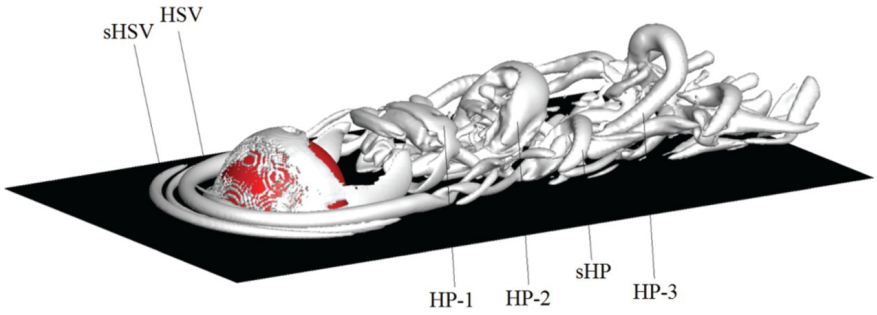

Figure 4.1: Turbulent structures of flow over a hemisphere visualised with the Q-criterion (Stoesser, 2014). Structures labelled HSV are 'Horse Shoe Vortices' whilst structures labelled HP are 'Hairpin vorticies'. Those with a lowercase 's' prefix are secondary vortices.

Singh et al. (2007) performed DNS on a hexagonal closed-packed bed with the flow depth equal to four times the sphere diameter (not revealed). Good agreement with experimental results is seen for the mean velocity, turbulence intensities, and Reynolds stress. This was achieved using a simulation domain of $4\sqrt{3}d \times 4d \times d$ (streamwise $\times$ spanwise $\times$ depth). The LES is run for around 30T (where $T = d/u_\tau$ is the large- eddy turnover time) to obtain a fully developed turbulent field. This was then mapped onto the DNS simulation.

Stoesser and Rodi (2007) used LES code, 'Multi Grid Large Eddy Turbulence' (MGLET) to simulate flow over a rough bed with spheres of 22mm in diameter in a hexagonal closed packed bed formation. The depth of flow was 94mm and the domain was 5h in streamwise, 2h in spanwise and 1h in vertical directions. In total, 46 million mesh points were used. The grid spacings in terms of wall units were $\Delta x^+ = 5$ in the streamwise direction and $\Delta z^+ = 7$ in the spanwise direction. In the vertical direction, the grid spacing was kept at a constant value of $\Delta y^+ = 2.5$ at the bed and then stretched towards free-surface. Periodic boundary conditions were applied in the streamwise and spanwise directions. A constant pressure gradient was maintained during the computation which yielded an average bulk velocity of $u_B = 0.8$ m/s and an average shear velocity of $u_\tau = 0.07$ m/s. The authors claim the results show excellent agreement with the measured data of Detert (2005), although the measured data from Detert were not made public. The authors also state that the results show conformity with the log law for rough walls.

Bomminayuni and Stoesser (2011) also repeated a similar LES simulation but using semi-spheres. They state that a $2\pi H \times \pi H \times H$ domain size for smooth bed flows is commonly accepted. A common theme is that periodic boundary conditions are used in both the span and streamwise directions. The flow is driven by a pressure gradient that maintains a steady flow rate instead of the gravitational force on a slope. Besides Alfonsi et al. (2019), most of these studies did not investigate the role of the free-surface and used a rigid lid approximation for the free-surface.

Table 4.1 summarises the overall hydraulics and software used whilst Table 4.2 highlights key simulation setup parameters.

Table 4.1: Summary of studies on rough bed simulations, software, simulation method, and domain ratio used.

Reference	Title	Domain ratio*	Software	Simulation Method
Xie et al. (2021)	Large-eddy simulation of turbulent free surface flow over a gravel bed	10H x 1.75H x 5H	Xdolphin3D	LES
Alfonsi et al. (2019)	Large-eddy simulation of turbulent natural- bed flow	5.6H x 2H x 0.8H	OpenFOAM	LES
Singh et al. (2007)	Numerical Simulation of Flow over a Rough Bed	6.9H x H x 4H	CgLes	DNS
Stoesser and Rodi (2007)	Large Eddy Simulation of Open-Channel Flow Over and Through Two Layers of Spheres	5H x H x 2H	MGLET	LES
Bomminayuni and Stoesser (2011)	Turbulence Statistics in an Open-Channel Flow over a Rough Bed	6.12H x H x 3.06H	Hydro3D-GT	LES

*(Streamwise x Vertical x Spanwise)

Table 4.2: Summary of studies on rough bed simulations and the key hydraulic and simulation parameters used.

Reference	Depth based Reynolds number	Roughness elements	Relative submer-gence	Δy^+	Δx^+	Δz^+	Vertical elements across free-surface	Total mesh size
Xie et al. (2021)	14,448	median grain size = 4.4mm	0.11	0.5 - 10	$2.1\Delta y^+$	$2.1\Delta y^+$	10.5	256 x 96 x 128 (3.14 x 10^6)
Alfonsi et al. (2019)	46,500	median size = 70mm	0.38	1	20	20	Not stated, hyperbolic tangent used near bed and free-surface	1024 x 160 x 512 (84 x 10^6)
Singh et al. (2007)	3,112	Spheres unknown diameter	0.25	3.6	4.2	4.2	Not modelled	1024 x 128 x 512 (67.1 x10^6)
Stoesser and Rodi (2007)	40,000	Hexagonal packed 22mm dia spheres	0.23	2.5	5	7	Not modelled	800 x 180 x 320 (46 x10^6)
Bomminayuni and Stoesser (2011)	13,680	Square packed hemi-spheres	0.29	2.6	6.6	6.6	Not modelled	1200 x 126 x 600 (91 x10^6)

*(Streamwise x Vertical x Spanwise)

4.3 Turbulence Modelling

Due to the large range of turbulent eddy sizes in a typical open channel flow, solving all of these directly through numerical simulation (DNS) is restricted to only the most simple cases (Zhou, 2018). Instead, two alternatives either use scale resolved simulation (only resolving eddies above a certain size and modelling the smaller eddies), or apply a Reynolds' decomposition and then using a turbulence model (Launder and Sharma, 1974).

Delving deeper, Hart (2016) presents an interesting comparison of different methods of turbulence modelling techniques when simulating flow over dimpled spheres such as golf balls. One figure is of particular interest as it illustrates the potential scales of turbulence which may be simulated on bluff spheres (non-dimpled shapes) such as the bed of spheres used in the experimental fluid dynamics part of this thesis (Figure 4.2).

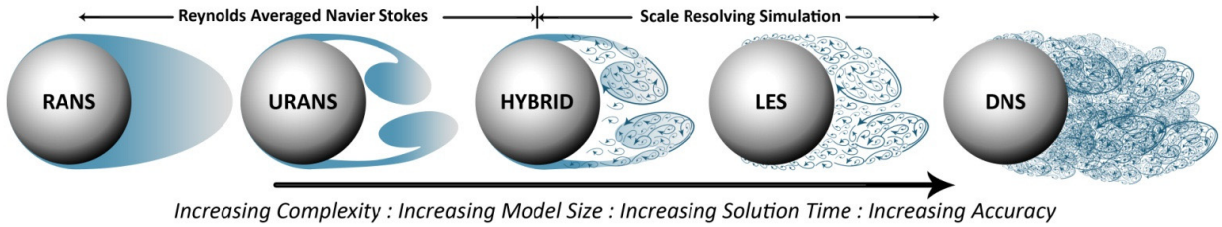

Figure 4.2: Flows over bluff spherical bodies (Hart, 2016). Different turbulent spatial scales can be resolved with different modelling approaches.

Whilst the spheres used in the experimental part of this thesis did not contain dimples, the ability of the models to simulate turbulent flows over spherical shapes is still important.

Figure 4.3 shows the results of Hart (2016)'s research on flow over dimpled spheres using different turbulence models. From left to right models of increasing computational demands. It can be seen that Delayed Detached Eddy Simulation is the least computationally demanding turbulence model to be able to resolve eddies in any significant way which suggests that similar delayed detached Eddy simulation turbulence models could be employed in the current work.

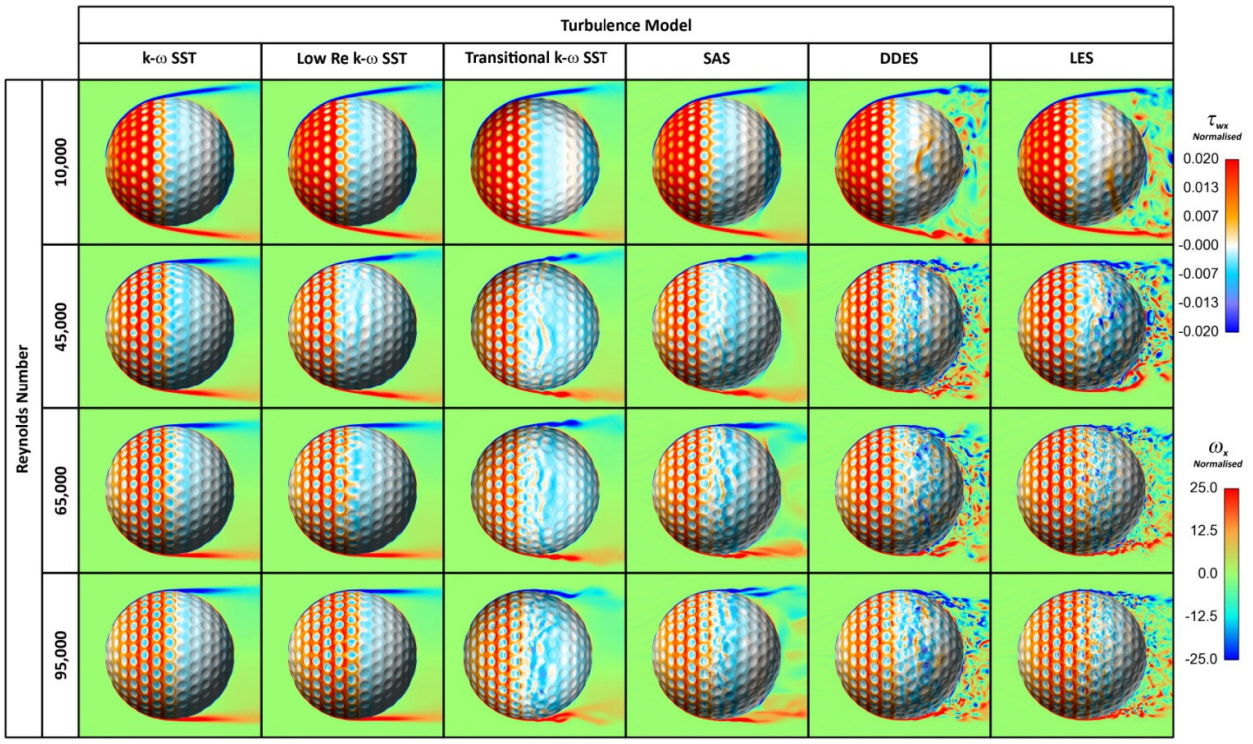

Figure 4.3: Results of flow over dimpled spheres using different turbulence models. Taken from Hart (2016).

4.3.1 Reynolds Averaged Navier-Stokes (RANS)

The Reynolds Averaged Navier-Stokes approach separates the instantaneous flow velocity into a mean component and a fluctuating component (as shown in section 2.3). Substituting this decomposition into the Navier-Stokes equation, an additional term ($\rho\overline{u_i'u_j'}$) appears as shown in Equation 4.3.1.

$$\frac{\partial(\rho U)}{\partial t} + \frac{\partial}{\partial x_j}.(\rho U_i U_j) = -\frac{\partial P}{\partial x_i} + \frac{\partial}{\partial x_j}\left[\mu\left(\frac{\partial U_i}{\partial x_j} + \frac{\partial U_j}{\partial x_i}\right) - \rho\overline{u_i'u_j'}\right] \tag{4.3.1}$$

This $\rho\overline{u_i'u_j'}$ term is known as the Reynolds' stress and needs to be known or at least estimated to solve the NS equation. This is known as the turbulence closure problem. Various models all try to develop methods to obtain realistic values of Reynolds' stress. One popular class of methods is eddy viscosity models. These attempt to obtain the Reynolds' stress via an artificial turbulent eddy viscosity model. Eddy viscosity models assume turbulent fluctu-

ations are random and follow Brownian motion and for most cases, this assumption reflects real-life behaviour even if turbulent fluctuations are not exactly random. Since the nature of a shear velocity profile always ensures momentum is transferred in the direction of the mean velocity gradient (towards the bed boundary), the Reynolds' stress must be proportional to the velocity gradient. This is the Boussinesq approximation (Boussinesq, 1877).

Contemporary models now use a two-equation method to obtain the eddy viscosity (Wilcox, 2008). These are the turbulence kinetic energy and turbulence dissipation equations. Since the presence of a wall limits the maximum size of the eddies in a flow, these models have the mixing length specified algebraically which depends on the distance to the nearest wall. But turbulence is diffused and convected through the flow, it is not static and fixed at some distance from the wall so a transport equation is also used to calculate the dissipation leading to a two-equation model (Launder and Sharma, 1974). The $k-\varepsilon$ model found that the near wall damping function was unreliable so the $k-\omega$ model was developed in response which adjusted the turbulence dissipation equation (Wilcox, 1988). Since both the $k-\omega$ and $k-\varepsilon$ models use a single eddy viscosity variable, the response is linear. More complex models such as the Reynolds' stress model exist to give non-linear features. However, since these are based on the statistical theory of turbulence, they are not able to recreate coherent structures such as bursting phenomena. To achieve greater accuracy, 'scale resolved simulation' approaches such as a 'Large Eddy Simulation (LES)' are needed.

4.3.2 Large Eddy Simulation (LES)

LES replicates the large-scale effects and uses a sub-grid model for the eddies which are smaller than the mesh size (these are also the most computationally intensive). According to Kolmogorov's theory, a cascade process exists whereby the kinetic energy of the mean flow is transferred to large-scale structures and then through the energy flux of smaller and smaller scales until dissipation by viscosity (Kolmogorov, 1941). A consequence of this is that large-scale eddies are more dependent on overall (unique) geometric boundary conditions whilst the smaller scales can be considered to be universal. This is achieved with the use

of low-pass filters that average over time and space. Different sub-grid scale models can be used depending on the filter and the cut-off wavenumber. Scale resolving simulation such as the Large Eddy Simulation (LES) is more computationally expensive and is only really useful if 80% of the turbulent kinetic energy can be simulated (Versteeg, 2007). However, it is more accurate than RANS because it calculates the larger eddies properly instead of using a model. Where the eddies become smaller, the mesh must be finer leading to more computational cost.

When 80%-90% of the turbulent kinetic energy is resolved, the LES method can use a sub-grid model to simulate the remaining turbulent energy within the mesh cells. With LES, it becomes possible to model and track coherent turbulent structures within the flow field.

4.3.3 Application in Hydraulics

Dey (2014) provides a good overview of how turbulence modelling is achieved in open channel simulations in the book 'Fluvial Hydrodynamics'.

Keylock et al. (2005) introduces the potential of LES for use in the field of fluvial sciences. In particular, it provides some useful examples of early work into the use of LES in a fluvial context. However, he states that a number of advances in computational power and numerical methods are required before LES can be effectively applied at the river reach scale. Unfortunately, the high mesh requirements of LES lead to very computationally expensive simulations. Although the paper was published in 2005, Nguyen (2015) also re-iterates this and provides an excellent explanation of why deploying LES in river engineering and hydraulics remains challenging even after 10 years; mainly due to the limitation in computational power and the large range of scales which must be calculated. Now in 2022, the computational power has increased and smaller-scale LES simulations are becoming possible (e.g. Alfonsi et al., 2019).

4.3.4 Hybrid LES-RANS

A LES technique known as Detached Eddy Simulation (DES) attempts to use RANS modelling as the sub-grid modelling. This combines the advantages of both methods by providing the accuracy of LES without the need for very fine and computationally intensive meshes near the walls. Detached eddies are those that are farther away enough from the walls to not be affected significantly by the presence of the walls. In DES, the areas away from the wall use the LES method whilst areas near the wall are calculated using RANS. Heinz (2020) presents an excellent review of current and past hybrid RANS-LES methods for turbulent flows. Although DES was originally designed in 1997 for use with the Spalart-Allmaras model (Spalart et al., 1997), in 2001, his co-author Michael Strelets proposed implementing this with other RANS models by modifying the length scale (Strelets, 2001).

Another LES approach is the wall-adapting local eddy-viscosity (WALE) model of Ducros et al. (1998). This method has been tested extensively and validated experimentally in previous works (Korachi et al., 2012; Nicoud and Ducros, 1999). Korachi et al. (2012) compared the ability of WALE and Smagorinksky to model 3D viscosity using the WALE in the case of an open channel expansion. The results show the Smagorinsky model did not perform as well as WALE, requiring a damping function to correct the viscosity in the near wall region.

Studies in the past often preferred to represent the rough channel bed using simpler and well-defined geometry (see e.g. Leonardi et al., 2003; Miyake et al., 2002). Whilst they enabled an understanding of near-wall behaviour and turbulent flow properties, they were not truly representative of a typical rough bed in open channels. A more suitable arrangement for 3D roughness elements involves close packing in a specific pattern. Stoesser et al. (2003) performed a LES simulation of open-channel flow over a bed roughened by a matrix of staggered cubes, Bhaganagar (2008) performed a DNS using regular three-dimensional roughness elements. Finally, similar studies were conducted by Stoesser and Rodi (2007) and Singh et al. (2007) using LES and DNS, respectively, by roughening the bed with a layer of spheres.

4.4 CFD Software

Many software for CFD simulations exist from companies such as Altair or ANSYS. For example, the Fluent package within ANSYS is one of the most well-known commercial CFD software programs because in addition to simulating CFD with its Fluent package, ANSYS has other capabilities such as Finite Element Analysis for solid mechanics and multi-physics coupled simulations. However, the software is not always readily available and the cost can be prohibitive. An alternative to commercial software is open-source CFD packages such as OpenFOAM. OpenFOAM is one of the leading open-source software packages with easy compatibility for parallel high-performance computing (HPC) architectures. Originally known as FOAM (Field of Operation And Manipulation), OpenFOAM is free and takes advantage of C++'s object-oriented programming. This makes the use of toolboxes, libraries and external functions convenient. The interface is primarily through command line and programming (unlike ANSYS which has a graphical user interface). Documentation and online support is community-based and less centralised compared to ANSYS (Schulze and Thorenz, 2014), nonetheless, the open-source nature makes it a necessary tool for research. It is capable of simulating a wide range of flows from open channels to jets and buoyancy-driven flows.

Many studies have been conducted to assess the abilities of ANSYS and OpenFOAM to provide realistic results (Ambrosino and Funel, 2006; Ariza et al., 2018; Welahettige and Vaagsaether, 2018). For example, Ambrosino and Funel (2006) compared OpenFOAM and ANSYS Fluent simulations using a steady turbulent flow over the car body simulation on an HPC platform. They used the same ANSYS generated mesh in OpenFOAM with the $k - \varepsilon$ RANS model and found comparable results between OpenFOAM and ANSYS. Most recently in 2020, Shahriari et al. presented selected applications of OpenFOAM in hydraulic engineering demonstrating its capabilities as an open-source piece of software. Based on these and many other literature (Bayon and López-Jiménez, 2015; Bayon et al., 2015; Teuber et al., 2019), OpenFOAM certainly has the potential to be a suitable open source equivalent to the commercial code of ANSYS. The following paragraph discusses the use of OpenFOAM

for simulating open-channel flows.

Hedlund (2014) presented an evaluation of RANS turbulence models for simulating fully developed channel flows with a Reynolds' number of 13,350. The results showed that the $k-\omega$ models generally performed much better than the $k-\varepsilon$ models. This seems reasonable since the $k-\varepsilon$ models do not predict near-wall turbulence with strong pressure gradients very well. The $k-\omega$ implementation in OpenFOAM is based on work by Wilcox (1988) and has been shown to perform well in wall-bounded flow.

Meanwhile in the LES method, Rezaeiravesh and Liefvendahl (2018) assessed the effect of grid resolution on an LES simulation of a wall-bounded turbulent flow and found that the selection of numerical scheme for the convective term has a significant impact on the error. This is reflected in work by Montecchia et al. (2019) which explains some of the issues with large numerical dissipation. The suggested improvements to LES utilise an anisotropy-capturing subgrid-scale (SGS) stress model capable of reducing the numerical dissipation. Home et al. (2009) used the hybrid DES Shear Stress Transport model to simulate turbulent open channel flows in OpenFOAM. They found that the turbulent variations scaled well and the OpenFOAM implementation of the DES method was viable. In normal DES simulations using RANS models, the anisotropic property of turbulence is not normally accounted for since all of them use an eddy viscosity model. However, Jee and Shariff (2014) investigates the use of a DES v^2-f model which is able to account for this property and possibly give more accurate results, especially near the bed.

4.4.1 Free-surface Modelling in OpenFOAM

The free-surface modelling within OpenFOAM can be achieved using several methods. These are reviewed here.

4.4.1.1 InterFoam

Schulze and Thorenz (2014) introduces one example of a Volume of Fluid (VoF) method through the *interFoam* solver and applies this to hydraulics by demonstrating some core functionalities, meshing process and the mathematics behind the solvers. Hänsch et al. (2013) presents a useful comparison between surface modelling with OpenFOAM's VoF method (*interFoam*), ANSYS' CFX VoF surface modelling and a new multi-size approach (MUSIG model) where not only interfaces for large gas structures are detected, but also smaller scale bubbles that are trapped beneath the free-surface. Since this present study does not contain free-surfaces with air bubbles, the benefit of the new approach is not so relevant. Of note, however, is the ability of the *interFoam* solver to properly capture the complex collapse of the water column. Deshpande et al. (2012) further provides evidence of *interFoam*'s capability with respect to pure advection, dynamics with high Weber numbers and dynamics in surface tension-dominated flows. Numerous studies have used the *interFoam* solver to analyse open channel flows with hydraulic applications. For example, Thorenz and Strybny (2012) used *interFoam* to simulate part of a lock filling process in canals using a multi-dimensional hybrid approach. Higuera et al. (2013) applied *interFoam* to coastal areas, Morgan (2013) applied *interFoam* to coastal wave structure interaction whilst Shuard et al. (2016) applied it to circular two-phase pipe flows. Of most relevance, Bayon et al. (2015) applied *interFoam* to the sewer simulation of the South Valencia sewage collection system when it had to be diverted in 2014 for new high-speed rail construction. Within the simulation domain, the presence of a stilling basin is of particular interest since it creates some large-scale roughness on the bed in a similar way to the experimental results obtained in this thesis. Three RANS models were used by Bayon et al. (2015) in the 3D simulation: Standard $k-\varepsilon$ (Launder and Sharma, 1974), RNG $k-\varepsilon$ (Yakhot et al., 1992) and $k-\omega$ SST (Menter, 1993). These

were compared to experimental results of a 1:20 scale physical model with similar Froude numbers to maintain the same sub-critical/critical flow regimes (the actual Froude numbers used were not stated). It was found that all three turbulence models were able to simulate the flows accurately.

4.4.1.2 PotentialFreeSurfaceFoam

As the focus is on the water behaviour and because the flow being simulated is sub-critical/does not involve any breaking waves it may not be necessary to use two-phase solvers such as *interFoam* and its variants. A solver called *potentialFreeSurfaceFoam* removes the air phase and simply calculates the velocity potential at the free-surface boundary. This is particularly useful for incompressible, steady-state flows such as open-channel free-surface simulations. The free-surface can be modelled as a dynamic pressure boundary (*waveSurfacePressure*) with a wave height field (zeta) being tracked through time (surface tracking algorithm). In effect, the wave heights are approximated using their potential energy. Because the solver is more simple than solvers using the full Navier-Stokes equations, it can reduce computational costs (Moura Paredes, 2012).

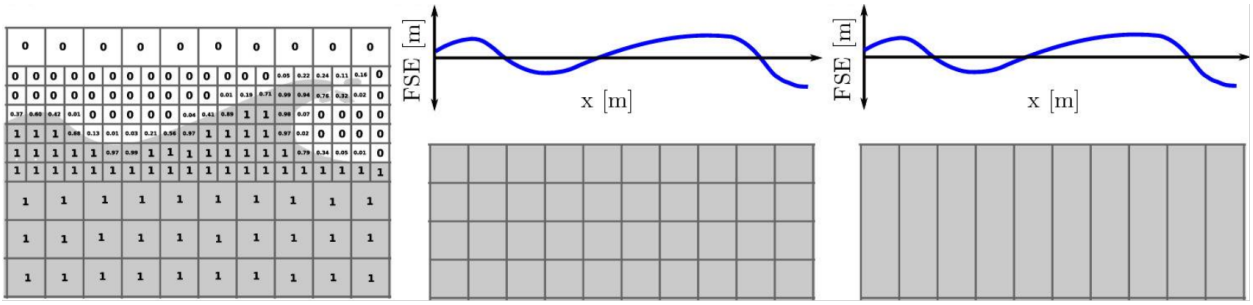

Figure 4.4: Depiction of methods to capture the free-surface in OpenFoam. Take from Schmitt et al. (2020). Left: The surface capturing method, where the VoF indicates the fraction of water present in each cell ranging from pure air (0) to pure water (1). Middle: The surface tracking method. Right: Shallow water approach, where the free-surface elevation is a single-valued function of position in the Numerical Wave Tank.

In literature, Feinberg et al. (2019) applied this solver to the study of cross-flow tidal turbines operating in shallow water. Schmitt et al. (2020) compared the performance of the *potentialFreeSurfaceFoam* solver with the more conventional *interFoam* as well as the *shallowWaterFoam* solver (Figure 4.4). One test that was carried out simulated flow over a

submerged obstacle (referred to as a shoal in their paper) and assessed the similarity of the free-surface behaviour immediately above and in the regions behind the submerged obstacle.

In Figure 4.5, the free-surface fluctuation above the source (WP1) and the submerged obstacle (WP2) is in close agreement for all the solvers. However, in the wave field after the submerged obstacle (WP3), the *potentialFreeSurfaceFoam* and *shallowWaterFoam* show some differences. For *shallowWaterFoam*, it is able to capture the main peak but not the subsequent wake field. Meanwhile, the *potentialFreeSurfaceFoam* solver is generally not able to capture the main peak or the wave field.

4.5 Summary

The field of CFD research is very active and improvements are always being made to CFD codes to increase accuracy whilst reducing computational demands. Since the commencement of this PhD in 2017, much research has been published with new ideas and methods. It is important to select a robust and well-established method rather than focus on the cutting-edge techniques which have higher risk and cannot be as easily replicated. OpenFOAM v7 was chosen as this was the latest version compiled and optimised on the supercomputer when the CFD work began. It contained the latest improvements to wave modelling for marine and offshore applications as well as turbulence modelling. The full release notes can be found on the OpenFOAM website (OpenFOAM, 2017).

The literature review conducted suggests that when used correctly, OpenFOAM is as capable as commercial software such as ANSYS. LES methods such as DES and WALE show the best potential when aiming for an accurate low computational cost approach to modelling turbulence in open channel flows. The *interFoam/potentialFreeSurfaceFoam* solvers also appear to be capable of simulating the free-surfaces in this present study.

The next chapters will introduce the development and final methodologies used in the experimental testing and CFD study.

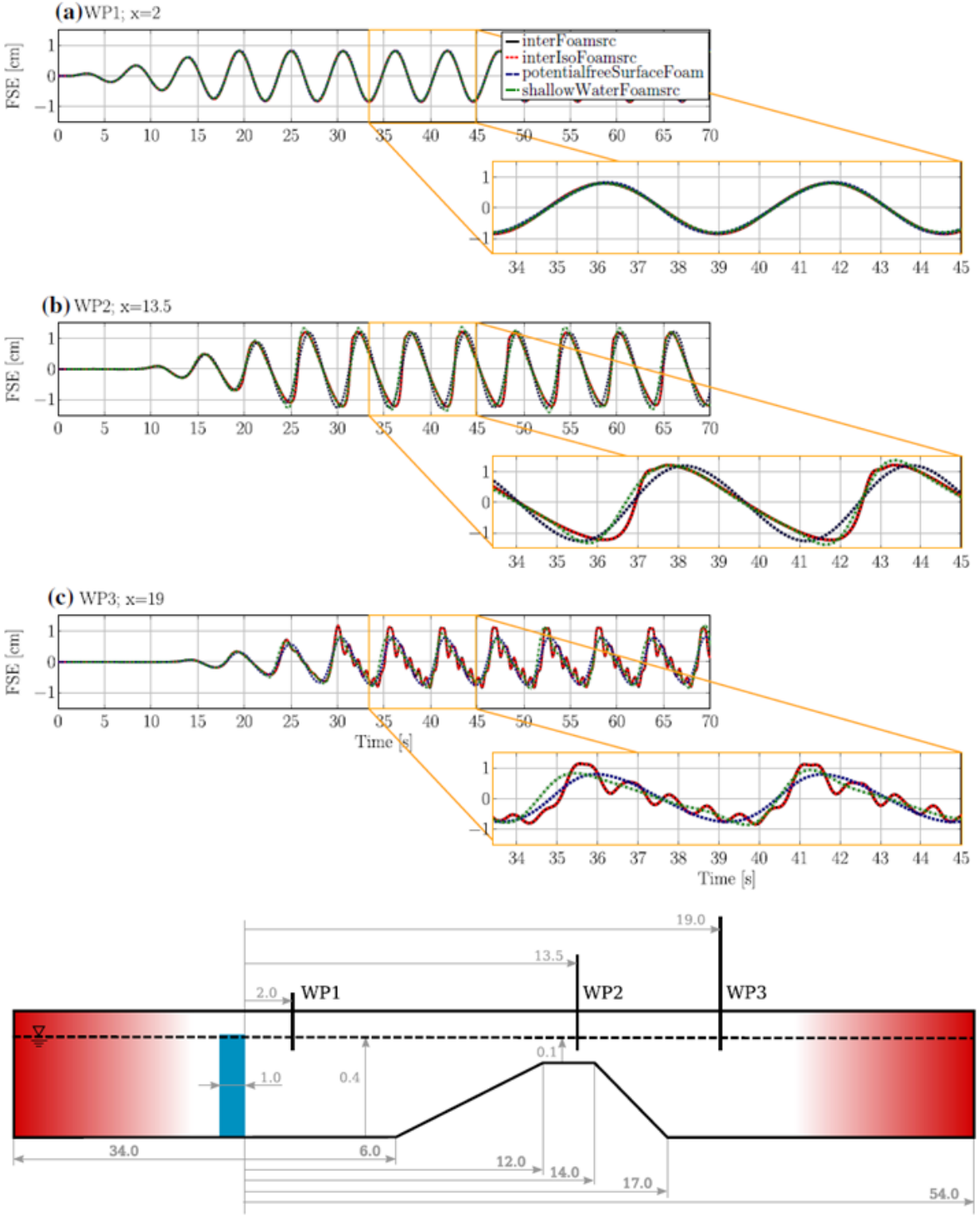

Figure 4.5: Figure from Schmitt et al. (2020). Time traces of the free-surface elevation (in cm), were measured at three different wave probe locations along the Numerical Wave Tank. Schematic not to scale. The source region is marked in blue. The up-wave and down-wave beaches are marked in red.

Chapter 5

Experimental Flow Testing Methodology

Within the Cartesian coordinate system, fluids can flow in three dimensions. In this thesis, the notation for these three directions is defined as:

- X - streamwise following the flow downstream
- Y - perpendicular to the flow representing the depth of the flow
- Z - transverse across the width of the flow

These are accompanied by their respective velocities $u(t)$, $v(t)$ and $w(t)$. Where a sensor has a different coordinate axis system, these will be converted to the axis system defined above at the earliest opportunity.

This chapter will begin by describing the development of the methodology through preliminary testing. This is because some sensors and novel whilst others are more established traditional techniques. Therefore, some testing is necessary, for example, to test the abilities of the Kinect infra-red sensors to measure the free-surface and understand how it works in conjunction with the other sensors. For example, the placement of intrusive probes into

the water immediately upstream of the remote infrared sensor's field of view could significantly affect the free-surface dynamics observed by the sensor. Section 5.1 introduces the preliminary testing and the development of the methodology by applying the sensors under various testing conditions. Section 5.2 presents the final methodology used to carry out the experimental open channel testing in the flume and explores some limitations and drawbacks regarding the setup and sensors used.

5.1 Preliminary Testing - Methodology Development

To test the remote infrared sensors mentioned previously, colourant needed to be added to water in order to create an opaque surface enabling the free-surface to be 'sensed'. Without this, the multi-path errors identified in the literature review will become prevalent due to the translucent nature of the water causing diffraction. Two colourants that have shown potential and will be explored here are milk and Titanium Dioxide (TiO_2). This section describes the preliminary tests which aim to:

1. Deduce the settling characteristics of the various colourants,
2. Identify the minimum concentration of colourant needed for the infrared sensors, and
3. Test the performance of the infrared sensors on water flows with large dynamic features such as gravity waves.

For continuity, the findings of these preliminary tests are also included here as they inform the setup of the final experiment. The results of this work have been published (Cho et al., 2017; Nichols et al., 2020).

5.1.1 Setup and calibration of the Kinect sensors

As shown in Figure 5.1, a rectangular container was used with a first-generation Kinect and a second-generation Kinect mounted onto a frame above the container.

Figure 5.1: Setup to assess the performance of the Kinect infrared sensors in detecting the free-surface with different colourant concentrations and the settling times of each colourant.

To mitigate the fish eye lens distortion effect mentioned by Hansard, 2012 and ensure the image is rectified and orthogonal, a spatial calibration was carried out using a 500mm x 1200mm x 9mm chequerboard (Figure 5.2). Each square was 50mm in length and width. Taking pictures of an object with known dimensions allows a pixel-to-mm ratio to be defined. Whereas the Kinect 1 depth sensor has the same resolution as its onboard colour camera, the Kinect 2 depth sensor has a different (lower) resolution compared to its onboard colour camera. Hence, a transformation was first applied to downscale the colour camera resolution to the same resolution as the depth camera.

Figure 5.2 shows the results of MATLAB identifying the points of the chequerboard in the Kinect 2 colour image. Figure 5.3 show the manual adjustment of the points to fit onto the depth image of Kinect. This was then fed into the transformation to downscale the colour image. The fact that a flat black and white chequered board can be seen by the depth sensor raises concerns that the depth it senses changes based on the colour. This is not good as the colour of an object does not affect its distance from a sensor.

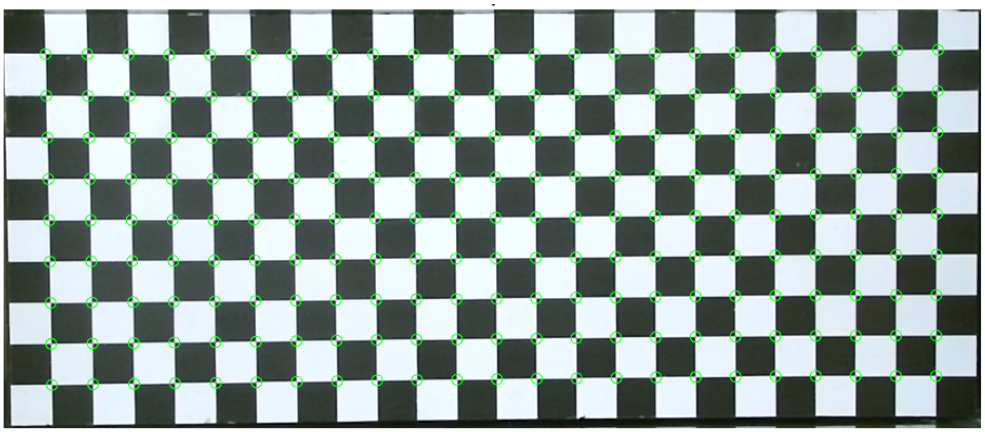

Figure 5.2: Colour grid image used for rectilinear spatial calibration. Points identified by the software are shown with green circles.

Figure 5.3: Depth image reconstructed from the Kinect v2 infrared sensor. Points identified manually for calibration are shown in green circles.

5.1.1.1 Spatial Calibration

After down-scaling, the spatial calibration was applied to both Kinect 1 and Kinect 2 cameras by calculating the lens distortion based on the colour camera (Figure 5.2) and then applying the same transformation to the depth images. Figure 5.5 and Figure 5.4 show the results after the transformation. It can be observed that the calibration grid is now orthogonal and free of lens distortion effects.

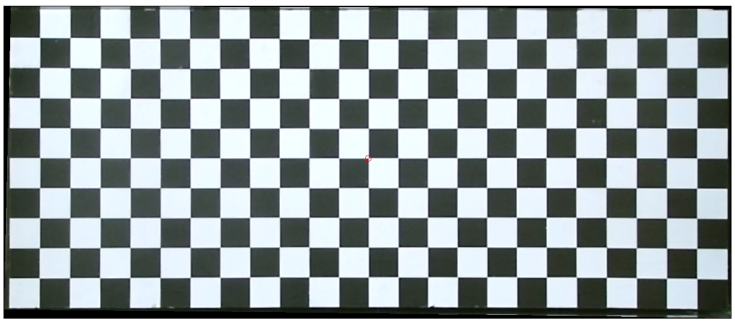

Figure 5.4: RGB image of the Kinect colour data after spatial calibration. The image of the grid lines is now rectilinear as the camera lens distortion has been removed.

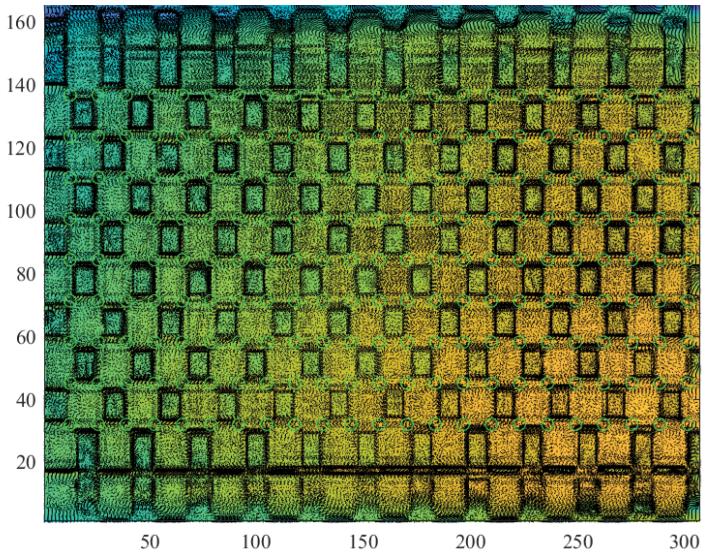

Figure 5.5: Contour map of the Kinect depth data after spatial calibration. The contours are now rectilinear as the camera lens distortion has been removed.

5.1.1.2 Depth Calibration

Depth calibration was carried out and established a linear relationship between the distance measured by the infrared sensor and the vertical height of the board from the bed of the container (Figure 5.6). This was done for each pixel, x using the *polyval()* and *polyfit()* functions in MATLAB such that the depth detected in that pixel, $f(x)$ is given by:

$$f(x) = P_1 x + P_2, \tag{5.1.1}$$

where P_n is a matrix containing the polynomials of a linear line (with n = 1 for the gradient and n = 2 for the y-intercept).

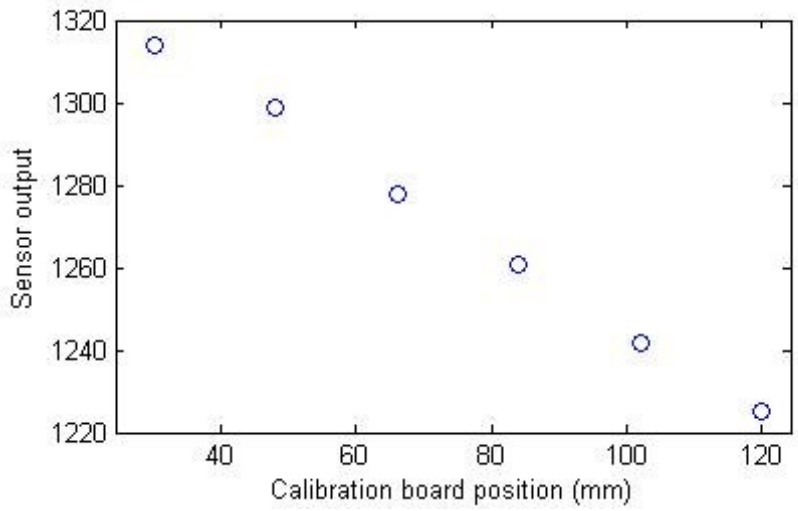

Figure 5.6: Depth calibration of Kinect sensors. Raw sensor output vs. various depth positions represented with a calibration board position. The datum was taken as the internal base of the container.

5.1.2 Settling Characteristics

The settling characteristics determine how often the water needs to be mixed and the window of opportunity to make free-surface measurements before the colourant settles and the free-surface becomes translucent again.

At the 2% concentration recommended by Hujaleh (2016), stability tests were carried out to investigate the settling characteristics of the colourants. It was suspected that some colouring might precipitate to the bottom of the container reducing the effective concentration and hence altering the apparent surface level. This test was intended to identify any settling issues during the experimental time scale that will be used within the main experiment.

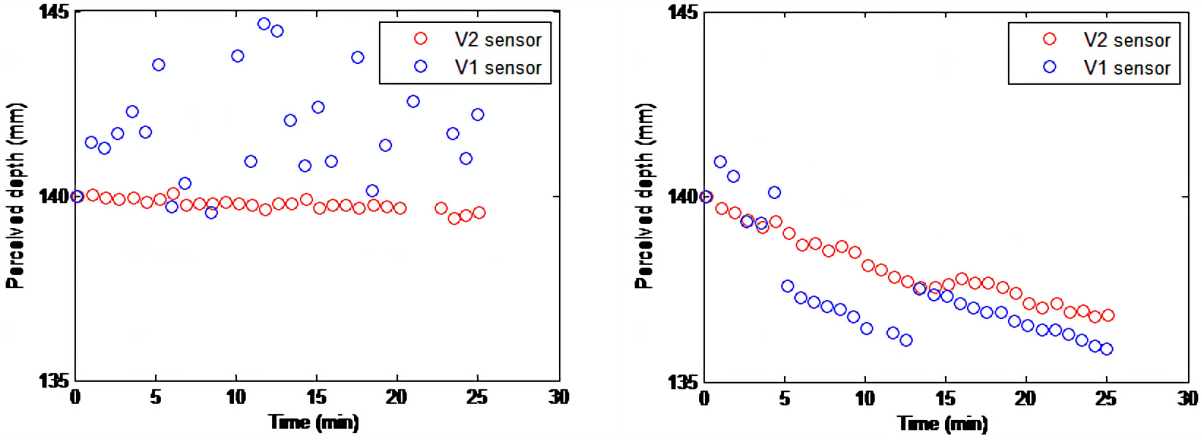

(a) Milk (b) TiO_2

Figure 5.7: Settling characteristics of two different colouring agents over time and their effect on the perceived depth for two generations of Kinect infrared sensors. Real depth was 140mm. Percentage colouring concentration (%) was calculated by mass relative to water.

Figure 5.7 show the change in perceived depth after mixing. The depth slowly decreases for both colourants but is much faster for TiO_2. For milk, the Kinect 1 sensor show scattered perceived depths, which suggest the concentration could be insufficient. While it may also suffer from potential issues with TiO_2, there is a clear potentially adjustable trend. Data points from Kinect 2 indicate a small deviation around 5 minutes. This maybe an uprising of colourant or sudden movement of the frame. Flows have minimal settling, these results suggest that the minimum concentrations used by Nichols are not sufficient. The following test investigates the minimum concentration required.

5.1.3 Threshold Concentration Test

The minimum concentration threshold is important because an opaque free-surface prevents the infrared sensors from detecting the bed or being diffracted by the water. Using the first generation of the Kinect infrared sensor, Nichols and Rubinato (2016) suggested the threshold concentration of milk was 2%. Similar work undertaken by Hujaleh (2016) suggested the threshold concentration of TiO_2 for the same sensor was 0.04 kg/m^3. Therefore a series of tests were performed to conclusively validate these claims and see if Kinect 2 has the same concentration requirements. For each test, 31 litres of tap water from Sheffield was used. The container was filled to a sufficient depth (140mm) and within the range of the maximum and minimum heights used for the depth calibration.

In the first test, the concentration of TiO_2 was incrementally increased from 0 to 0.100 kg/m^3. TiO_2 is anatase titanium (IV) oxide from Acros Organics (Fair Lawn, New Jersey, United States) with a molecular weight of 79.88 kg/kmol. The container was then cleaned.

In the second test, the concentration of full-fat milk was varied from 0 to 2%. Depth maps of the container were generated by the Kinect at each concentration. Figure 5.8 indicates the perceived changes in depth detected by both infrared sensors as the concentrations are increased for milk and TiO_2. It is clear that the concentration of milk used previously by Nichols may not have been optimal. 4% milk or 0.01 kg/m^3 TiO_2 should be used as a minimum so that the perceived depths are accurate. At low concentrations, the Kinect 2 sensor senses a depth which is too low whilst the 1 sensor senses abnormally high depths.

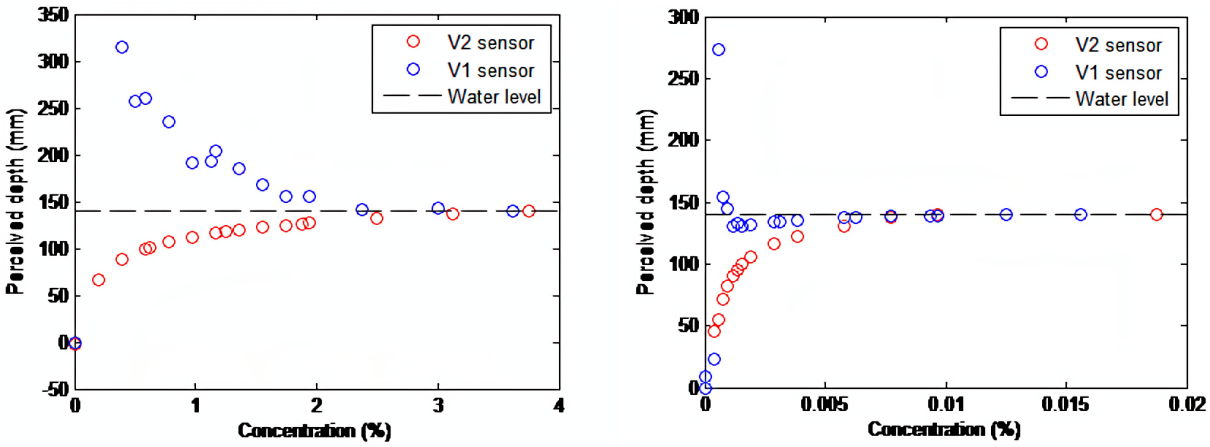

(a) Milk (b) TiO_2

Figure 5.8: Concentration of two different colourants and their effect on the perceived depth by the Kinect infrared sensors. Real depth was 140mm. Concentration of TiO_2 was 0.01%.

5.1.4 Gravity Waves Test

5.1.4.1 Methodology

Since both colourants appeared to have advantages and disadvantages regarding settling time and threshold concentration, further testing with both colourants was deemed necessary. Larger surface features were generated to test the dynamic performance of the second generation of Kinect. This is compared to the Kinect 1 and a conductance wave probe.

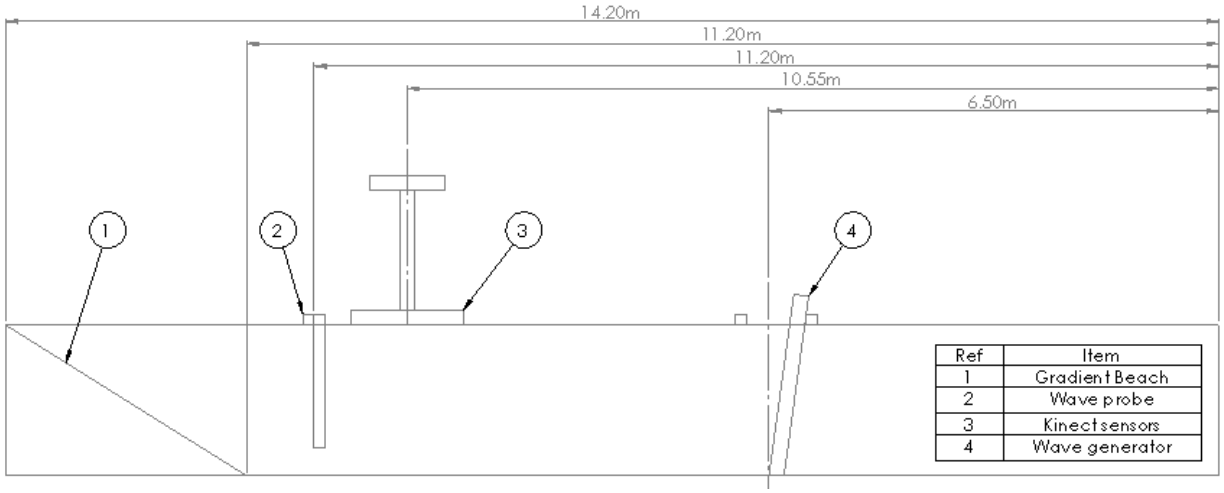

Figure 5.9: Schematic of the experimental wave tank setup for testing the sensitivity of infrared Kinect sensors using artificial gravity waves (Not to scale). The wave generator has end stops to improve the consistency of waves. Generated waves travel from right to left.

5.1.4.1.1 Water Tank: A wave tank was created by blocking off a recirculating flume within the University of Sheffield RA8 Mining Block laboratory. This enabled tests to be conducted in still water. The wave tank (Figure 5.9) had an experimental length of 6.0 m, a width of 0.5 m and a maximum depth of 0.450 m. A partition was used to block and shorten the flume to create the wave tank, this also reduced the amount of colourant needed. For this set of tests, there was no gradient and the measurement section was 10.1 - 11.2 m from the upstream end of the re-purposed flume.

5.1.4.1.2 Colourant Pure water and two colourants were tested, milk and TiO_2. As determined from the static tests, the concentration of milk was 4% and the concentration of TiO_2 used was 0.161 kg/m^3. The TiO_2 powder was first pre-mixed in a beaker with some water in small batches before being poured into the flume. This ensured a more homogeneous mixture preventing the powder from simply settling into the flume bed. Figure 5.10 show TiO_2 mixture being added.

Figure 5.10: TiO_2 colourant mixture being added to the flume after pre-mixing preparation in a beaker.

5.1.4.1.3 Testing hydraulic conditions For each colourant (and clear water), a set of 24 gravity wave conditions were examined. Still water was established at depths of 49, 89, 129, 169, 209 and 249 mm. For each depth, four gravity wave conditions were established using a reciprocal wave generator, using two different frequencies (0.5 and 1 Hz) and two different horizontal stroke lengths (175 mm and 350 mm). To avoid the reflection of waves from the wall at the opposite end of the flume, a scaled beach was used to dissipate waves. Figure 5.11 shows an example wave condition at 209mm depth, 1 Hz and 175mm stroke length.

Figure 5.11: Gravity wave in the measurement region, generated at 209mm depth at 1Hz and 175mm stroke length.

5.1.4.1.4 Sensors: The flume was fitted with Microsoft Kinect 1 and 2 sensors. This allowed a comparison of the device's performance. A conductance-based wave monitor was also installed as an established technique to validate measurements (Dolcetti, 2016b).

5.1.4.1.4.1 Kinect Infrared sensors: The Microsoft Kinect 1 and 2 devices were mounted 11.20m away from the upstream end of the flume. These are mounted onto an aluminium extrusion frame as seen in Figure 5.12. The distance from the front face of the depth camera to the bed is 1.5m. The Kinect sensors were calibrated using the same method presented in section 5.1.1. As a range of depths were tested, aluminium extrudes of 40mm thickness were used to lift the calibration board (9mm thick) so that seven different calibration heights were obtained (9, 49, 89, 129, 169, 209 and 249mm).

5.1.4.1.4.2 Conductive wave probe: In order to validate the Kinect data, a conductance-based wave probe was installed to measure depth data in a small area. The probe consists of two stainless steel wires, 1.5mm in diameter and 12.5mm apart (Figure 5.13). The probe was insulated against the metal support bracket using rubber inserts.

(a) Base of the Kinect mounting frame attached to the flume

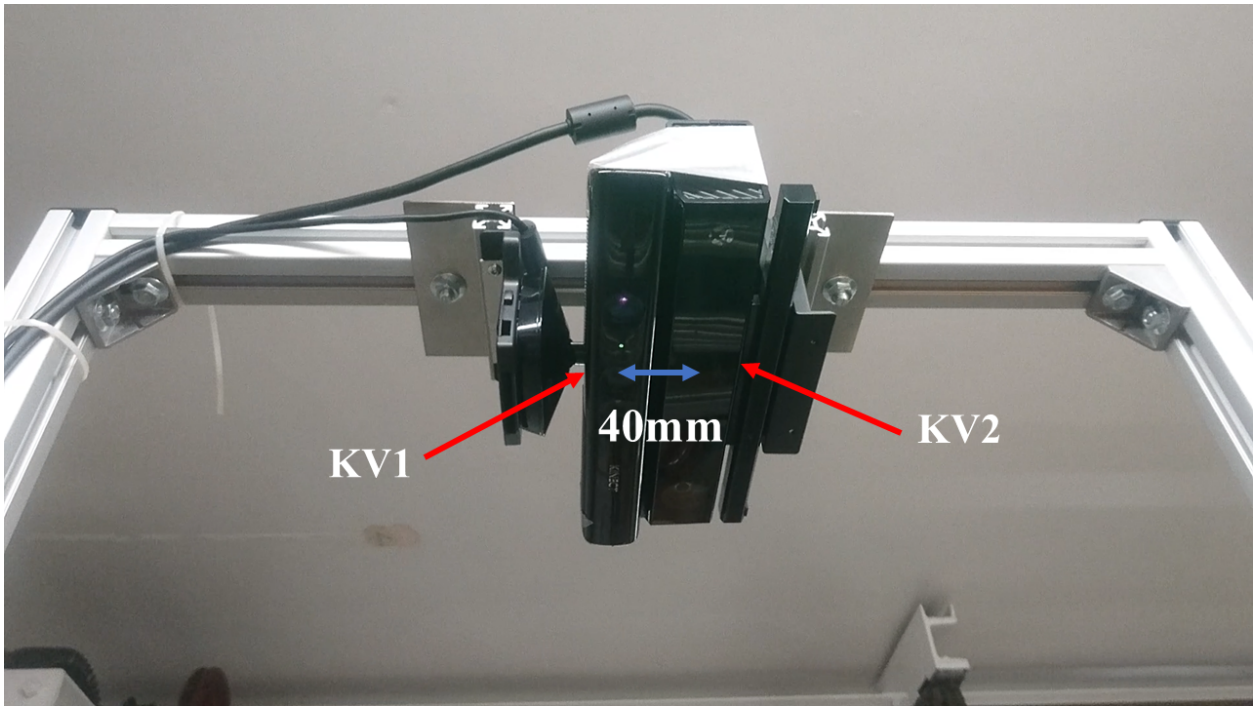

(b) Kinect devices on the Kinect support frame above the flume

Figure 5.12: A rigid mounting frame for the two infrared Kinect sensors. These are located above the flume pointing down towards the free surface and shown from different viewing angles.

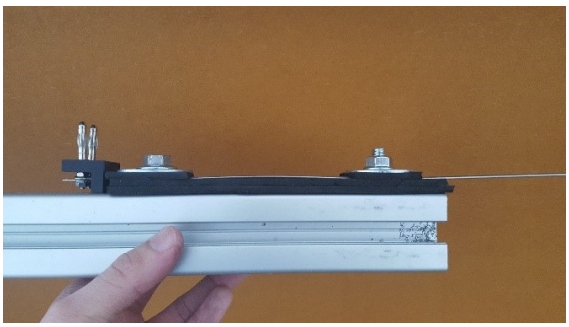

(a) Wave Probe assembled

(b) Wave Probe assembly

Figure 5.13: Conductance wave probe assembly. Used to measure the free-surface fluctuation by detecting the change in conductivity with changing water depth.

Two screws connected the wave probe to the metal rail. The area of the wave probe that was near the screw was insulated using cellophane tape and was insulated against the connecting washer using additional rubber inserts. The probe was placed in the middle of the flume (250 mm from the side edge of the flume) and 100mm within the downstream edge of the measurement area (Figure 5.16). This ensured any secondary patterns (wake effect) generated by the wave probe did not affect the free-surface in the Kinect measurement area.

Voltage readings from the wave probe were taken by a Churchill wave monitor (Figure 5.14a) and sent to a laptop via a 'National Instruments' analogue to digital converter (Figure 5.14b). Depending on the conductance, the wave monitor can measure voltage fluctuations between ±10V. Hence, to maximise the range, the sensitivity and datum were adjusted so that +10V and -10V correspond to just above and below maximum and minimum fluctuations at the maximum and minimum depths in the range of flows tested.

30-second voltage measurements were made at a range of depths in still, stationary water. Each time series measurement was time-averaged into one voltage reading per depth. A plot of these voltage readings was made against the real depths as shown in Figure 5.15 and a linear relationship between the voltage and depths was established in the form of a first-order polynomial. This is so that voltage readings can be converted to depth measurements.

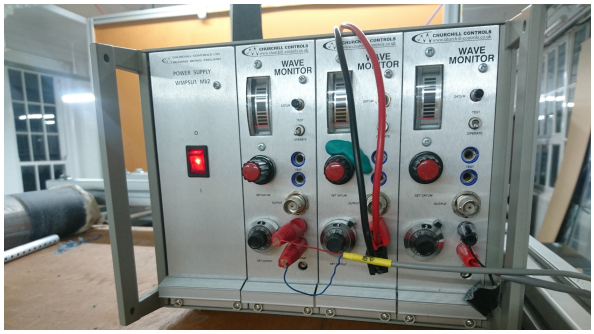

(a) Wave probes enter the front of the wave monitor with analogue signals.

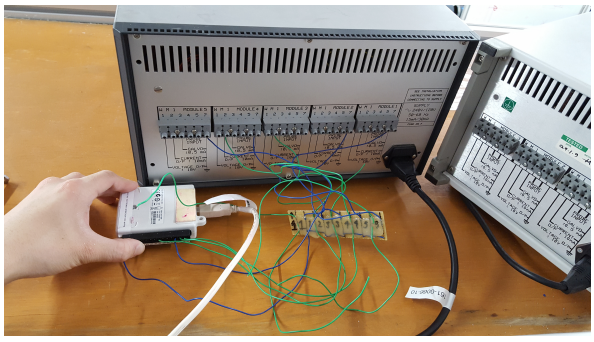

(b) Data is converted from analog to digital and transferred to a PC via USB (in white).

Figure 5.14: Images of the Churchill wave monitor used in experiments to collect data from the three conductance probes.

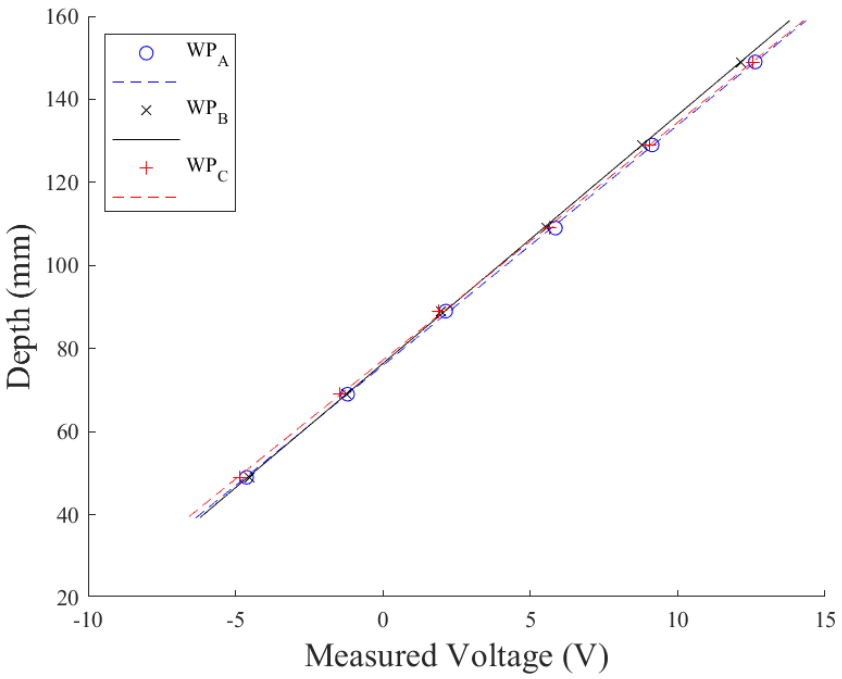

Figure 5.15: Conductance wave probe depth calibration. Markers represent depth and voltage readings. The dashed line is a linear line of best fit calculated using *polyfit* in MATLAB. Each real water depth corresponds to a particular voltage reading. As the water depth changes, the conductance of the probe changes and hence the measured voltage changes. This is used to deduce the depth fluctuation.

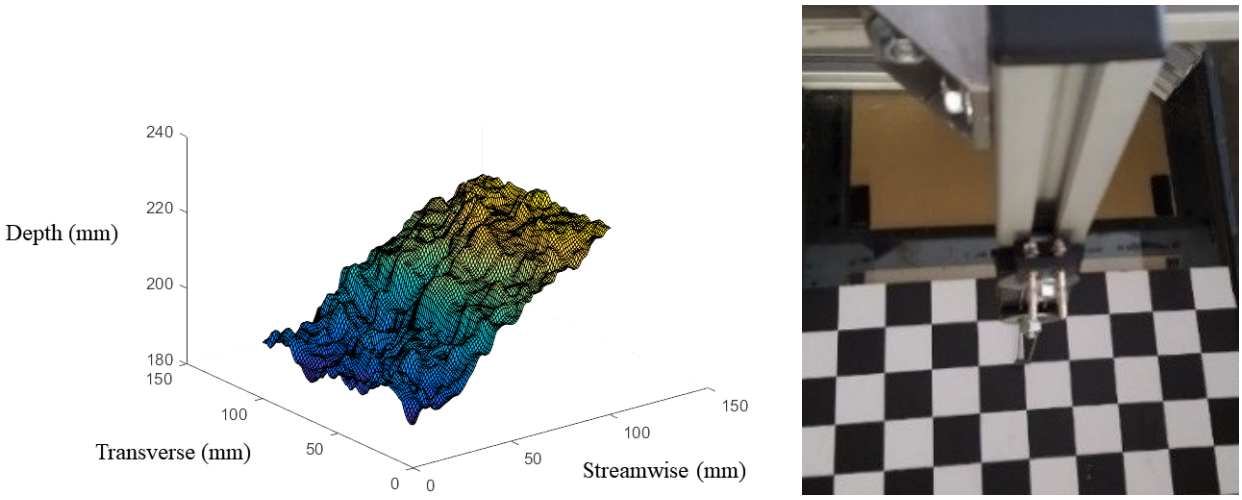

(a) (b)

Figure 5.16: Instantaneous snapshot of the Kinect infrared sensor's free-surface data extracted for comparison against the wave probe (left), and wave probe installation (right).

5.1.4.2 Results and Discussion

During testing, it was discovered that generating waves using 350mm of horizontal movement at 1Hz in the deeper flow depths was very challenging as the mechanical paddle started to flex. The inertial from the water motion affected the quality of the wave generation. This can be reflected in the results shown in Figures 5.17 and 5.18.

Figures 5.18, 5.20, 5.22 and 5.24 show the measured depth and wave height (wave amplitude) of flow coloured by TiO_2 whilst Figures 5.17, 5.19, 5.21 and 5.23 show the same results using milk as the colourant.

Focusing on Figure 5.19 as an example (175mm stroke length at 1Hz), the inconsistency across both Kinect devices suggests that for low depths, the concentration of milk may vary throughout the fluid. Although the recommended 4% milk concentration from prior studies was used; in lower depth flows, even any settling effect would cause a larger relative error.

The TiO_2 figures shows that the Kinect sensors consistently underestimates the wave amplitude. This is also observed from the milk colourant and could be due to the median filter applied to the Kinect frames to remove anomalies. However, this effect was also reported by Wasenmüller and Stricker (2017) as an inherent problem with the Kinect 2 sensor. However, not all is lost, the systematic error suggests that the wave height can potentially still be estimated using a conversion factor. In contrast, the mean depth detected by the Kinect is very close to the detected value from the wave probe (a 0.997 coefficient of determination with a 3.9 % maximum error). It is likely that using the moving median filter to remove outliers can assist with deriving an accurate measurement of the mean depth but can have a negative impact on the amplitude calculation when used excessively.

Figure 5.25 show the dominant frequency component of the Kinect signal versus that of the wave probe signal for gravity waves. These were determined from the maximum amplitude in the Fourier spectrum of the signals. Overall, 70% of the Kinect frequency readings appear to be similar to the wave probe, with the rest being outliers. These could be due to noise in the frequency spectrum from excessive light reflecting off the free-surface and obstructing the

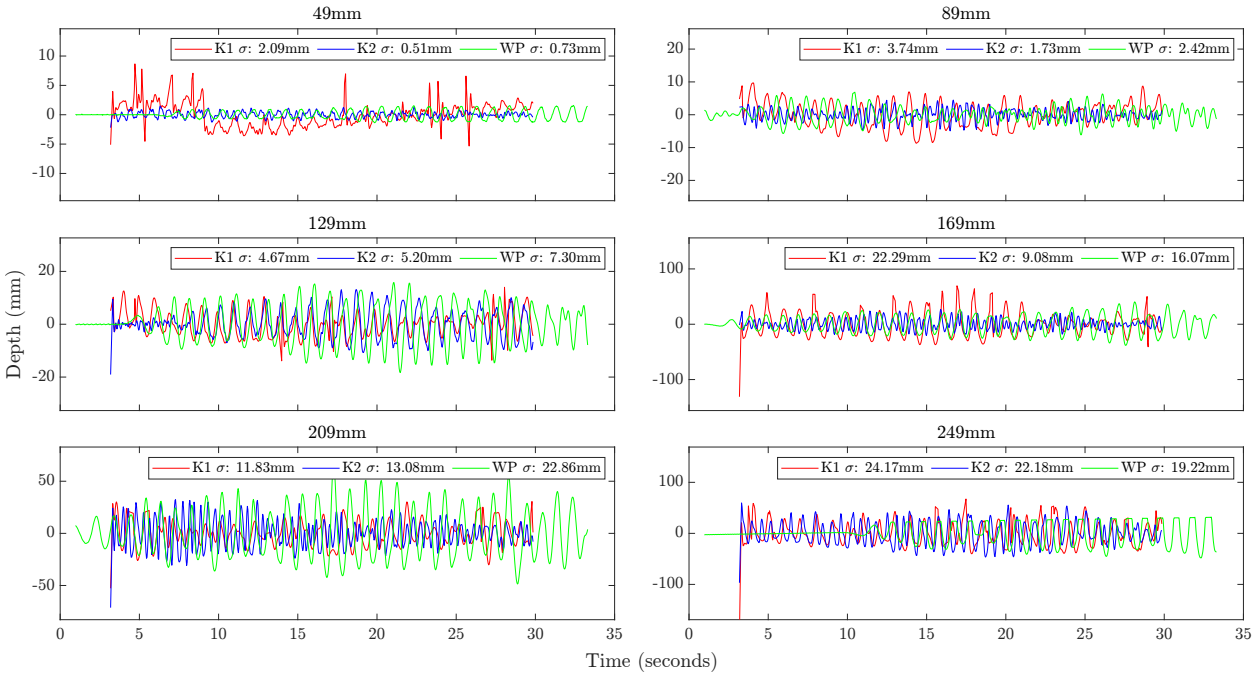

Figure 5.17: Free-surface fluctuation as detected by the Kinect infrared sensors and wave probe in flows coloured using Milk. A stroke of 350mm at 1Hz was used to generate the waves. The Kinect depth readings were extracted near the conductance wave probes for comparison.

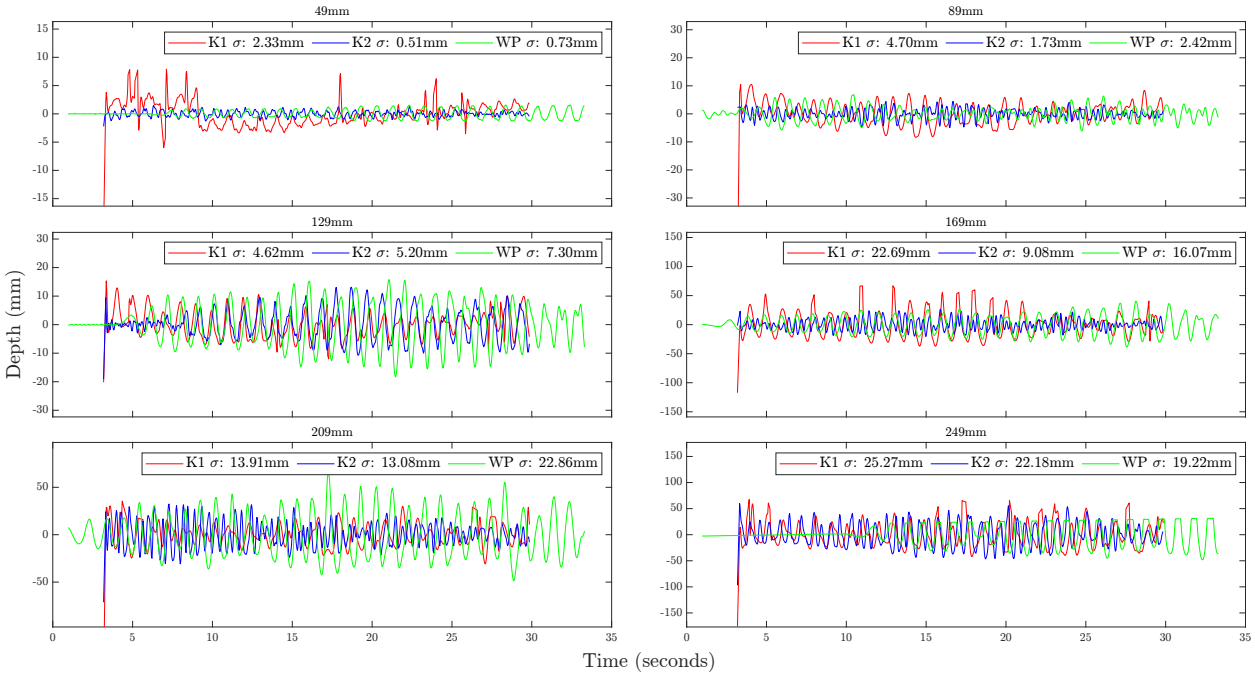

Figure 5.18: Free-surface fluctuation as detected by the Kinect infrared sensors and wave probe in flows coloured using TiO_2. A stroke of 350mm at 1Hz was used to generate the waves. The Kinect depth readings were extracted near the conductance wave probes for comparison.

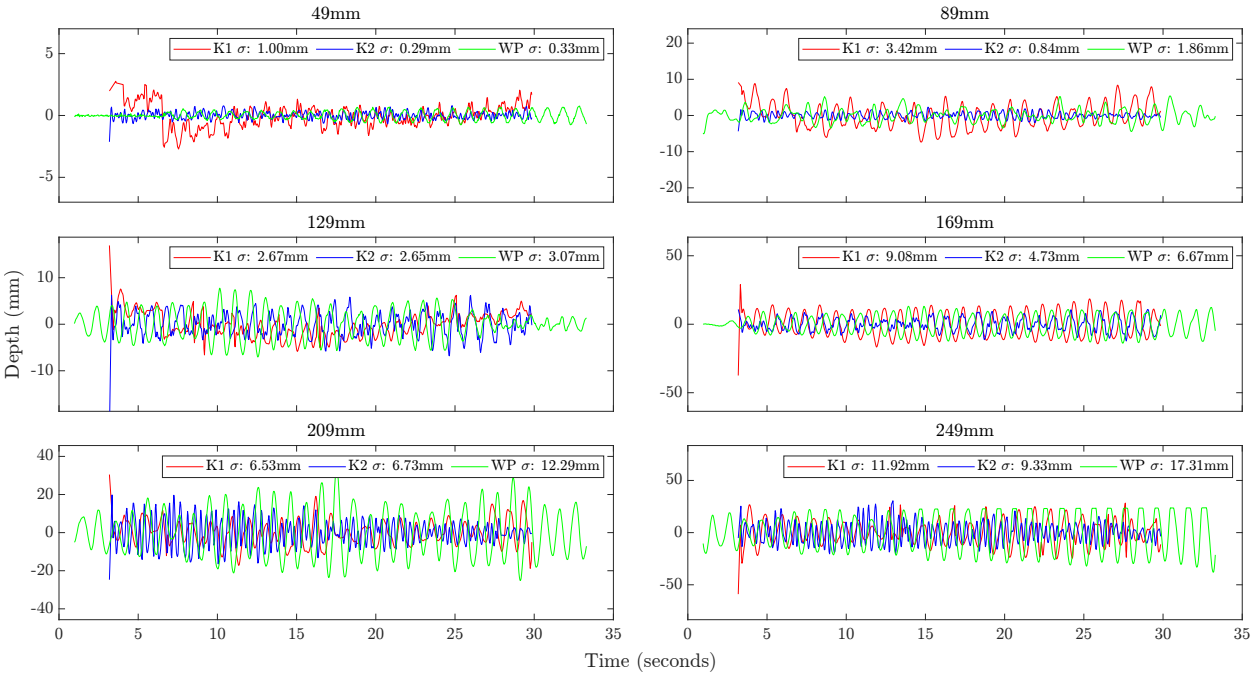

Figure 5.19: Free-surface fluctuation as detected by the Kinect infrared sensors and wave probe in flows coloured using Milk. A stroke of 175mm at 1Hz was used to generate the waves. The Kinect depth readings were extracted near the conductance wave probes for comparison.

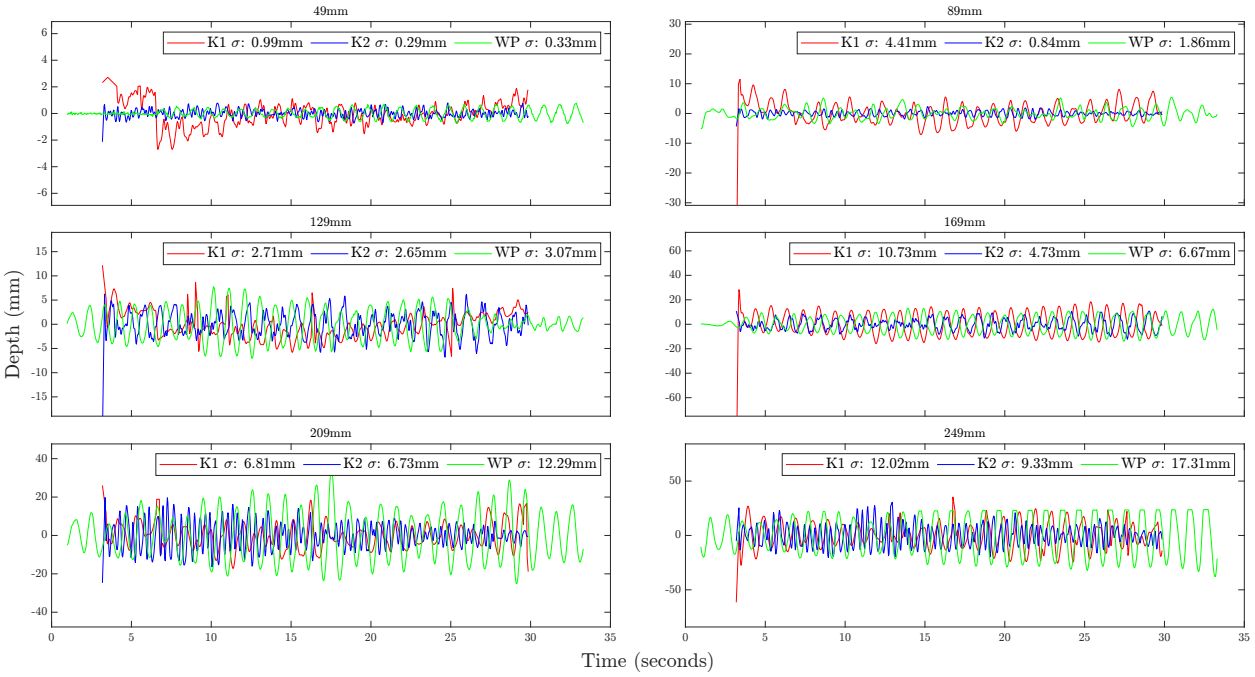

Figure 5.20: Free-surface fluctuation as detected by the Kinect infrared sensors and wave probe in flows coloured using TiO_2. A stroke of 175mm at 1Hz was used to generate the waves. The Kinect depth readings were extracted near the conductance wave probes for comparison.

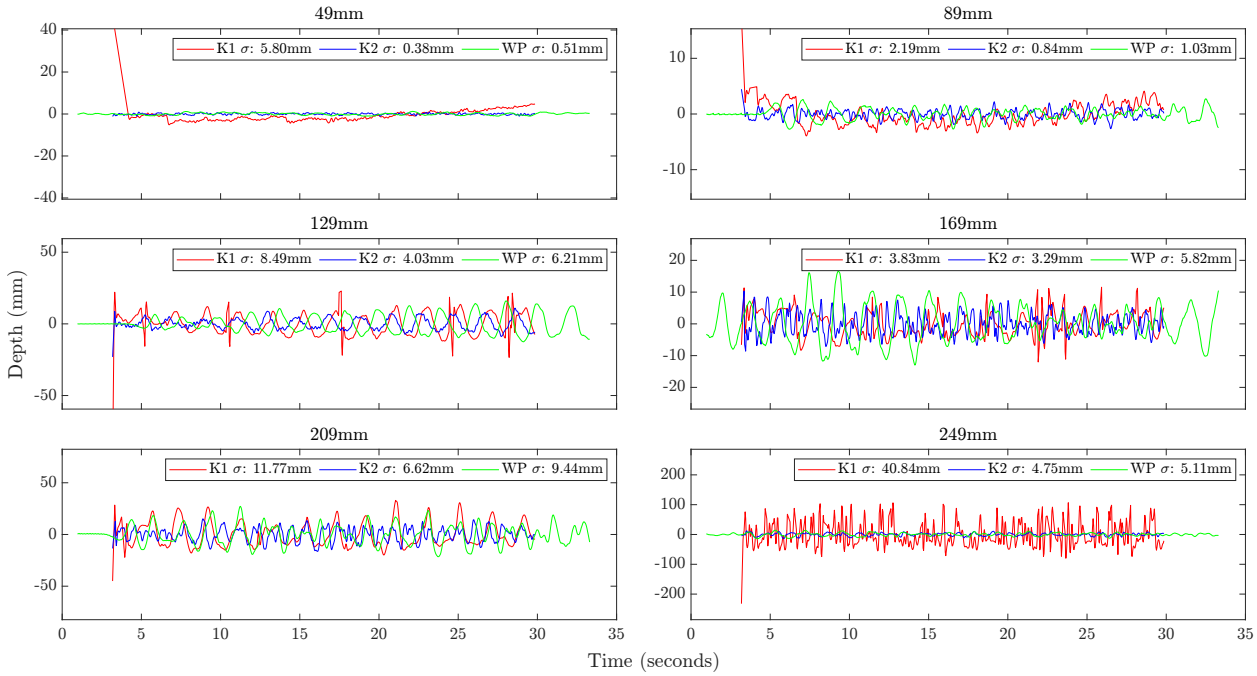

Figure 5.21: Free-surface fluctuation as detected by the Kinect infrared sensors and wave probe in flows coloured using Milk. A stroke of 350mm at 0.5Hz was used to generate the waves. The Kinect depth readings were extracted near the conductance wave probes for comparison.

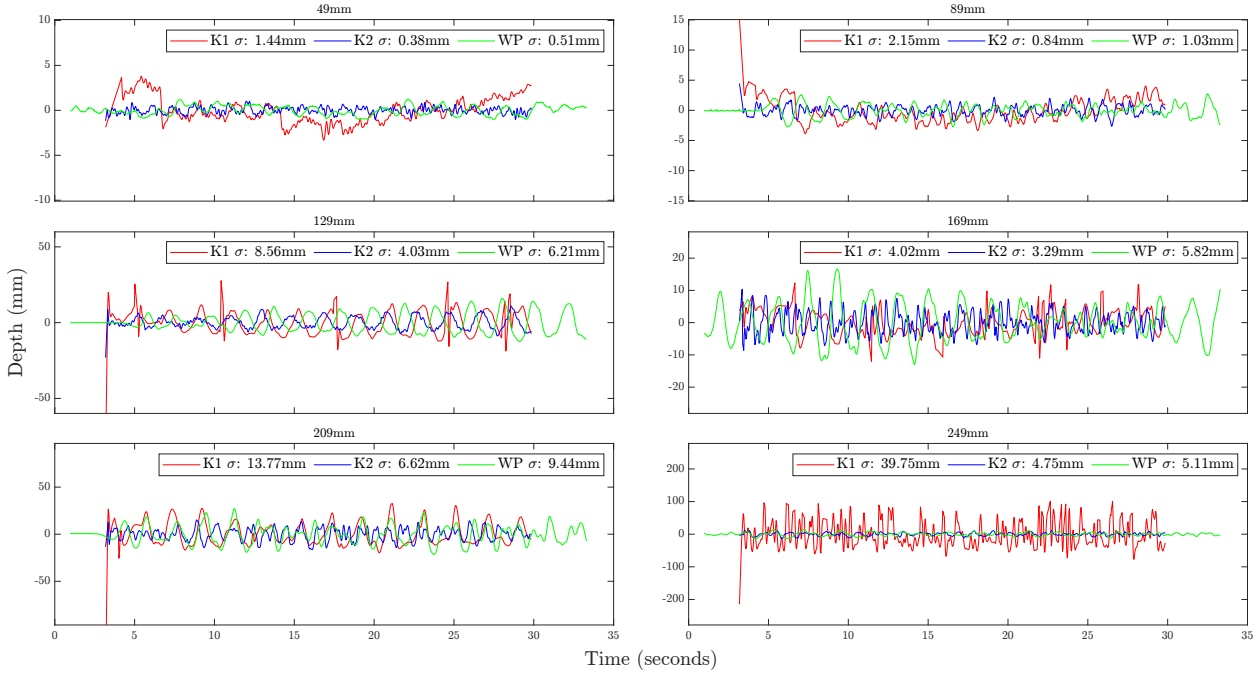

Figure 5.22: Free-surface fluctuation as detected by the Kinect infrared sensors and wave probe in flows coloured using TiO_2. A stroke of 350mm at 0.5Hz was used to generate the waves. The Kinect depth readings were extracted near the conductance wave probes for comparison.

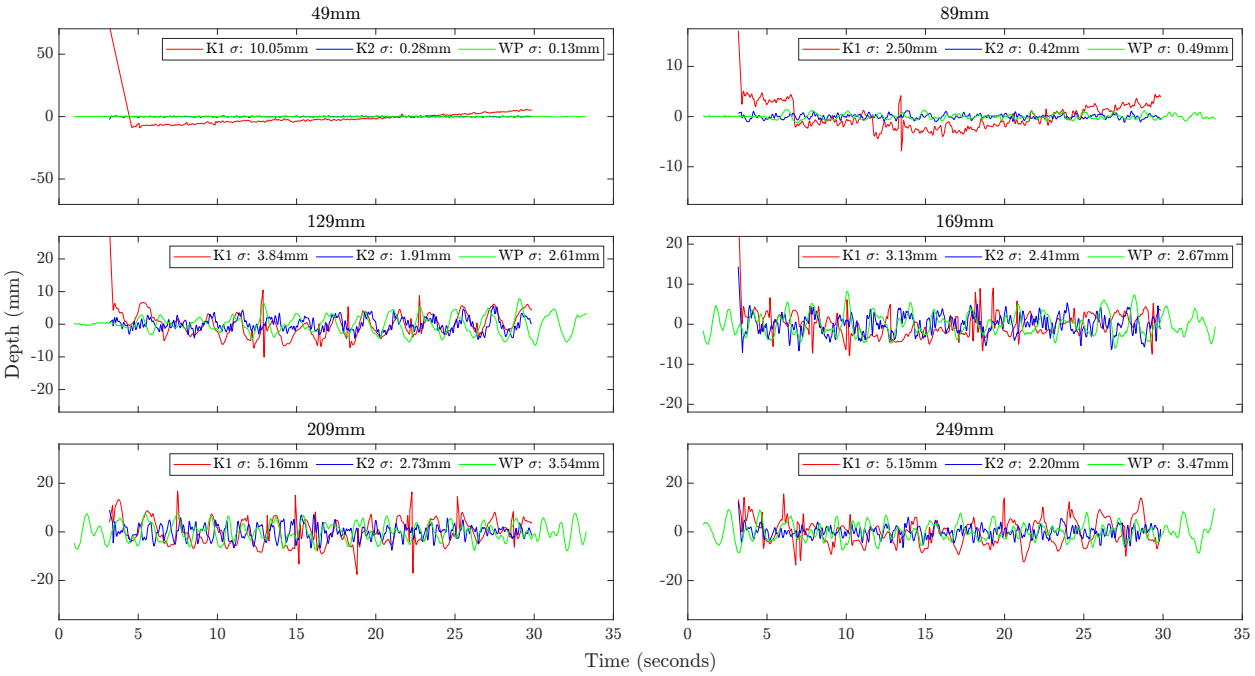

Figure 5.23: Free-surface fluctuation as detected by the Kinect infrared sensors and wave probe in flows coloured using Milk. A stroke of 175mm at 0.5Hz was used to generate the waves. The Kinect depth readings were extracted near the conductance wave probes for comparison.

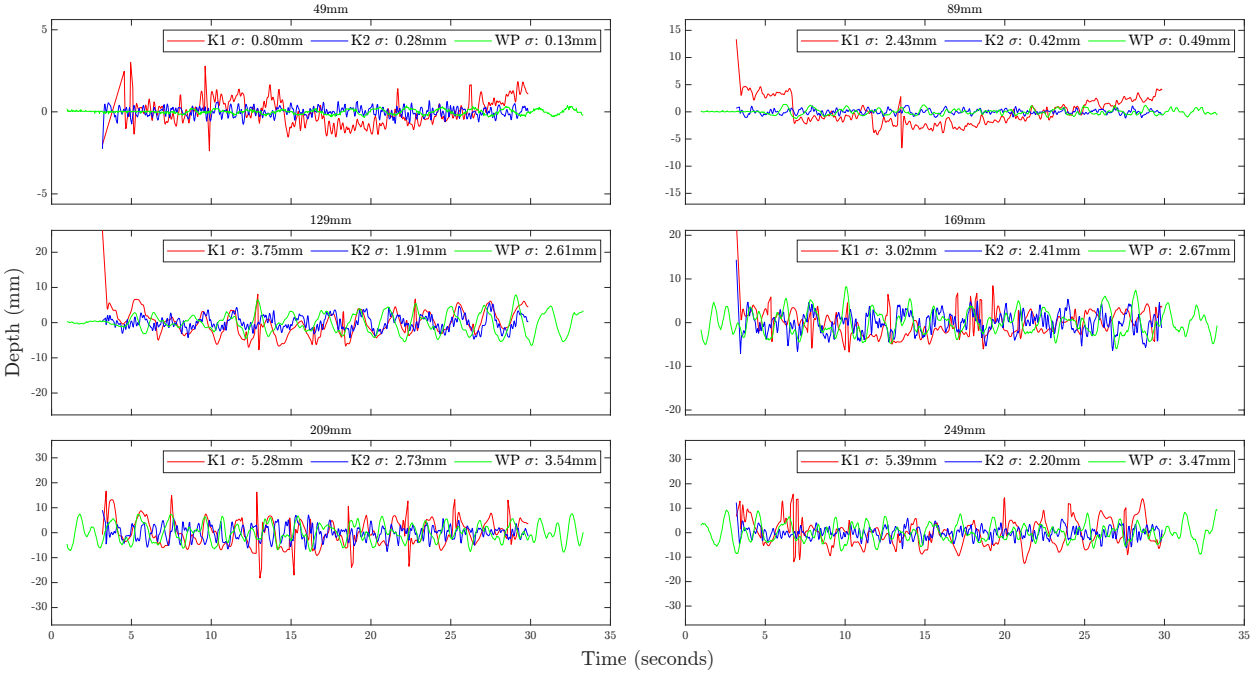

Figure 5.24: Free-surface fluctuation as detected by the Kinect infrared sensors and wave probe in flows coloured using TiO_2. A stroke of 175mm at 0.5Hz was used to generate the waves. The Kinect depth readings were extracted near the conductance wave probes for comparison.

Kinect 1 sensor's pattern recognition detection of the infra-red pattern. Ignoring outliers, the frequency relation with the wave probe is almost identical however a linear fit indicates a gradient of 1.04. Since waves are generated at a consistent frequency, and the sampling frequency of the wave probe is known to be reliable, this would suggest the Kinect may sample at a slightly lower rate of 28.9 Hz instead of the specified 30 Hz. Careful examination show that the sampling rate of the infrared sensor actually varies from 25.9 to 31.9 Hz. This uncertainty should be taken into account in future experiments using the Kinect sensors.

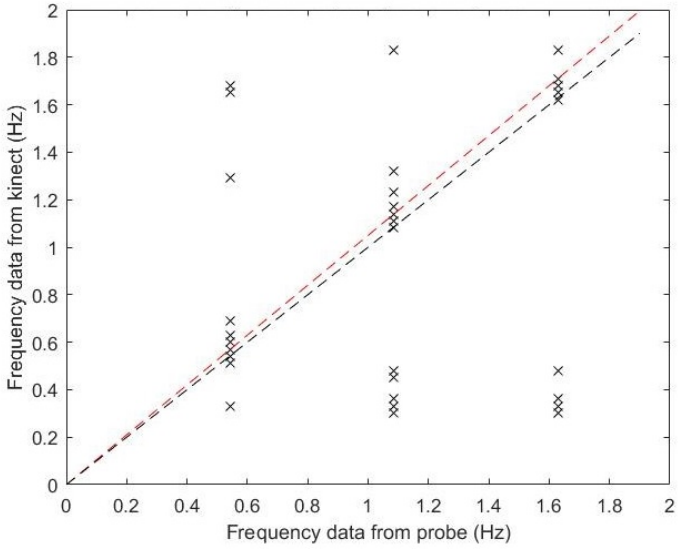

Figure 5.25: Maximum frequency response detected by Kinect infrared sensor compared against the conductance wave probe. The black dashed line is a 1:1 linear relationship between the two sensors. Data points that lie on this line suggest a 100% match between the two sensors. The red dashed line is a linear line of best fit to the data shown. It can be seen that the lines are similar suggesting a close match between the two types of sensors.

5.1.4.3 Summary

Although there remains an issue with the depth calibration of the Kinect sensors, it has now been established that TiO_2 is a more reliable colourant than milk. Although 4% milk concentration was used (the amount determined to be necessary from the static tests), the accuracy of the free-surface detection was still low compared to using TiO_2.

Due to milk becoming stale very quickly, it was also realised that the feasibility of using milk for the main experiment was very low. There was a notable odour within the laboratory

after a few days and the water viscosity had notably changed due to the milk fermenting.

Combined with the cost and logistics of purchasing and transporting such large quantities of milk, it was decided that TiO_2 would be the more suitable colourant to use for the main turbulent flow tests. To avoid temperature affecting the device's sensing accuracy, the Kinect devices were turned on at least 30 minutes before recording data as suggested by literature (Wasenmüller and Stricker, 2017).

5.2 Final Methodology - Steady Flow Tests

5.2.1 The Flume

Testing was performed in the same laboratory as presented in section 5.1.4.1.1. However, the water tank partition was removed to enable recirculating flow. At the upstream end of the flume, at the top of the vertical inlet, a honeycomb/mesh structure was used to dampen any residual pump vibrations and reduce incoming turbulence (see Figure 5.26). For this set of tests, the slope was set to 0.01 (1% or 1:100) with the measurement section 9.5 to 12m from the upstream end of the flume. This slope gradient is the recommended minimum in many drainage design standards across the world. For example in USA, Fort Wayne's City Utilities Design Standards Manual Stormwater (2017) Book 2, Chapter SW9 on Open Channels; the SW9.08 General Design Requirements point 3 states that any channels less than 1% require an underdrain. The city of Fort Wayne is located in a very flat topographic region, therefore, stormwater drainage is vital to prevent flash flooding from surface run-off. Any increase in due to extreme storms and heavy rainfall would have the greatest impact on open channels with 1% gradient.

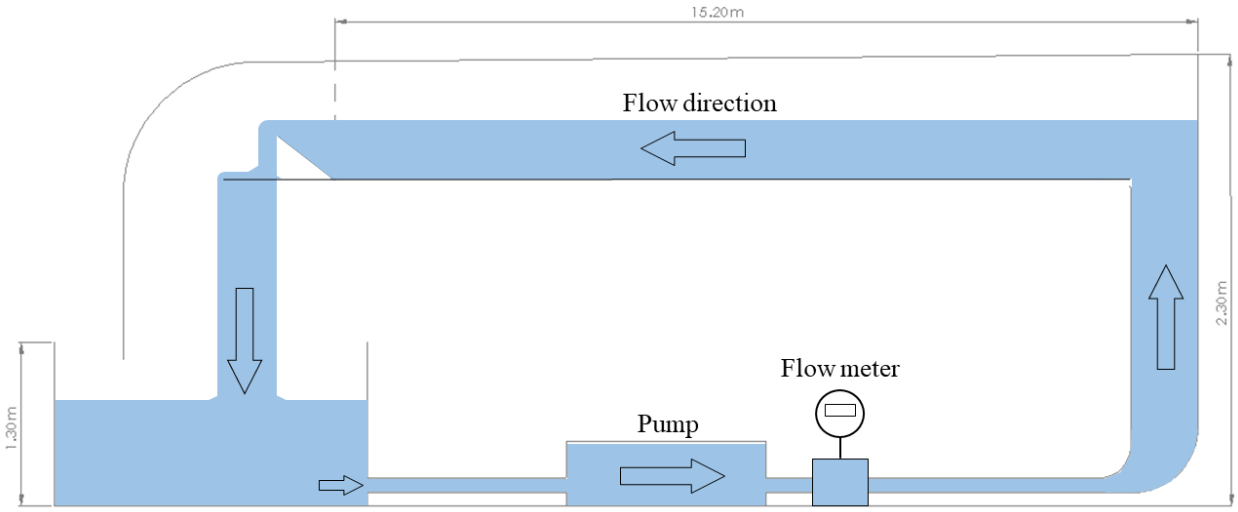

Figure 5.26: Flume schematic showing the recirculating flume water flow process. The pump beneath the flume takes water from a tank and supplies it upwards to the upstream end of the flume. The water then flows downstream through the measurement region towards an exit ramp and back down into the tank. The exit ramp is adjustable and controls the depth of the flow in conjunction with the adjustable slope of the flume.

The downstream flow control was achieved with a mechanised weir at the outlet. This can be used to adjust the depth to achieve uniform flow in the measurement section. The flow rate was measured by a magnetic flow meter in the flume supply pipe. The local water temperature was measured to be 23 ± 0.7 °Celsius.

5.2.1.1 Bed Type

Experimental studies have shown that flow over beds with hemi-spheres is a good representation of open-channel beds in nature (Dancey et al., 2000; Defina, 1996; Grass et al., 1991; Manes et al., 2009). For example, hexagonally packed spheres are not dissimilar to the bed of dunes studied by Best (2005). A bed with 24mm diameter spheres, packed in a hexagonal configuration was used in this study for these tests (see Figure 5.27).

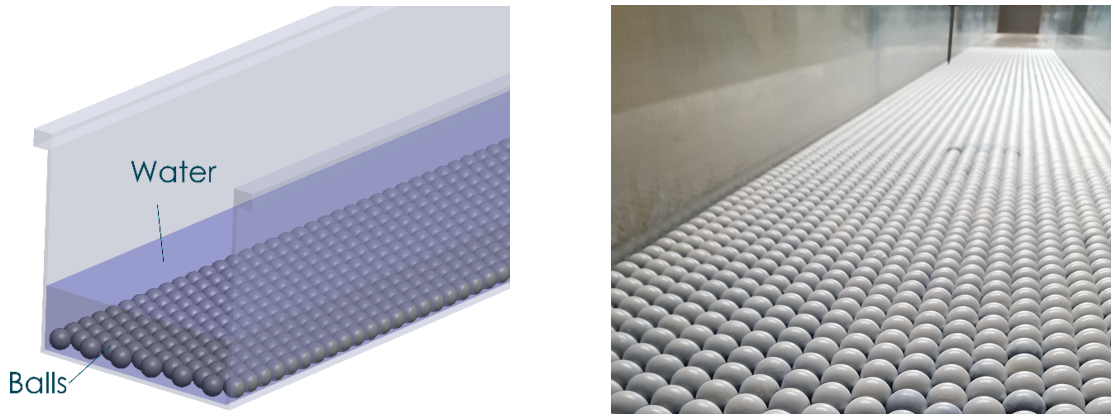

(a) Bed of spheres (dark grey), Solidworks CAD visualisation

(b) Bed of spheres with white TiO_2 residue after experiment

Figure 5.27: Bed of spheres arranged in a hexagonal close packing pattern with the hydraulic flume. Shown in CAD (left) and in the lab after the experiment (right).

The spheres are plastic injection moulded with a density of 1400 kg/m^3, and a specific gravity greater than 1 so they settle on the bed in still water. The hexagonal packing left enough clearance at the edges to accommodate any variation in the flume width, but still provided a stable close packing pattern (see Figure 5.28).

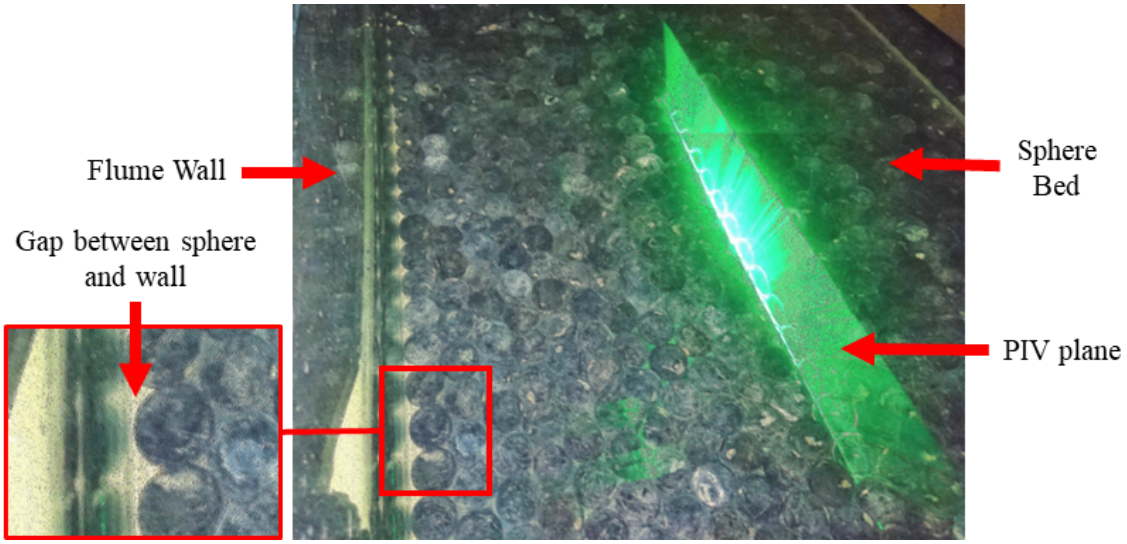

Figure 5.28: View of the PIV region from above. The flume shown here was filled with clear water. The laser plane was projected from beneath the flume bed and travelled through the transparent spheres, the depth of the water, before being refracted into the air at the free-surface boundary.

5.2.2 Test Cases - Flow Conditions

Six different steady uniform flows were established over the spherical bed to generate different free-surface patterns via the inherent flow turbulence. Overall flow conditions can be found in Table 5.1. Three flow depths matched those used for gravity waves, with the mean flow velocity varying from 0.08 to 0.28 m/s.

Within the experiment, the flow rate and depth were measured. Knowing the width of the flume was 0.5m and the gradient was 0.01, this allows the Manning's number to be calculated using Equation 2.1.1. This is important because it is a representation of the roughness applied to the flow by the channel. The flows tested have a Manning's number between 0.049 and 0.023, typical for shallow river flows.

The Kinect sensors require an opaque flow but the PIV system requires a clear flow with seeding particles, thus the tests were conducted twice. Once with TiO_2 white colourant (see Figure 5.29) for the Kinect sensors and a second time for the PIV measurements. In both instances, the depth gauge was used to check for uniform depth at both ends of the flume. The flow meter was checked to ensure the same flow rate and the ADV was used to check the velocity profiles had stabilised and the overall flow conditions were the same. The fastest and most turbulent flows were tested first to avoid colourants settling over time. This also gave more time for the pump to warm open as small fluctuations in flow rate during the lower flow depths can lead to large percentage errors being propagated into the system. The pump was controlled by a PID system using LabVIEW which monitored the flow rate and adjusted the flow valves.

(a) Top view

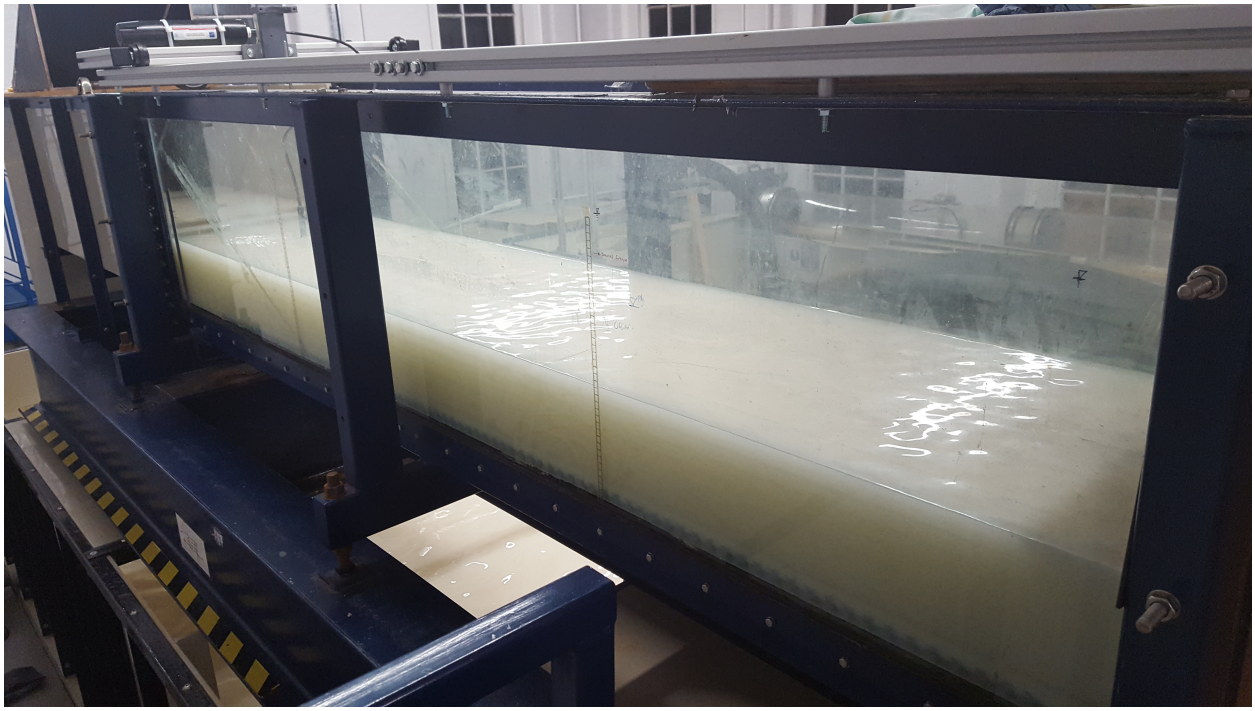

(b) Side view

Figure 5.29: Images of the experimental flume in the hydrodynamics lab RA8 at the University of Sheffield. The water has been coloured with 0.04% TiO_2 to increase the opacity and assist the infrared Kinect sensors with identifying the position of the free-surface.

Table 5.1: Experimental flow conditions with dimensionless numbers. A range of depths, flow rates and Reynolds' numbers are tested.

Water Depth (m)	Hydraulic Diameter D_H, (m)	Flow rate (l/s)	Velocity (m/s)	Reynolds' number (with D_H)	Reynolds' number (with depth)	Manning's number	Froude number	Weber number	Relative Submergence
0.049	0.1639	1.87	0.08	12,508	3,740	0.049	0.11	3.96	2.04
0.069	0.2163	5.05	0.15	31,700	10,100	0.031	0.18	20.53	2.88
0.089	0.2625	7.46	0.17	44,000	14,920	0.031	0.18	34.74	3.71
0.109	0.3036	11.21	0.21	62,500	22,420	0.028	0.20	64.05	4.54
0.129	0.3404	15.4	0.24	81,300	30,800	0.026	0.21	102.14	5.38
0.149	0.3734	20.7	0.28	103,800	41,400	0.023	0.23	159.77	6.21

Figure 5.30 takes Muraro et al. (2021)'s adaptation of Peregrine's L-q diagram and adds the flow condition designs presented in Table 5.1. This enables a comparison of the flow with previous studies. The 49mm depth flow is much closer to region 0 whereas the other flows are more in between region 0 and region 3. This implies the surface behaviour for the 49mm case may also display a different set of free-surface characteristics compared to the other flows due to its proximity to the bed. The dominant property of region 0 is that it has very little surface disturbance. Where small turbulence exists, small surface fluctuation can exist following Teixeira's proposed mechanisms (Teixeira, 2006). Region 3 is mostly dominated by gravitational effects and is the most common region observed in nature. The surface deformations remain small however the surface contains a number of local features that can be identified such as upwelling dimples or small waves.

The Weber number can be used to predict the behaviour of the 49mm case. As the Weber number presents the ratio between the inertia and surface tension forces, it can provide information on the effect of surface tension in limiting or damping any surface features. The surface tension in water is particularly strong due to intermolecular forces from hydrogen bonding. In most free-surface flows, the gravitational forces are vastly bigger and the effect of surface tension should normally be negligible, however, in the case of the 49mm case, both the depth and velocity of the flow are small. Novak and Cabelka suggest the critical value of Weber number should be higher 11 if effects of surface tension are to be minimised (Peakall and Warburton, 1996). The Weber number of the 49mm case is just 3.96 whereas all the other flows have Weber numbers higher than 20. Therefore, the free-surface amplitude in the 49mm case will likely have more attenuation from the water's surface tension.

The flows studied by Fujita (2011) were approximately 0.4m/s at 40mm flow depth over a bed with similarly sized roughness elements (Fujita used 30mm whilst this study uses 24mm diameter elements). In this present study, the flow condition at 49mm flow depth only has a 0.08 m/s bulk velocity. The flow conditions in Fujita (2011) are faster and more turbulent. This is reflected in the Froude numbers which are 0.110 in the present study but 0.586 in Fujita's tests. Thus, it will be important to see if the same discoveries found by Fujita (2011) can be observed here.

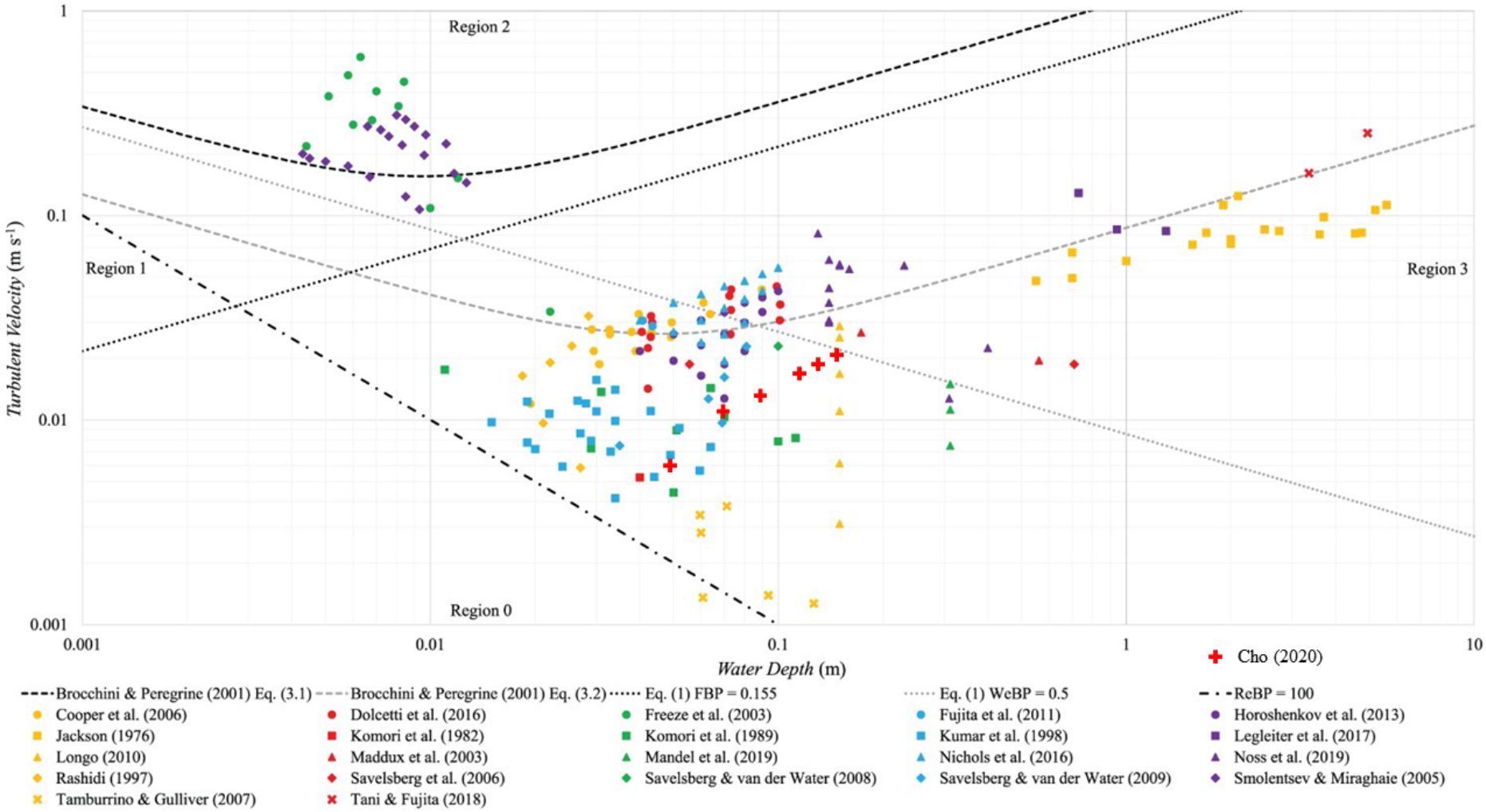

Figure 5.30: "Turbulent velocity - Water depth" diagram adapted by Muraro et al. (2021) from Brocchini and Peregrine (2001). The experimental flow conditions tested in this current study have been added to the diagram as red + signs and labelled in the legend as Cho (2020). Refer to Figure 3.2 for an explanation of regions and boundaries.

5.2.3 Sensors

The flume was fitted with Microsoft Kinect generation 1 and 2 infrared sensors introduced and tested in section 5.1. This allows comparison of the difference in performance between the two versions under dynamic free-surface conditions. A particle imaging velocimetry system and three conductance-based wave probes were also installed as established techniques to validate measurements.

Due to a faulty camera and delays from the supplier in getting it repaired, LIF could not be deployed in this study. Free-surface data would be obtained from the wave probes and Kinect infrared sensors. Table 5.2 summarises the suite of sensors deployed. The following section introduces the PIV, ADV and conductance probe setup in more detail.

Table 5.2: Summary of sensing instruments used in the flow tests and the type of data measured. Please refer to Figure 5.43 for illustration.

Instrument	Data Type	Type of measurement
PIV	2D map of 3C* velocity vectors	Flow
ADV	1D point source of 3C* velocity fluctuations (collected at different 3D locations)	Flow
LIF (removed)	2D free-surface depth in streamwise direction	Free-surface
Wave Probe	Pseudo-point source (depth)	Free-surface
Kinect	3D positions	Free-surface

*C presents velocity components in the three Cartesian directions.

5.2.3.1 Particle Imaging Velocimetry (PIV)

5.2.3.1.1 Laser System The laser used in the PIV measurements was the Litron Nano PIV Series, Pulsed Nd:YAG Laser. A diagram is shown in Figure 5.31 to illustrate its operation. This is a dual laser system with two lasers that can be independently triggered allowing very fast double-frame illumination. In the diagram, Laser 2 is uncovered to show the internals (it is adjacent to Laser 1). The two independent lasers are pulsed and q-switched allowing energetic short pulses of light to be generated. Resonators produce infrared laser light at 1064nm. The two lasers are combined together using a polariser before a Harmonic Generation Assembly converts the infrared 1064nm light to 532nm laser light with excess energy being sent to a beam dump. Individual pumps use de-ionised water to cool each laser and physical shutters block any unintentional laser emissions from the unit.

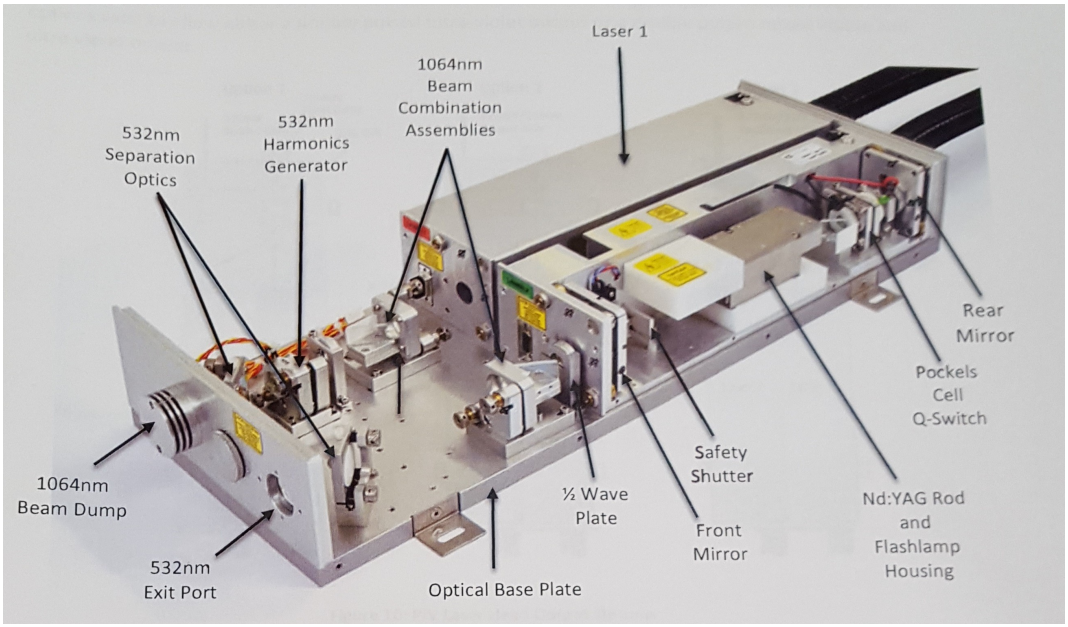

Figure 5.31: Schematic of the LaVision PIV lasers' internal operation (LaVision, 2018). Two Nd:YAG lasers are used to generate pulses of light in quick succession to illuminate the tracking particles. The raw 1064nm light from the laser is converted to 532nm using a harmonics generator. Excess energy is deposited in the beam dump with the remaining light sent out of the enclosure.

Once the 532nm laser leaves the laser unit exit port, it will hit the front mirror that reflects the laser beam from a horizontal position to a vertical upward position. From here, it enters the laser guiding arm and is reflected internally until it reaches the focuser and the planar lens at the end of the arm (Figure 5.32b). The lens distributes the concentrated overlapping

circular laser beams into a light sheet which will illuminate the PIV particles (Figure 5.32).

In the measurement section, a row of spheres was replaced with transparent glass spheres of the same diameter to allow the PIV laser to shine through (see Figure 5.28 and 5.32a).

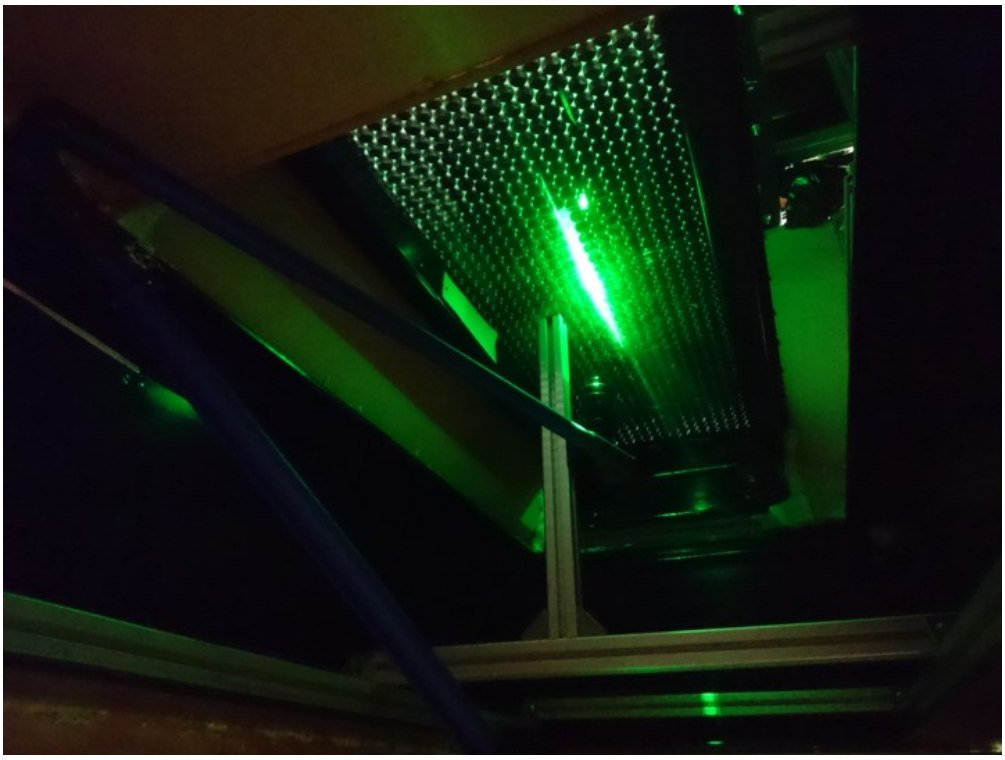

(a) View from below the flume with laser plane illuminating the bed

(b) View from below the flume with calibration grid above laser guide arm

Figure 5.32: Images of the laser guide arm below the flume. It can be seen that the laser plane is aligned with the centerline of the flume.

5.2.3.1.2 Imaging System In order to capture the position of the particles as they are illuminated by the laser, two Imager MX cameras are used in a stereo configuration to record the images of the particles in the laser plane (see Figure 5.34b). Whilst traditional single PIV only allows the streamwise and vertical velocity to be measured (when the PIV plane in in the centerline), a stereo setup also allows the through-plane spanwise direction to be measured. Command to initiate image acquisition of a frame was achieved via a trigger line. The trigger command originates from a triggering unit (PTU). This was connected to the central computer allowing the user to set the frame rate. It was also connected to the laser to synchronise the frames with the flash lamps of the laser. Taking pairs of images at 92.6 Hz, each pair of images was separated by 1400 μs. Once the camera was triggered, the image was acquired and sent via two camera link cables to the central computer. These camera link cables also provide power to the camera and allow high frame-rate capability. 8 bits per pixel was used in greyscale mode. When compared to 10 and 12 bit resolution, this allows an increase in frame rate. Overall operation of the system was conducted using the LaVision 'Davis 8' software. From here, calibration, image acquisition, laser control, and post-processing can be executed.

Figure 5.33: Imager MX camera(s) used to conduct Particle Imaging Velocimetry in open channel water flows. These were operated in a mode with 8 bits per pixel to deliver maximum high frame rate (LaVision, 2022). Each image from contains 2048 x 2048 pixels.

The central computer used to store the images and control the system was an Intel Xeon E5-1650v3 processor with a clock speed of 3.5 GHz and 915 threads. It has 192 GB of RAM for saving the raw camera data straight into RAM cache before being written to the hard drive afterwards (see Figure 5.35).

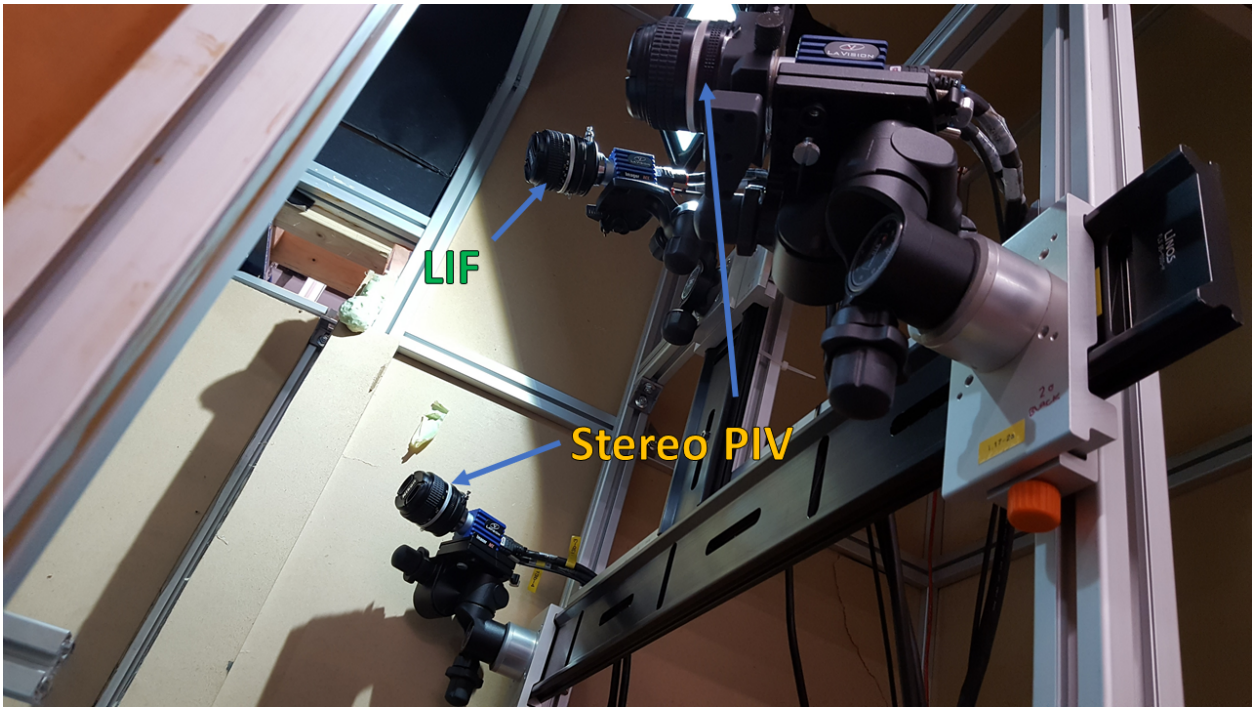

(a) Imager MX cameras setup, two PIV cameras in stereo setup and one LIF camera (topmost). The LIF capability was later removed due to device malfunction.

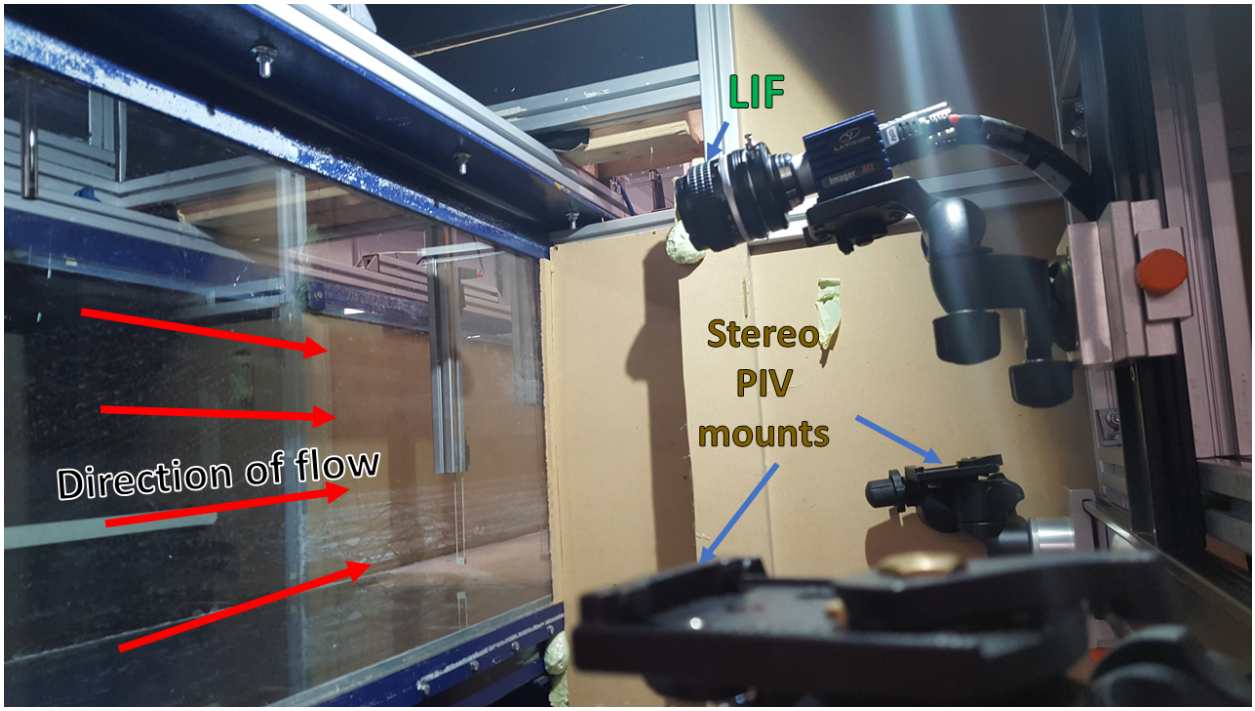

(b) Imager MX camera(s)' view of the flume, only the mounts for the PIV cameras are shown for clarity.

Figure 5.34: Images of the PIV camera setup besides the flume (Cho et al., 2022). The laser and camera system are enclosed by opaque walls to prevent high-energy laser light from posing a hazard to nearby humans.

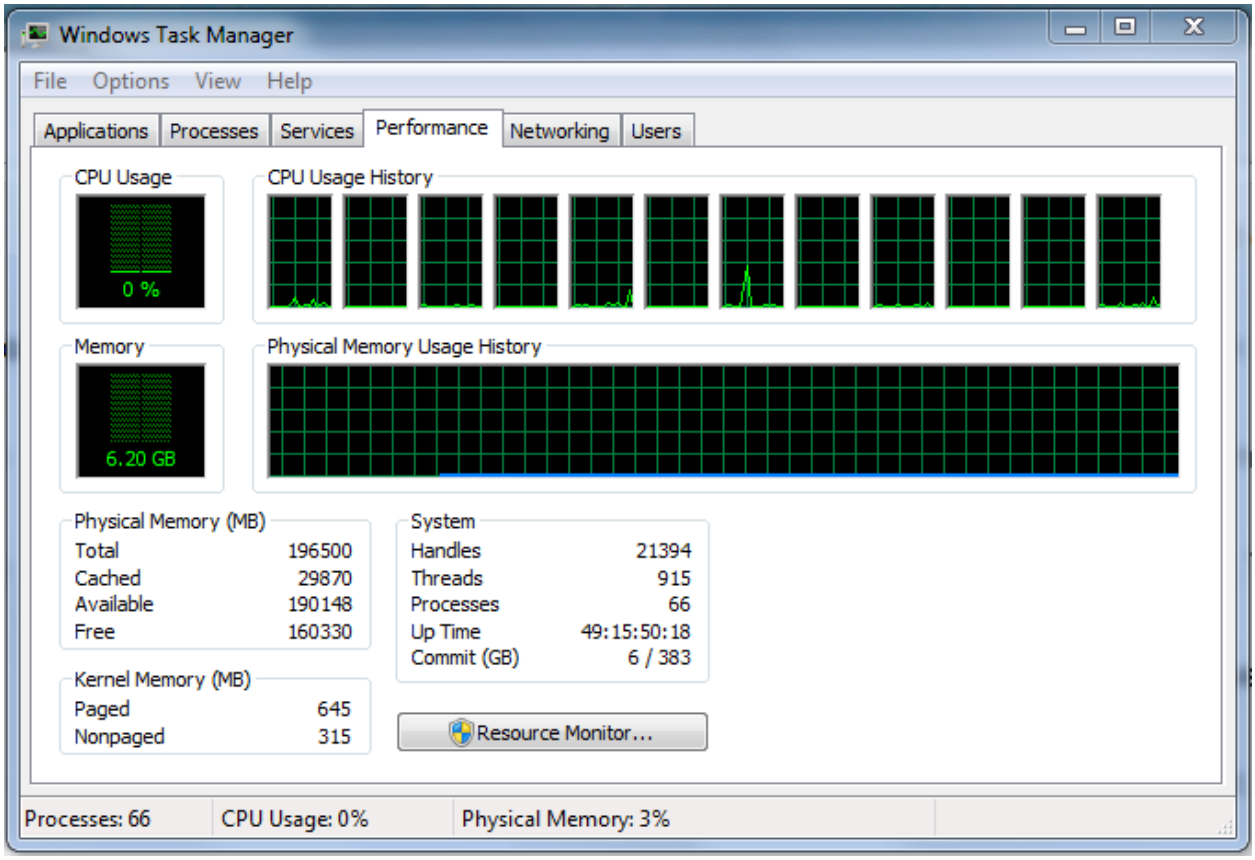

Figure 5.35: PIV computer specification. Almost 200GB of RAM is necessary as the high sampling rate (92.6 Hz) requires the double frame image pairs to be saved directly to the RAM cache. After the PIV imaging was stopped, the data was transferred more slowly to the hard drive.

5.2.3.1.2.1 PIV Calibration The stereo calibration process is conducted by first placing the S/N 309-15, two-level calibration grid from LaVision inside the flume (Figure 5.36a). The front of the grid represents the front plane of measurement whilst the back represents the through plane depth. Once the plate is in position, the distance of the front side to both sides of the flume on all four corners is checked. This ensures the plate is vertical and not twisted in any unintended way. Figure 5.36b shows an image of the calibration plate in place halfway across the width of the flume after calibration. A third order polynomial fit was used to correct the lens distortion and create a rectilinear Cartesian coordinate system.

- Camera 1 had a focal length of 37.9mm, distance to the calibration plate was 1146.2mm. The camera was rotated -33, 9 and -5 degrees in the X Y Z directions respectively.
- Camera 2 had a focal length of 35.9mm, distance to the calibration plate was 1099.9mm. The camera was rotated 33, 7 and -175 degrees in the X Y Z directions respectively.

After calibration, a scale factor of 0.243 mm/pixel was achieved with a detected datum of 924.76 pixels in the local X and 1087.17 pixels in the local Y directions. Since the camera lens was rotated approximately 90 degrees, the local X and local Y are vertical and horizontal instead.

5.2.3.1.2.2 PIV Laser settings A 4mm thick laser sheet was used in a vertical-streamwise plane across the width of the flume from the sidewall (see Figure 5.32b).

Vestosint Polyamind 12 2178 seeding particles with a diameter of 20µm was used. These particles are almost neutrally buoyant with a specific gravity of 0.99 (Evonik Industries, 2018). This allows it to follow the flow field of the fluid. Images were taken at a rate of 92.6 frames per second (Hz) using the double-frame technique. This takes two snapshots close to every one-hundredth of a second. According to Dey and Das (2012), this sampling rate is sufficiently high to capture the turbulent quantities in a statically significant manner.

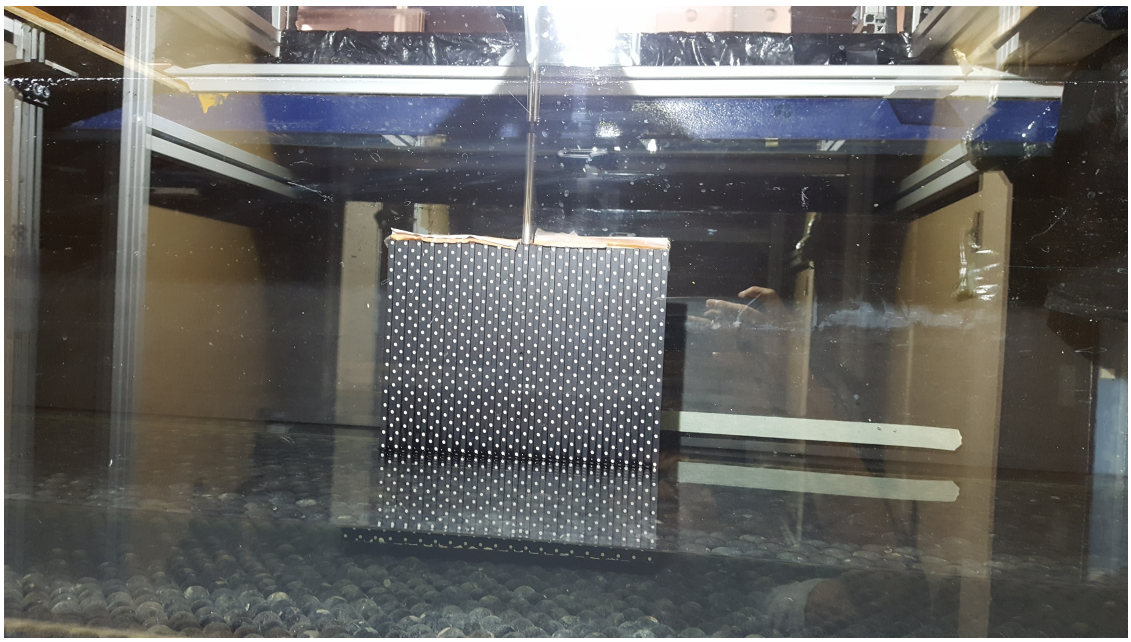

(a) PIV two-level calibration grid inside the flume before the hydraulic tests.

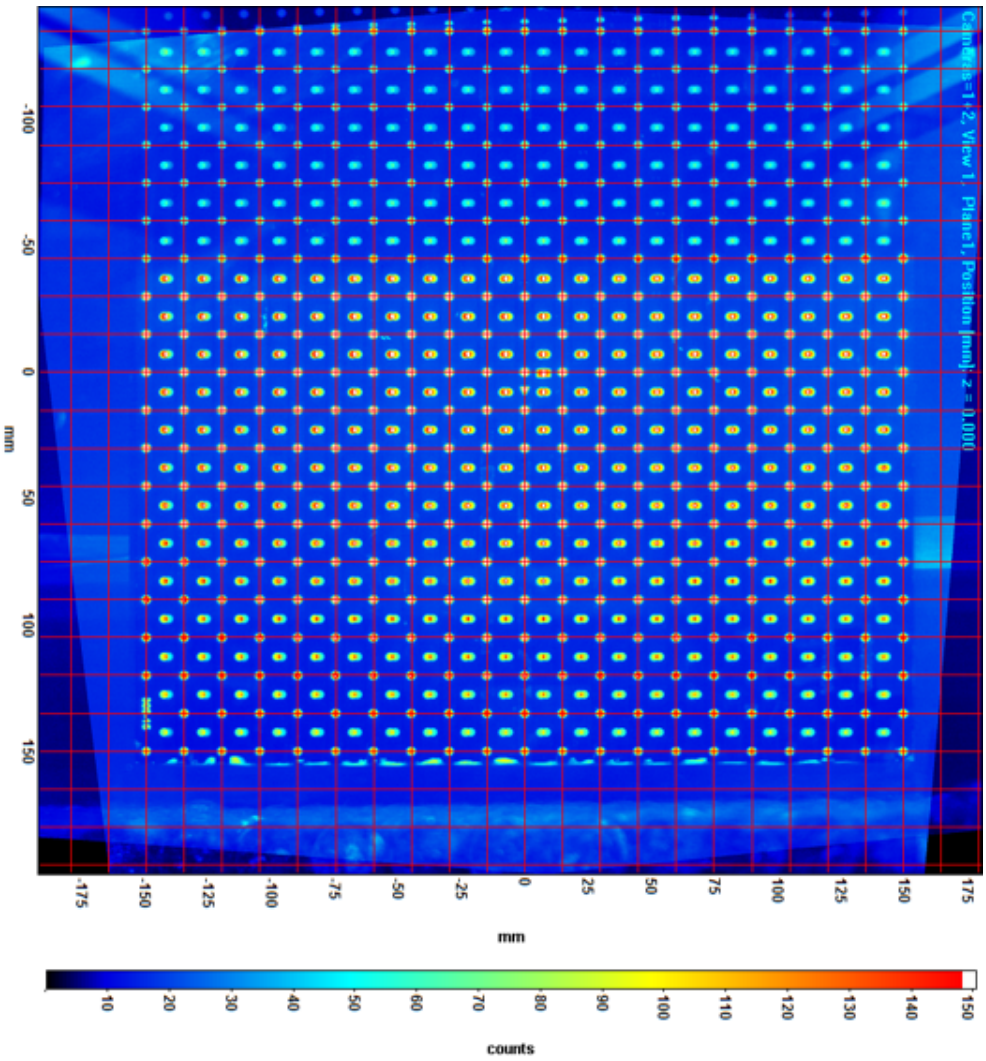

(b) View of PIV calibration Grid after spatial and depth calibration.

Figure 5.36: Two-level PIV calibration grid for stereo PIV capability. This enables velocity measurements of particles in 3D by adding spanwise velocity detection capability.

5.2.3.2 Acoustic Doppler Velocimetry (ADV) and depth gauge

To ensure the flows had stabilised to the correct uniform depth and flow profile, a depth gauge and a side-facing ADV probe were used (see Figure 5.37). An ADV probe operating at 100 Hz was used to record centreline depth-wise velocity distributions at a range of streamwise positions. According to Ruonan et al. (2016), this sampling rate is sufficient to capture the velocity fluctuation within the flow. Figure 5.37 shows an example of an image of the ADV and a depth gauge during setup. The ADV probe can detect the changes in the cross-sectional velocity profile and in conjunction with point depth gauges, checks the flow conditions are stable before the fluid enters the measurement section.

Six vertical measurement points throughout the flow depth were taken at each streamwise position to capture the velocity profile. Measurements were conducted at 7, 8 and 9m downstream from the upstream flume entrance.

The duration of ADV velocity measurements must be sufficient to accurately capture the statistical properties of the time series, therefore a series of convergence tests were conducted to identify the variation in the mean and standard deviation. In Figure 5.38, the mean and standard deviation of the velocities stabilise to within 5% after 3 minutes. 5% error is deemed to be acceptable since there would be diminishing returns for longer time series at great cost in terms of storage space and experimental time. Hence longer duration measurements would not be conducive to the study.

5.2.3.2.1 Conversion of ADV Coordinate Axis Since the default ADV coordinate axis is X in streamwise, Y in transverse, and Z in vertical; a coordinate axis conversion was applied to ensure the data matched the coordinate axis defined in this PhD (see Table 5.3).

Table 5.3: Conversion of coordinate axis for ADV sensor from local instrument coordinate system to global coordinate system (used throughout the thesis).

Default ADV coordinate axis	Coordinate axis used for PhD
X (streamwise)	X (streamwise)
Y (transverse)	Y (depthwise)
Z (depthwise)	Z (transverse)

5.2.3.2.2 ADV data processing Since ADV data is prone to spiking as described by Goring and Nikora (2002). A modified phase space detection method presented by Mori et al. (2007) was used to identify the spikes for removal. Identified outliers were replaced using a spline interpolation (Ulanowski and Mori, 2014). Figure 5.39 show a comparison of the de-spiked and raw ADV signals. It can be seen that the raw signal is generally very similar to the de-spiked signal for both the streamwise and transverse directions. At this measurement location, the ADV probe position is just beneath the free-surface. The upper ADV prongs are in the air resulting in the signal for the vertical direction to be very noisy.

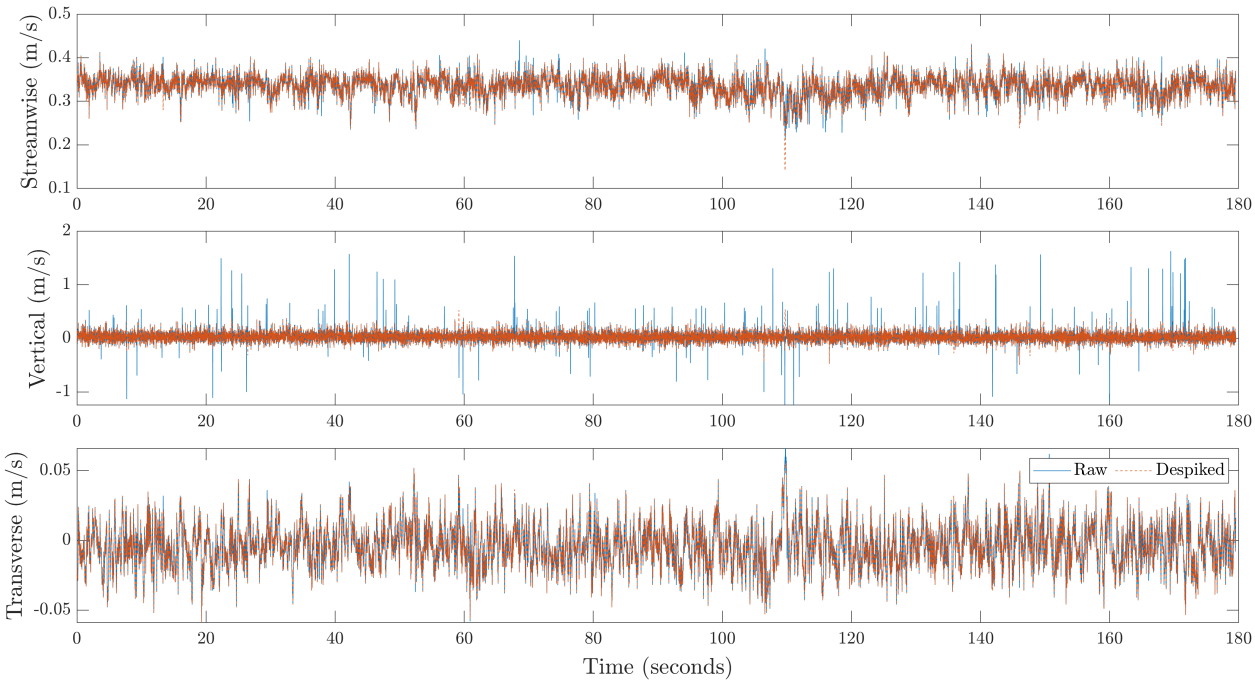

Figure 5.39: Comparison of raw and de-spiked ADV signals taken for the 149mm flow condition at 9m downstream in the centerline of the flume, 139mm up from the bed. Spline interpolation was used to replace spikes detected by the phase space detection method was used (Goring and Nikora, 2002; Mori et al., 2007; Ulanowski and Mori, 2014). Note, the ADV probe position here is just beneath the free-surface with the upper ADV prongs in the air, hence the signal in the vertical direction for this location is particularly noisy. The vertical direction data should not be used.

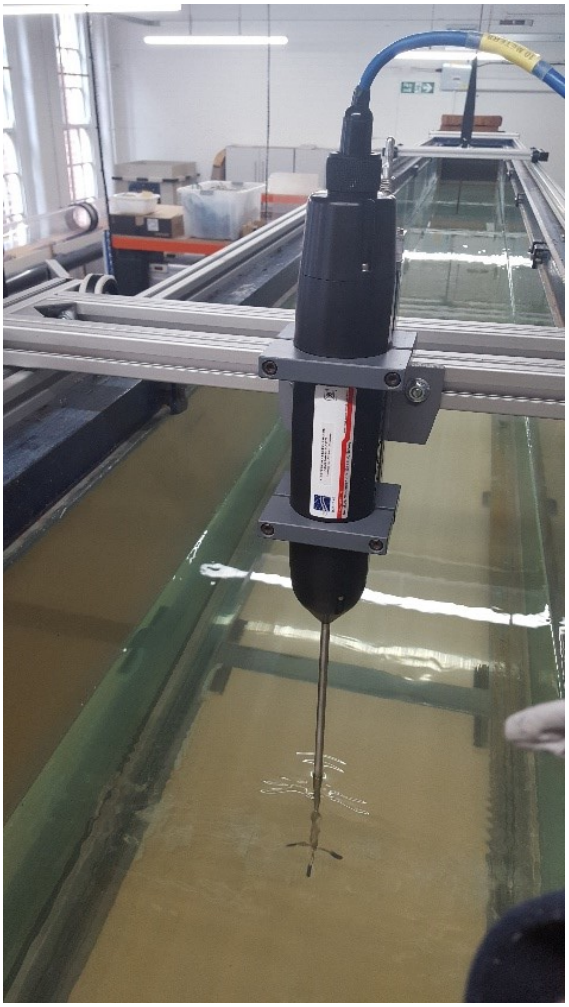

(a) ADV Probe being tested during setup (a side-facing ADV probe is used in the final test campaign).

(b) Depth gauge instrument to ensure a uniform depth of flow.

Figure 5.37: Images of an ADV probe and depth gauge in clear water. The depth gauge is used to check the flow depth is uniform along the streamwise direction. The ADV probe is used to check the flow has stabilised before the PIV measurement region. The ADV probe is removed after use to minimise the generation of a wake which would disturb the flow downstream.

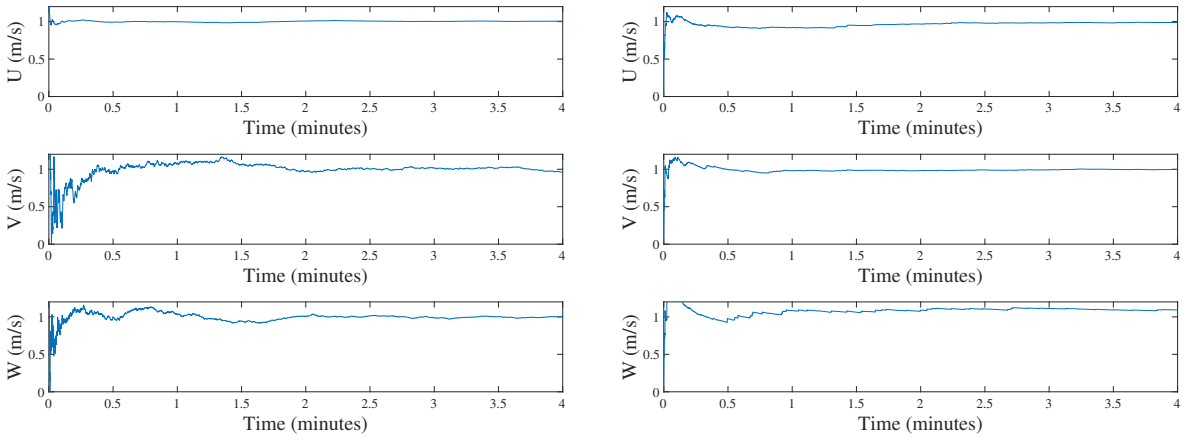

(a) Mean (b) Standard Deviation

Figure 5.38: Temporal convergence of ADV flow statistics at a single point in the flow (flow condition shown here was the 109mm flow depth). It takes up to 3 minutes to converge.

5.2.3.2.3 Conductance Probe Three conductance probes were installed for the steady flow tests. These are shown with their labels in Figures 5.40. Probes A and B are in the centerline whilst probe C is at the midpoint between the centerline and the wall. Figure 5.41 and 5.42 show the probes during the experiment. The supporting structures extend as close as possible to the free-surface of the flow (without impinging on it). This is to provide the conductance probe wires with maximum structural rigidity for preventing deflection and oscillation against the force of the water flow.

Figure 5.42b show the supporting structure does not impinge on the free-surface even at the maximum depth. As a side note, the sub-critical nature of the flow can also be observed with the ripples travelling in front of the wave probe despite the flow flowing in the opposite direction. The supporting structure shown in Figure 5.42b is the closest to the flow, it is also the last instrument in the flume and downstream of all the other sensors. Therefore, even in the event that contact is made between the supporting structure, the effect would be minimal.

(a) View of the conductance probe positions. Probe C is partially hidden.

(b) Different perspective of probe positions.

Figure 5.40: Images of the wave probe setup in the flume. Probe B (analogue input 2) and C (analogue input 7) are upstream of Probe A (analogue input 0). Probes A and B are along the flume centerline whilst probe C is placed at a quarter length across flume width.

Figure 5.41: View of the conductance probe during the experiment at 149mm flow depth. Water has been coloured for the Kinect infrared sensor to enable simultaneous free-surface measurements.

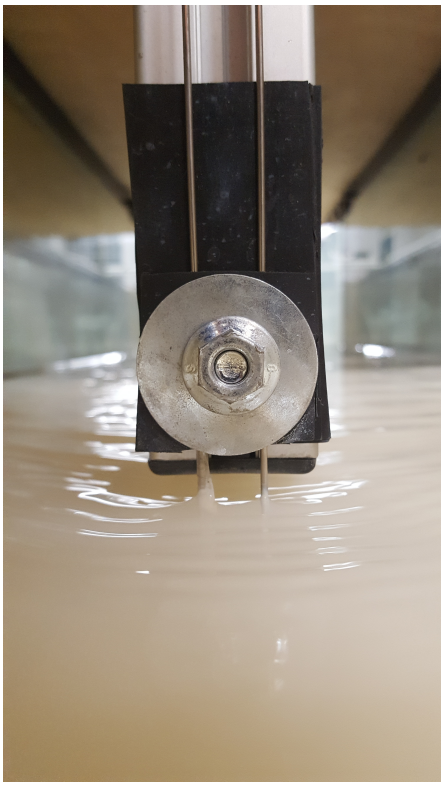

(a) Frontal view of probe.

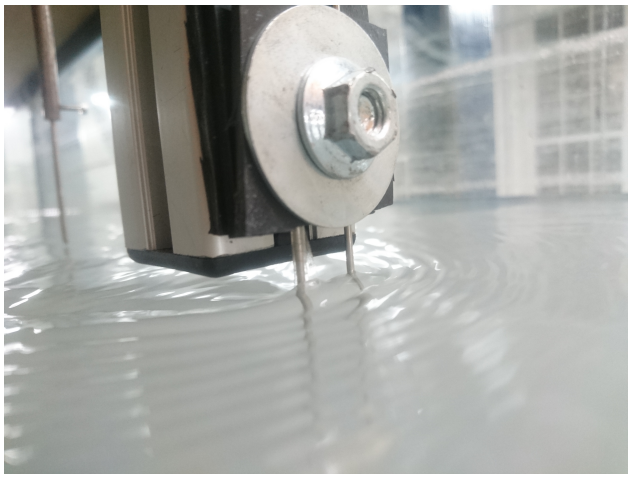

(b) Dimetric view of the conductance probe.

Figure 5.42: Close-up images of a wave probe during setup to check the supporting structure did not impinge on flow (Probe A is shown). Water is partially clear as not all colourant has been added yet.

5.3 Summary

The aim of the experimental flow testing was to measure a set of new, shallow open channel flow conditions representative of real flows (i.e., those shown in Figure 2.2) using a combination of novel and traditional; intrusive and non-intrusive; sensors to detect the underlying flow and free-surface movements.

Two types of infrared 3D range measurement devices (Kinect V1 and V2) were adapted from the gaming industry and applied to remote sensing of free-surfaces. Since these devices work better with opaque surfaces, the concentration of colourant additives (milk and TiO_2) necessary to create an opaque water surface was investigated. A minimum of 4% milk concentration or 0.01% TiO_2 was found to consistently detect the correct surface position. The settling characteristics of these colourants over time and their impact on the free-surface sensing capability were assessed. With TiO_2, it was discovered that after 20 minutes the perceived depth may drop by up to 4mm. With milk, the drop was less. However the practical constraints around the milk going stale prevents it from being used for larger scale flow testing. Finally, the performance of the Kinect infrared sensors in measuring large-scale free-surface features was demonstrated by measuring gravity waves in a wave tank. The results of this work have been published in MDPI and form one of the few publications which has evaluated these infrared sensors for water surface sensing (Nichols et al., 2020).

Based on the literature and research, six new uniform flows over a rough bed were designed with the aim of creating a range of different free-surface and open-channel flow behaviours to collect a novel dataset (the full details are in Table 5.1).

Traditional conductance-based wave probes and Kinect infrared sensors were deployed to collect free-surface measurements. To measure inside the flow field, high-speed Particle Imaging Velocimetry (PIV) mounted in a stereo configuration enabled the 3D velocity vector field at the centerline plane of the flow to be captured. This allows turbulent structures to be detected with high temporal and spatial resolution. A rail-mounted Acoustic Doppler Velocimetry (ADV) sensor was placed at different upstream positions to check and confirm

that flow had stabilised before the PIV measurement zone. These were removed after use to prevent the wake from affecting the measurements downstream with the other sensors.

Figure 5.43 shows an illustration of the experimental flume with the sensors used. A section cut has been applied with one of the flume side walls has been hidden to allow better visualisation of the PIV laser plane.

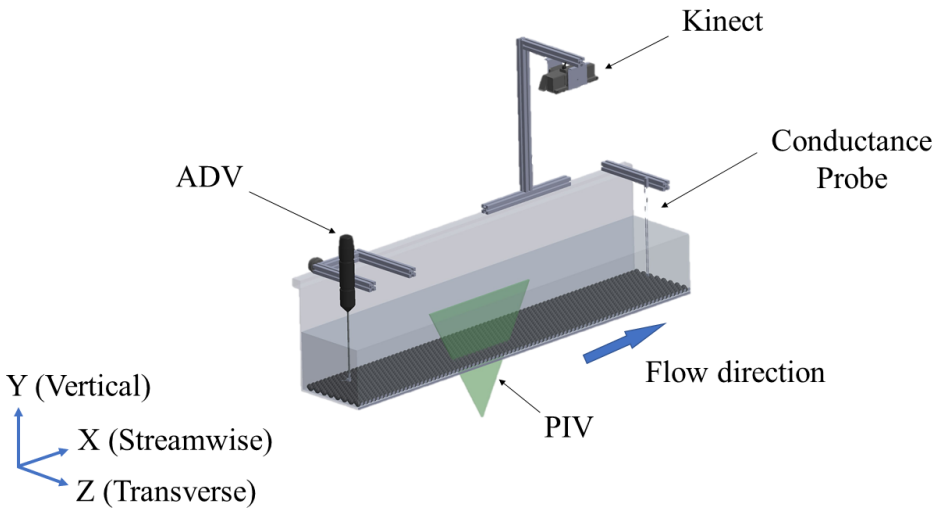

Figure 5.43: Illustration of sensors used in experimental hydrodynamic tests. ADV and PIV were used to measure the conditions inside the flow whilst the conductance wave probe and the infrared Kinect sensors were used to measure the free-surface. Only one wave probe is shown for clarity.

The following chapter will detail the development of the CFD models for studying the rigid lid approximation.

'All models are wrong, but some may be useful.'

Professor George E. P. Box (1976)

Chapter 6

Methodology of CFD Simulations

This chapter begins with an introduction to the CFD software selected (based on the literature review). Two main strategies were tested and presented. The first approach simulates the majority of the flume and is presented within the development section. The second approach applies periodic boundary conditions and was selected as the final methodology. Details including the domain geometry, mesh, turbulence model, initial conditions, boundary conditions and other settings are also discussed.

6.1 Software

The typical OpenFOAM simulation folder structure consists of three main directories (Figure 6.1). The 'system' folder contains files to control the simulation and run additional functions. The '0' folder contains the initial conditions as the first time step. The 'constant' folder contains the mesh, the fluid properties and the settings of the solver. Together these state the key settings used to mesh, check and run the simulation.

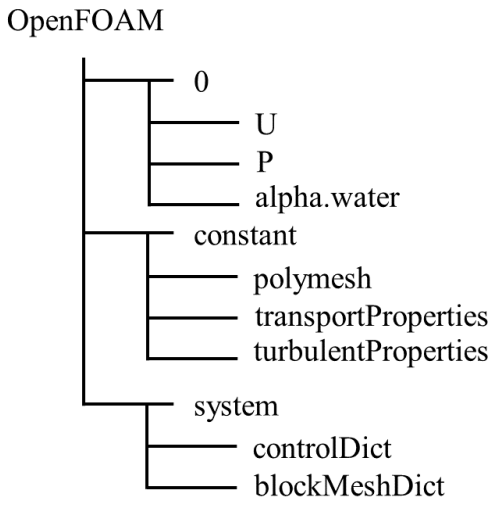

Figure 6.1: Typical OpenFOAM case directory with minimum required files to run. The 'system' folder holds the majority of the settings including runtime control, solver scheme, mesh settings and sampling tools (virtual sensors). The 'constant' folder contains the mesh and turbulence settings whilst the '0' folder contains the initial conditions.

6.2 Development

The CFD simulation work in this thesis begins with creating the simulation (computational) domain. Figure 6.3 shows the domain with a vertical inlet representing the relevant part of the experimental flume. This geometry which constrains the flow was initially created within OpenFOAM using the *BlockMesh* utility. The utility uses a series of Cartesian coordinate points to define a 3D block of space (see Figure 6.2). Edges connect these points together to form blocks. By default, the edges are straight although curves may be specified through keywords with their accompanying curvature parameters. Typically, each block is a hexahedra containing 8 vertices. Other 3D shapes such as trapezoidal prisms can be formed by repeating the coordinates to merge two points together. This is useful for creating meshes around curved geometry.

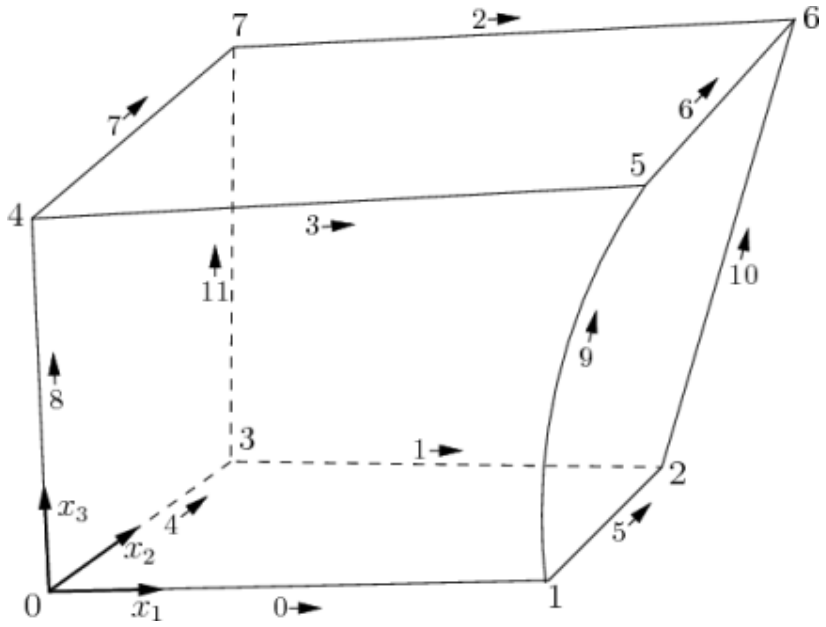

Figure 6.2: First stage meshing is achieved by splitting the domain into virtual blocks with different settings for each block. Definition of a block and its order of vertices using the *BlockMesh* utility. Simple regular mesh with gradients and curves can be defined using *BlockMesh* (OpenFOAM, 2016). x_1, x_2 and x_3 are orthogonal cartesian coodinate axis.

6.2.1 First approach: Simulating the entire flume

As stated in section 5.2.1 on the experimental fluid dynamics part of the thesis, the experimental flume was a 14.20m long, 0.5m wide, 0.5m high flume at a 0.001 gradient (see Figure 5.26). This was supplied with recirculating water coming up from a vertical shaft. Both of the vertical inlet shaft and the outlet weir were initially captured within the CFD model. Extra attention was paid to create a smooth mesh transition as the water rose up and around the curve to flow down the flume. As shown in Figure 6.4 and Figure 6.7, this involved adding special blocks to split the vertical shaft into two vertical parts and adding mesh gradient to concentrate the number of elements at the curve.

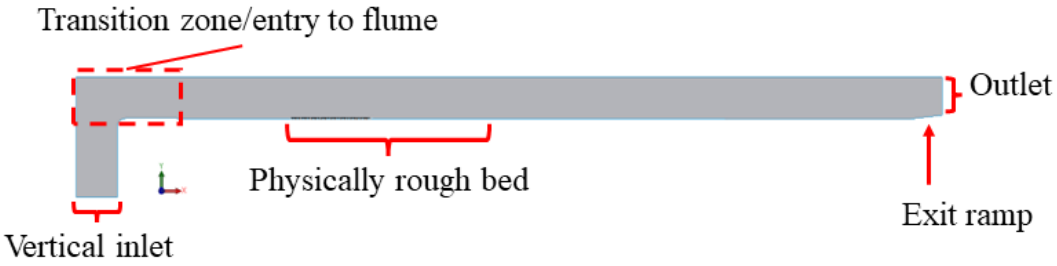

Figure 6.3: Full sized computational domain with a vertically oriented inlet shaft representing the physical hydrodynamic recirculating flume used in the experiments.

Figure 6.4 shows the blocks defined for use by the *BlockMesh* utility. The points used for the *BlockMesh* are shown in Figure 6.5 as a 2D diagram. The faces of the block can be assigned to boundary groups or labelled as an internal face against other blocks. Each block then has mesh settings applied to specific the density and gradient of the mesh.

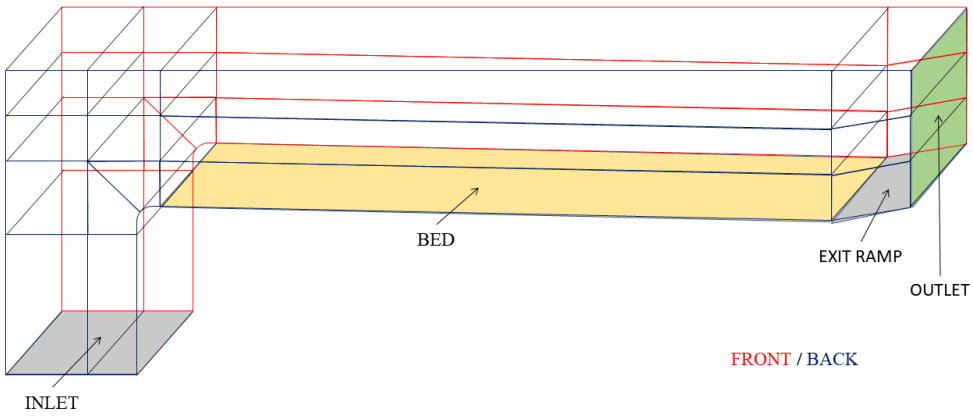

Figure 6.4: 3D figure of the *BlockMesh* flume showing the blocks. Individual mesh settings are defined for each block to create more complex gradients within the mesh.

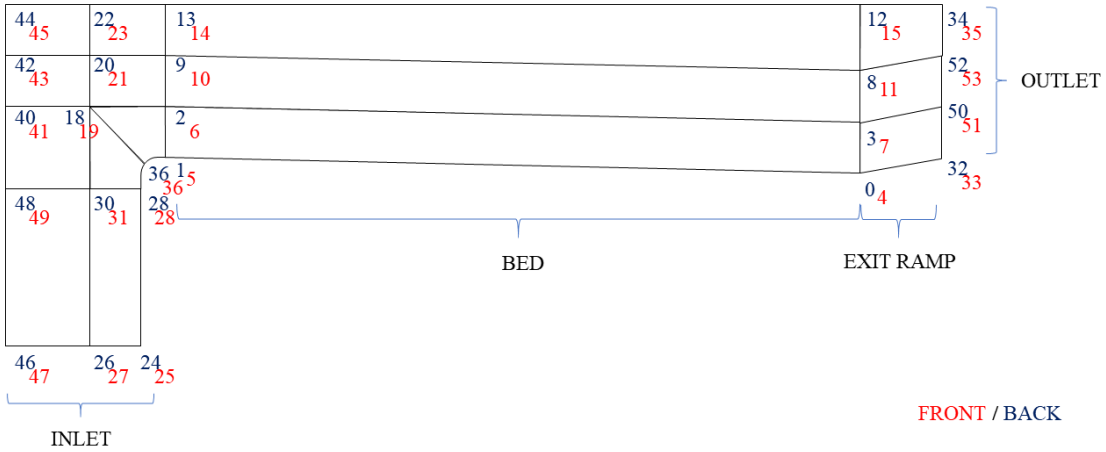

Figure 6.5: Side view of the computational domain with numbered vertices for the definition of spatial coordinate points for the *BlockMesh* utility. Vertices labelled in red/dark blue represent the respective points on the near/far side of the flume in the transverse/spanwise direction respectively (out of the page).

In the experimental tests, an adjustable weir acted as the flume exit. The angle of this was slowly adjusted until the free-surface became parallel to the bed surface indicating uniform depth. Since there can only be one combination of flow rate and bed gradient which will result in a uniform flow depth, this was an appropriate strategy to use experimentally. In the simulation, a series of different meshes and simulations were carried out to determine the exit ramp angle. As the flow conditions are sub-critical (as reflected in the Froude numbers), an incorrect exit ramp angle could cause waves to be transmitted back upstream leading to inaccurate free-surface behaviour. Table 6.1 shows the results of this study.

Table 6.1: Preliminary tests to determine correct exit ramp angle. CFD simulations were first conducted in 2D to narrow the approximate range of possible ramp angles before further 3D simulations further narrowed the ramp angle to $\pm 0.1°$. A smooth bed with no physical protruding obstacles was used.

Depth (mm)	Ramp exit angle (deg)	
	2D	3D
149	15.0	12.4
129	12.0	11.4
109	07.0	09.6
89	09.0	08.7
69	07.0	07.0
49	06.0	06.3

After the main flume geometry was created and the exit angle determined, the sphere bed was modelled using Solidworks and exported as an STL file. To give more control over the shape of the mesh without using a large number of elements, the meshing tool from ANSYS fluent was used. Figure 6.3 shows a side view of the 3D domain in ANSYS. The mesh was then imported back into OpenFOAM for the simulation.

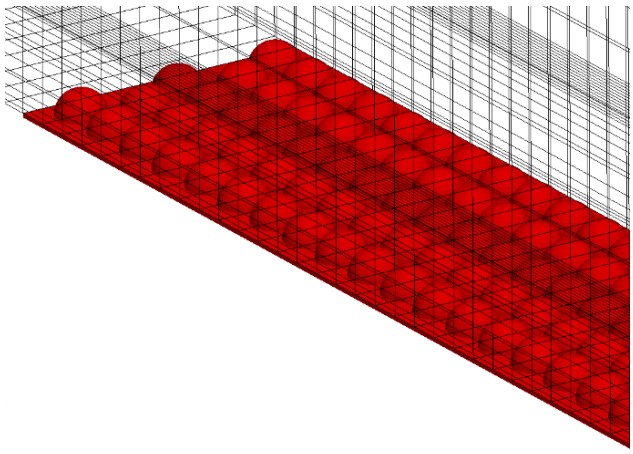

Figure 6.6: Stereolithography file (.STL) format containing 3D spherical elements (in red) overlaid with the coarse mesh generated using *BlockMesh* (in black). This is in preparation for further refinement of mesh around the elements in the STL file using SnappyHexMesh.

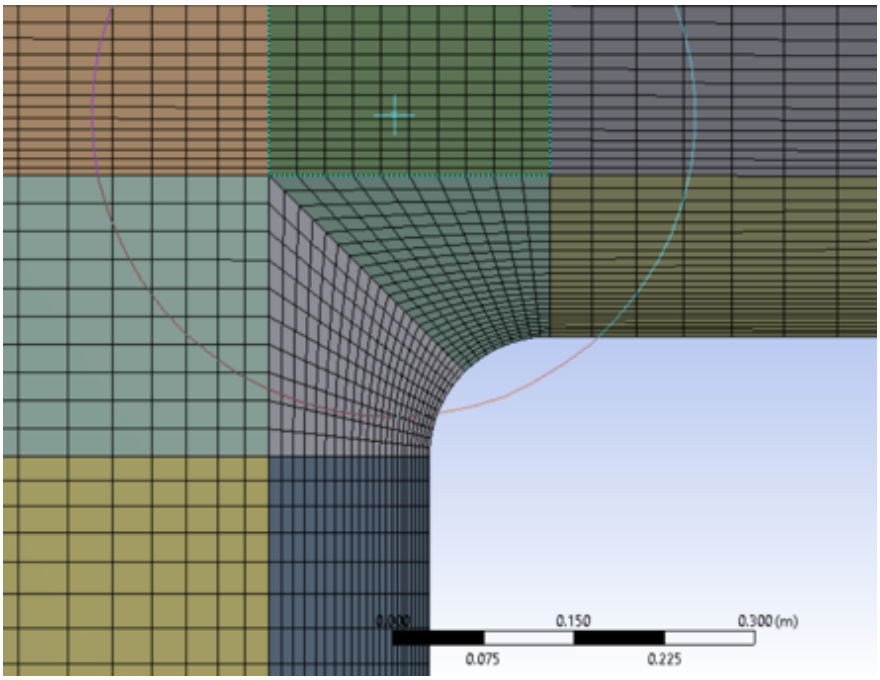

Figure 6.7: Closeup view of the computational domain geometry with the vertical shaft inlet reflecting the same physical setup as in physical laboratory hydraulics experiments. Mesh shown was meshed in ANSYS with individual blocks cut out for better quality mesh around the curved turn.

The initial conditions were set using the *setFields* utility with cells being selected via the 'Box to Cell' method. The initial velocities for each cell is shown in Figure 6.8. For the main part of the flume, an approximate velocity profile was used whilst ensuring that the correct flow rate was maintained. This profile set the initial streamwise velocity near the surface, in the middle flow region and near the bed. For the vertical shaft, the vertical velocity calculated from the bulk flow rate whilst the transition zone lower right corner used a mix of vertical and horizontal velocity components at 45 degrees.

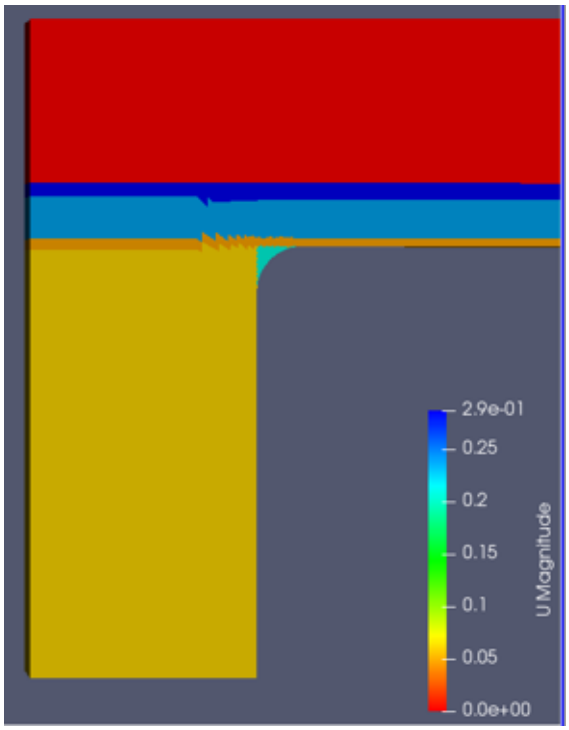

Figure 6.8: Initial velocity conditions set using the *setFields* utility. Different colours represent different velocity magnitudes to help the simulation converge to a realistic flow behaviour in less time. The yellow region is velocity in the vertical direction (water flowing up the shaft to the upstream end of the flume),the orange, blue, indigo and red regions represent different streamwise velocities. The lilac coloured region is a 45 degree combination of streamwise and vertical vectors calculated using Pythagoras' theorem (representing water flowing around the bend). These help the simulation to stabilise faster.

After testing, it was shown that the vertical shaft could be removed to save computational cost and a streamwise inlet 2m upstream from the measurement region was sufficiently far away for the water to stabilise into a behaviour representative of the experiments. Further details are provided in the following section showing the model setup.

6.2.2 First approach (modified): Using Shortened Computational Domain

In this version, the inlet region was designed specifically with the aim of introducing the water to the flume without creating additional artificial turbulence. Thus the water and air phases are separated with a single phase water inlet being used. As before, a 3D computer aided design model was created in Solidworks and imported into ANSYS Space modeller for geometry clean-up. Figure 6.9 shows the domain with Figure 6.10 showing the bed of spherical caps. The CFD coordinate axis is horizontal and vertical but the flow is at a 0.01 gradient. The coordinate system used in this study is aligned with x parallel and y perpendicular to the bed, therefore the CFD data is re-aligned using simple trigonometry.

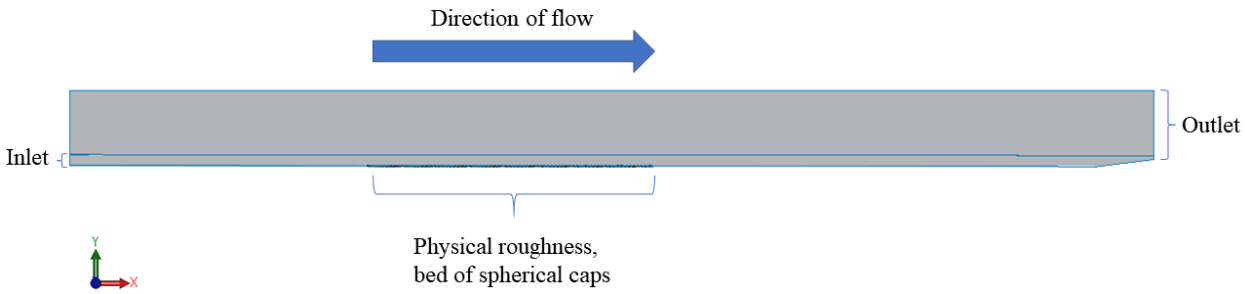

Figure 6.9: Computational domain after simplification of the inlet. The vertical inlet shaft has been replaced with a streamwise inlet. An idealised velocity profile will be used as an initial condition. Physical roughness elements are placed in a downstream region after the velocity profile of the flow has stabilised. The red X and green Y arrows represent streamwise and bed-normal coordinate directions respectively.

6.2.2.1 Bed

The bed in the physical experiments consisted of a hexagonal pattern of 24mm diameter spheres. In this CFD model, only the top 8mm of spheres were modelled to prevent tangential errors at the intersection between two spheres as this would generate bad elements (a triangular prism element with a bad aspect ratio will be formed). The study focuses on the generation of turbulent features from the spheres and since there is limited flow beneath the

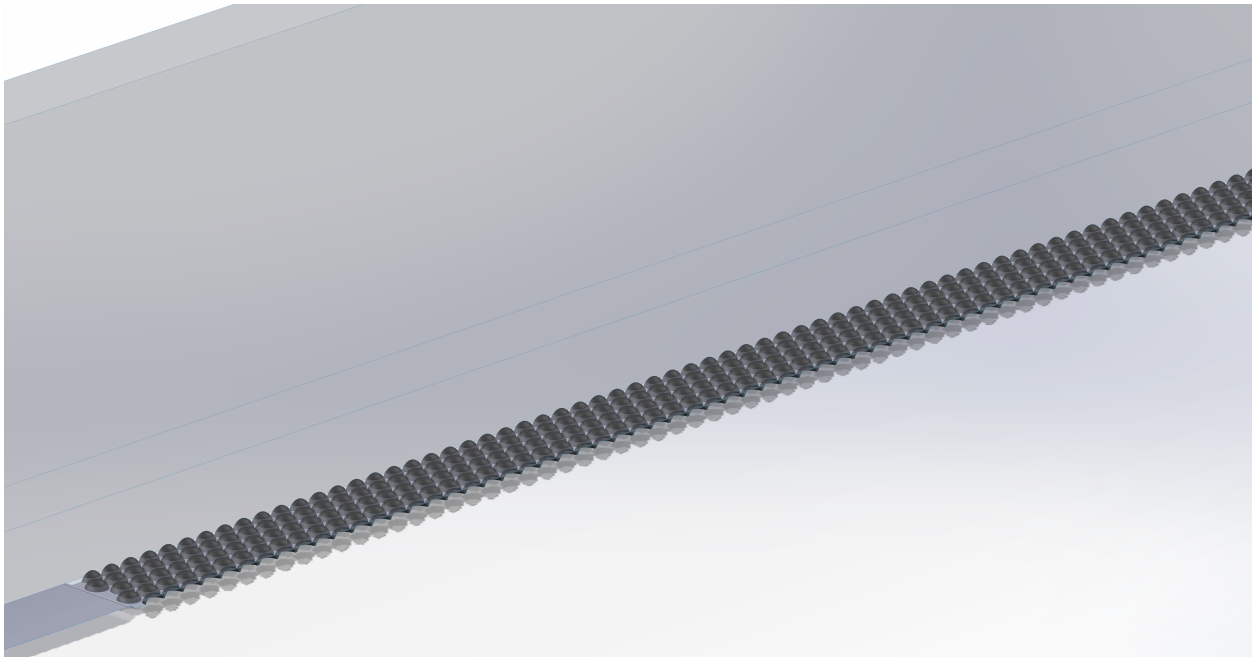

Figure 6.10: Closeup view of the physical spherical cap roughness elements located at the central part of the flume after the flow has stabilised. 3D model created using Solidworks Professional 2019.

spheres, only the topmost 8mm was necessary. To aid transition from the smooth bed flow to flow over a physically rough geometric bed, 4mm fillets were added to the start and end of the bed of spherical caps region. This will help the flow adapt whilst generating minimal artificial disturbance. This can be seen in Figure 6.11.

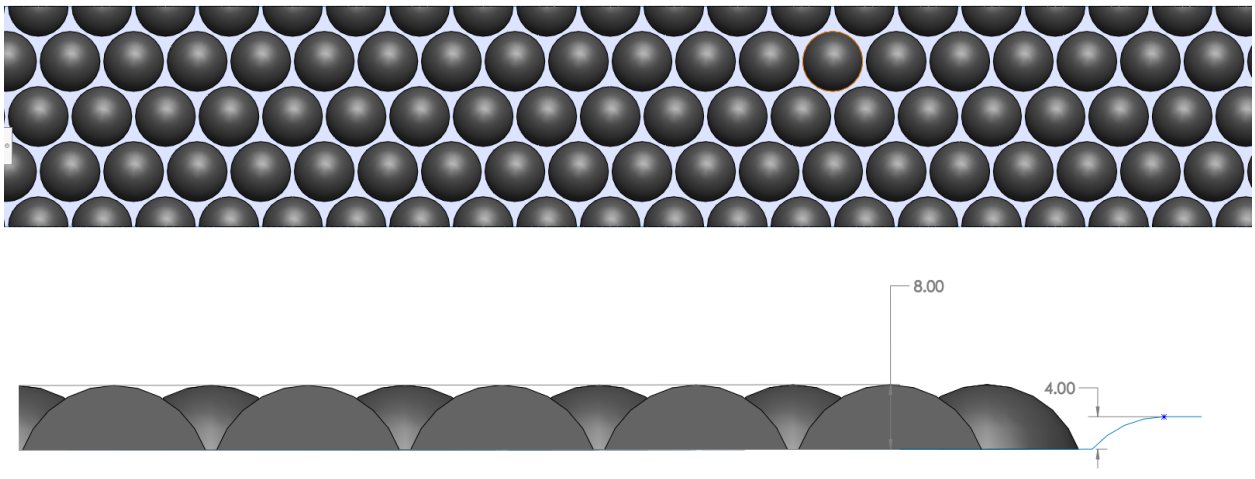

Figure 6.11: Hexagonal packing layout of spherical cap roughness elements: Top View (upper), Side View (lower). Measurements shown are in mm.

6.2.2.2 Computational Domain and Flow Conditions

To reduce the computational volume and concentrate on capturing the streamwise development of turbulent features, the width of the modelled flume was reduced to 84mm (4 sphere diameters) and represented the flow around the centreline of the experimental flume.

The depth of flow simulated was 49, 69 and 109mm with the datum being 4mm below the top of the spherical caps. This matches three of the experimental flow conditions. Table 6.2 shows the CFD flow conditions.

Table 6.2: Computational flow conditions which match the experimental flow conditions and dimenionless numbers in Table 5.1.

Water Depth (m)	Hydraulic Diameter D_H, (m)	Flow rate (l/s)	Velocity (m/s)
0.049	0.1639	1.87	0.08
0.069	0.2163	5.05	0.15
0.109	0.3036	11.21	0.21

6.2.3 Boundary Conditions

For velocity, the slip condition was imposed on the side walls to simulate a wide channel with negligible side wall effects. A no-slip condition was applied to the bed and the spherical caps. The inlet was a fixed flow rate and the outlet was set to *zeroGradient*. The 'ceiling' of the domain and the air 'inlet' above the water inlet use the *pressureInletOutletVelocity*. These conditions are set in the '0' folder inside the velocity field.

The pressure field at the walls and on the spherical caps were *fixedFluxPressure*. The inlet was *zeroGradient*, the outlet and the atmosphere was *totalPressure*. For more information, please refer to the appendix (A).

6.2.3.1 Mesh

The 'Selective Meshing' feature in ANSYS allows incremental meshing of bodies. This is advantageous because the meshed bodies influences neighbouring bodies through a process called mesh seeding. This means that some parts can be meshed first, checked and used to help guide the generation of an optimal mesh for the subsequent bodies. Automated meshing can be used at any time to mesh remaining bodies. When new mesh parameters/controls are added or edited, only the affected bodies require re-meshing, giving rise to selective body updating and great interoperability for combining different meshing methods.

Inflation generates additional layers for a more uniform mesh around certain geometrical features and thus better capture of near wall effects (Figure 6.12).

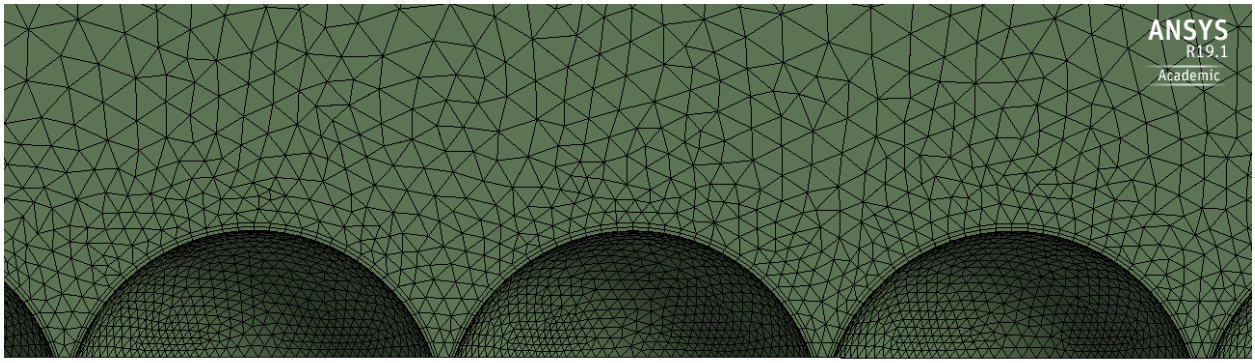

Figure 6.12: Close up view of the mesh around the spherical cap bed in ANSYS 19.1. Two inflation layers are visible on the spherical cap to improve capture of turbulence near the physical surface (boundary layer).

Another method to create a good hexahedra mesh is to use 'sweep' meshing. A source and target face can be selected automatically, or manually by the user; this was used in the inlet region to help merge the mesh between the air and the water phase (see Figure 6.13).

Edge sizing was applied to carefully control the distribution of elements and maintain a good aspect ratio/skewness at the point of merging the flows. A 'sweep' mesh was used on the two blocks surrounding the air and water phase separation to further ensure a smooth transition into open channel flow. Figure 6.14 shows the dimensions of the inlet.

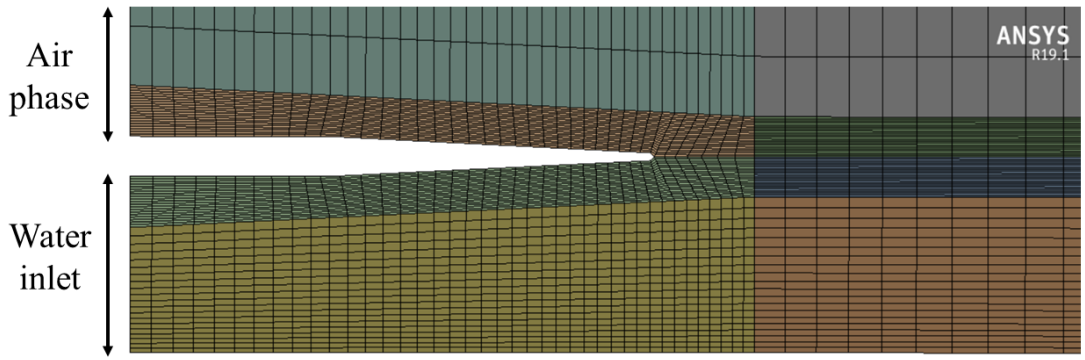

Figure 6.13: Custom flume inlet region designed to smoothly merge the water and air phases without creating artificial eddies. The inlet region utilises an underwater inlet in the shape of an expanding nozzle. The mesh has been split and meshed by region.

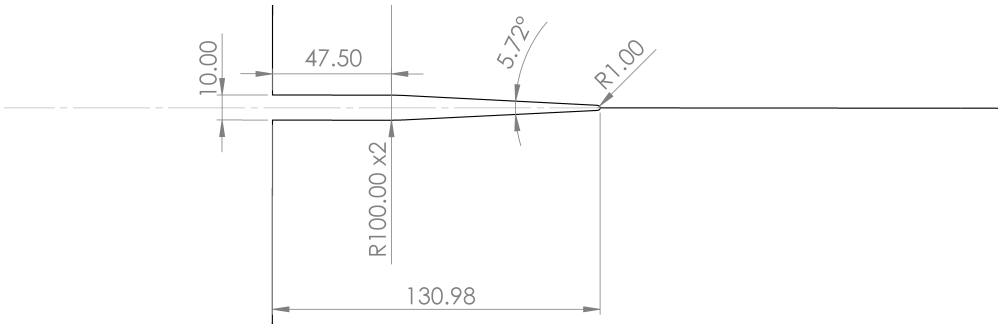

Figure 6.14: Drawing of the custom flume inlet region designed to smoothly merge the water and air phases without creating additional eddies. Dimensions shown are in mm.

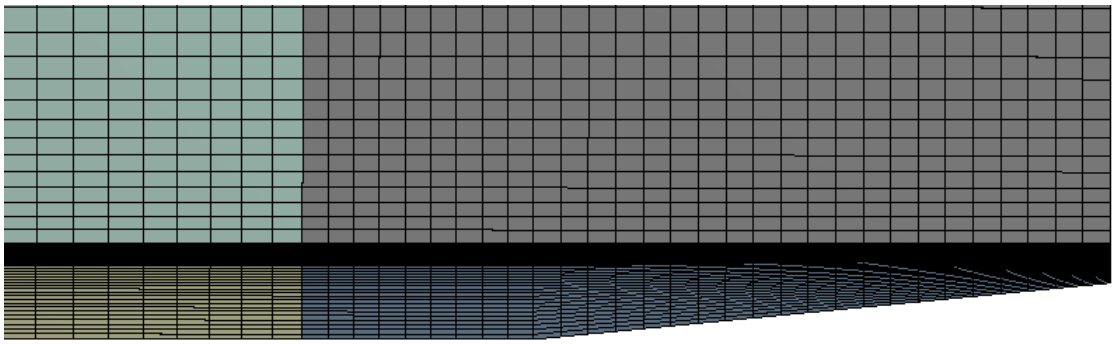

Figure 6.15: Flume outlet region, the mesh is maintained horizontally without any change to prevent back propagation of surface errors as the flow goes up the ramp.

The exit region uses the results of the ramp study in section 6.1 to control the height of the free-surface and ensure a uniform flow depth. The mesh is carried horizontally until the end of the flume without any change to ensure minimal errors from the free-surface hitting the exit ramp. Such errors have been known to propagate back into the domain (Figure 6.15).

6.2.3.2 Mesh Quality

The quality of the mesh can be checked using several factors. These are aspect ratio, skewness and orthogonal quality. As shown in Figure 6.16, the aspect ratio in 2D is defined as the ratio between the length and height. In 3D, this becomes an area ratio or a ratio of a mesh element's circumscribed circle radius to its inscribed circle radius.

There are two methods for determining skewness. For triangles and tetrahedrons, the equilateral volume deviation equation is used. This is the difference between the optimal cell size and current cell size (θ_{max}) normalised by the optimal cell size. For hexahedrons, prisms and pyramids, the normalised angle deviation equation is used. This is calculated by:

$$Skewness = \max\left[\frac{\theta_{max} - \theta_c}{180 - \theta_c}, \frac{\theta_c - \theta_{min}}{\theta_c}\right], \tag{6.2.1}$$

where θ_c is the equiangular face/cell ($\theta_C = 60$ for tetrahedron and triangle, and $\theta_C = 90$ for quadrilaterals and hexahedrons).

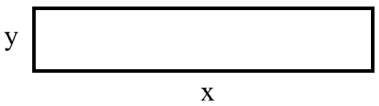

(a) 2D element where y and x are the vertical and horizontal lengths

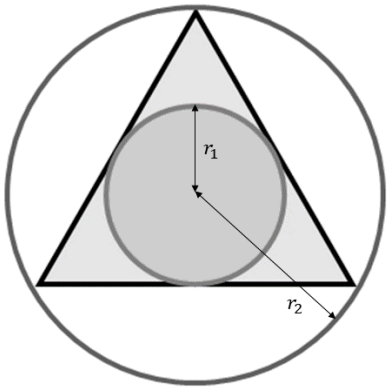

(b) 3D pyramidal element enclosed by an external sphere with radius r_2 surrounding an internal sphere with radius r_1

Figure 6.16: Calculation of aspect ratio of a cell in the mesh. In 2D, this is achieved by dividing the length by the height (y/x) whilst in 3D, this is achieved by dividing the cell internal sphere radius with the external sphere (r_1/r_2).

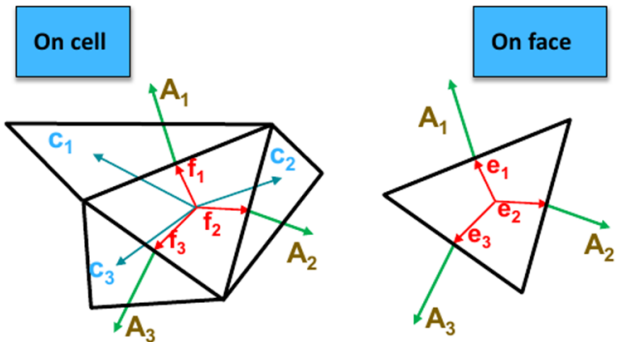

Figure 6.17: A visual representation from ANSYS of the variables used to calculate Orthogonal Quality as defined in Equation 6.2.2 (for cells) and 6.2.3 (for faces).

The orthogonal quality (OQ) can be calculated for both faces and cells; this is derived from the fluent solver discretisation. For a cell, this is calculated by:

$$OQ_{cell} = \min \left[\frac{A_i . f_i}{|\overrightarrow{A_i}| \, |\overrightarrow{f_i}|}, \frac{A_i . c_i}{|\overrightarrow{A_i}| \, |\overrightarrow{c_i}|} \right], \tag{6.2.2}$$

where the i subscript denotes the value for each face. A_i is the face normal vector, f_i is the vector from the centroid of the cell to the centroid of that face, c_i is the vector from the center of the cell to the centroid of the adjacent cell. Figure 6.17 shows a visual representation of these variables. For a face, this is calculated by:

$$OQ_{face} = \min \left[\frac{A_j . e_j}{|\overrightarrow{A_j}| \, |\overrightarrow{e_j}|} \right], \tag{6.2.3}$$

where the subscript j is each edge and e_i is the vector from the centroid of the face to the centroid of the edge. At boundaries, the c_i is ignored when calculating the OQ.

It was found that the region with the worst mesh occurred at the transition between the smooth bed and the rough bed of spherical caps. Thus, the mesh transition was shifted further upstream so that any minor inaccuracies from the poor cells have a chance to dissipate before the flow hits the bed of spherical caps. Figures 6.18, 6.19 and 6.20 show this transition region with the maximum and minimum values of the aspect ratio, skewness and orthogonal quality respectively. It can be seen that even in this region, the vast majority of the mesh is

still at least good or acceptable. Where there were bad cells in close proximity to the bed of spherical caps which could affect the turbulence generation, the vertices of the cells/faces were manually adjusted until it achieved the minimum acceptable mesh quality.

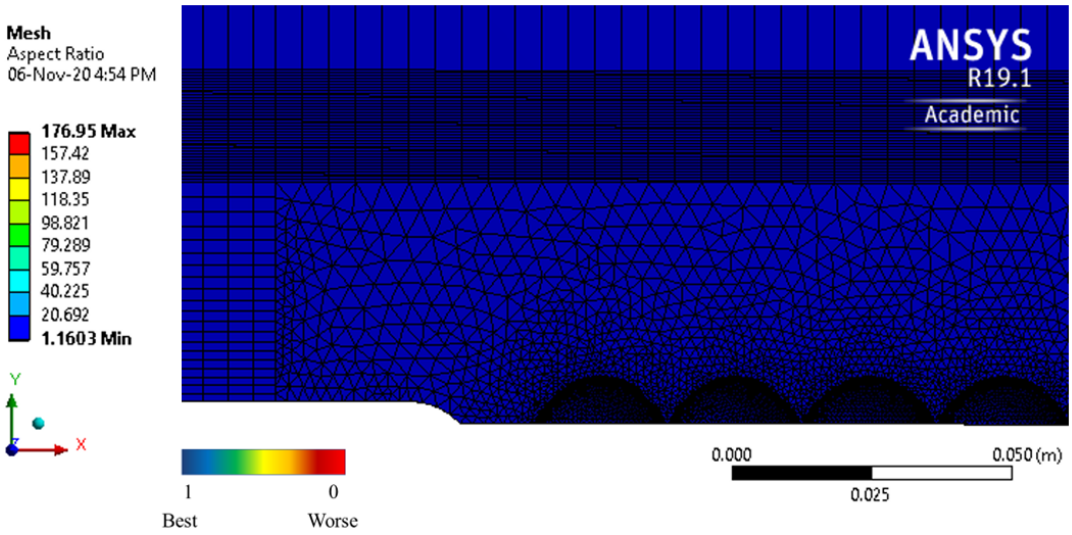

Figure 6.18: Assessment of the mesh quality at the bed transition zone using the aspect ratio. The majority of the mesh quality is very good with a minimum aspect ratio of 1.16. Figure 6.16 explains how the aspect ratio is calculated.

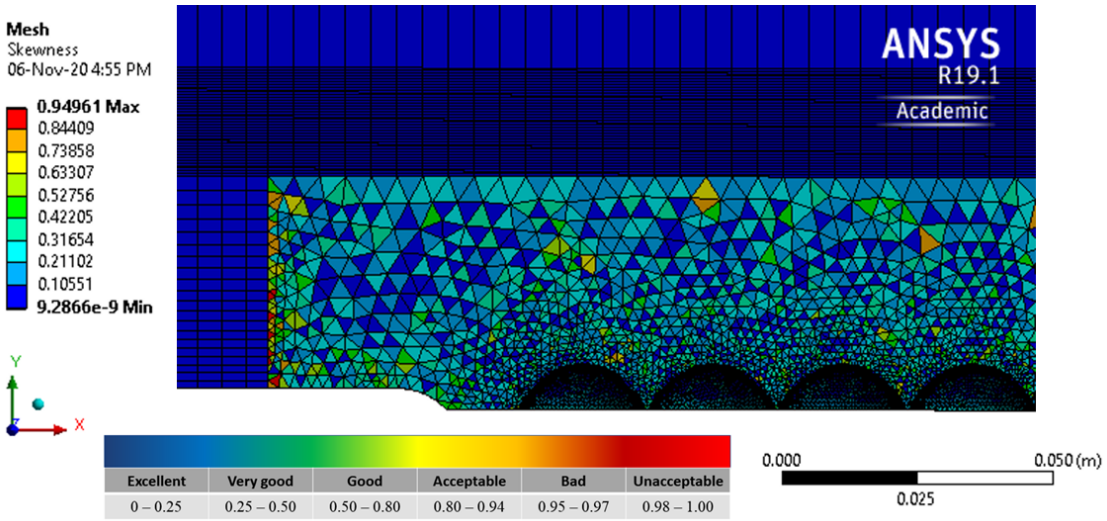

Figure 6.19: Assessment of mesh quality at the bed transition zone using element skewness. The worse elements are located near the transition from uniform mesh to more of an unstructured type mesh.

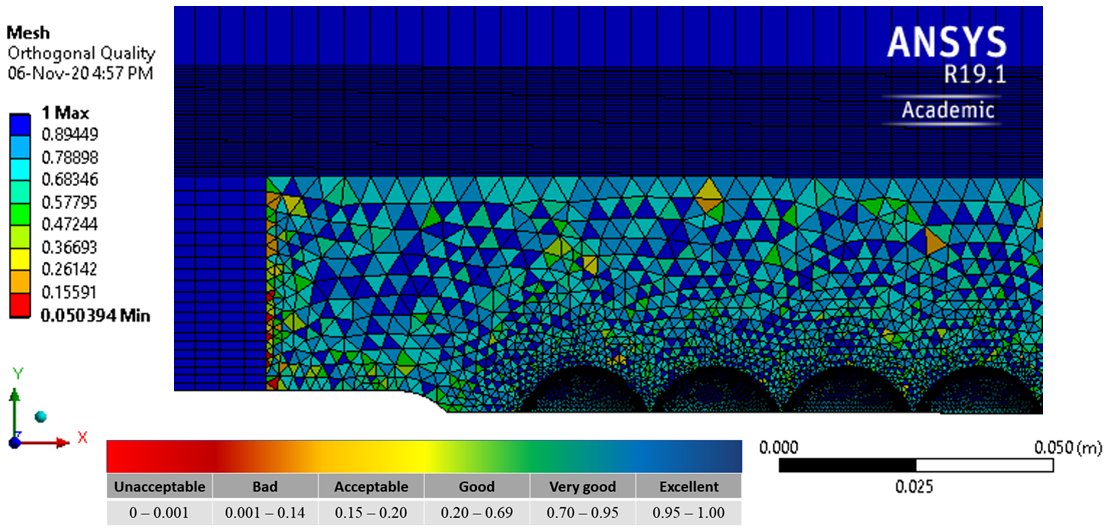

Figure 6.20: Assessment of mesh quality at the bed transition zone using orthogonal quality. The worse elements are located near the transition from uniform mesh to more of an unstructured type mesh.

6.2.3.3 Solver Model

Volume of Fluid free-surface modelling was achieved with the *interFoam* solver of OpenFOAM. As discussed in the literature review in chapter 4, this is a solver for incompressible flows with a phase-fraction based interface capturing approach.

6.2.4 Turbulence Modelling

To model the turbulence in the flow, a DES simulation with a RANS $k-\omega$ subgrid turbulence model was used in this simulation. This method provides an advantage because DES that uses a hybrid approach to turbulence modelling by combining aspects of RANS and LES to reduce intensive near-wall meshing requirements that are normally imposed by LES. It also is better than the standard RANS turbulence models such as $k-\varepsilon$ because it includes a Shear Stress Transport (SST) term that can help improve the freestream values of k and ω. The $k-\omega$ model is a two equation model used to estimate the turbulent eddy viscosity μ_t. The turbulent kinetic energy equation (discussed in Chapter 4) for the implementation of the $k-\omega$ model in OpenFOAM is publicly available (Guide, 2022).

6.2.5 Initial Conditions

Water was placed in the flume at the approximate depth of flow. As the flume is slightly inclined, it is expected that some water near the exit of the flume will need to be drained before the flow stabilises.

The final initial conditions for the simulation was set with an initial velocity profile based on the ADV velocity profile from the physical experiments.

During the simulation, some parameters were adjusted to improve the efficiency. At the beginning of each new simulation, the maximum Courant number was limited to 0.1 so the progress is very slow but also minimises the chance of a divergence. During this initial period, the simulation is rapidly altering the pressure gradient to reach the mean flow velocity specified and the probability of the divergence is higher. After the first few seconds of flow has been simulated, the flow stabilises and a higher Courant number can be used to increase the progress of the simulation (up to a maximum of 1). Adjustable time step is also enabled to allow the simulation more control in selecting the correct duration for each time step. Lastly, the full flow field is only saved to the hard drives once per second to minimise storage space during stabilisation of the flow (live monitoring of the simulation still uses all time steps).

6.2.6 Sensitivity Analysis

6.2.6.1 Mesh Convergence

Mesh convergence was checked with the 49mm flow depth condition and running the simulation with meshes of varying density. Three meshes are presented here representing a coarse mesh, a fine mesh and a medium mesh. Table 6.4 show the mesh parameters which were changed for the study whilst Figure 6.21 shows the definition of the parameters on the mesh.

The main differences between the mesh are additional vertical elements in the flow, smaller face sizing on the bed and the use of inflation layers to better capture the turbulence boundary layer. This should help capture any bursting or ejection motion stated by others in the literature (Kline et al., 1967; Nagaosa, 1999; Nezu, 2005). Table 6.5 show the mesh quality indicators for the meshes whilst Table 6.3 show the mesh size and a breakdown of cell types.

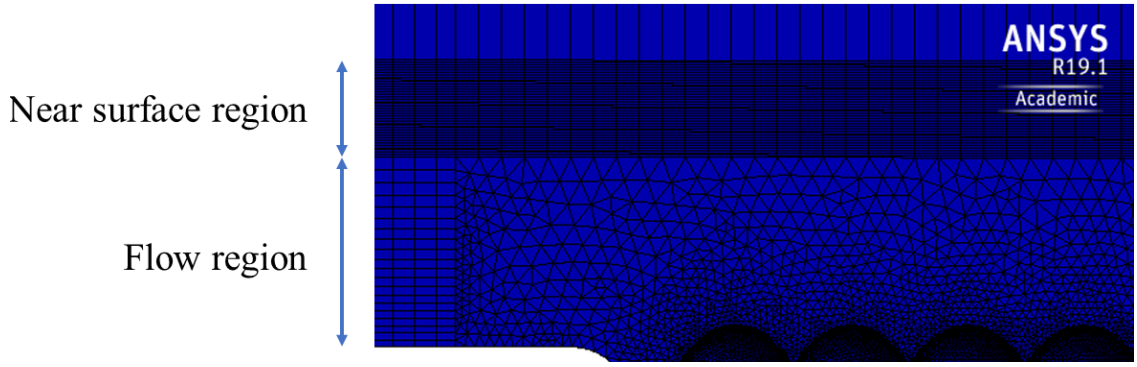

Figure 6.21: Definition of mesh convergence variable parameters used in Table 6.4. The near surface region refers to the fine mesh at around the free-surface. The flow region refers to the region beneath the fine mesh and above the bottom of the computational domain.

Figure 6.22 show the velocity profile of all three flows are within 0.01m/s. The coarse mesh shows some deviation from the other meshes especially near the bed in the vertical direction. This is expected due to the reduced number of mesh elements in the sphere region. In particular the lack of inflation layers likely introduced more uncertainty. As a result, the parameters for 'normal' were used for the main simulation. For other depths, these parameters were scaled up according to the same ratio to give the same spatial resolution of the mesh.

Table 6.3: Comparison of the mesh size and cell type for the simulations used in the mesh sensitivity tests (49mm flow depth simulation).

Mesh statistics	Fine	Medium	Coarse
Points	5,064,086	2,681,790	963,988
Faces	40,456,024	21,428,934	5,990,339
Internal faces	39,480,564	20,639,334	5,722,149
Cells	18,979,630	10,001,367	2,670,802
Overall number of cells of each type			
Hexadedra	1,488,000	529,480	511,000
Prisms	1,025,268	996,440	0
Wedges	0	0	0
Pyramids	16,800	7,392	7,280
Tetrahedra wedges	0	0	0
Tetrahedra	16,449,562	8,468,057	2,152,522
Polyhedra	0	0	0

Table 6.4: Variable mesh parameter settings used in mesh sensitivity analysis with the 49mm flow depth simulation. Refer to Figure 6.21 for visual explanation of these settings.

Variable Mesh parameters	Mesh Fine	Medium	Coarse
Vertical elements within the flow	20	14	10
Face sizing on spherical caps (Growth rate: 1.05)	1*	1*	2*
Inflation layers (Growth rate: 1.1)	2	2	None
Side face of flow (Size: 5*)	Disabled	1.2	1.2
Vertical elements across free-surface region	20	10	10
Block meshing in sphere region	2*	2*	Disabled

*10^{-3}m

Table 6.5: Maximum and minimum mesh quality indicators for mesh sensitivity analysis with the 49mm flow depth simulation. These are acceptable or better as defined by the colorbars in Figures 6.20, 6.19 and 6.18.

Variable Mesh Parameters	Fine		Medium		Coarse	
	Max	Min	Max	Min	Max	Min
Aspect Ratio	88.476	1.1032	88.473	1.160	88.473	1.103
Skewness	0.875	3.25*	0.873	3.25*	0.852	1.35*
Orthogonal Quality	1.000	0.125	1.000	0.127	1.000	0.148

*$\times 10^{-9}$

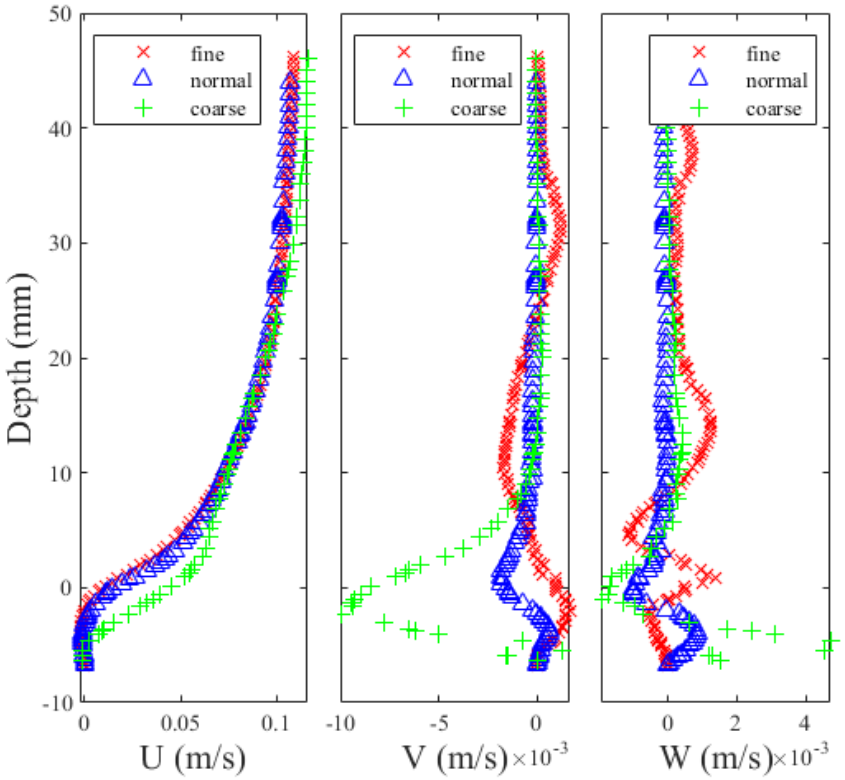

Figure 6.22: Mesh sensitivity analysis using velocity profiles from the 49mm flow depth simulation. In the streamwise direction, the fine and moderate meshes give similar results suggesting that mesh independence maybe reached. However, there are some discrepancies between the meshes in the vertical and transverse directions suggesting that the fine mesh simulation may not have fully stabilised.

6.2.6.2 Minimum sample size needed for convergence of statistics

To check that the flow as stabilised and converged temporally, a point near the bed was selected to do a time convergence analysis. A near the bed location was used because this region typically has the most turbulence and would take the longest to converge. Since various settings such as the Courant nunmber and the density were altered during the simulation to assist with a faster stabilisation and convergence, only the time steps that will be used for further data analysis are used in the time convergence assessment.

In Figure 6.23a, it can be seen that the mean in the streamwise and vertical directions have both stabilised. Figure 6.23b show the same with the standard deviation which is also an indication of the turbulence fluctuation. The lateral direction velocity component is very small, as expected, since the majority of the flow is going downstream.

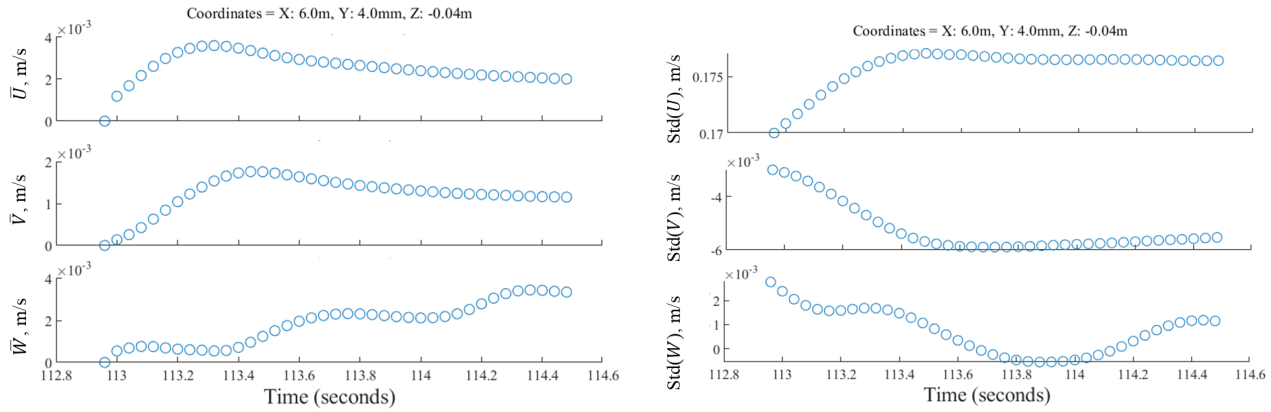

(a) Mean average (b) Standard deviation

Figure 6.23: Convergence of velocity statistics taken at a single spatial coordinate from the 109mm flow depth simulation. The statistics are re-calculated at every time step using data up to and including the latest time step. After several seconds the resulting statistics no longer fluctuate with time (converged temporally).

6.2.7 Optimisation of the parallelisation

Simulations were run at the National Supercomputing Centre in Singapore. ASPIRE-1 (Advanced Supercomputer For Petascale Innovation Research and Enterprise) is a national facility with a 1 PFLOPS System, 1,288 nodes (dual socket, 12 cores/CPU E5-2690v3), 128GB DDR4 RAM/node and 10 large memory nodes (1x6TB, 4x2TB, 5x1TB). It has a total of 13PB Storage using GPFS and Lustre File Systems and an I/O bandwidth up to 500GB/s. Communication within the cluster is achieved with an Infiniband Interconnection EDR (100Gbps) Fat Tree with full bisectional bandwidth.

Each simulation was decomposed into processor directories for parallel computing using the *decomposePar* utility. A scotch method decomposition technique was used, this automatically optimises the load between processors. For each simulation, the case was tested with various numbers of CPU nodes to identify the optimal number of CPUs. Too many CPUs leads to excessive communication between the CPUs instead of actually solving the simulation. Too few CPUs means the simulation could be run faster if more workers were used. Since CPUs are placed within 'nodes' of 24 CPUs, testing with multiples of 24 would be advantageous for the scheduling system.

Figure 6.24 shows the time simulated in 24 hours for different cores on the 69mm case. More simulated time equates to a faster simulation. Using this as an example, it was found that 192 cores was the optimal number of CPUs on the NSCC Lusture system. Comparing the 120 core simulation to the 240 core simulation, this was able to simulate almost double the amount of time steps compared to using double the computational power (and budget) with 240 cores.

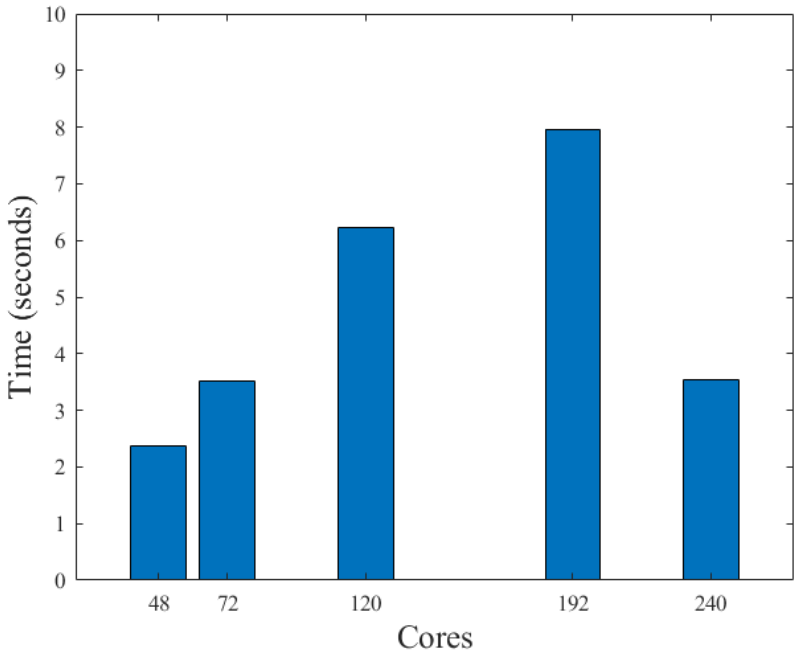

Figure 6.24: Optimisation the utilisation of parallel computing resources. The same simulation was run over 24 hours using different number of CPU processors to assess which configuration could simulate the maximum time. The 69mm flow depth simulation was used for these tests. Multiples of 24 cores are used because each node has 24 available cores.

6.2.8 Evaluation of ANSYS-OpenFOAM simulation approach

Using ParaView, the simulated flows could be visualised although large storage space is required for each time step. Based on the flow visualisation imagery, a clear velocity gradient is seen with slower flow at the bed and faster flow towards the free-surface. It is also clear that some shedding behaviour from the bed can be observed in Figure 6.25. Further downstream in Figure 6.25, this seems to be propagated along the flow and spreads towards the free-surface supporting the literature by many researchers (Kline et al., 1967; Nagib and Guezennec, 1986; Tamburrino and Gulliver, 1999). This could indicate a combination of the type one and type three boils postulated by Nezu and Nakagawa (1991) since the individual spherical cap on the bed can be considered an obstacle, whilst the whole bed can be considered a wall region which generates turbulence that rapidly expands as they move towards the free-surface.

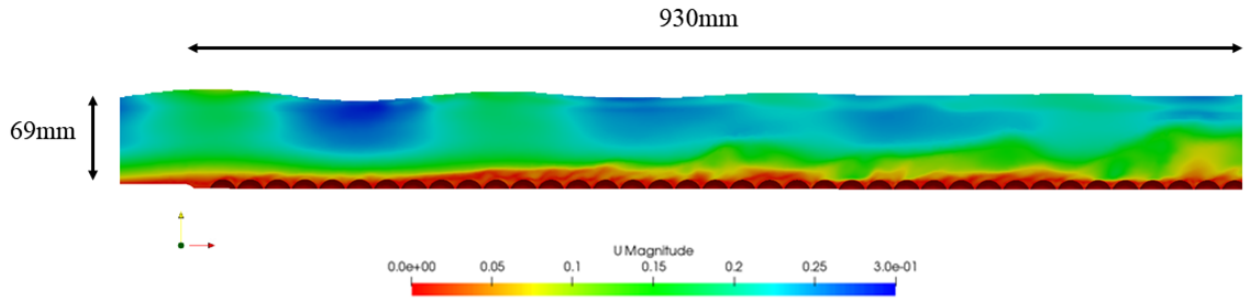

(a) Upstream half of the rough bed

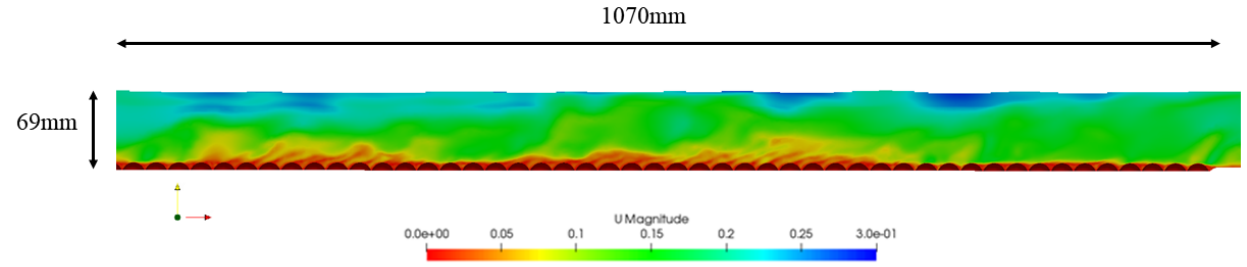

(b) Downstream half of the rough bed

Figure 6.25: Instantaneous flow field over the rough bed region in the 69mm flow depth simulation. Colours represent the magnitude of the velocity vector field.

6.2.9 Comparison of time-averaged statistics

Figure 6.26 shows the time averaged velocity profiles and a comparison with the experimental results. The streamwise CFD velocity is within 0.01m/s of the experimental PIV and ADV data while the transverse and vertical profiles match to within 0.005m/s.

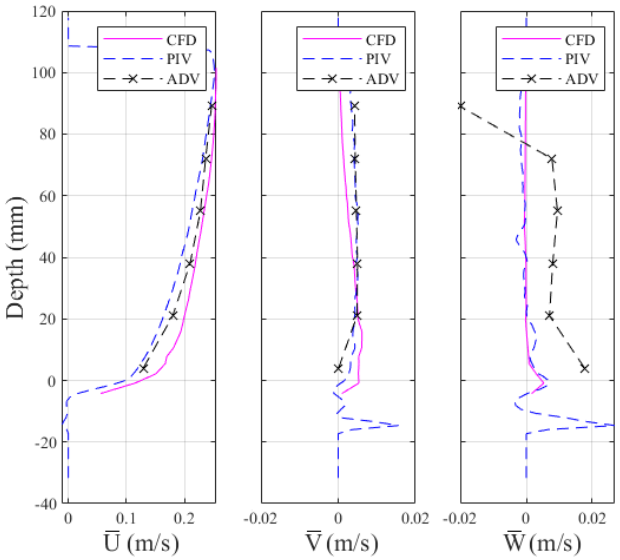

Figure 6.26: Comparison of CFD velocity profiles to the experimental PIV and ADV data using the 109mm flow depth simulation. The ADV transverse data suffers from some noise.

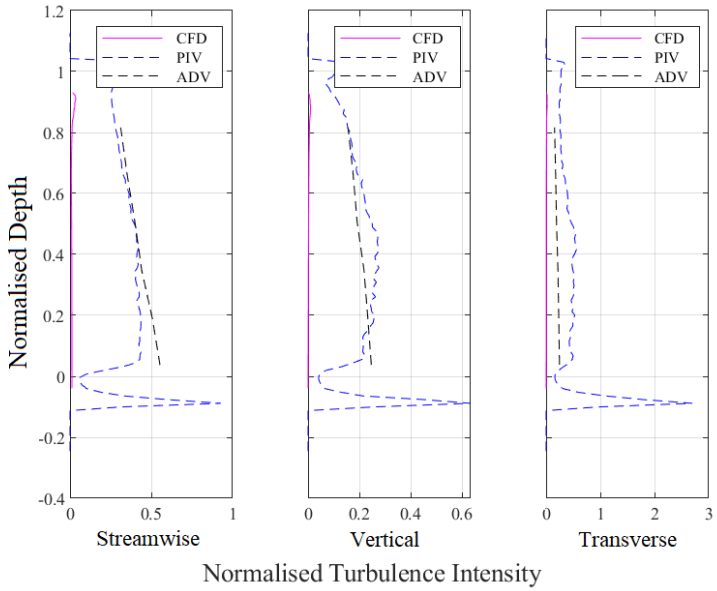

Figure 6.27: Turbulence intensity profile comparison between CFD and experimental PIV and ADV data. The CFD turbulence intensity is very low compared to the PIV and ADV.

Figure 6.27 presents a comparison between the CFD turbulence intensity profile and the experimental results. The turbulence intensity measured by in the experiments are significantly higher than the CFD.

This is a big concern because turbulence very important in generating coherent structures. It is likely that the use of RANS as a subgrid model is unsuitable and a full LES would require a much finer mesh. The resulting simulation would exceed the available computational power.

Therefore, a new approach was developed. This is presented in the following section.

6.3 Second Approach: Using Periodic Streamwise Boundary Conditions

Since it was shown that the computational domain would be too large to fully simulate, a different approach was needed. In order to create a 3D simulation domain with a rough bed, periodic conditions were explored and applied.

1. Firstly, a smooth bed simulation was created. This used a RANS approach to identify the correct necessary turbulence length scales near the wall and integral length scale within the flow. The free-surface was not modelled.

2. Secondly, a smooth bed simulation with a single hemi-sphere was carried out. This tests the meshing capabilities around an imported STL geometry and the RANS/LES turbulence modelling.

3. Thirdly, a small rough bed simulation with a rigid lid and flexible lid was carried out.

For all simulations, a periodic boundary condition was applied on the spanwise and streamwise boundaries. A uniform mean flow velocity corresponding to the experimental tests was specified with the *fvOptions* file in OpenFOAM.

As with the previous simulations, some parameters were adjusted to improve the efficiency. At the beginning of each new simulation, the maximum Courant number was limited to 0.1 to minimises the chance of a divergence. During this initial period, the simulation is rapidly altering the pressure gradient to reach the mean flow velocity specified and the probability of the divergence is higher. After the first few seconds of flow has been simulated, the flow stabilises and a higher Courant number can be used. Adjustable time step is also enabled to allow the simulation more control in selecting the correct duration for each time step. The full flow field is only saved to disk once per second to minimise storage space during stabilisation of the flow (live monitoring of the simulation still uses all time steps).

6.3.1 Smooth Bed Simulations

Based on Bomminayuni and Stoesser (2011), a computational domain of $2\pi H \times \pi H \times H$ should be used where H is the flow depth. Table 6.6 shows the potential simulation domains using the flow depths from the experiments.

Table 6.6: Size of the computational domain in smooth bed simulations based on the ratio presented by Bomminayuni and Stoesser (2011).

Water depth (m)	Streamwise (m)	Span (m)
0.049	0.31	0.15
0.069	0.43	0.22
0.109	0.68	0.34

To model the near wall region properly, RANS with wall function was used. A y^+ value of 30 was selected. This was intended to avoid the buffer layer. Although a k-omega SST model is supposed to be wall insensitive y^+ values, this selection will allow other RANS models to be tested if necessary in the future. By rearranging equation 6.3.1, the distance between the wall and the centroid of the first layer cell (y_p) can be calculated.

$$y^+ = \frac{\rho u_* y_p}{\mu}, \tag{6.3.1}$$

where u_* is the shear velocity.

It should be noted that the first layer cell height (Δy^+) is twice the distance from the wall to the centroid of the first layer (y_p).

Since the streamwise (Δx^+) and spanwise (Δz^+) cell length can be up to 300 times the cell height and the mesh requirements are very low for smooth wall simulations, a ratio of 1.2 is selected to maintain good aspect ratio. Table 6.7 shows the estimated maximum first layer height.

Table 6.7: Height of the mesh's first layer in the RANS simulation (mm).

Water depth (mm)	X (Stream-wise)	Y (Vertical)	Z (Spanwise)
49	4.56	2.74	4.56
69	3.84	2.31	3.84
109	3.06	1.83	3.06

A growth ratio of 1.2 was used in the vertical direction whilst no mesh grading was used in the streamwise and spanwise directions. Table 6.8 shows the estimated minimum mesh dimensions with the vertical element count being estimated from summation of a geometric series (Equation 6.3.2).

$$D_x = \sum_{i=0}^{n} ar^n = \frac{a\,(1-r^n)}{(1-r)}, \tag{6.3.2}$$

Where D_x is the total height of the flow, a is the first layer height, r is the growth rate and n is the number of elements. By rearranging and using some log properties, the number of elements, n can be obtained:

$$n = \log\left(1 - \frac{D_x(1-r)}{a}\right) - \log\left(r\right). \tag{6.3.3}$$

Table 6.8 shows the mesh size which is very low. Figure 6.28 shows the mesh used for the RANS simulation.

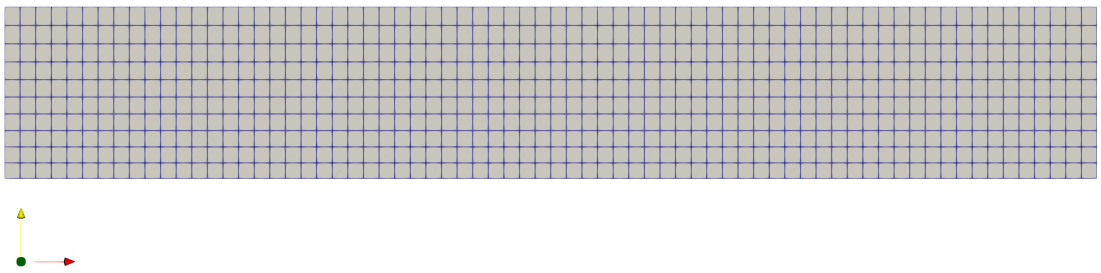

Figure 6.28: Mesh of the periodic simulation at 49mm with a smooth bed and no free-surface.

Table 6.8: Dimensions of the mesh in the RANS simulation.

Water depth (mm)	Mesh (Total number of cells)			
	X	Y	Z	Sum total
49	68	9	34	21,295
69	113	12	56	74,175
109	224	15	112	376,605

6.3.2 Flow Over a Hemi-sphere Without Free-surface

Working towards a full bed of hemi-spheres, a single hemi-sphere was meshed and placed on the bed as an obstacle to test how the periodic boundary conditions handle the simulations. This is similar to the work done by Stoesser and Rodi (2007). The settings used for generating the mesh around the hemi-sphere is later used as a starting point for meshing the entire bed of roughness elements. Figure 6.29 shows the mesh created.

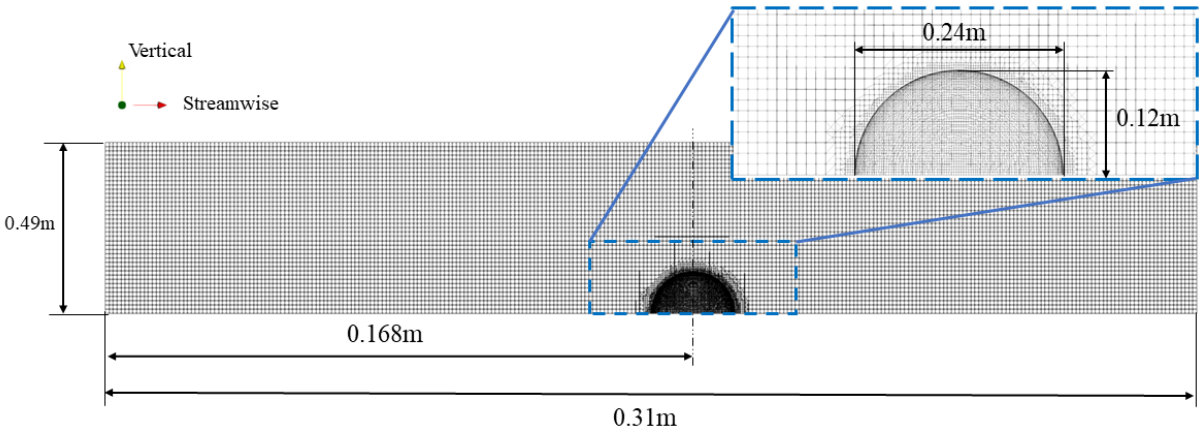

Figure 6.29: Mesh domain for flow over a hemi-spherical obstacle.

The simulation is split into two stages. The first stage uses a RANS simulation until the average statistics have stabilised and the second stage uses an LES WALE simulation. Unlike the previous approach (modelling the full flume), DES is not used as a turbulence model. This is because it could not be ruled out as a factor in not being able to properly account for the turbulence. In addition, studies by Alfonsi et al. (2019) and Stoesser (2014) both used LES WALE with good success (validated against experiments).

Within OpenFOAM, the *pimpleFoam* algorithm is used, this combines the *PISO* (Pressure-Implicit with Splitting of Operators) and *SIMPLE* (Semi-Implicit Method for Pressure Linked Equations) algorithms. *PimpleFoam* solves the general momentum equations and is intended for incompressible, single-phase, transient flows (Holzmann, 2019). In this simulation, the *momentumPredictor* is enabled with $nOuterCorrectors = 1$ (equivalent to PISO mode), $nCorrectors = 2$, $nNonOrthogonalCorrectors = 1$ and max $Co = 1$.

6.3.3 Rough Bed Simulations Without Free-surface (rigid lid)

A hexagonal close-pack bed of spherical tops with a diameter of 24mm was tested in the flow.

Since the majority of the turbulence generation occurs from the upper half of the spheres, in the CFD simulation only the upper parts are used. As shown in Figure 6.30, the spheres touch at a tangential point which causes issues with the mesh. To allow a small distance between each sphere ($d_2 = 0.5mm$), the spheres are further sunken into the bed. This assists in creating a good mesh without requiring infinitesimally small elements. By using Pythagoras' theorem, Equations 6.3.4 and 6.3.5 were used to calculate the distance, t by which the hemi-spheres need to be sunk into the bed.

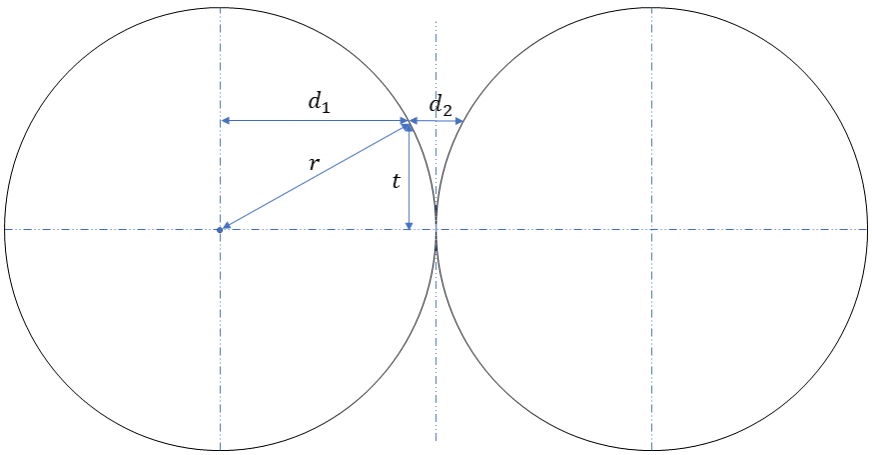

Figure 6.30: Close up view of the spheres. r is the radius of the sphere, d_2 is the space between the spheres at height t above the mid line of the spheres. d_1 is the horizontal distance between the vertical centerline and the circle at height t above the mid line of the spheres.

$$d_1 = r - \frac{d_2}{2} \tag{6.3.4}$$

$$t = \sqrt{r^2 - (d_1)^2} = 4.8734mm \tag{6.3.5}$$

Figure 6.31 provides a visual comparison of the flow depth between the CFD domain (D_{CFD}) and the laboratory flume experiments (D_{EXP}). It shows the submergence of the virtual bed below the bed of spherical roughness elements. To move between the computational domain and the experimental domain, Equation 6.3.6 can be used.

$$D_{CFD} = D_{EXP} - (r + t) \tag{6.3.6}$$

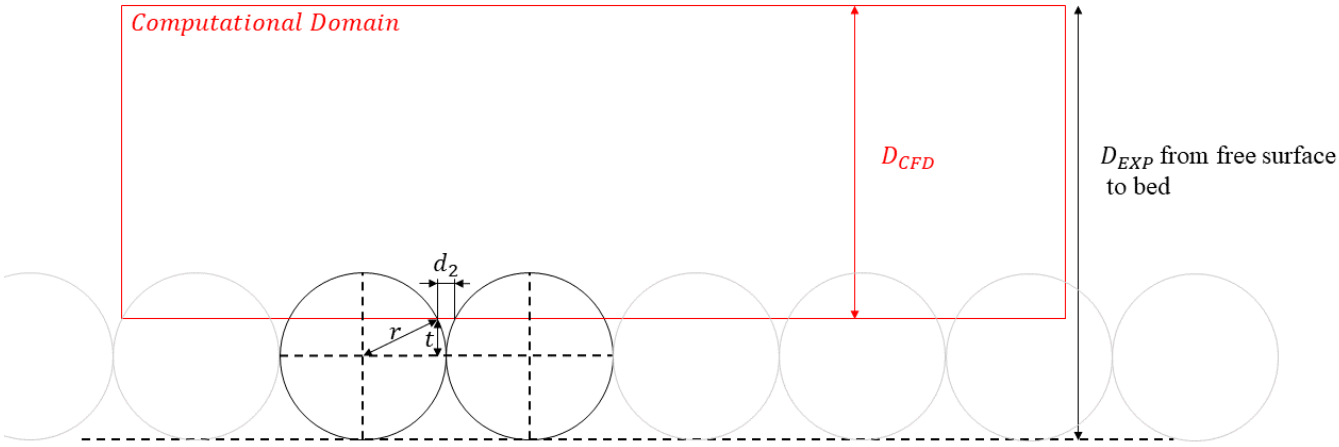

Figure 6.31: Computational domain compared to real life experiments. D_{CFD} represents the depth of the CFD domain whilst D_{EXP} represents the depth of the experimental tests.

As with flow over a single hemi-sphere, the simulation is split into two stages. Unlike the previous work, the domain size changes (see Figure 6.35). A larger domain with a coarser mesh is used for RANS whilst a smaller domain with finer mesh is used for LES. For the larger 'stage 1' domain, the computational domain was 312mm in the streamwise direction (13 sphere diameters), 166.24 mm in the transverse direction (8 sphere diameters in hexagonal close packed configuration) and a flow depth of 33mm (Figure 6.32). For 'stage 2', the computational domain was shrunk to 96mm in the streamwise direction (4 sphere diameters in hexagonal close packed configuration) and 82mm in the transverse direction (4 spheres). This can be seen in Figure 6.34. As the main turbulent structures are constrained by the depth, the transverse and streamwise periodic boundaries are deemed far enough apart. The depth of flow was not changed.

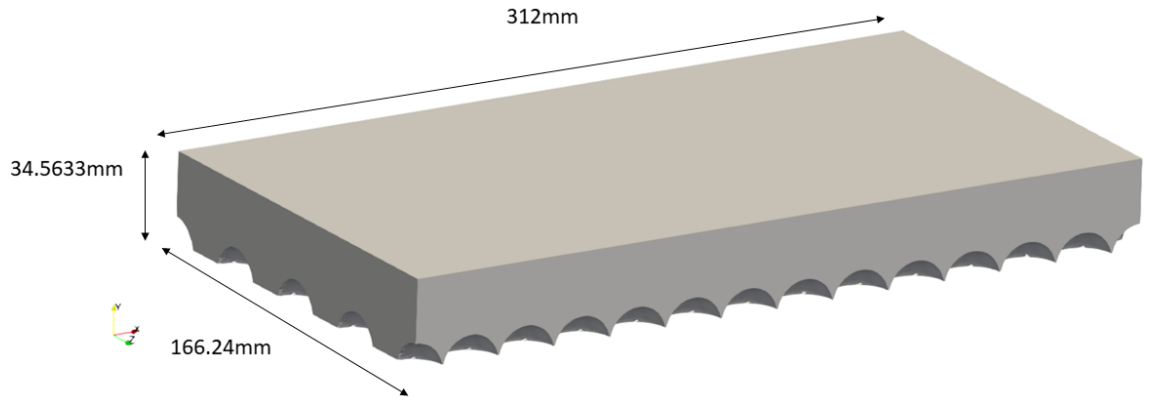

Figure 6.32: Computational domain for stage 1 of the simulation.

To create the mesh, several steps are taken. Firstly, the general computational domain without the rough bed is created using *BlockMesh*.

Secondly, the rough bed is saved as a 'Stereolithography' file (.STL) and imported into OpenFOAM. This is used by the SnappyHexMesh utility to generate a mesh of the rough bed. The edges of the spherical tops are extracted and used to refine the mesh around the physical roughness elements. Mesh points which are located inside the physical roughness elements are removed, elements are moved to conform to the bed geometry and additional layers are added around the spherical tops to improve near bed performance. The minimum mesh size was originally determined by the desired $y+$ to capture near wall effects. However, it was later discovered that the mesh needed to be much finer than this minimum requirement due to the complex bed geometry. Therefore, the mesh was dictated by the quality of the mesh around these complex bed features. Notably in the second stage of the simulation, the fine mesh is able to fully capture the curvature of the spherical caps even in the small gaps between the spherical cap elements.

Figure 6.32 show the computational domain. Figure 6.33 shows the mesh created for the stage 1 simulation. Figure 6.34 shows the refined mesh used for the second stage of the simulation.

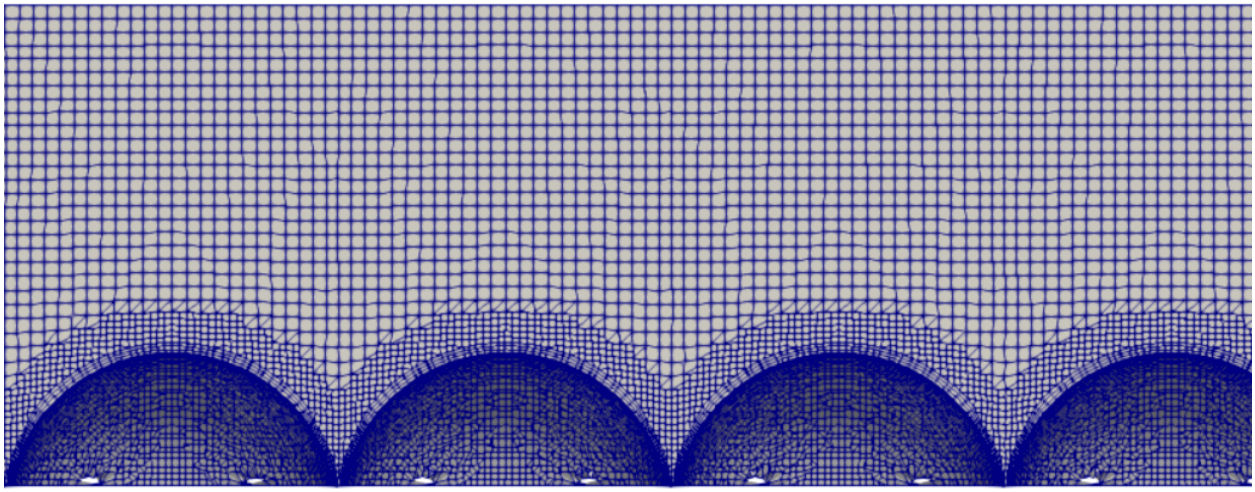

Figure 6.33: Mesh for stage 1 of the simulation, small section of 4 spheres shown.

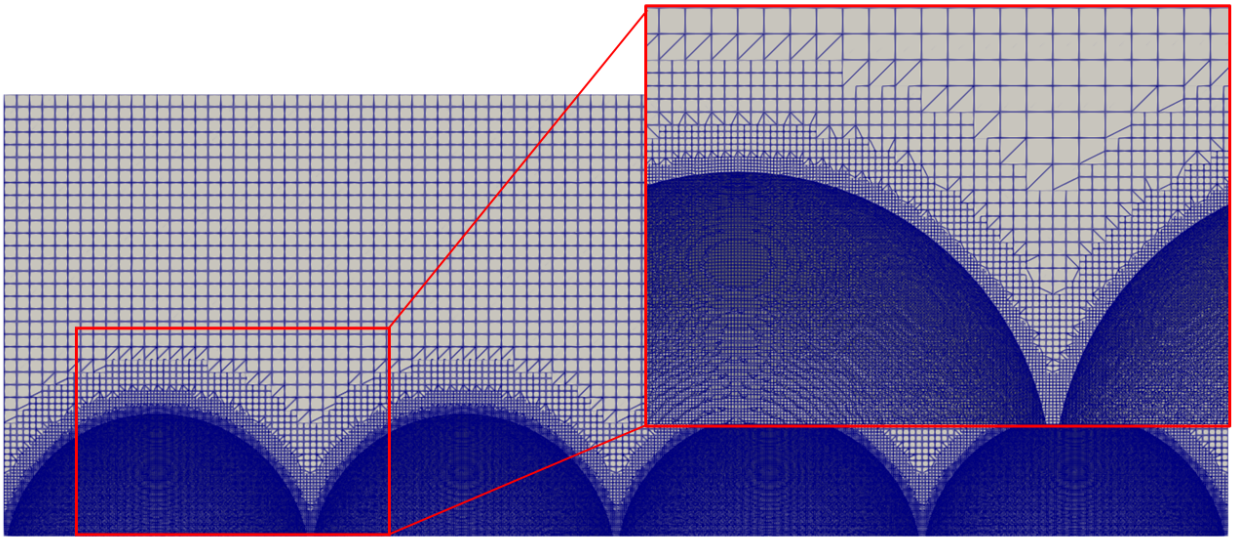

Figure 6.34: Mesh for stage 2 of the simulation (mesh has been refined as shown in the close up view).

6.3.3.1 Boundary conditions

The same boundary conditions were applied to both stages of this CFD simulation.

As in the previous smooth bed simulation cyclic/periodic boundary conditions are applied to the upstream and downstream faces.

As the experimental flow conditions were classified as shallow and the channel's width is sufficiently larger than the water depth, the sides of the open channel should have minimal effect on the center of the flow. Hence, symmetrical conditions were imposed on the side walls of the truncated CFD model. Periodic boundary conditions on these side walls were considered but not selected to minimise any artificial transverse velocity errors from being propagated and magnified. Based on the conservation of mass, there should be no time averaged net movement of fluid across the open channel in the transverse direction.

A no-slip condition was applied to the bed and the spheres. As discussed previously, the free-surface was modelled as a rigid lid with symmetry boundary condition applied.

The pressure force applied to the fluid ensures an average velocity the same as the experimental tests. According to Lien et al. (2004), the streamwise length needed to develop the flow is equivalent to around 130 flow depths. With an effective depth of 25mm, that would translate to 3.25m if using the smaller stage 2 computational domain. This would correspond to 3,250mm/96mm = 34 FTP. At a bulk flow rate of 0.08m/s, the time taken is 3.25/0.08 = 40.6 seconds. However, as the stage 1 RANS simulation is used to initialise the stage 2 LES simulation, the time to reach stabilisation is likely to be lower.

Table 6.9 shows a comparison of the mesh size for each of the different simulations. With increasing depth, the number of mesh points increases for both RANS and LES approaches. This is due to the vertical increase in computational domain size.

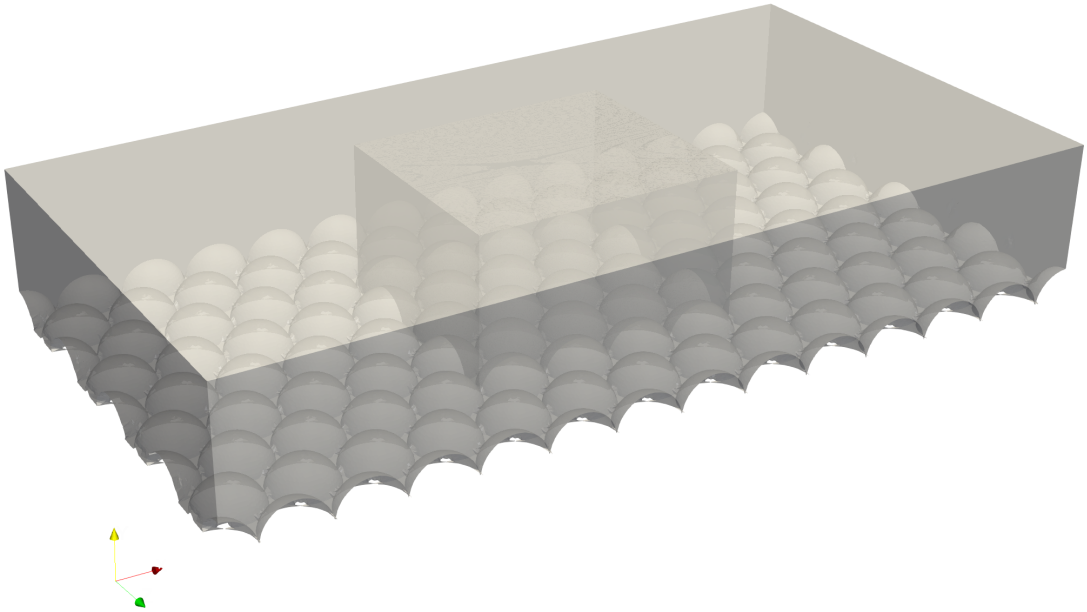

Figure 6.35: Computational Domain of rough bed simulations with RANS (large domain) and LES (small domain). Depth of flow is 49mm.

Table 6.9: Summary of the periodic simulations carried out

Simulation	Mesh Points
49mm Rough Bed RANS	1,678,845
49mm Rough Bed LES	6,516,674
69mm Rough Bed RANS	3,915,481
69mm Rough Bed LES	6,665,994
109mm Rough Bed RANS	6,004,980
109mm Rough Bed LES	7,002,482

Unlike experiments, CFD time steps can be saved and restarted to obtain the same results. These time step files can also be used in a different simulation with little loss in accuracy. The next section uses the results of the last time step to initialise a new simulation where the free-surface is modelled.

6.3.4 Rough Bed With Free-surface

Although not fully necessary to study the rigid lid, a final simulation the stabilised and converged stage 2 LES rough bed rigid lid simulation was used to attempt a new simulation with a free-surface modelled using *potentialFreeSurfaceFoam*. Since the mesh and computational domain remains the same, no illustrations are necessary.

6.4 Summary

This chapter covered the development of the CFD simulations. It has highlighted the vast challenges that exist when trying to model an entire 500mm wide, 12m long experimental flume. These relate to the large domain (10> m) relative to the small size of the free-surface fluctuation (>1 mm). In order to capture the generation and movement of transient, 3D turbulent structures and the free-surface movement, the mesh density must be 1mm per cell or finer. Without any optimisation, this would require a mesh of 500 million; an effectively impossible task to achieve within the span of several years (even for supercomputers). This was demonstrated with the initial approach attempting to model the entire experimental domain (Section 6.2.1). Immediately, efforts were made to simplify the vertical inlet shaft which existed in real life. This was possible since unlike real life, water can be pumped into the computational simulation with minimal artificial turbulence. Several strategies were then deployed to reduce the mesh size. Firstly, the width was decreased with symmetrical boundaries applied to simulate an infinitely wide shallow flow. Secondly, the length of the rough bed was reduced. Lastly, hybrid LES-RANS turbulence model was used to reduce the computational requirements. Whilst this method was able to capture the velocity profile, the turbulent kinetic energy was too low. This was likely to be due to a combination of the turbulence model and the cell size being too large, resulting in excessive artificial numerical dissipation.

Thus, a new suite of simulations using a different approach was tested (section 6.3). The key difference being the use of periodic boundary conditions. Water leaving the computational domain at the downstream end re-enters at the upstream end. This effectively creates an infinitely long flume which stabilises after fluid has travelled an equivalent of 130 water depths. A smooth bed was initially used to test the RANS functionality which would be used to develop the flow statistics to initialise a subsequent LES simulation. Flow over a single hemi-sphere was used to test the mesh with an external geometry and verify the periodic boundaries were functioning. A simulation with a full bed of roughness elements and a rigid lid was then created. A larger domain using RANS was used to initialise a smaller

domain with a higher mesh density. This was used for testing a simulation with the LES WALE turbulence modelling. Lastly, a fully rough bed with a free-surface was attempted using *potentialFreeSurfaceFoam*.

Table 6.10 summaries the periodic simulations which were carried out.

Table 6.10: Summary of the periodic simulations carried out

Name	Turbulence Model	Section number
Smooth Bed with rigid lid	RANS	6.3.1
Single hemi-sphere obstacle with rigid lid	RANS	6.3.2
	LES (same domain)	6.3.2
Rough Bed with rigid lid	RANS (large domain)	6.3.3
	LES (smaller domain)	6.3.3
Rough Bed with free-surface	LES (small domain)	6.3.4

The following chapter details the post processing and validation of the data generated from the experimental tests and the CFD simulations before moving onto more detailed analysis and identification of turbulent structures in chapter 8.

Chapter 7

Data processing and validation

This chapter outlines the post processing steps that were taken prior to deeper analysis of the flow. These include processing of the experimental flow and free-surface data in section 7.1, checking the stabilisation of the experimental tests and CFD simulations in section 7.2 before validating them with each other and published literature in section 7.3.

7.1 Processing Sensor Data

Section 7.1.1 to 8.1.1 outlines the processing of the free-surface data from the wave probe data and Kinect after calibration. It also compares the data highlight any differences. Section 7.1.3 and section 7.1.4 investigates the experimental flow data of the PIV and ADV sensing techniques.

7.1.1 Conductance Wave Probe

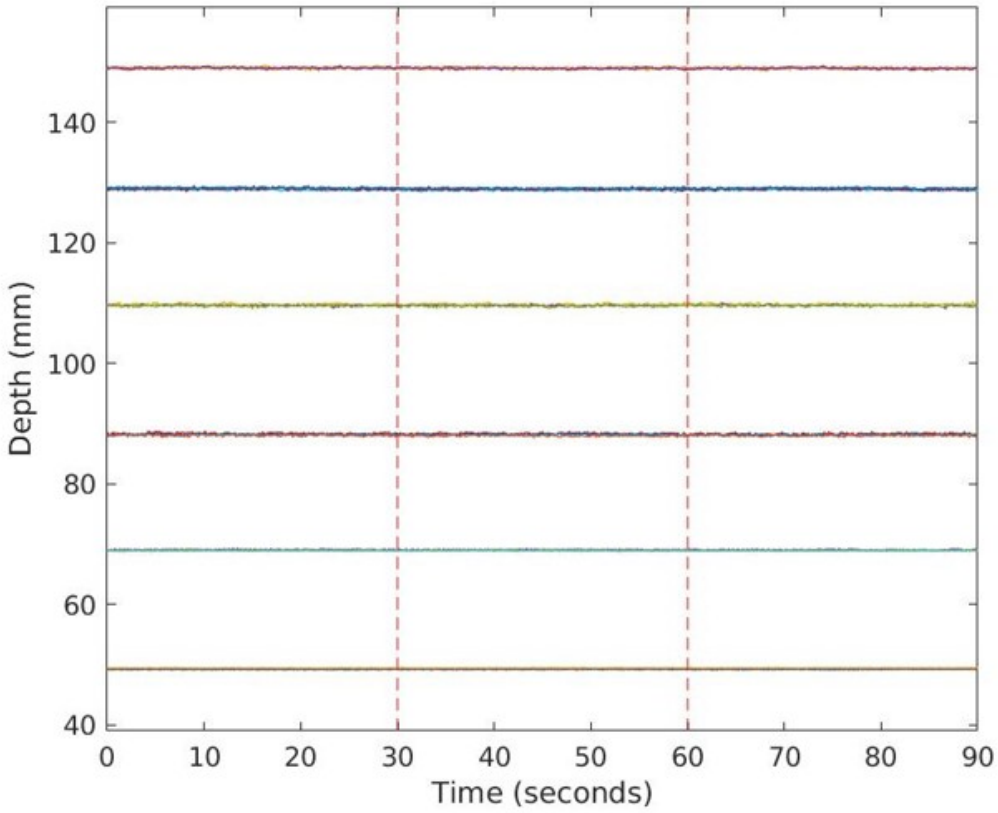

Figure 7.1: Detected water surface fluctuations by wave probe B at the six different flow depth conditions (49mm, 69mm, 89mm, 109mm, 129mm and 149mm). Refer to Table 5.1 for full set of flow parameters. Three consecutive periods of 30 seconds each were measured (separated by the red dashed lines).

Figure 7.1 show the depths detected by the conductance wave probes after calibration. The small fluctuations at each depth indicates the free-surface fluctuations detected. It can also be observed that the flow depth at the position of the conductance probe did not change significantly over the period of time when data was gathered. The duration of time recorded was 90 seconds split into three sets of 30 seconds as indicated by the dashed lines. This is in comparison to the Kinect which can only take a maximum of 30 seconds of measurements before the RAM buffer is full.

Figure 7.2a to Figure 7.2f show the same calibrated wave probe data but with one figure for each flow condition over 20 seconds. The stepping behaviour of the raw (calibrated) data is due to the analogue to digital conversion (ADC) process. To smooth out this high

frequency noise, differing thresholds of a Butterworth low pass filter were applied to identify the level of information filtered out. This is designed to remove any high frequency noise since surface fluctuations are known to be generally below 10 Hz and predominately below 5 Hz (Nichols et al., 2020). For the deeper depths, a fluctuating signal still appears to to be obvious, even after the filtering. However, for the lower depths (especially for the 49mm case), the fluctuation is not so clear. To investigate further the effect of the low pass filter, the signal was translated into the frequency domain.

Looking more closely at the frequency spectrum of the wave probe data, the effect of the different low-pass filters can be more easily identified in Figures 7.3a to 7.3f. For example, the frequency spectrum for the 49mm case shows a sudden higher amplitude at 5 Hz and 10 Hz. It is likely that the amplitudes at these two frequencies are caused by noise. In these cases, the 3 Hz and 5 Hz low pass filter was able to almost completely remove these noise features whilst the time series signals in Figure 7.3e to 7.3f suggest the overall trend can still be identified. The same is true for the other cases, the filtered time series data clearly still displays the trend of data albeit with slightly less amplitude. The frequency spectrum of a free-surface should have varying scales and a gradual decrease in the amplitude as the frequency increases. The 5 Hz low pass filter is able to remove the noise whilst maintaining the free-surface dynamics.

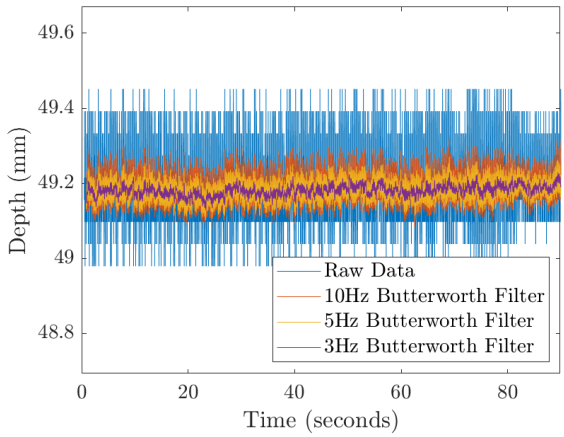

(a) 49mm depth flow condition

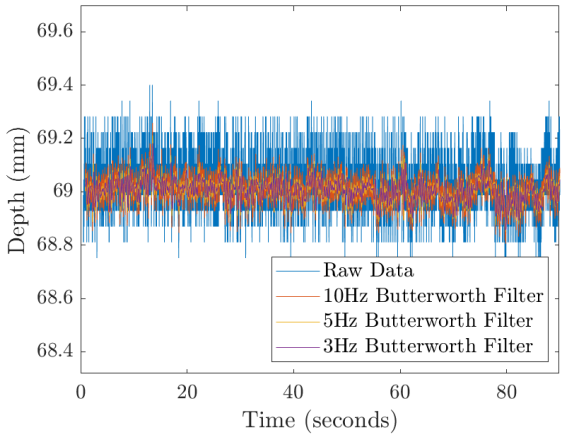

(b) 69mm depth flow condition

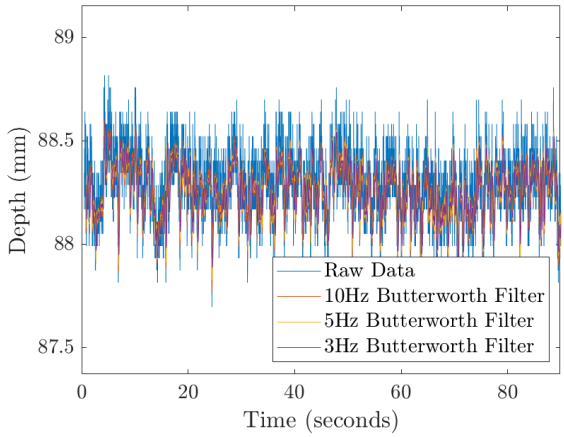

(c) 89mm depth flow condition

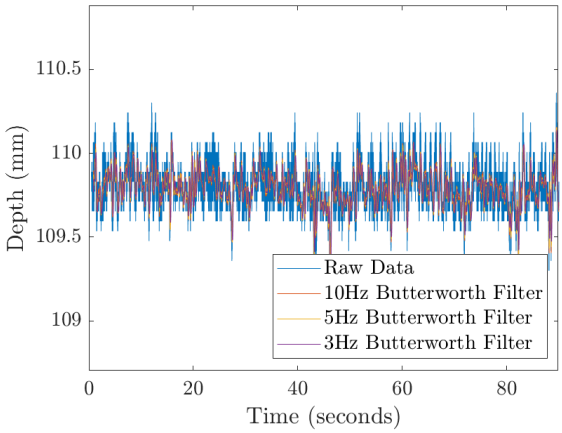

(d) 109mm depth flow condition

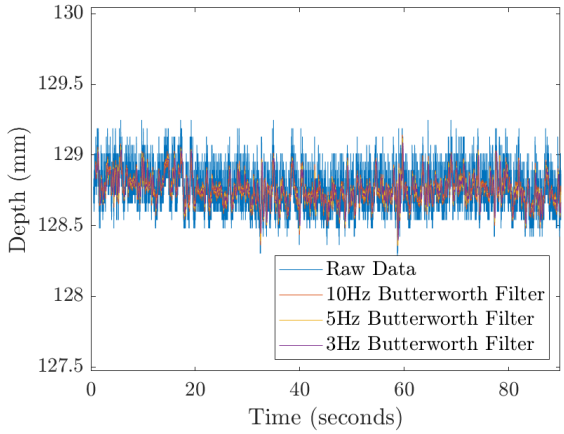

(e) 129mm depth flow condition

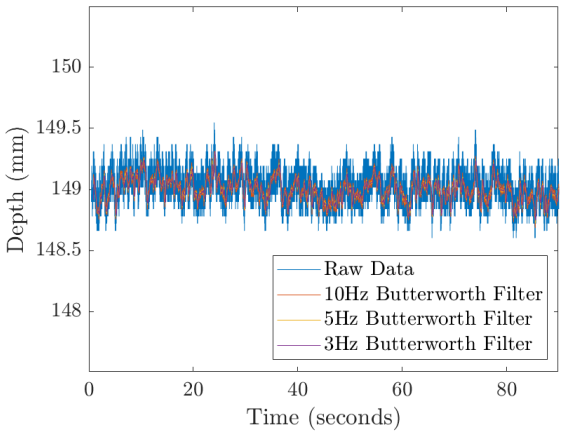

(f) 149mm depth flow condition

Figure 7.2: Detected depth signal from wave probe A, processed with varying low pass Butterworth filters (20 seconds of signal is shown). It can be seen that much of the high frequency noise is removed without affecting the general shape or amplitude of the lower frequency features.

7.1.2 Kinect infrared sensors

Figure 7.4 shows the water surface as detected by the Kinect v2 sensor after any errors were removed. A short video animation clip of the water flow can be seen here: www.youtube.com/playlist?list=PLBxWPtPkf1M_8a_3Y1E4TTlvL-ZCYGaF_. Figure 7.5 contains a QR code for the same video link.

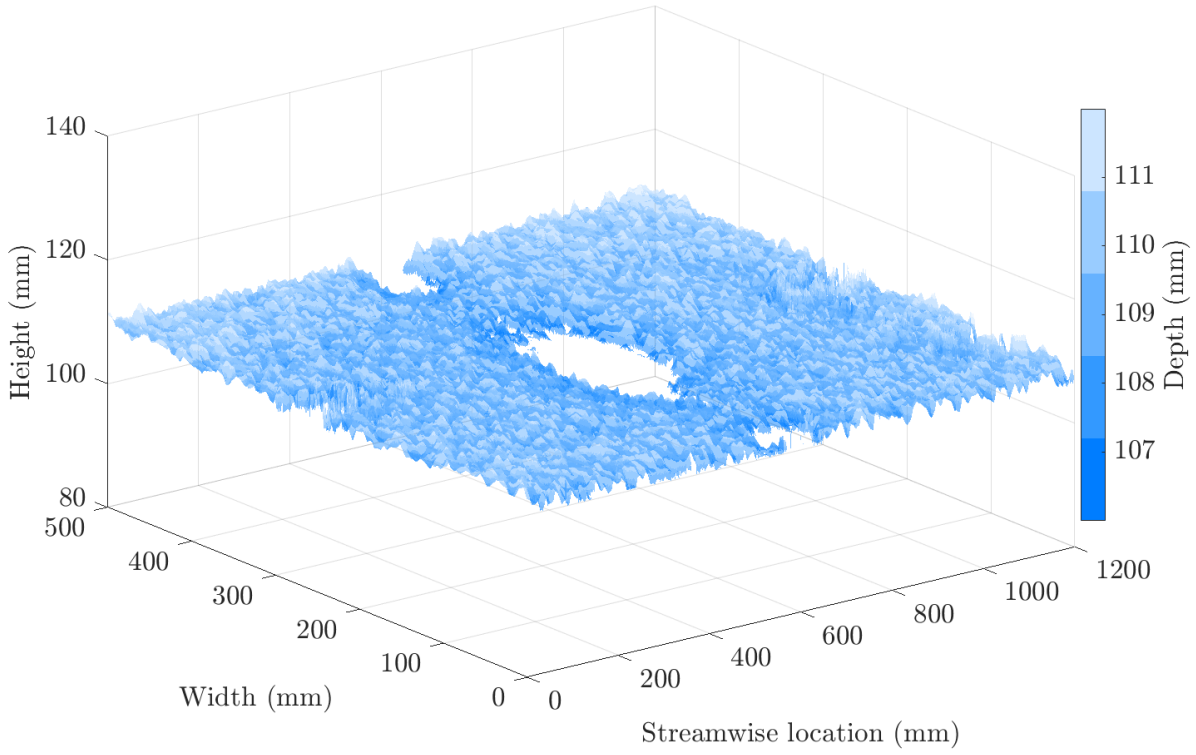

Figure 7.4: Snapshot of the water surface as detected by the Kinect at 109mm flow depth.

Figure 7.5: QR code for video of the flow surface as detected by Kinect v2 sensor.

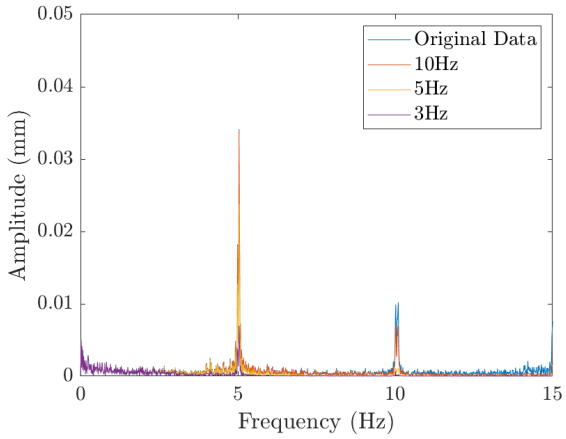

(a) 49mm flow depth condition

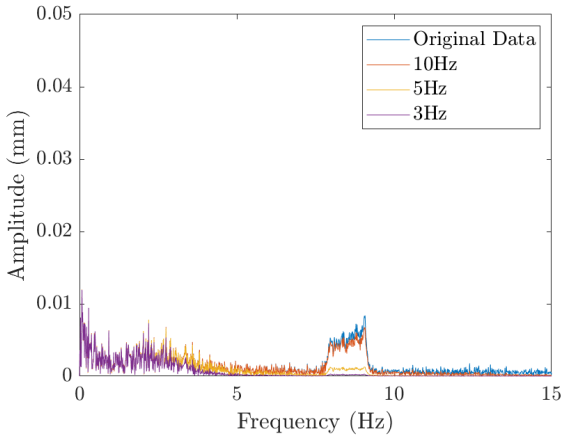

(b) 69mm flow depth condition

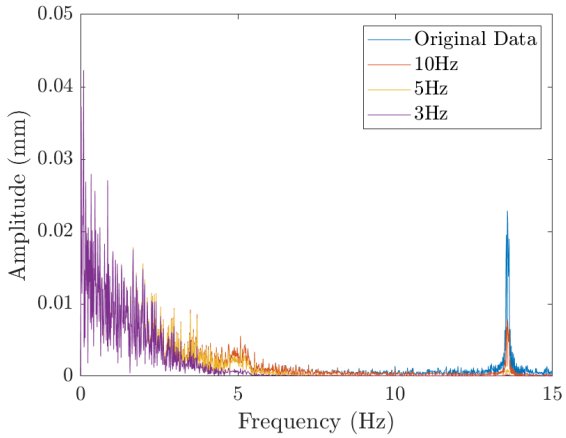

(c) 89mm flow depth condition

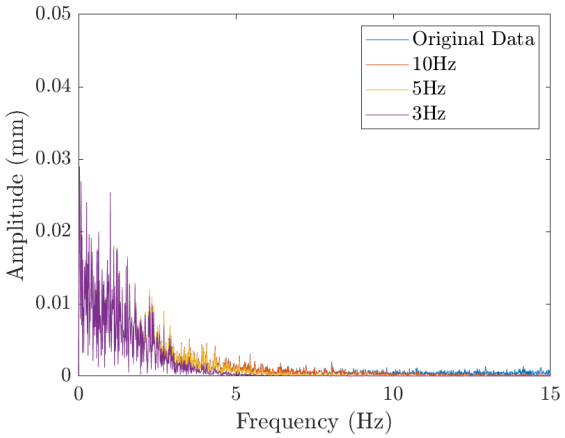

(d) 109mm flow depth condition

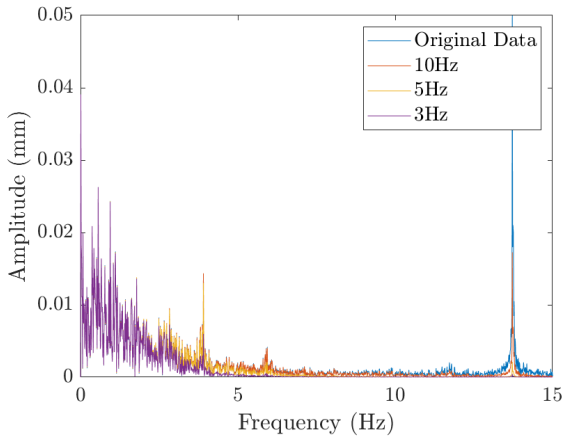

(e) 129mm flow depth condition

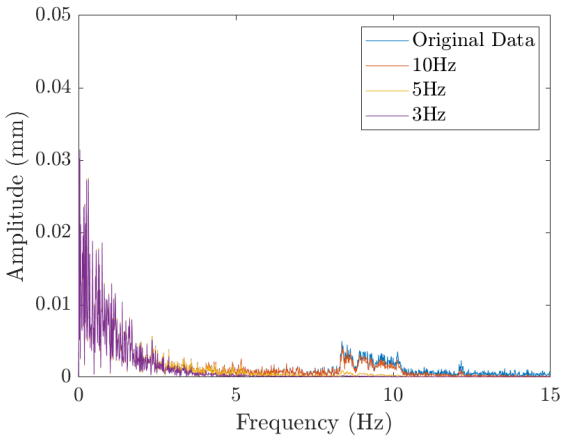

(f) 149mm flow depth condition

Figure 7.3: Examples of frequency spectrum of the wave probe signals after Butterworth filtering with different frequencies. The noise at 14 Hz can be removed as demonstrated with the 129mm flow condition.

During data analysis, it was discovered that the Kinect measured free-surface was not parallel to the bed resulting in uneven depth of flow across the free-surface in both transverse and streamwise directions. This was despite applying the exact same depth calibration from the preliminary testing with the gravity waves. On further investigation, it was found that the Kinect cameras on the mounting frame had shifted slightly. This can be seen in Figure 7.6 which show the colour image data where images from the calibration setup and the steady flow are superimposed together. The only changes observed in the image should be in the replacement of the calibration grid with the flow as well as the movement of some conductance probes (the calibration board could not be placed into position with the probes in place. However, it can be seen in Figure 7.6 that the Kinect mounting frames is in a different position with respect to the camera. This means the relative position between the camera and the mounting frame has changed. Since it is quite certain that the mounting frame attachment to the flume could not be easily shifted (it is mounted with four bolts), the only reasonable explanation is that the cameras have shifted slightly in their mounting frames and thus this misalignment has resulted in small errors recorded at the free-surface.

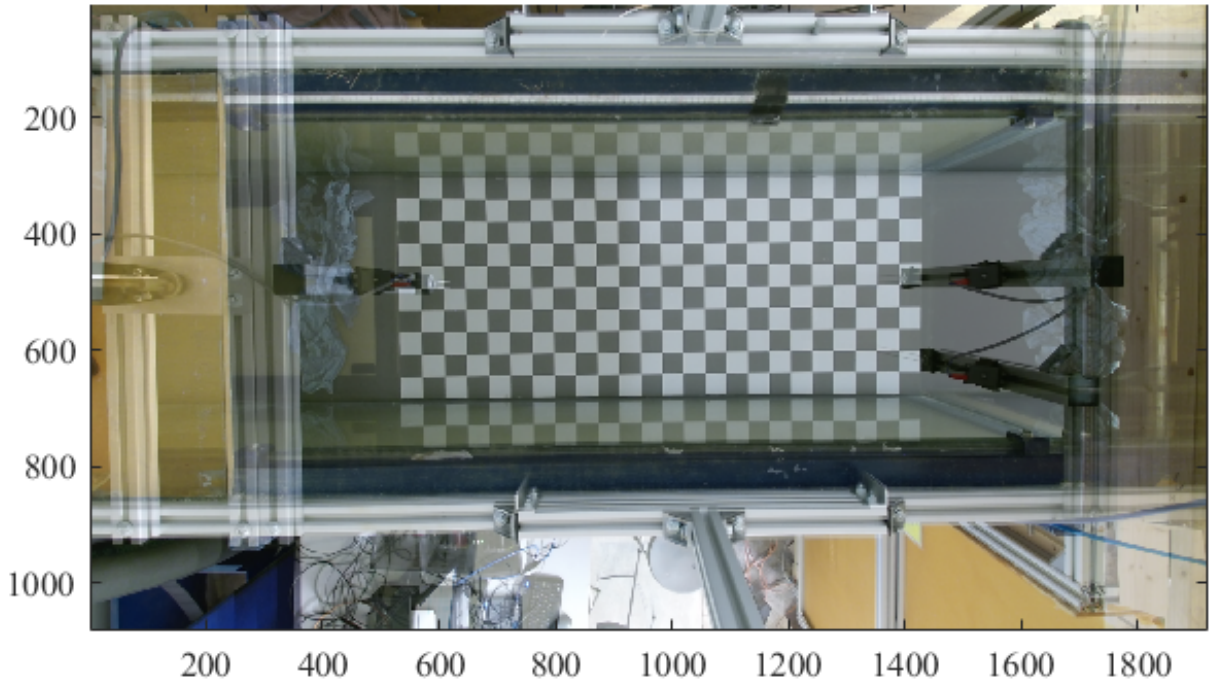

Figure 7.6: View from the Kinect 2 sensor during calibration and during experimental flow. The position of the Kinect mounting frame should be in the same relative position but it has shifted slightly as seen by the blur of the frame. Units are in pixels.

Since the angle of the Kinect shift could not be precisely determined, a self-calibration was used. The time series mean of each flow was calculated so that the average Kinect value reading over time was obtained. Each pixel (x, y) position was plotted against the six flow depths and fit a line of best fit for each (x, y) position was calculated. This line of best fit was then applied to the spatially calibrated data as the new depth calibration (customised for each pixel) so that each Kinect value reading was converted to a depth reading.

The Kinect data at this point contained a number of outliers, mainly due to flying pixels from depth discontinuities caused by the wave probe structure and the reflectivity multipath errors at the center of the camera and from the wave probes. The Kinect data was post processed to remove obvious anomalous data points, and outlier analysis investigation was performed to find the most appropriate outlier identification method. The *isoutlier* function in MATLAB was used and Figure 7.7 shows the results of this. The black is the raw data and the coloured points are identified outliers. It can be see that the Grubbs method was the most conservative but failed to identify most of the points in the spike at the edge of the flume. The median filter was the most effective and removed all the obvious outliers. However, it also removed a portion of the free surface that appeared to be reliable. In the end, data that was more than 20% higher or lower than the depth were removed and replaced with NaNs. A median filter with an 800 x 800 moving window was then introduced to constrain the power of the median filter. These large patches of obvious outliers were replaced with NaNs as the surface information at those spatial coordinates cannot be accurately recovered using nearby points. To address location fluctuations which may contain surface information, a smaller median filter was applied using the *nanmedfilt* function. A smaller window of 27 by 27 pixels was used to identify any remaining localised outliers that were not able to be detected using the previous median threshold.

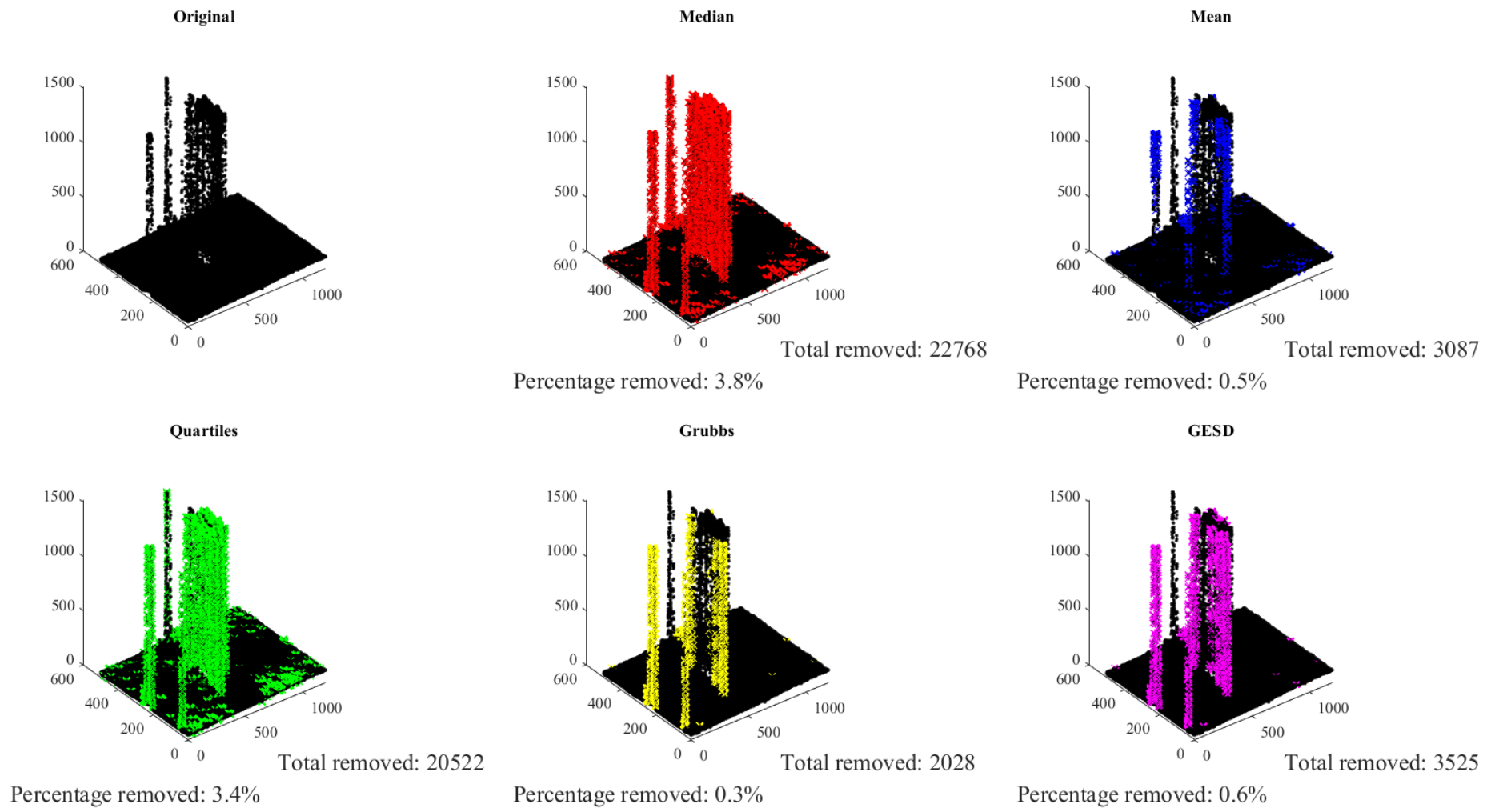

Figure 7.7: Comparison of different outlier identification methods. The Median Outlier (in red) method was able to identify the maximum outliers for removal.

Using the known position of the wave probe, windows of data were extracted from each frame of collected Kinect data, covering a small patch (15 mm x 15 mm) close to the position of the wave probe as shown in Figure 7.8. This represents the area that was occupied by the wave probe so the readings from both sensors should be correlated.

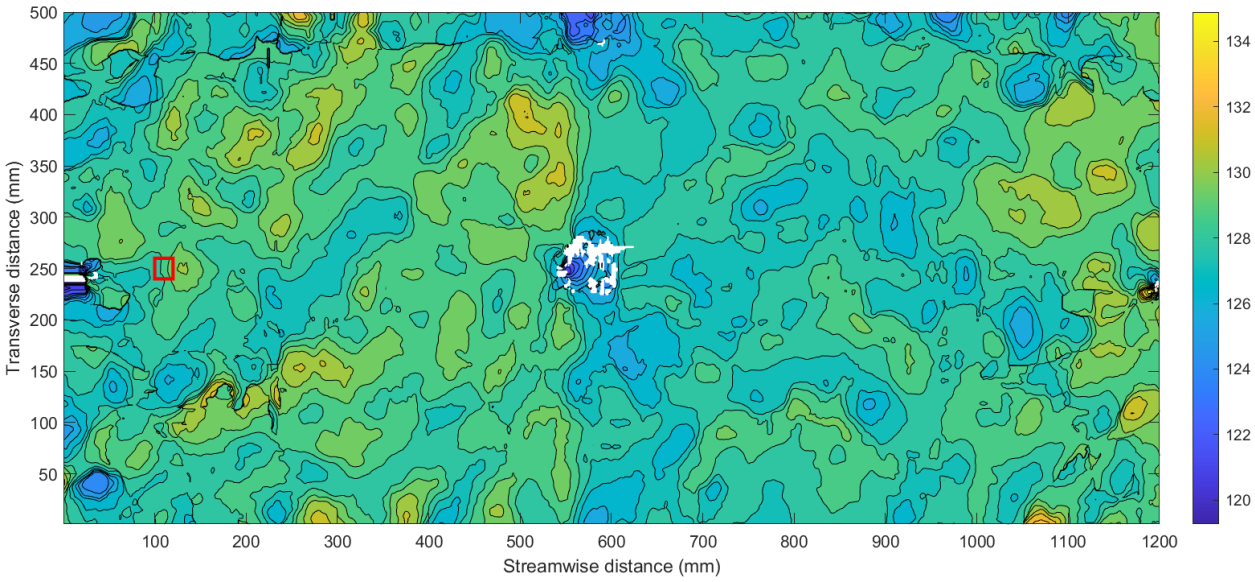

Figure 7.8: Instantaneous snapshot of the Kinect data shown as a contour map. The rectangular region of data enclosed in red was extracted for comparison with wave probe. The colourbar represents the instantaneous flow depth detected by the Kinect sensor V2.

A low pass filter was used to cut out any high frequency noise. A median filter was then applied to each frame, with a window size of 29 x 29 mm. This window size was selected based on window size analysis undertaken to investigate the relationship between window size, noise and precision of the data. The smaller the window size, the higher the precision but the more likely it would be affected by noise. Window sizes larger than 29mm by 29mm tended to reduce the peaks and alter the data beyond realism. Further details on this were published and for brevity not repeated here (Nichols et al., 2020). These windows were then spatially averaged to produce a single depth reading for each recorded time frame.

7.1.3 ADV Processing

On analysis of the ADV data, the vertical velocities did not have a mean of zero. However, it is assumed that the mean flow is in the streamwise direction (no net vertical or lateral motion due to the constraints of the bed, the side walls, and the free-surface). This small discrepancy was most likely due to a minor misalignment of the probe by a few degrees (as illustrated in Figure 7.9).

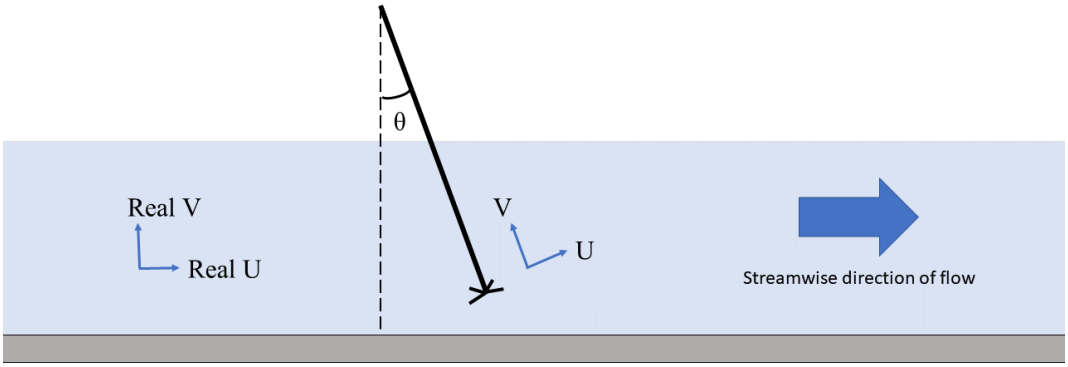

Figure 7.9: Correcting the minor misalignment of the ADV probe (exaggerated to help illustrate $\theta \approx 5\,\text{deg}$, the angle of misalignment. U and V are the streamwise and vertical velocity readings from the ADV sensor. Real 'U' and 'V' are the real streamwise and vertical velocity within the flow after correcting for the misalignment.

A correction algorithm was applied using trigonometry with components of the streamwise flow being detected in the other directions. Here, U_{raw} and V_{raw} are the raw streamwise and transverse velocities detected by the ADV probe. $U_{corrected}$ and $V_{corrected}$ can be calculated assuming a θ degrees misalignment between the vertical direction and the streamwise direction.

$$U_{corrected} = U_{raw}\cos(\theta) + V_{raw}\sin(\theta) \tag{7.1.1}$$

$$V_{corrected} = V_{raw}\cos(\theta) + U_{raw}\sin(\theta) \tag{7.1.2}$$

The misalignment angle θ was found to be 5.1 degrees using the time averaged velocity profiles of U_{raw} and V_{raw}. Based on this, the data was corrected using Equations 7.1.1 and 7.1.2.

7.1.4 PIV Processing

7.1.4.1 PIV Pre-processing of the Images

Figure 7.10 shows a raw image frame captured from one of the Imager MX PIV cameras. It can be observed that the laser light sheet varied in brightness due to refraction around the transparent spheres. To improve the PIV vector calculation, some image processing was necessary to increase the illumination of the particles. Image processing consisted of subtracting a sliding minimum with a scale length of 3 pixels. Each image was further normalised with a local average calculated from 300 pixels. Gaussian smoothing with was applied with a 3 x 3 pixel window. Sharpening was applied and each pixel was multiplied by a factor of 10 to increase the brightness for the PIV vector calculation processing. Figure 7.11 show the result of these procedures.

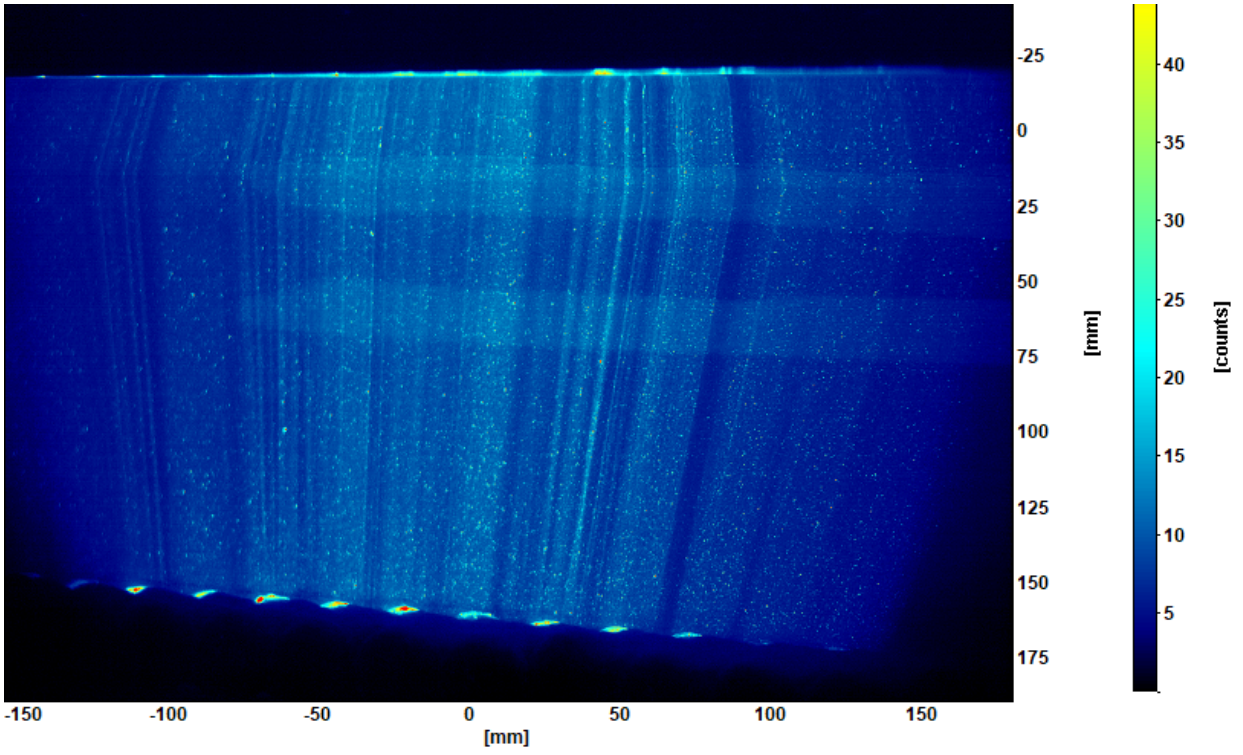

Figure 7.10: Raw camera image frame shown in Davis 8 software. The laser light sheet varied in brightness due to refraction around the transparent spheres. 149mm flow condition is shown as it is the deepest flow with the most evident effect.

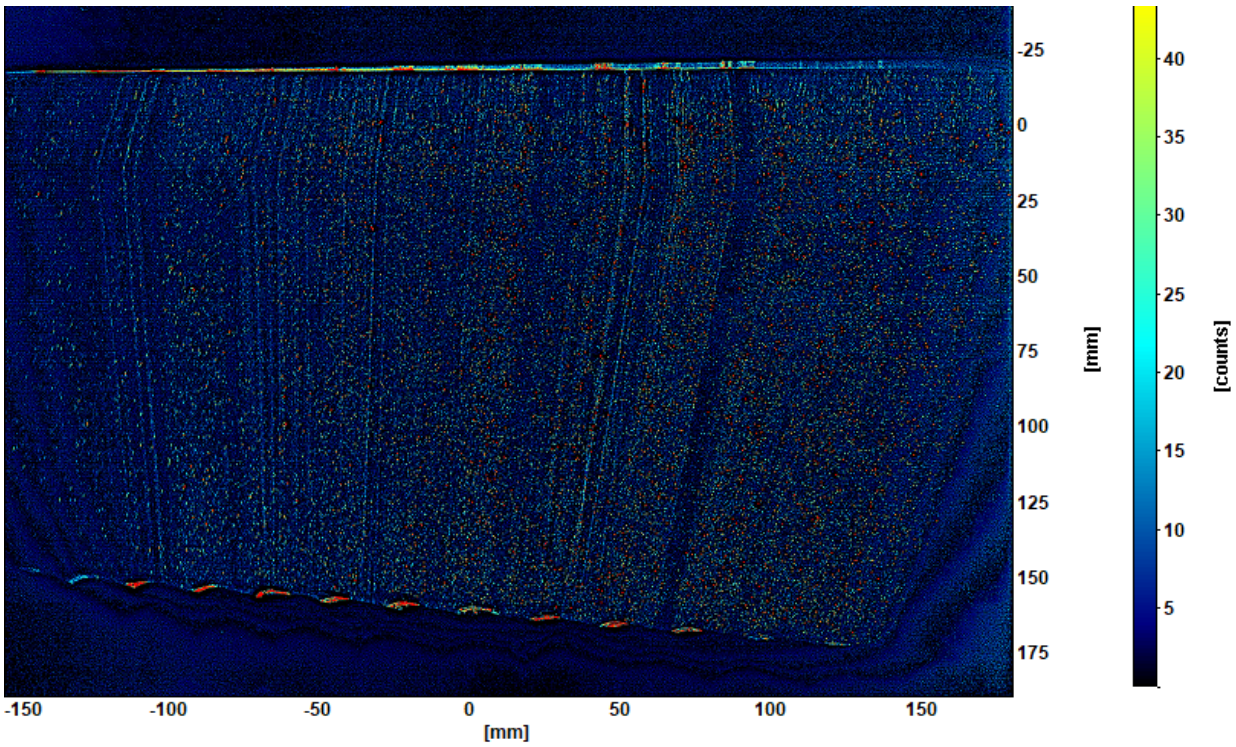

Figure 7.11: Image after pre-processing in Davis 8 software. 1) sliding minimum with a scale length of 3 pixels. 2) To increase contrast, each image was normalised with a local average calculated from 300 pixels. 3) Gaussian smoothing with was applied with a 3 x 3 pixel window. 4) Sharpening was applied and each pixel was multiplied by a factor of 10 to increase the brightness for the PIV processing. Stationary background items have been successfully removed.

An example of an image after pre-processing with the lens distortion correction applied can be found in Figure 7.12. Before the PIV vector calculation, a subtracting a sliding background with a scale length of 24 pixels was first applied to compliment the pre-processing. A geometric mask was used to isolate the flow region from the air phase and reduce the area for PIV analysis. A four pass stereo cross correlation of decreasing interrogation window sizes was used. The first pass was a 64 x 64 window size with an overlap area of 50% and a weighting function square ratio of 1:1. As the window size is big, it runs fast and helps to quickly identify potential particles for correlating in subsequent passes. The subsequent passes used a 32 x 32 window size with an overlap area of 75%. An elliptical Gaussian weighting function was used with a ratio of 4:1 search area stretched in the streamwise flow direction. The high accuracy mode was used for the 32 x 32 final passes with a 6 point B-spline reconstruction and uncertainty estimates.

The correlation function used between the pairs of PIV images for all passes was a standard —1*—2 convolution process achieved via a fast fourier transform (FFT) with zero padding (Smith and Neal, 2016). A symmetric shift position was used for both frames when deforming interrogation windows. The 3D vector is deemed as within the acceptable range if the stereo reconstruction error is less than 5 pixels.

In multipass post processing, a vector is deleted if the peak ratio Q is less than 1.3. Q is a metric for assessing the quality of a vector. It is calculated as the ratio between the highest correlation peak and the second highest peak (Lu and Sick, 2013). If the ratio is equal to one, it means there is no difference between the highest peak and the second highest, suggesting that a false peak as been detected. A median filter was used to remove and replace a vector if the difference to the average value was more than 2 times the standard deviation of its neighbours. A further vector processing applied two median filters with the same settings. Vectors with a low correlation were removed and replaced using interpolation. Finally a smoothing filter with a window of 3x3 was used.

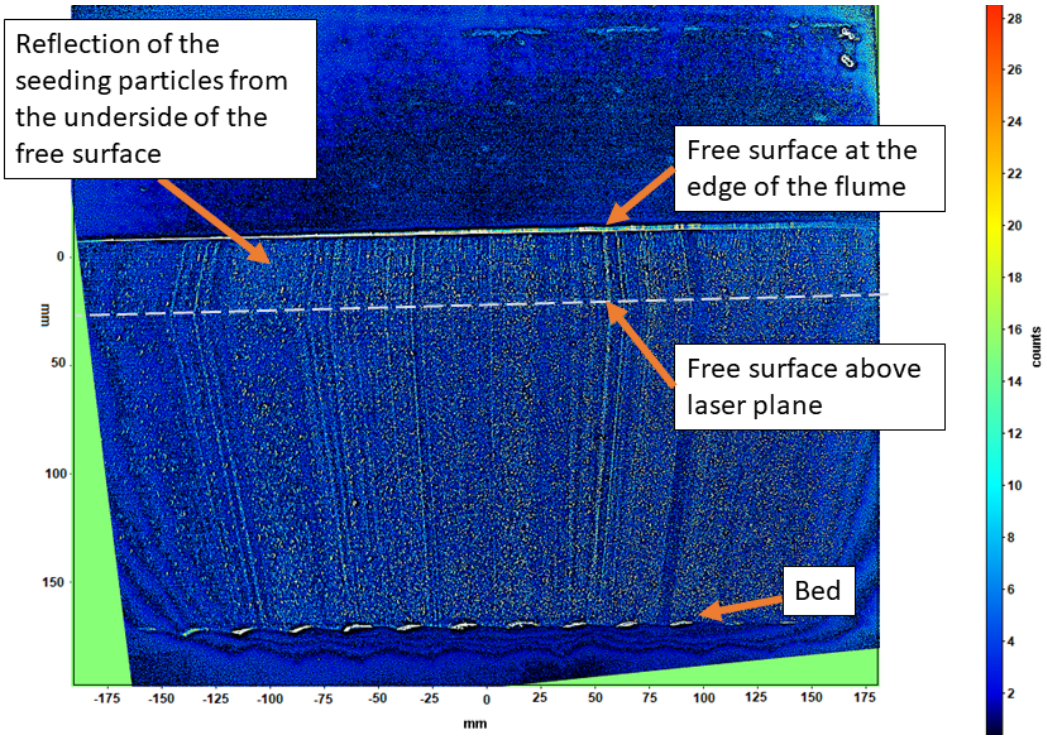

Figure 7.12: PIV image in Davis 8 software after calibration to correct for lens distortion. Each dot within the flow is the laser reflecting off a seeding particle. Striations within the flow show different light intensities as the laser plane passes through the transparent spheres in the centerline of the flow.

7.1.4.2 PIV Post-processing of the Vector Field

The PIV images were converted into a velocity vector field. Some areas had lower seeding density leading to a lower number of particles in the interrogation window, which caused slightly lower correlation values but still within acceptable limits stated by the manufacturer. Areas at the edges of the image were not well illuminated by the laser light sheet and thus had a poor correlation value. The difference in the refractive index between the water and the transparent plastic spheres meant some areas of the light sheet were brighter than others. Although this is typically a disadvantage, with the lower number of seeding particles, the concentrated regions of light actually increased the correlation value in those areas, especially at the center of the image. Thus, the velocity data from center of the image is carefully compared against the average data across the image.

Figure 7.13 shows an instantaneous velocity field of the PIV data where the colours represent the magnitude of the velocity vectors. The purple region is the stationary bed. Regions of velocity fluctuations can be observed near the bed and are likely to be signs of turbulence generation as mentioned by Fujita (2011).

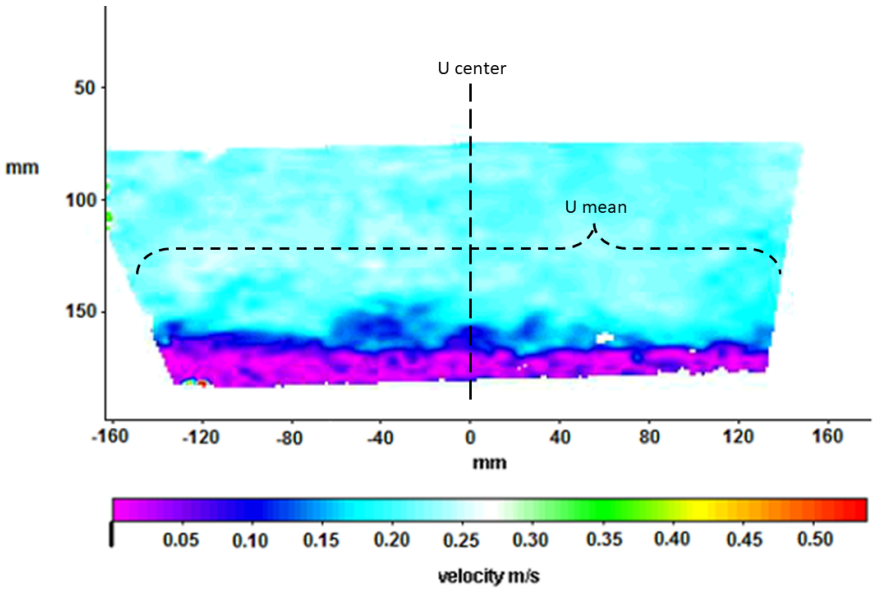

Figure 7.13: PIV velocity vector map of 109mm flow condition using 'Davis 8' PIV software. Purple = stationary bed. Regions of velocity fluctuations can be observed near the bed. Data exported from Davis 8 using a '.vc7' format for ingest and analysis with MATLAB.

Plots of the time averaged velocity profile and turbulence intensity are presented in Figure 7.14. The streamwise velocity profile detected with the data at the center of the PIV field is similar to the spatial average for the entire image. However, the two datasets diverge near the free-surface.

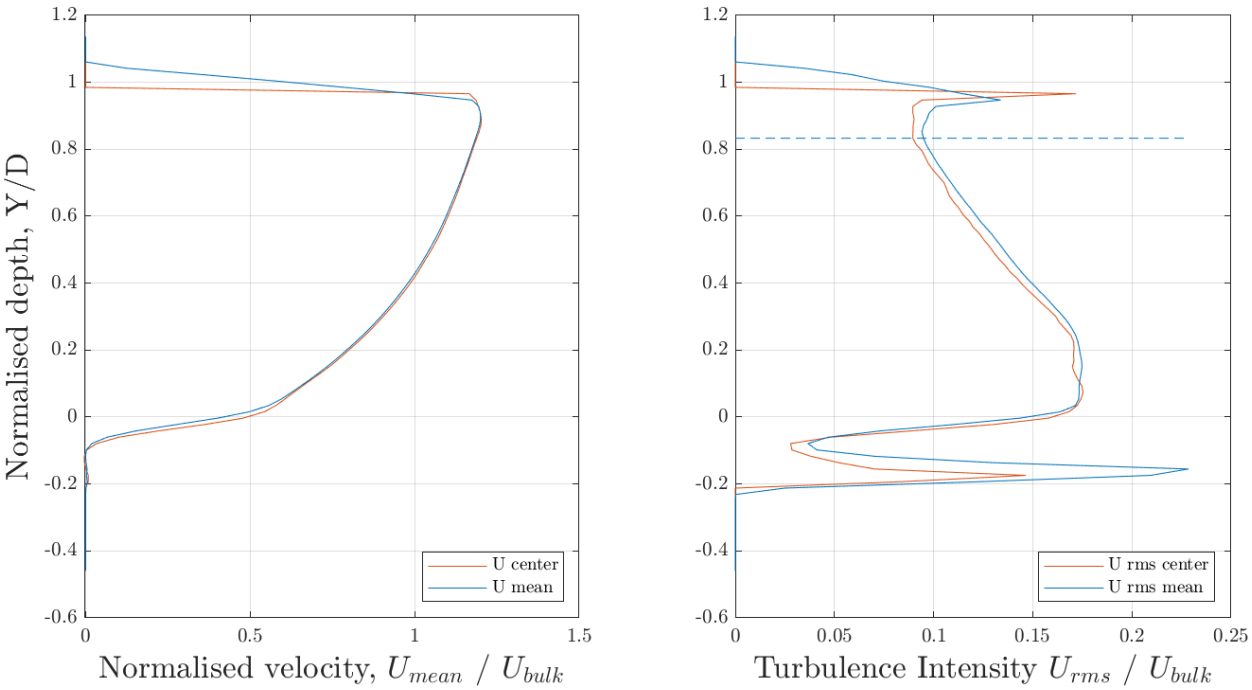

Figure 7.14: Time averaged PIV Velocity (left) and Turbulence intensity plot (right). Above the dashed line, the turbulence intensity appears to be affected by the free-surface. 'U center' is the temporal mean velocity profile generated by taking the data in the middle of the PIV image. 'U mean' is the temporal and spatial average (as illustrated in Figure 7.13).

Looking at Figure 7.13, it can be seen that the bed is inclined very slightly, this could be due to the calibration grid being slightly misaligned. This effect is visible in Figure 7.14 as the spatially averaged velocity profile does not fall straight to zero as quickly as the velocity profile extracted at the center of the PIV image. To correct for this, the cartestian coordinate system was rotated clockwise by 1.15 degrees. The vector field were interpolated from the old coordinate system to the new coordinate positions (using the *interp2* MATLAB function). The directions of the vectors were then rotated by the same angle (using the *QuiverRotate* MATLAB function (Danz, 2020)). To check that enough data had been generated for representative statistics, Figures 7.15 and 7.16 show the mean and standard deviation throughout the simulation progress. This is normalised against the final calculated value (using the full time series). After 120 seconds, the statistics have converged to ±10%.

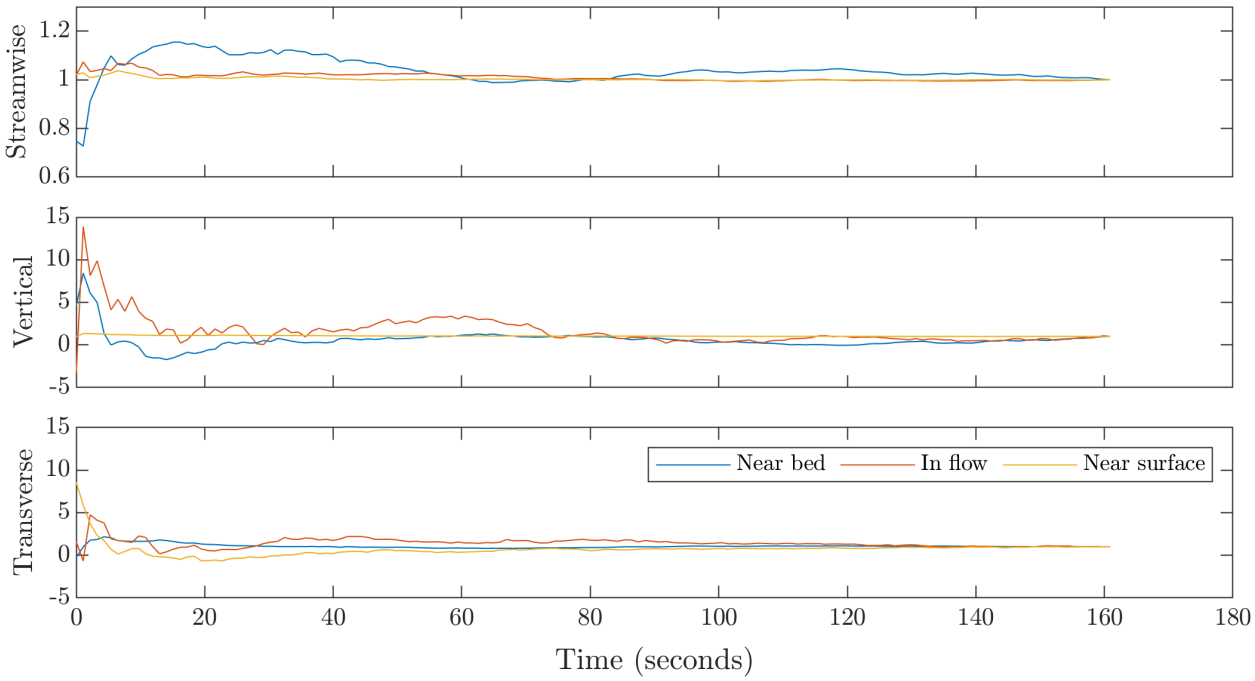

Figure 7.15: Convergence of mean time average statistics. The values are normalised against the final calculated mean. Data taken from three locations in the flow. All calculations converge to within ± 10%.

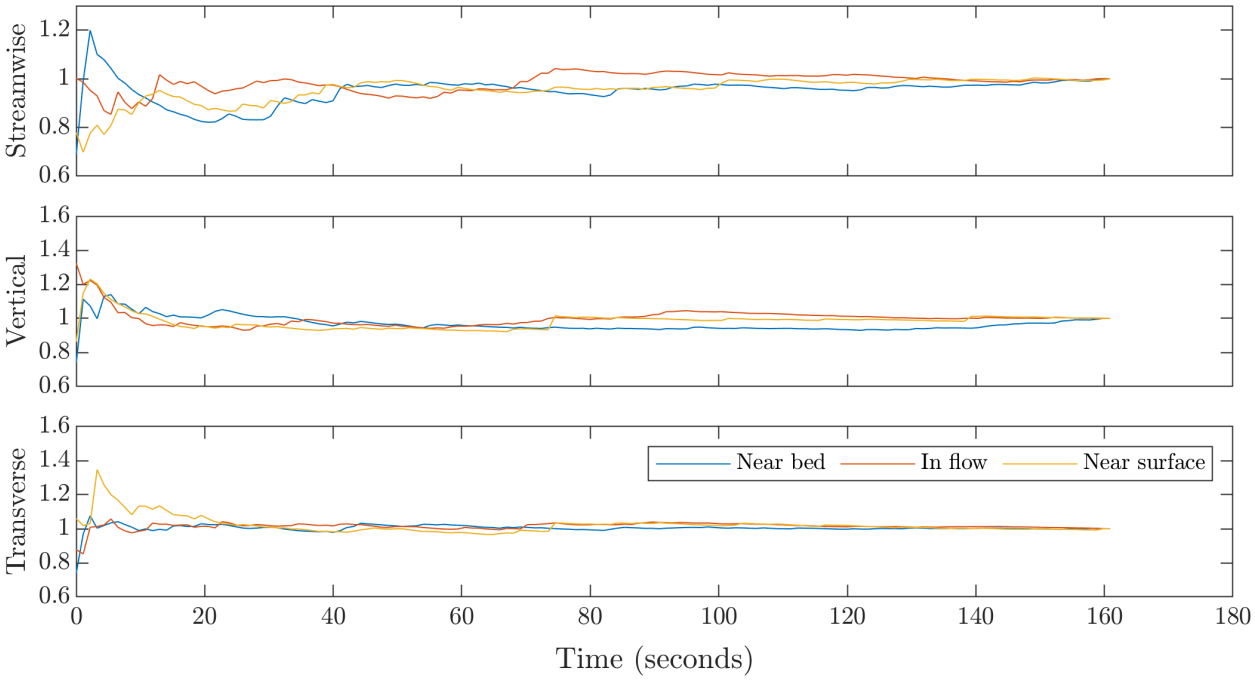

Figure 7.16: Convergence of standard deviation statistics. Normalised against the final calculated standard deviation. Data taken from three locations in the flow. All calculations converge to within ± 10%.

7.2 Flow Stabilisation

7.2.1 Experimental Flow Stabilisation

Figure 7.17 shows the velocity profiles detected by the ADV in the streamwise direction taken at 7, 8 and 9m downstream of the flume entry point. It can be seen that the profiles are all very similar. In particular, the readings at 8 and 9m are within 0.003 m/s (1.5%) which confirms the flow has stabilised before it enters the PIV measurement region at the 9.2m marker.

Figure 7.18 shows the turbulence intensity profiles. As before, all three are very similar. In particular, the profiles taken at 8m and 9m downstream are almost identical with a constant offset through the flow. This suggests a minor misalignment in the yaw direction during the setup but overall, the results demonstrate that the flow has stabilised.

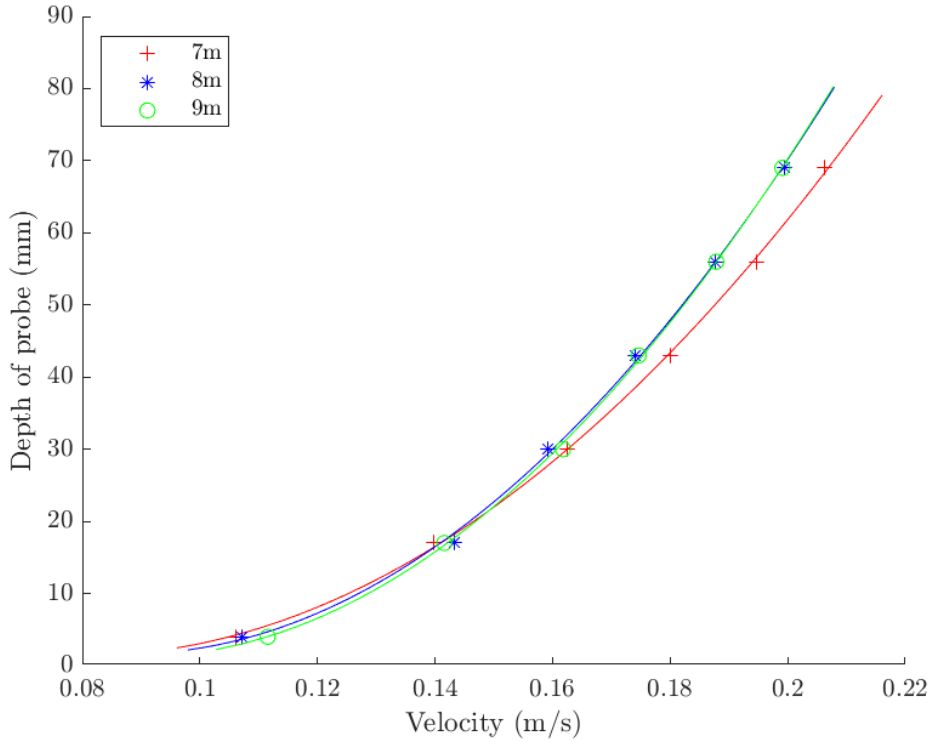

Figure 7.17: Velocity profiles detected by the ADV taken at different streamwise locations to measure the stabilisation of the flow in the streamwise direction at 89mm flow depth. The similarity between the 8m and 9m profiles confirms that the flow has stabilised by the 8m reference marker.

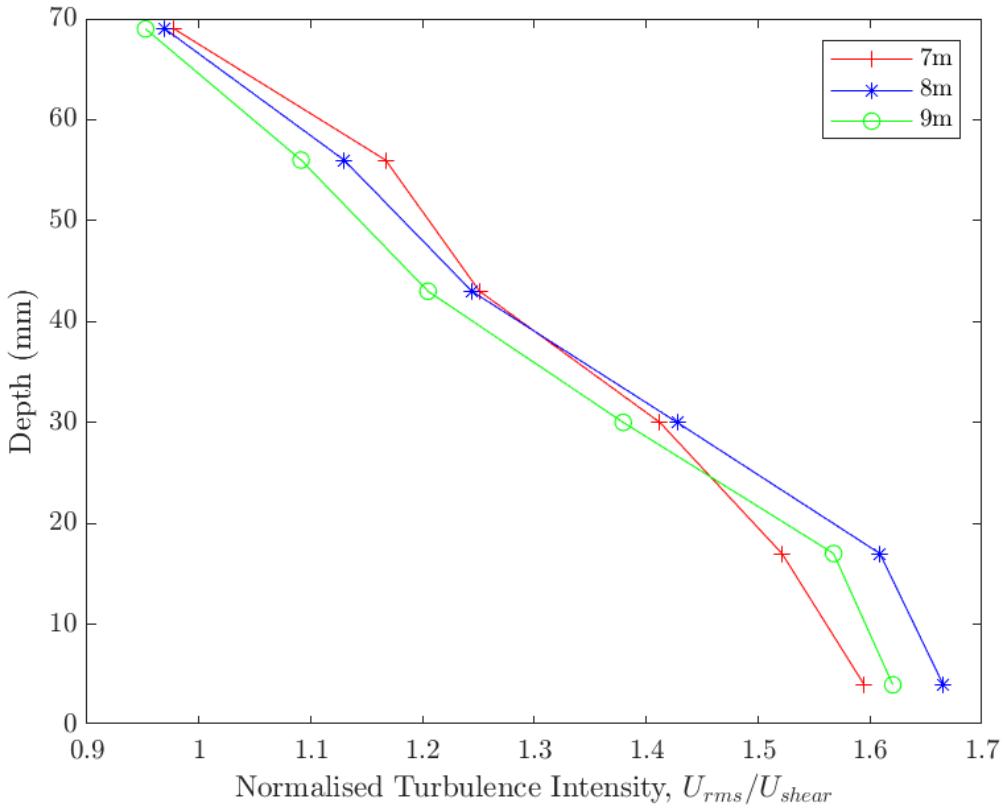

Figure 7.18: Turbulence Intensity profiles taken at different streamwise locations to measure the stabilisation of the flow in the streamwise direction at 89mm flow depth. All three profiles are very similar suggesting that the turbulence intensity has stabilised by the 9m marker.

7.2.2 CFD Flow Stabilisation

The stabilisation of residuals was checked to ensure a good accuracy had been reached numerically. Residuals are computational errors which arise from the discretisation of the fluid continuum into a grid. If these errors are not minimised, then over time, the simulation will diverge from reality with the model unable to simulate realistic flow behaviour. A representative residual should give a good understanding of the residuals across the simulation domain and provide information on the errors within each cell of the simulation.

The L_1 norm (also known as the Taxicab or Manhattan norm) gives equal weighting to all residual components and is done by taking the summation of all the magnitudes in each residual vector. The L_2 norm or euclidean norm takes the magnitude of all the residual vectors (i.e. $\sqrt{\sum residuals^2}$). This provides greater weighting to larger residual components. The L_∞ norm takes the maximum magnitude of all the residual vectors in the mesh and ignores all other residual vectors.

Because the L_1 and L_2 norms depend on the length of the residual vectors (the number of cells in the mesh), a normalisation is applied. For L_1, the length of the vector is normalised by dividing the value with the number of vectors (this becomes the mean average residual magnitude). For L_2, the term used for normalisation is the square root of the number of vectors which essentially results in the root mean square of the vectors.

Compared to L_1, the L_2 and L_∞ give more weighting to larger residuals to highlight any large errors that appear within the mesh. However, all three approaches are valid. OpenFOAM uses the L_1 norm.

Scaling of the residuals allows a better comparison of the local momentum/pressure imbalance relative to the magnitudes of the variables in the cell. For example, an error of 0.01N in a cell with 100 N is significantly less vital compared to an error of 0.01N in a cell with 0.1N (OpenFOAM, 2022). This scaling factor used is calculated automatically by OpenFOAM and not explicitly stated.

A utility called *pyFoam* was used to read the OpenFOAM output script and parse residual

outputs. This has several benefits over a manual extraction for every timestep saved to disk. Firstly, not every timestep is saved to disk, whereas the *pyFoam* utility scans the log files which output at every simulation time step so the temporal resolution of the data is much higher (e.g. 0.01 seconds instead of 1 second). Secondly, as the simulation reaches its maximum runtime on the supercomputer, the job must be re-queued to continue running. *pyFoam* is able to scan multiple log files and show which timesteps belong to which job run and this enables the reader to check if there are any effects due to the restarting of the simulation.

Figure 7.20 shows the residuals in the continuity calculation. This ensures that the mass flow is conserved and not diverging (i.e. water steadily filling the domain or draining out). It can be seen that the mass flow remains consistent through the simulation (global residual). The cumulative residuals are reset with every restart of the simulation (i.e. when the job is re-queued after the 24 hour runtime limit is reached).

Monitoring of the local and global pressure and velocity errors was also conducted and is shown in Figure 7.21).

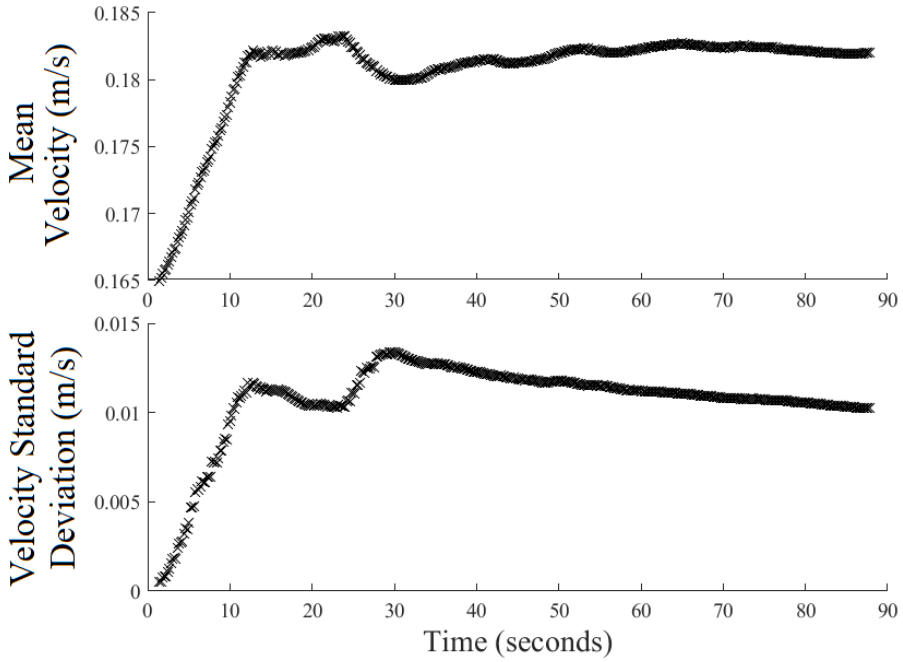

Figure 7.19: Statistical convergence of the flow physics (mean and standard deviation of streamwise velocity fluctuation for 109mm flow depth LES simulation).

The change in the mean and standard deviation of the velocity in the flow were then assessed to ensure the physical flow had statistically converged for data extraction (see Figure 7.19).

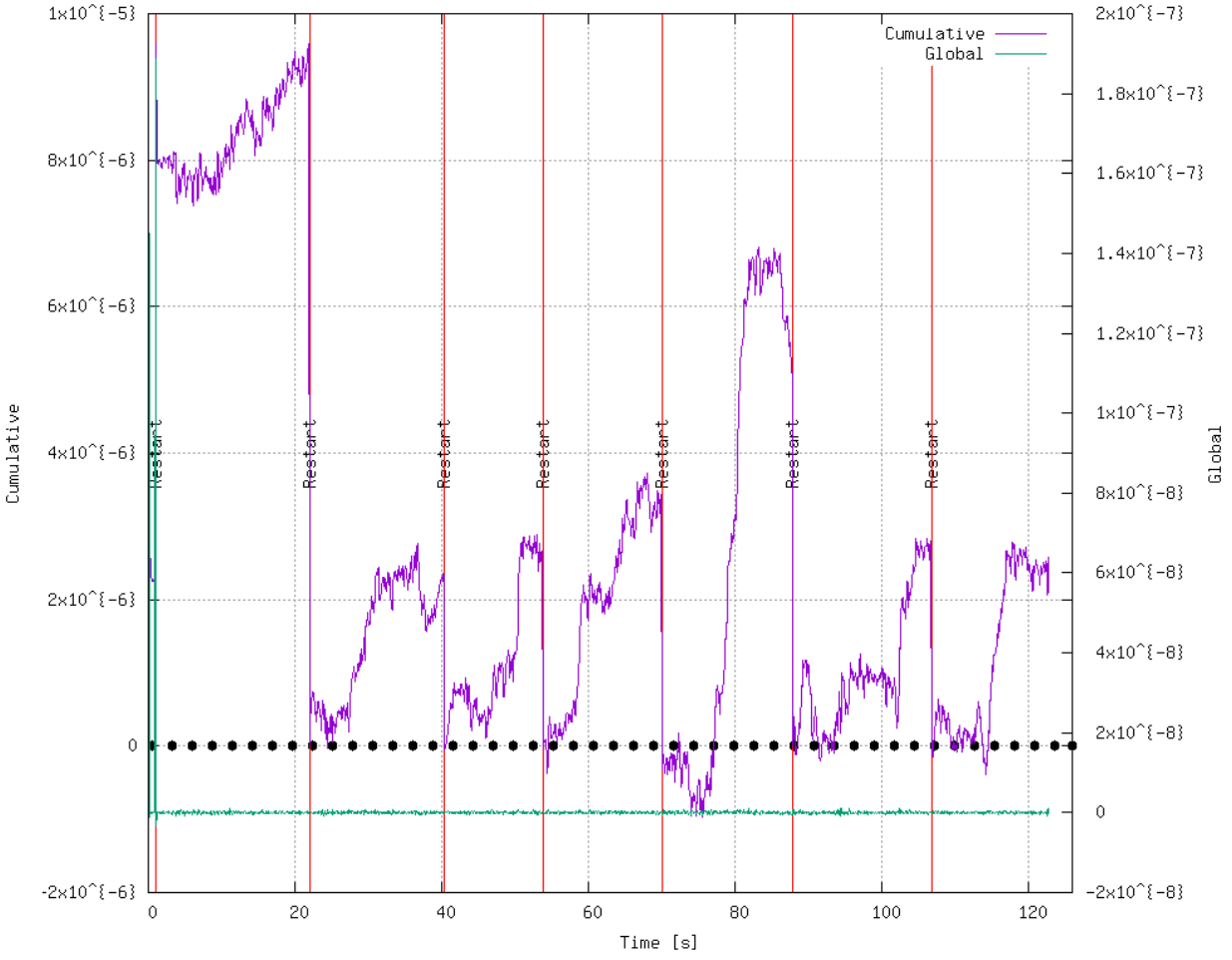

Figure 7.20: Stabilisation of the mass continuity errors in LES simulation of 69mm flow depth with a rigid lid. Generated with the *pyFoam* utility. As the supercomputer has a 24 hour runtime limit, a new simulation request must be submitted every day, resetting the cumulative residual. The global residual shows that the overall error remains low.

The CFD data was extracted every 0.01 seconds using the *singleGraph* function in OpenFOAM. This extracts a line of data within the flow field for further analysis.

Figure 7.22 shows the power spectrum analysis of the streamwise velocity fluctuation taken at $X = 0$mm, $Y = 32$mm, $Z = 0$mm. The non-parametric, periodogram method by Welch (1967) was used. Kolmogorov's -5/3 power law is also shown to indicate the turbulent dissipation across the energy spectrum (Kolmogorov, 1941). Data was extracted every 0.01 seconds (100 Hz). As can be seen from the power spectrum, most of the energy is concentrated in the low frequency region of the spectrum which suggests that the sampling interval

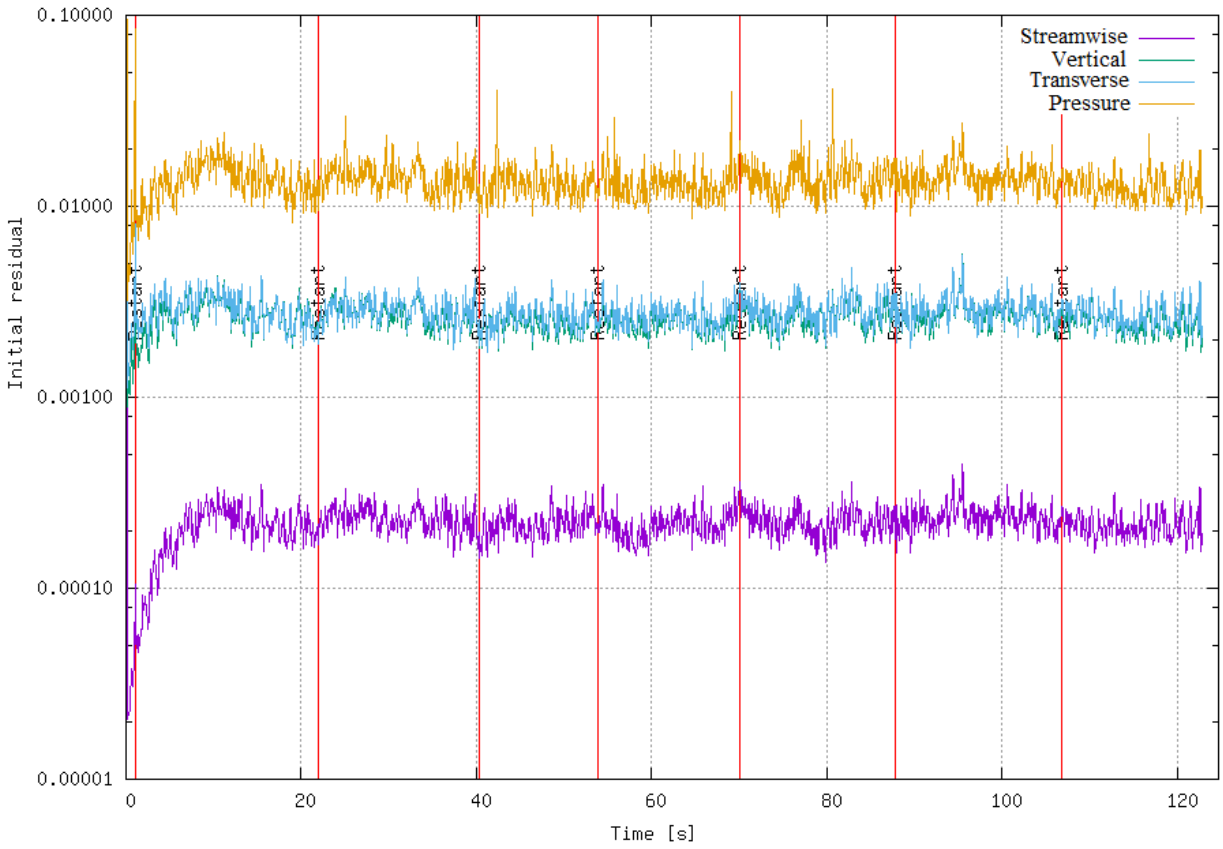

Figure 7.21: Stabilisation of local and global velocity errors in LES of 69mm depth flow with a rigid lid. Figure generated using the *pyFoam* utility.

is sufficient. The results show a reasonable capture of the turbulent energy cascade within the CFD simulation. This suggests that the turbulence processes are simulated correctly. The following section will compare the data to validate the experimental and computational results.

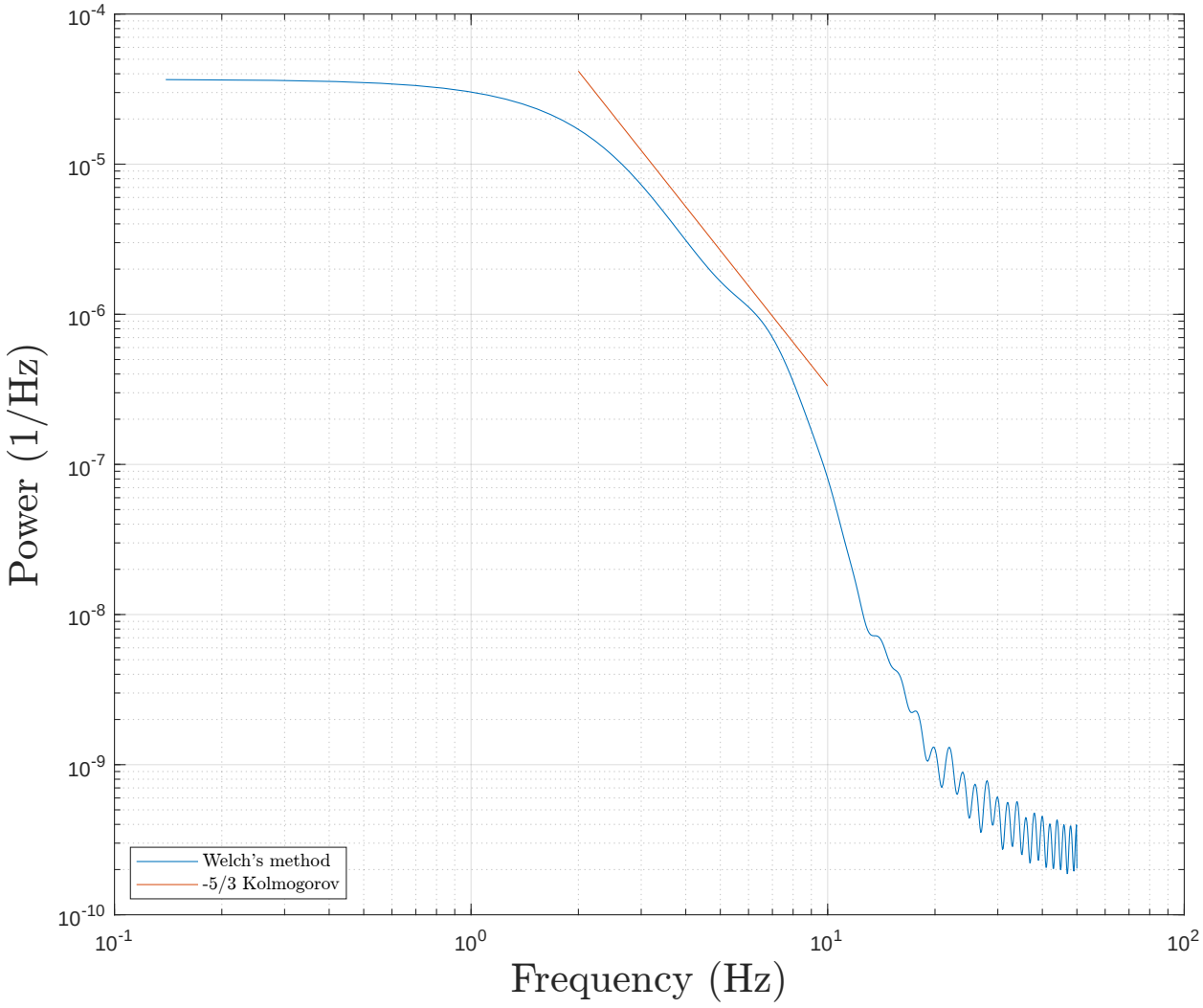

Figure 7.22: Power Spectrum Analysis of streamwise velocity fluctuation (Cho et al., 2022). Taken at spanwise centerline, 2.5mm below the free-surface in the middle of the domain (X = 0mm, Y = 32mm, Z = 0mm).

7.3 Validation

7.3.1 CFD Validation

This section will look at the the results of the CFD simulation and make a comparison against the experimental tests.

The experimental tests of Nichols (2015) contain a flow condition with a bed composed of two layers of identical 24mm diameter spheres and a flow depth of 70mm. This is comparable to the 69mm flow depth condition presented in the experimental methodology. Thus, this will be useful when validating the PIV and ADV data.

ADV and PIV methods have different types of errors. For example, the PIV method is affected by the image quality, which influences the accuracy of the vector field calculation. The ADV method is affected by vibration of the flume apparatus due to the operation of the water pump. Error bars have been added to the PIV to demonstrate the expected uncertainty of the velocity.

7.3.1.1 Initial validation of RANS model using a smooth bed with no free-surface

A smooth bed is initially used to test the RANS model as this avoids many problems arising from mesh around complex geometries. In particular, it enables testing of wall functions. Please refer to section 6.3.1 for more information regarding the setup.

Figure 7.23 shows a snapshot of the smooth bed 49mm flow depth simulation in the vertical-streamwise plane. It can be seen that there is a clear velocity gradient towards the smooth bed suggesting a functioning no-slip bed and a rigid lid free-surface with slip condition. There is also an absence of any transient turbulent structures which is consistent with the typical RANS results since transient effects cannot be simulated.

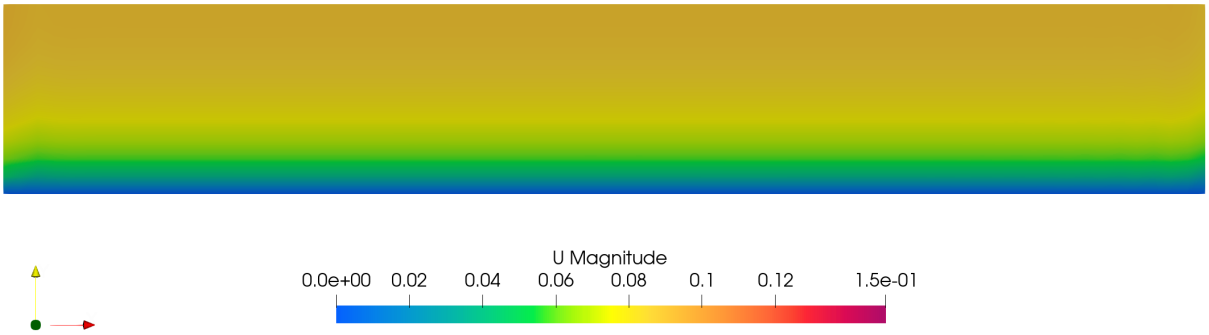

Figure 7.23: Instantaneous velocity flow field of smooth bed (RANS) simulation at 49mm flow depth. The colourbar represents the magnitude of the streamwise velocity (m/s). It can be seen that the velocity decreases with distance to the no-slip bed and that the profile does not appear to change in the streamwise direction. This suggests the periodic boundary conditions and no slip bed is functioning correctly.

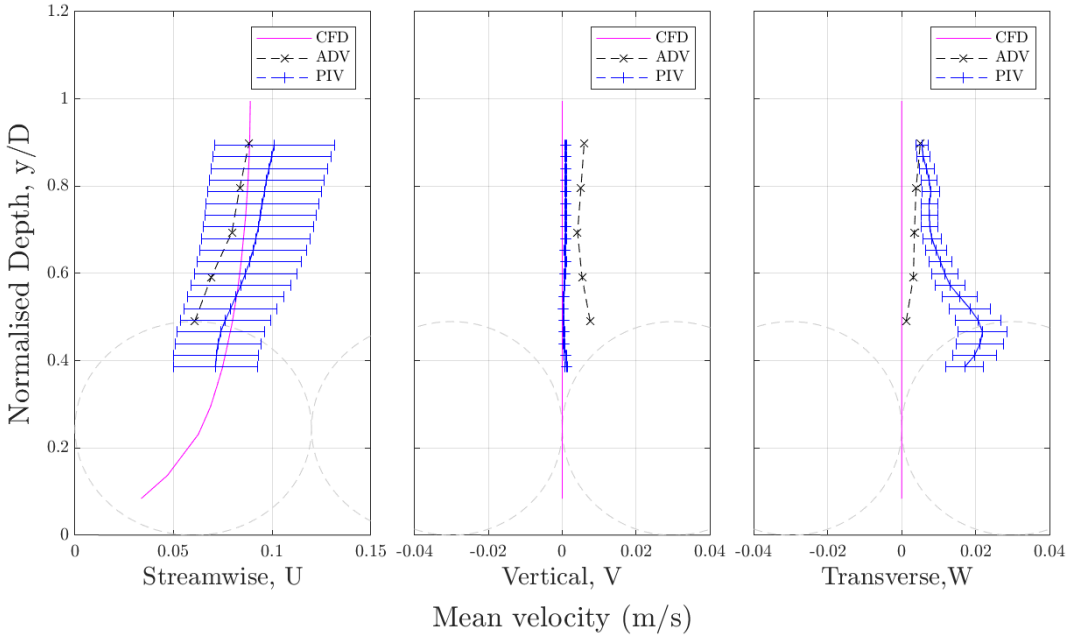

Figure 7.24: A comparison of the mean velocity profile between the experimental PIV/ADV with the CFD at the 49mm depth flow condition. The vertical depth coordinate has been normalised by the flow depth, D.

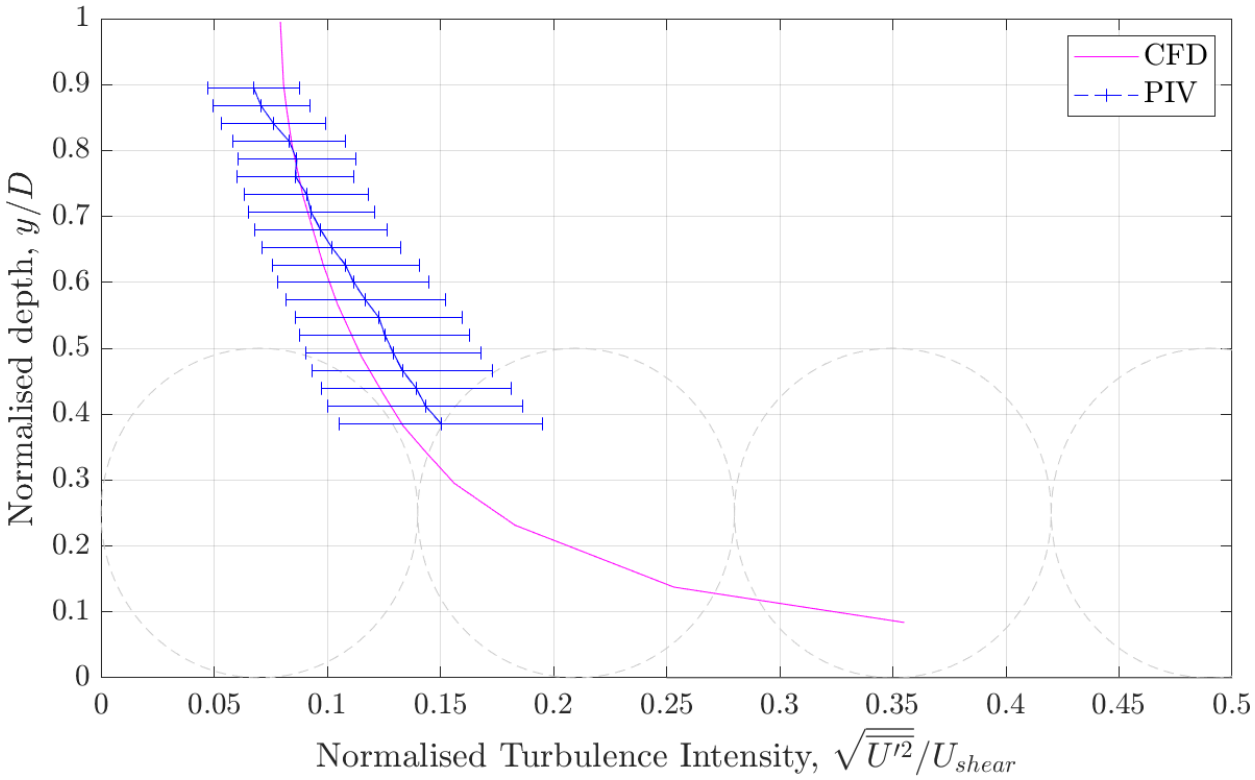

Figure 7.25: A comparison of the turbulence intensity profile between the experimental PIV with the CFD at the 49mm depth flow condition. The vertical depth coordinate has been normalised by the flow depth, D. The turbulence intensity has been normalised using the shear velocity calculated.

Comparisons with experimental tests at 49mm flow depth show similar velocity profiles (Figure 7.24). Since the velocity fluctuations (and hence turbulence) are entirely modelled, the turbulent intensity from the CFD is extracted using the turbulent kinetic energy field (k).

To compare against the PIV data from the experimental tests, an equivalent turbulent intensity is calculated from the velocity fluctuations detected by the PIV (CFD-Wiki, 2022). From Figure 7.25, it can be seen that the resulting turbulence intensity is very similar for both CFD and PIV. This was not the case with the first approach using DES. THe success of the RANS model in this cases suggests that the RANS subgrid modelling for the DES turbulence model may not have been the cause of the poor match in the previous approach.

7.3.1.2 Validation of RANS simulation using flow over a hemi-spherical boulder

Figure 7.26 to Figure 7.29 show results generated from the RANS simulation of flow over a hemi-sphere. Please refer to section 6.3.2 for more information regarding the setup.

The mean velocity field is shown in Figure 7.26 and highlights a low-speed region immediately behind the hemi-sphere. The no-slip condition is also evident as the flow near the bed and also on the surface of the hemi-sphere is zero. This shows that boundary conditions on imported geometry/faces are functioning correctly (the previous smooth bed was generated within OpenFOAM's *blockMesh* without any external .STL being supplied unlike the hemi-sphere boulder used here).

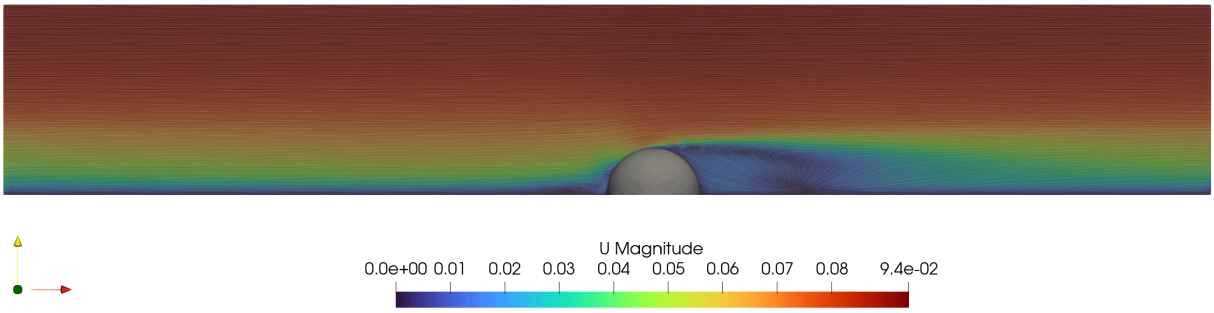

Figure 7.26: Flow over a hemi-sphere at 49mm depth visualised using Surface Line Integral Convolution (LIC). The colourbar represents the streamwise velocity (m/s). A low speed region is evident behind the semi-sphere similar to Stoesser (2014).

Figure 7.27 shows the turbulence generation mechanism mainly occurs in the wake directly behind the top of the hemi-sphere. This is supported by the extracted turbulence intensity which also shows some turbulence in a small region directly in front of the sphere (Figure 7.28). Meanwhile, the resulting turbulent eddy viscosity (Figure 7.29) also highlights a region from the upper front part of the hemi-sphere. This region consists of lower turbulent viscosity than the adjacent streamwise regions suggesting that the flow in this region is especially less turbulent as the flow is forced to consistently travel in the same direction (over the obstacle). Overall, the performance of the RANS turbulence model in capturing turbulent features (lack thereof) is very similar to the expected results presented by Hart (2016). See Figure 4.2 for a comparison between different turbulence capture methods.

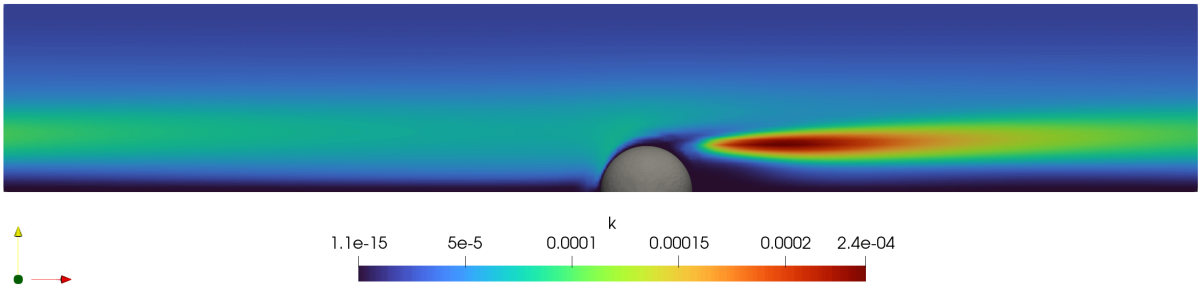

Figure 7.27: Turbulent Kinetic Energy field for flow over a hemi-sphere at 49mm depth. The region immediately behind the top of the hemi-sphere is responsible for a large generation of turbulent kinetic energy.

The effect of the periodic conditions that were applied to the upstream and downstream faces are clearly evident in Figure 7.27 where the turbulent kinetic energy is seen trailing behind the hemi-sphere downstream and re-entering at the upstream face. Were this a study into flow over a single hemi-sphere, such periodic conditions would never be used. Instead a longer domain with the sphere further upstream would be more suitable. However, the purpose of this simulation was to develop the mesh around a single hemi-sphere and test the ability of the RANS model to work with periodic boundary conditions where there are distinct obstacles within the flow. As the RANS model can clearly handle periodic conditions and simulate turbulence, focus is now shifted to the LES model and transient effects of flow over hemi-sphere. This would be analogous to flow in natural rivers with relatively smooth beds periodically encountering an obstacle that is a significant size in comparison to the depth of flow (i.e. a large submerged boulder).

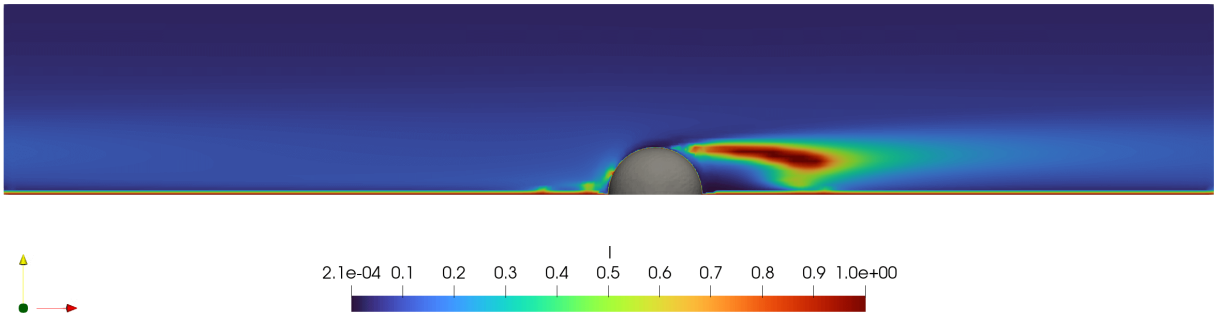

Figure 7.28: Turbulence intensity field for flow over a hemi-sphere at 49mm depth. The turbulent kinetic energy is transferred into flow turbulence and distorted towards the bed due to the flow reattaching after separating around the top of the hemi-sphere.

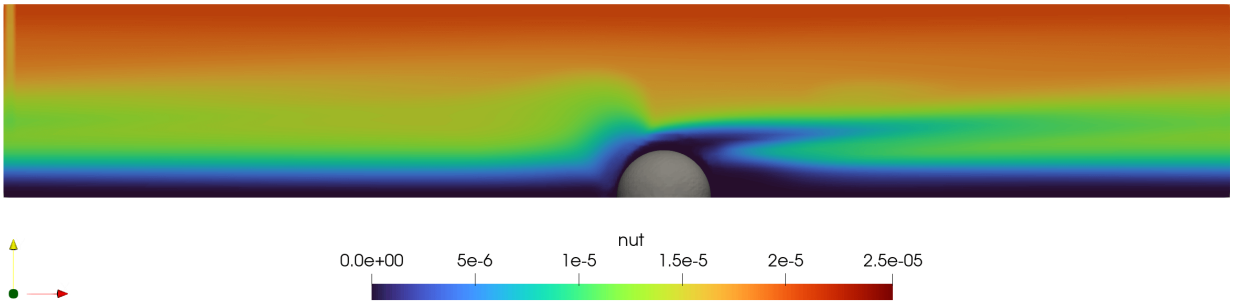

Figure 7.29: Turbulent viscosity ν_t field for flow over a hemi-sphere at 49mm depth. The region in the upper frontal area of the hemi-sphere is especially low in turbulent viscosity as the fluid is consistently forced to flow over the obstacle in the same manner.

7.3.2 PIV Validation

In Figure 7.30, the PIV velocity field in the streamwise direction has been spatially averaged across the width of the PIV image and then averaged over time.

In Figure 7.31, the double averaged streamwise velocity profiles from Figure 7.30 have been non-dimensionalised using $U+ = U/U_*$ and $y+ = \rho U_* y/\mu$ following Figure 2.8 in section 2.3. Comparing against Figure 2.8, there is a clear linear log law region as well as a viscous sub-layer region.

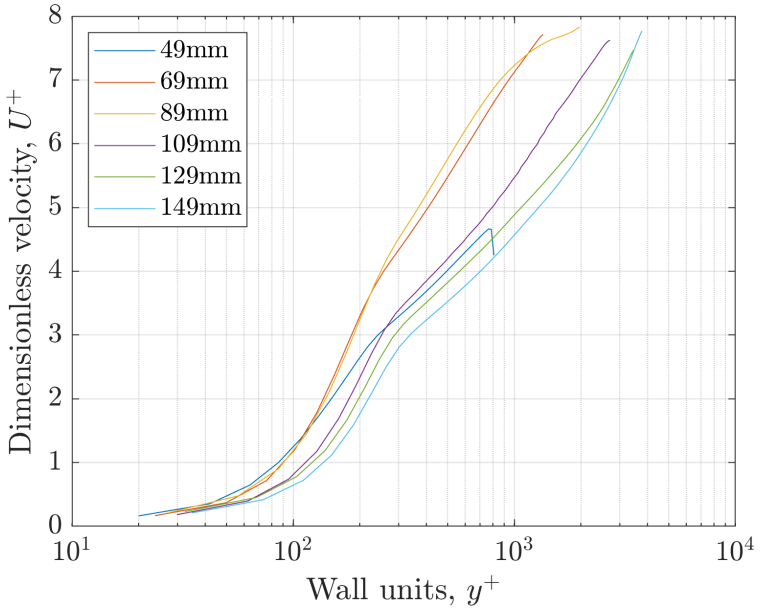

Figure 7.31: Double Average (Time and Spatial) streamwise velocity profile from the PIV non-dimensionalised using U^+ and $y+$.

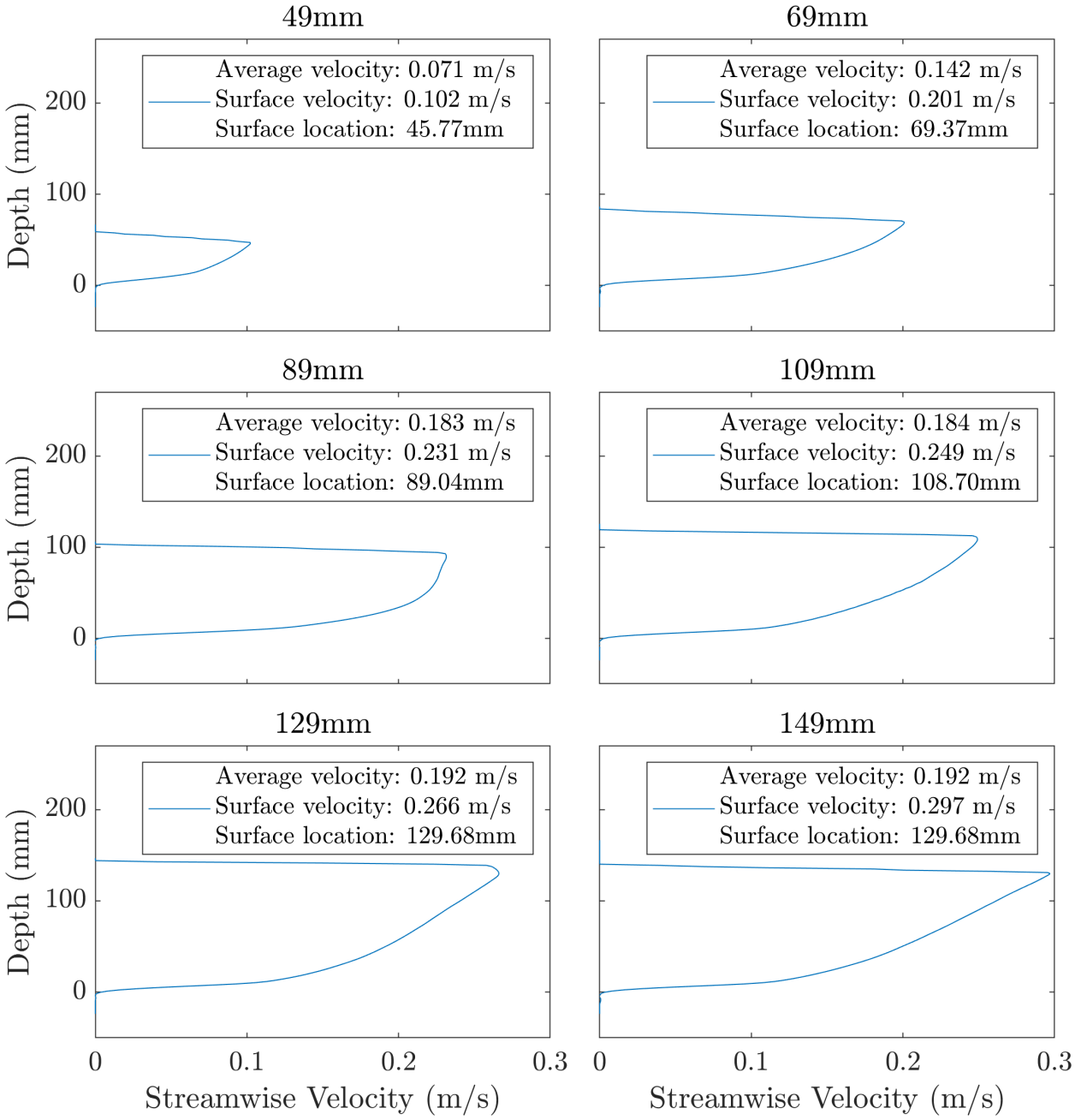

Figure 7.30: Double Average (Time and Spatial) streamwise velocity profile from the PIV. The maximum velocity occurs at a depth close to the free-surface. The average velocity is similar to the bulk flow. The 149mm flow condition does not appear to have been set correctly during the experiments.

7.3.3 Characteristic Roughness From Experimental Tests

Figure 7.32 show a log version of the streamwise velocity data with the y-intercept representing the characteristic roughness, y_0. For the 69mm depth case shown, the y-intercept characteristic roughness was measured to be 0.78mm. Using Nikuradse's findings on bed roughness (Thakkar et al., 2017), the effective sand grain roughness, ε for a fully turbulent flow should be $30y_0$ which corresponds to 23.4mm, almost exactly the same diameter as the plastic spheres on the bed.

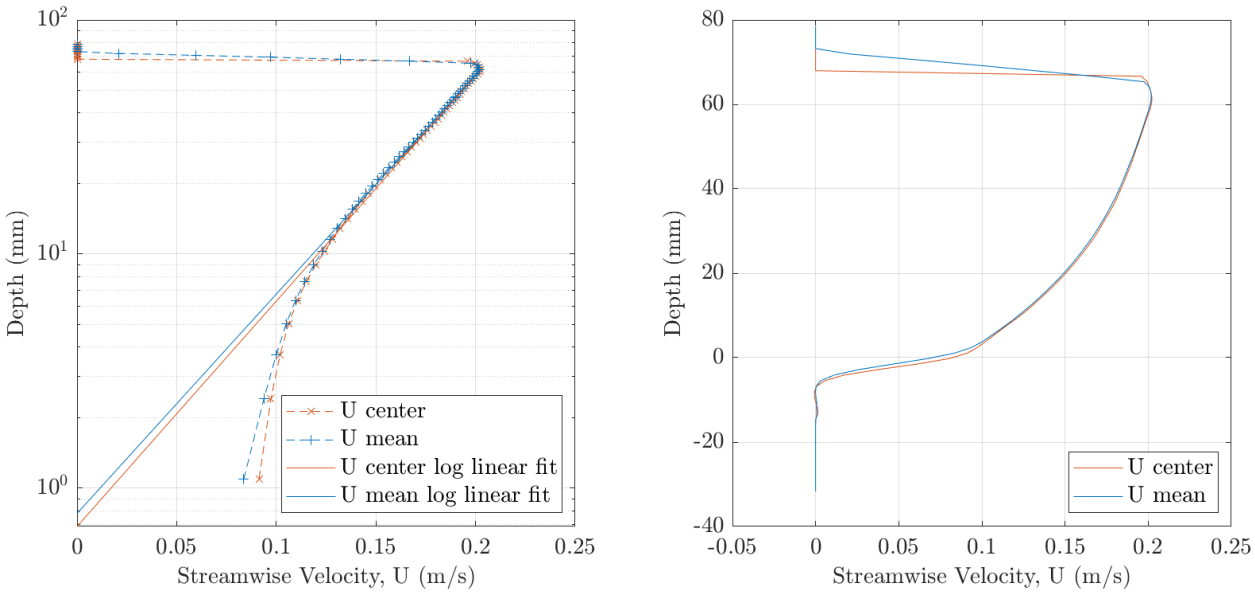

Figure 7.32: Time averaged PIV streamwise velocity profile on log-linear axis (left) and standard axis (right). The profile taken from the center of the PIV image is slightly different to the profile created from the spatial average across the width of the PIV image. This could be due to edge effects in the laser illumination or calibration. The data from the center of the PIV image is the most well illuminated and will be used for further analysis.

7.3.3.1 Initial validation of LES model using flow over hemi-spherical boulder

The transient effects of flow over a hemi-sphere can be studied using LES. Figure 7.33 shows a closeup snapshot of the velocity field. It can be seen that there is a small low speed region (in blue) immediately before the hemi-sphere followed by a much larger low speed region immediately after the hemi-sphere. Visualisation of the vorticy field in Figure 7.35 shows that these two regions contain some re-circulation. The presence of the hemi-sphere also causes the flow to deflect into the bulk flow where it interacts downstream.

In the low speed region behind the hemi-sphere, the re-circulation zone causes inflow of fluid towards the bed which is then ejected from the bed towards the free-surface. This region of low velocity is also characterised by low pressure streamlines in Figure 7.34 show the flow deflecting around the hemi-sphere before being sucked towards the centerline. The size of the re-circulation zone is about equivalent to the height of four obstacles. The shape and direction of the re-circulation zone after the hemi-sphere also matches the findings in literature on flow past hemi-spheres (Hyun et al., 2003; Savory and Toy, 1986b; Stoesser, 2014). Likewise, the behaviour of the turbulence generated is also similar to literature (Savory and Toy, 1986a; Stoesser, 2014).

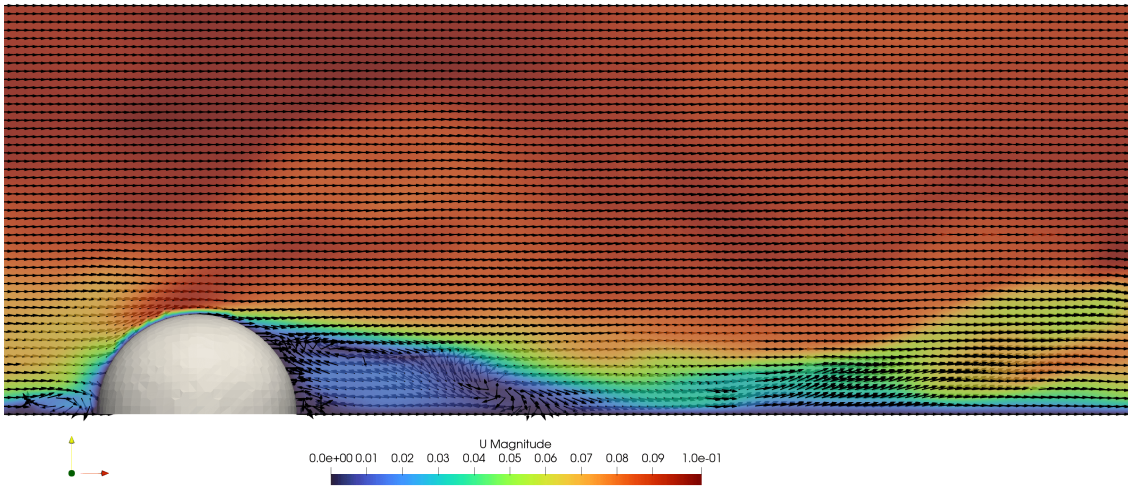

Figure 7.33: Instantaneous snapshot of the velocity field from LES simulation of flow over a hemi-sphere at 49mm depth. Lower speed packets of flow are ejected from the rear of the obstacle. Additional effects are also observed further downstream as the flow recombines with the bed.

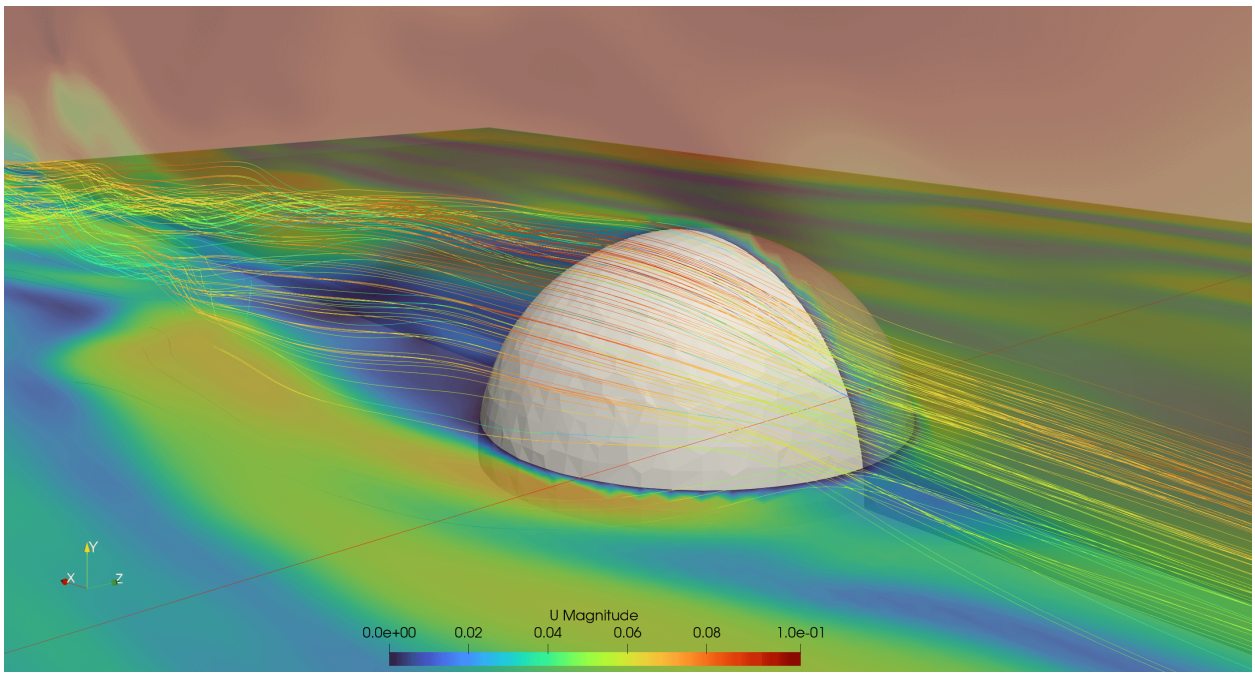

Figure 7.34: A streamline visualisation from LES simulation of flow over a hemi-sphere at 49mm depth. Low and high speed streaks are observed in the lateral spanwise direction. The flow moves smoothly over the front of the hemi-sphere and around the low-speed tail region. This matches Figure 4.1 from Stoesser, 2014 on flow over a hemi-sphere.

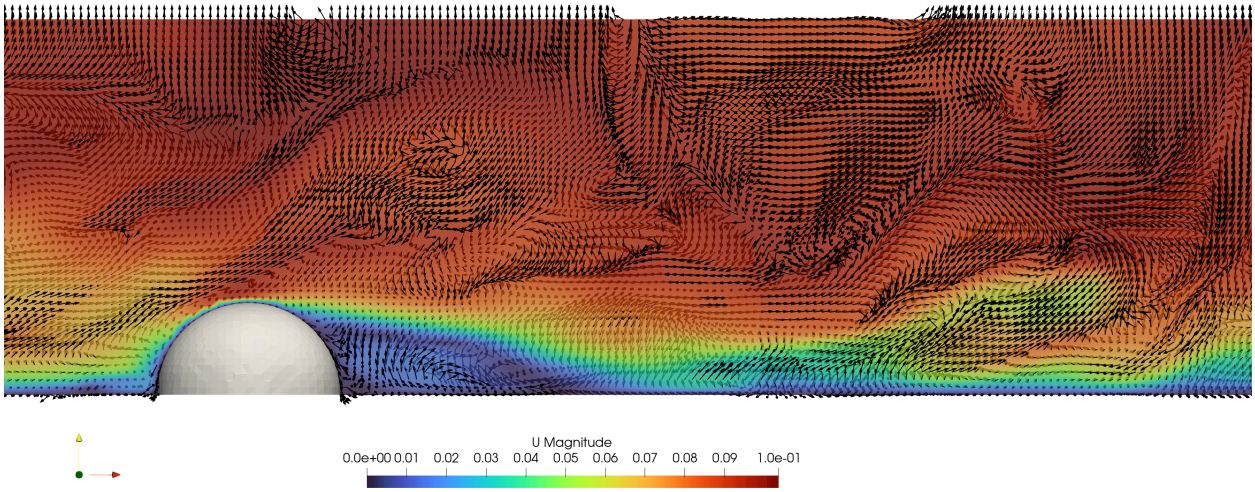

Figure 7.35: Instantaneous snapshot of the vorticity field from LES simulation of flow over a hemi-sphere at 49mm depth. The regions of lower velocity identified in Figure 7.33 are in the midst of high vortex motion.

7.3.3.2 Validation of LES method in simulation of a full bed of spherical caps

Figure 7.36 shows a comparison of the velocity profiles between the ADV, PIV and CFD at 69mm flow depth and experimental PIV data of Nichols (2015) at 70mm flow depth. As explained in section 6.3.3, the CFD simulation used a full bed of spherical caps. These caps had a no-slip boundary on the faces whilst the virtual bed itself had a slip condition since the real bed (beneath the spheres) was outside the computational domain. One of the experimental flow conditions presented by Nichols (2015) also used a hexagonal close packed bed of 24mm spheres at a depth of 70mm and a slope of 0.001. Unlike the current work, Nichols (2015) used 2 layers of spheres rather than the 1 layer deployed here. The data from Nichols (2015) was collected as a PIV plane at the centerline of the flow (Figures 7.37 to 7.38). For comparison, PIV data from the current study is extracted at the center of the PIV image as a vertical line (see Figure 7.13).

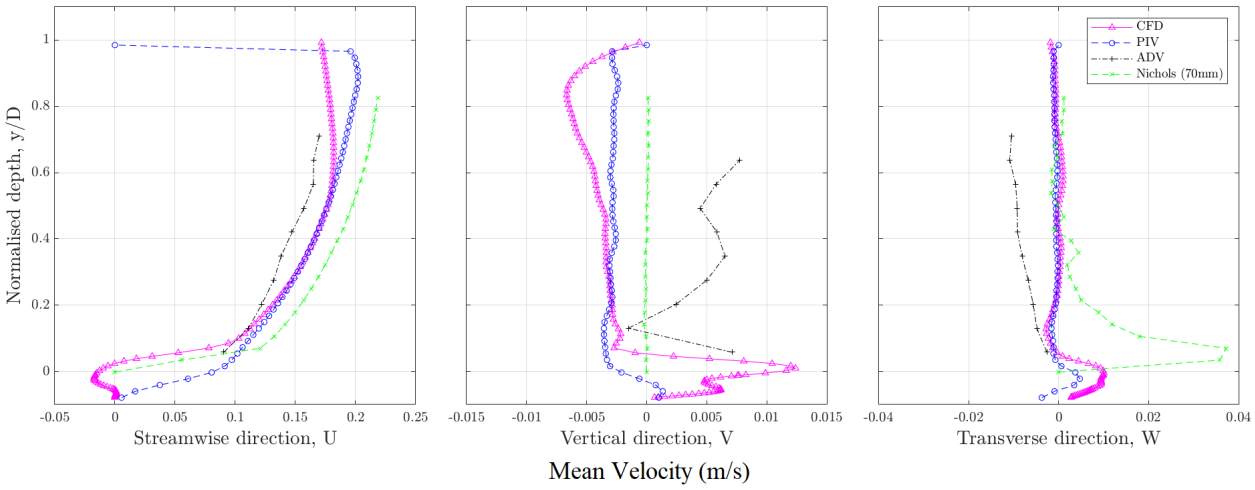

Figure 7.36: Comparison of velocity profiles from 69mm depth flow condition between different experimental instruments (PIV and ADV), CFD simulation and previous work of Nichols (2015) at 70mm flow depth. The vertical axis has been normalised by the flow depth, D.

It can be seen that near the bed and within the flow, the streamwise mean velocity profiles are within <0.05 m/s of each other. The PIV data from Nichols (2015) is slightly faster. Near the free-surface, the CFD streamwise velocity decreases. This seems abnormal as the free-surface has a free slip condition with air (in simulation and in real life). As there are no experimental data very close to the free-surface, it is not possible to precisely determine if

the reduction in streamwise velocity from the CFD is realistic or not. It is possible that the rigid lid approximation led to a reduction in streamwise velocity.

Looking at the other directions, the vertical and transverse mean velocity profiles are also very similar. However as with the streamwise direction, some deviation is present near to the free-surface for the vertical direction. This is highly likely due to the rigid lid approximation which forces the vertical velocity to be zero at the edge of the computational domain.

7.3.3.2.1 Evaluating Nichols (2014) Figure 7.38 shows a contour plot of RMS velocity fluctuation from the work of Nichols (2015). It can be observed that the velocity fluctuations appear to change with position away from the center of the PIV image. This strongly suggests that the PIV data at the fringes of the PIV camera's field of view are not reliable. Furthermore, Figure 7.38 shows an abnormally high velocity fluctuation in the transverse direction. As the PIV system primarily detects changes in the streamwise and vertical direction, 'through-plane' (transverse) movement is difficult to capture and this is also supported by Nichols (2015) who did not use the transverse data collected. Thus, the transverse PIV data from Nichols et al. (2014) is not used for further comparison.

7.3.3.2.1.1 Turbulent Strength Figure 7.36 looks more closely at the velocity fluctuation by comparing the turbulence strength (root mean squared) profiles in each study. It can be seen that in all three directions, the CFD and the experimental results from the present study are very similar. However, the discrepancy between the CFD and the experimental results (PIV and ADV) is more noticeable towards the free-surface. In the vertical direction, the rigid lid approximation forces the vertical velocity to zero towards the free-surface. In the streamwise direction however, unlike the experimental results, the streamwise velocity fluctuation from the CFD also increases near the free-surface which may indicate the rigid lid causes a different type of physical interaction between the free-surface and the flow. An outlier from the ADV at the point closest to the free-surface in the transverse direction is also detected.

Comparing against Nichols (2015) shown in green, the turbulence strength from that study is significantly larger. This is due to Nichols using a larger flow rate of 9.6 l/s (a bulk velocity of 0.21 m/s). The current study used a flow rate of only 5.05 l/s (a bulk velocity of 0.15 m/s). As the flow condition in Nichols (2015) is faster, it is also slightly more turbulent. The flow rate difference is likely due to the double layer of spheres which results in a higher flow through/within the bed itself. This also helps explain the differences in streamwise mean velocity profile in Figure 7.36.

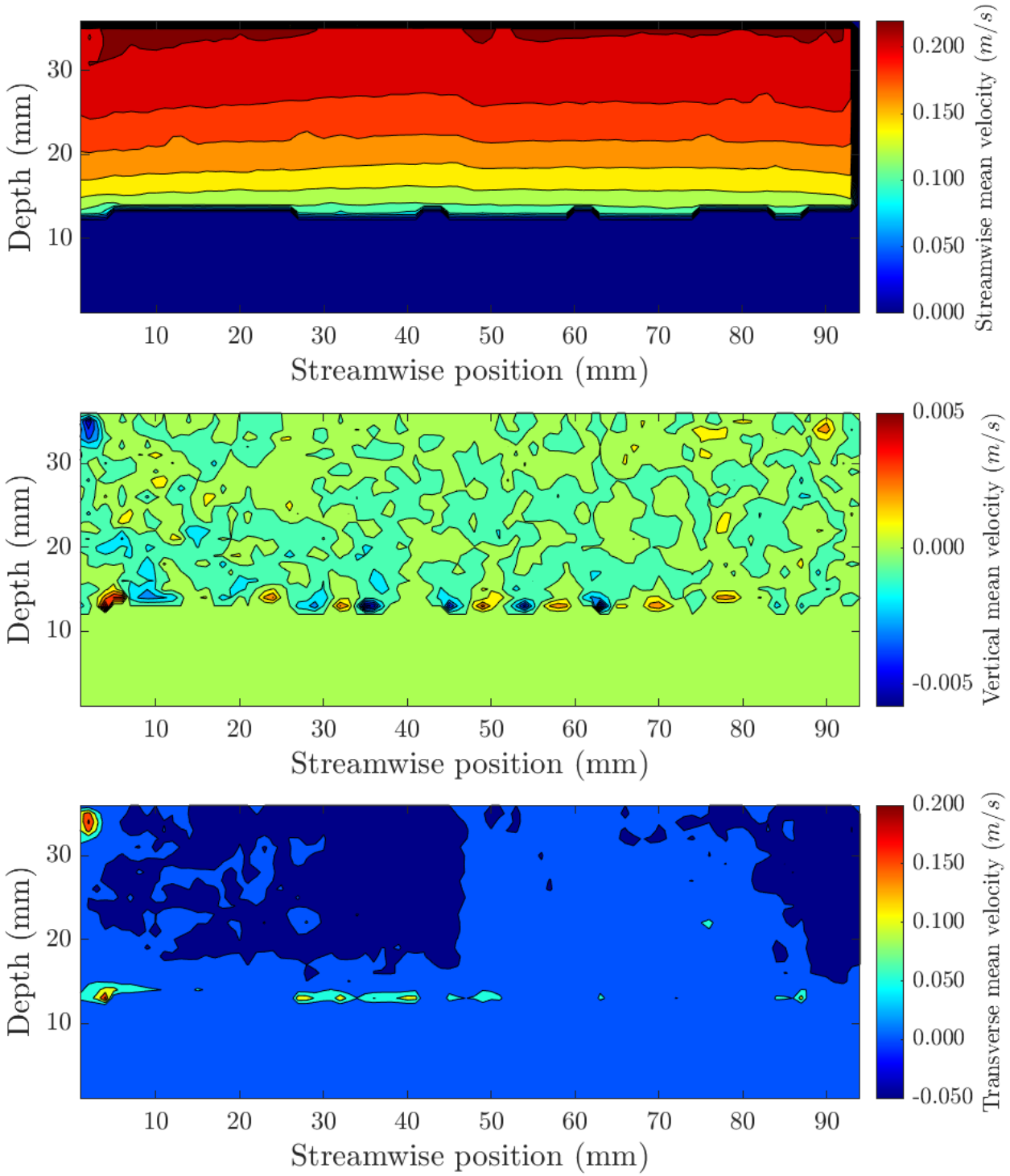

Figure 7.37: Contour visualisation of the mean velocity distribution from PIV flow testing conducted at 70mm flow depth (Nichols, 2015). The data shown is a vertical plane through the spanwise center of the flume. Physically, the time-averaged behaviour of the flow should not change significantly from the upstream to the downstream end of the measurement region. This is reflected by the contour plot for the streamwise direction. The contours shown for the transverse direction appear somewhat dubious and were also deemed to be unreliable by Nichols (2015).

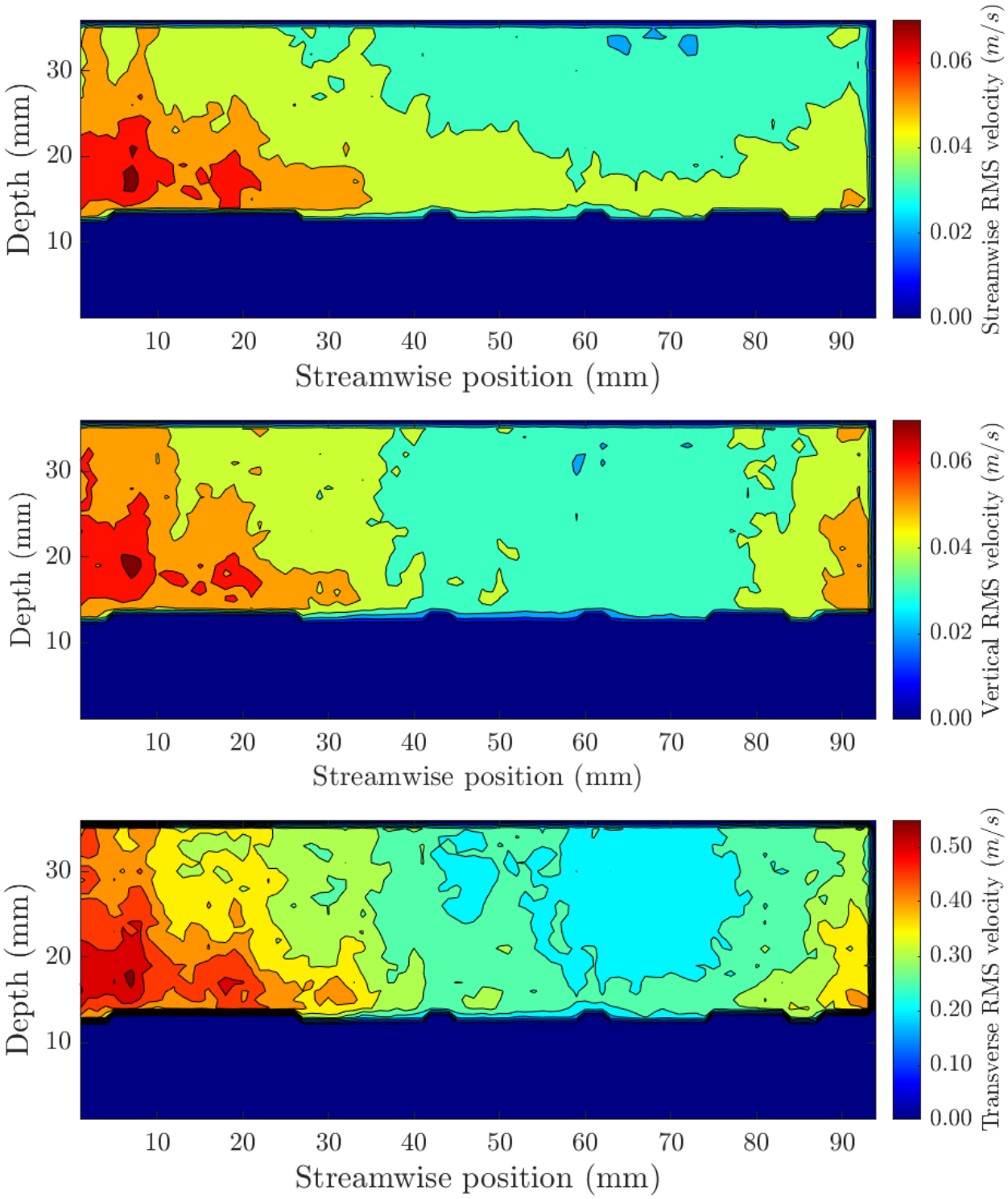

Figure 7.38: Contour visualisation of the RMS velocity fluctuation from PIV flow testing conducted at 70mm flow depth (Nichols, 2015). The data shown is a vertical plane through the spanwise center of the flume. The RMS data appears to suggest different turbulence strength in one zone of the measurement region, this is physically unlikely to occur. One explanation is that the PIV illumination was much stronger in this zone and hence, the RMS readings appear different.

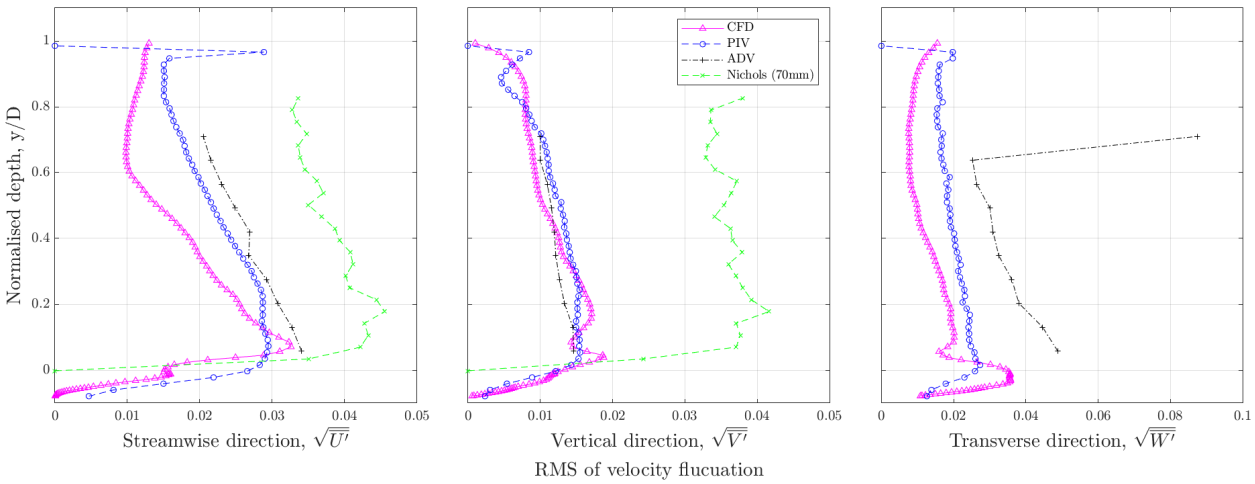

Figure 7.39: Comparison of turbulence strength profiles from 69mm depth flow condition between different experimental instruments (PIV and ADV), CFD simulation and previous work of Nichols (2015) at 70mm flow depth. The vertical axis has been normalised by the flow depth, D.

Since the flow rate is different between the Nichols (2015) and the current study, a normalisation is necessary for a fair comparison. In the Nichols (2015) study, the exact shear velocity used to calculate a normalised turbulence intensity was not available so the profiles are normalised against their respective bulk flow velocities. After accounting for the different flow rates, the results are much more closely aligned (See Figure 7.40). However, the turbulence intensity in the vertical direction is still slightly higher than expected against the results of the present study. One possible explanation is the flume width in Nichols was 459mm whilst the flume used in the present study was 500mm. With the flow being relatively deep, a 70mm flow depth may not have been fully immune from the effects of the side walls. Secondary currents could cause regions of recirculating flow in the central part of the flow and raise the vertical turbulence intensity.

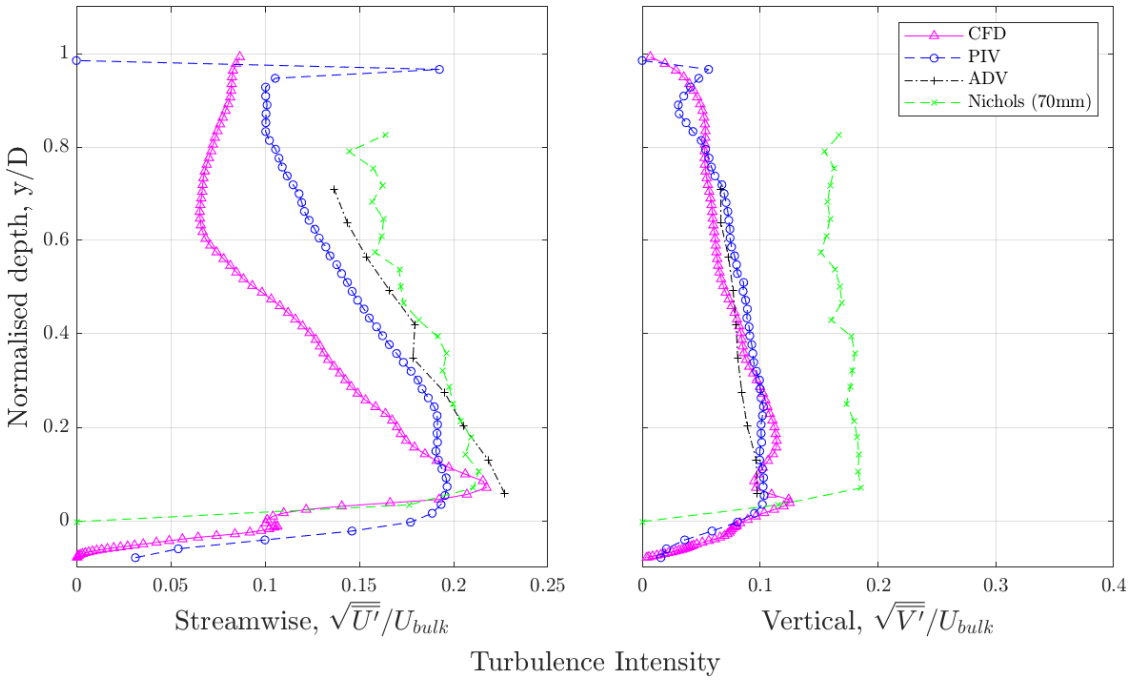

Figure 7.40: Comparison of normalised turbulence intensity profiles from 69mm depth flow condition between different experimental instruments (PIV and ADV), CFD simulation and previous work of Nichols (2015) at 70mm flow depth. The vertical coordinate has been normalised by the flow depth, D. NOTE: The turbulence intensity has been normalised using the bulk velocity calculated from the mean velocity profile (the shear velocity was not explicitly stated by Nichols (2015)).

7.3.3.3 Comparison Against Literature

A comparison is also made against published literature. Figure 7.41 shows the turbulence intensity profiles from the experimental and computational results with the 49mm flow condition and makes a comparison against the published works of Grass et al. (1991), Singh et al. (2007), Defina (1996), Dancey et al. (2000) and the log-law theory. The experiments and simulations form an excellent match with the literature.

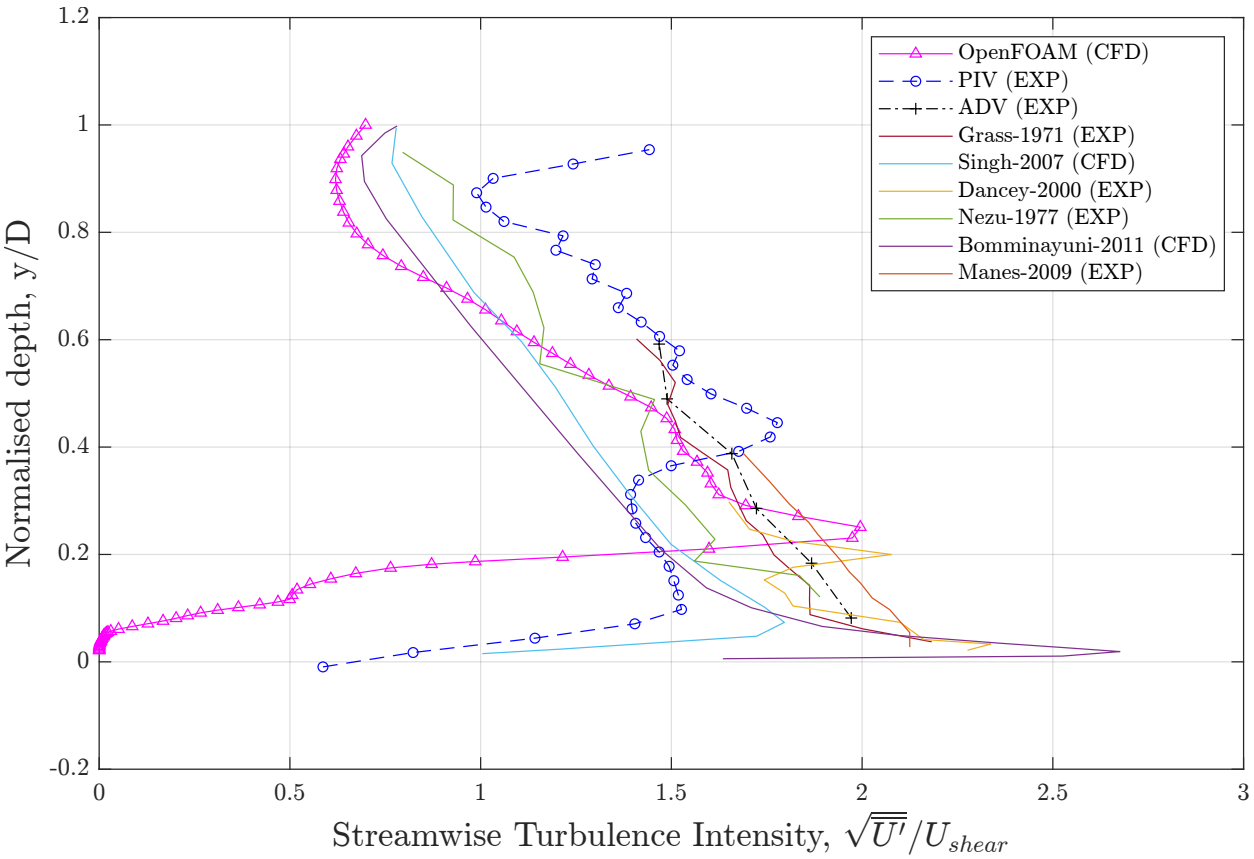

Figure 7.41: Comparison of turbulence intensity profile from experiments and simulation against published literature at 49mm flow depth. All the profiles follow a similar trend and are closely clustered together, suggesting a good match. The CFD appears to be slightly different towards the free-surface.

Figure 7.42 shows the U^+ and y^+ experimental and computational profiles against Grass (1971), Singh et al. (2007), Dancey et al. (2000), Nezu (1977), Bomminayuni and Stoesser (2011) and Manes et al. (2009). Due to log scale for the $y+$, minor differences in the definition of the bed datum are highlighted. The results from Defina (1996) seem very rough and suggests that there may have been insufficient temporal data to obtain statically

converged results. The gradient of the profiles mostly follow the linear log law. The CFD in particular is also able to capture the full classic turbulent boundary layer that was presented in Figure 2.8 in section 2.3.

In the CFD, there is clearly a viscous sub-layer (y^+ from 3 to 40), a buffer layer (y^+ from 40 to 200) and log-law region (y^+ from 200). The viscous sub-layer appears to occur higher in the flow compared to the theory and this is due to the presence of the rough bed pushing the datum higher into the flow. The near bed region is rougher and hence the buffer and log-law region can only begin to develop higher in the flow.

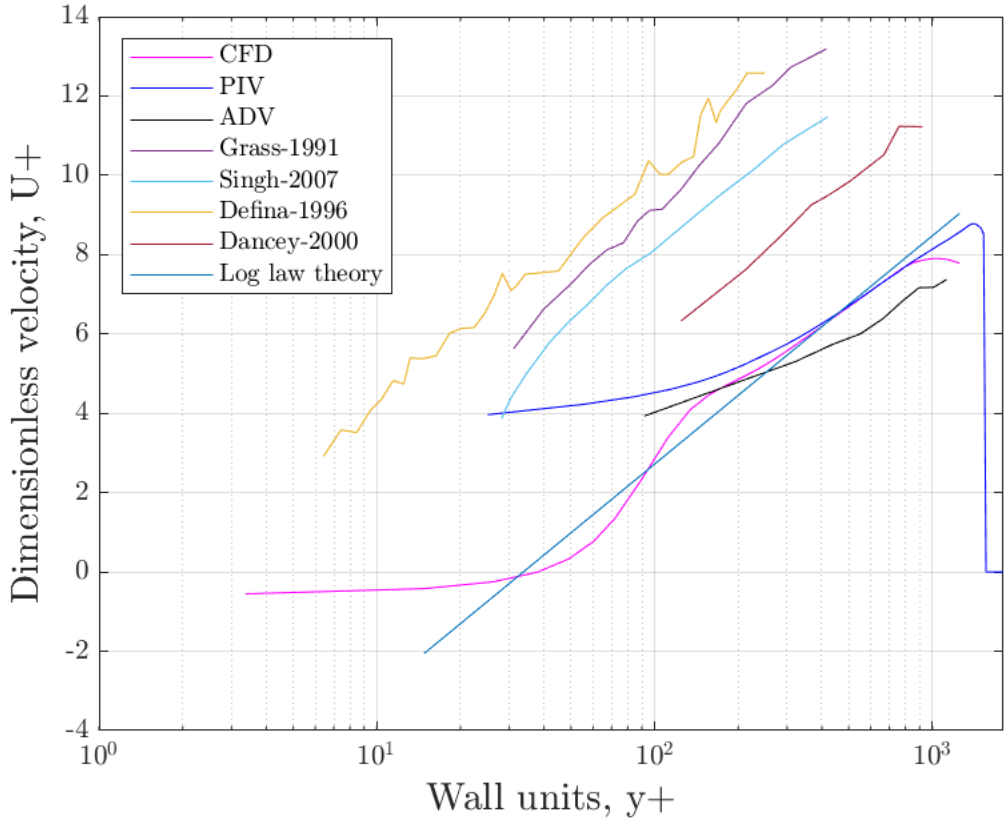

Figure 7.42: Comparison of turbulence boundary layer against literature using the 69mm flow depth simulation. Whilst the profiles are not in the same location, this is due to slightly different definitions of the bed location (for flows over rough beds). The gradient of the profiles are very similar between all the datasets suggesting that the law of the wall is well modelled or captured by the sensors (as explained in Figure 2.8).

7.3.4 Summary of validation

The errors around experimental data collection with PIV and ADV were discussed and explored. Boundary conditions were tested on simulations of flow over a smooth bed and over a hemi-sphere. These results successfully demonstrated for open channel flows:

a) periodic boundaries at the up/downstream faces,

b) no-slip at the bed and hemi-sphere obstacle and

c) the slip condition on the rigid lid.

Turbulence modelling techniques (RANS and LES) were validated against experimental flows and literature. Overall, the CFD simulations are able to realistically replicate many of the same physical behaviours found in experimental laboratory flows. The following section will explore in further detail turbulent structures and their implications on the rigid lid approximation for shallow flows.

Chapter 8

Results and Discussion

This chapter begins with section 8.1 on free-surface analysis. This will compare the behaviour of the conductance wave probes and the Kinect infrared sensors to answer the first research question.

Since flow visualisation has been shown in the literature to be an important tool towards the discovery of new mechanisms, a closer assessment of the turbulent structures was conducted using U-level, Proper Orthogonal Decomposition (POD) and Quadrant analysis. This is presented in section 8.2.1 to answer the research question regarding the validity of the rigid lid approximation.

8.1 Free-surface analysis

The three wave probes were compared to each other to see if there were any differences. Figure 8.1 shows a 20 second time series extracted for the wave probes. Figure 8.2 shows a probability density function for the amplitudes detected. This shows a very similar set of amplitudes detected, which is expected since all three probes are measuring the same flow at the same time.

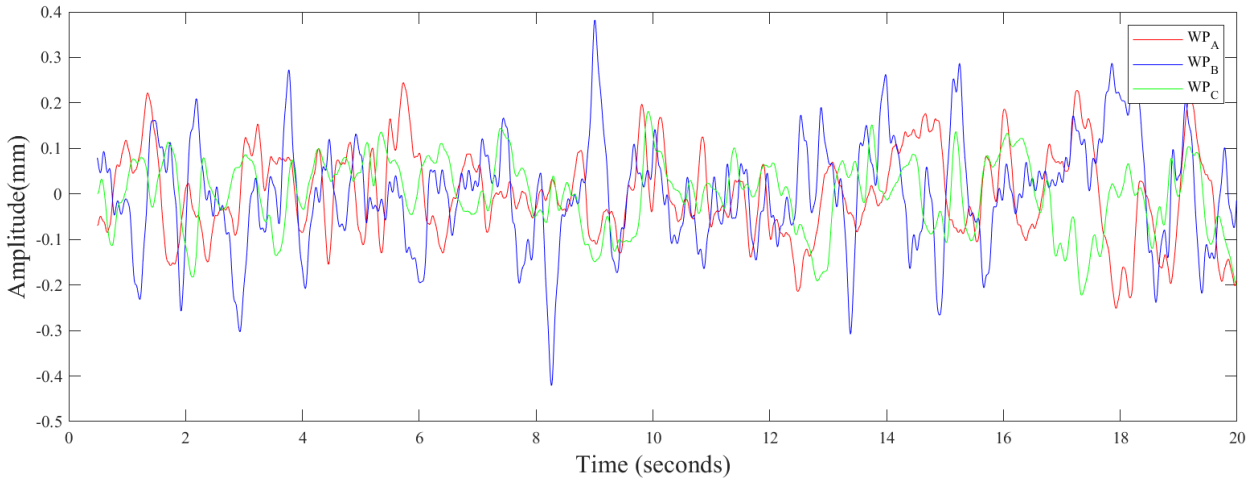

Figure 8.1: Amplitude of the three signals detected by the three wave probes for the 129mm flow depth condition (20 seconds shown).

In the deeper flows, there is some correlation between Wave Probe A and Wave Probe C as they are close together (see Figure 5.40). Figure 8.3 shows the frequency spectrum for the 129mm flow condition which indicates some noise in wave probe B. Figures 8.4 and 8.5 shows the cross correlation between the wave probes and their signals. The wave probe fluctuation amplitude generally increase with flow depth, suggesting that all three wave probes detect similar patterns.

There is a high correlation between wave probe A and C, this can be visually seen in Figure 8.1 where the wave probe A and C are clearly related. The relationship to wave probe B is more difficult to determine, possibly because of the noise due to large (1.2m) separation distance and disturbance from the upstream probes possibly causing a double slit interference pattern.

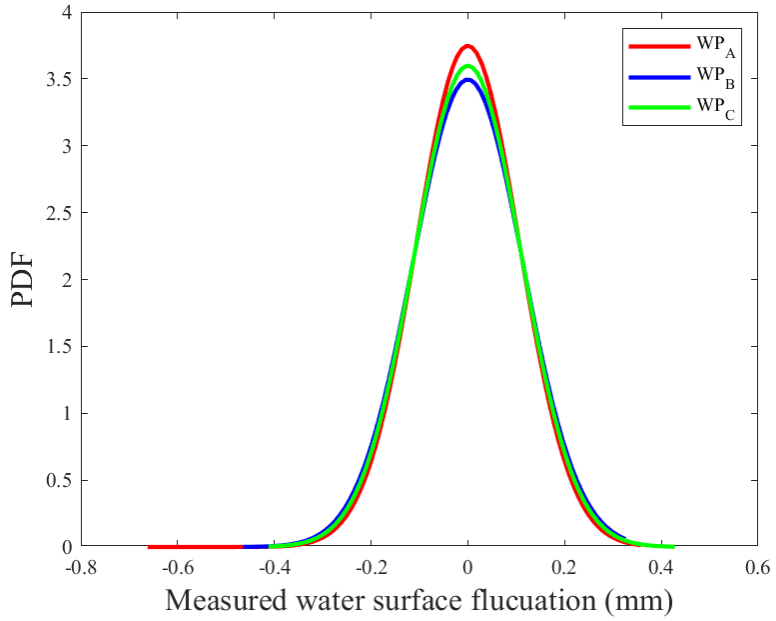

Figure 8.2: Probability density function of the three wave probes. 109mm flow depth condition is used to demonstrate that all three distributions are very similar suggesting that the free-surface fluctuation distribution does not change with spatial measurement location in the streamwise and spanwise lane.

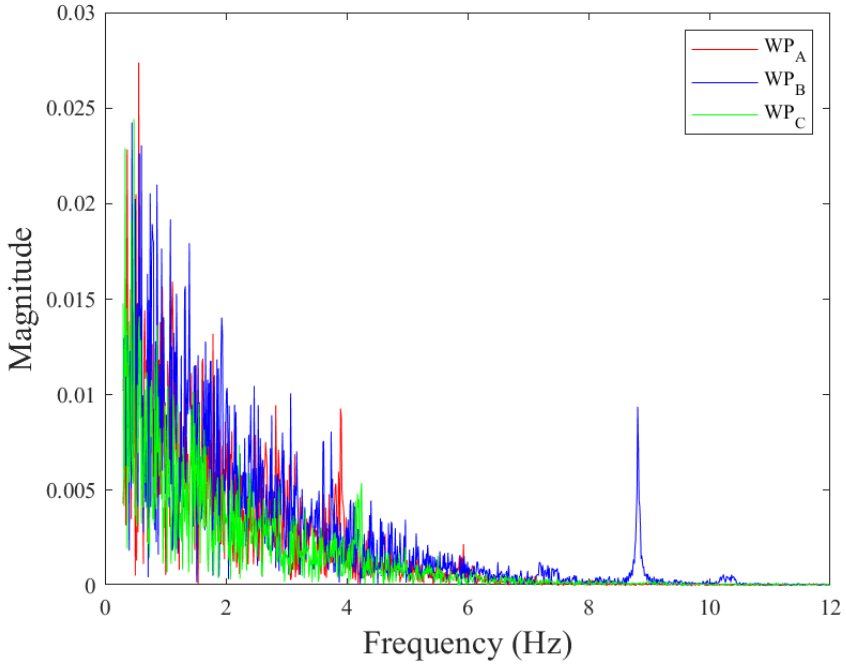

Figure 8.3: Frequency spectrum of the three wave probes signals, A, B, and C for the 129mm depth experimental flow condition. Wave Probe B appears to suffer from external noise at 9 Hz. This could be due to vibrations from the pump being transmitted to one of the mounting frames housing that particular wave probe.

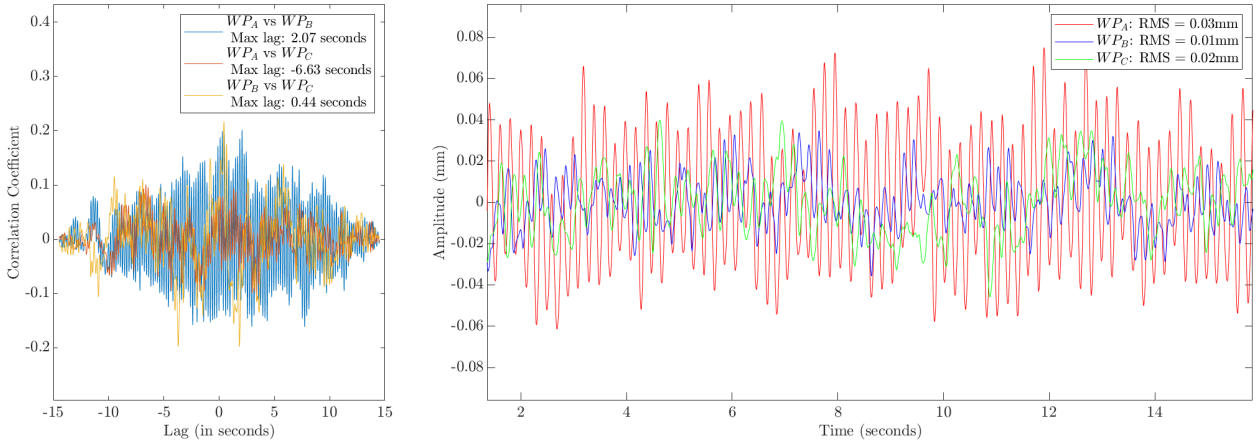

(a) 49mm depth experimental flow condition

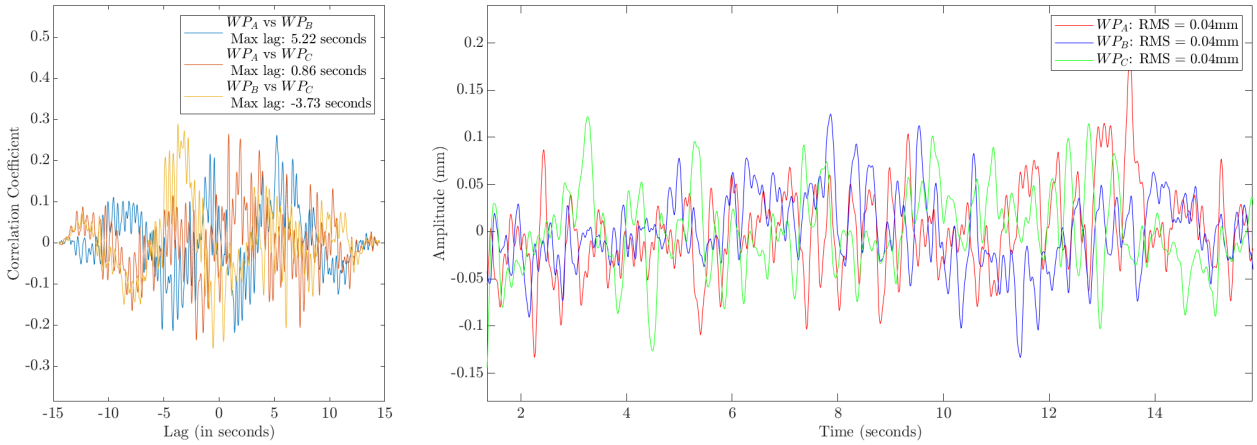

(b) 69mm depth experimental flow condition

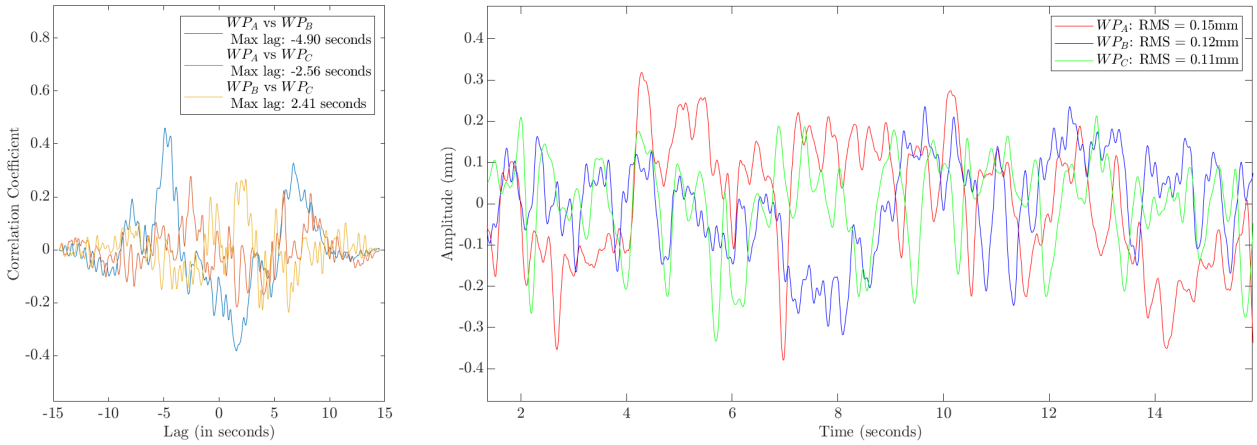

(c) 89mm depth experimental flow condition

Figure 8.4: Cross correlation (left) and raw signal (right) between the three wave probes at depths 49mm, 69mm and 89mm.

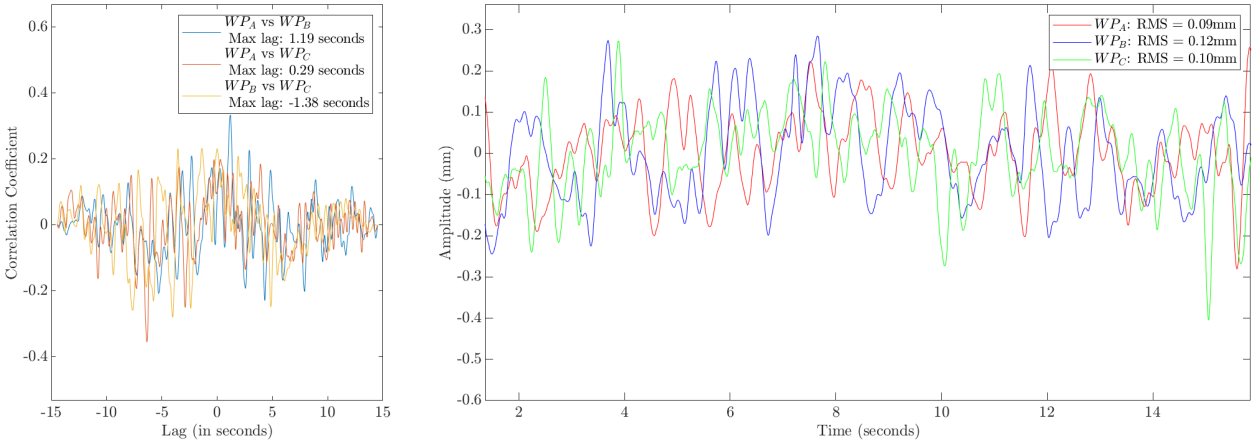

(a) 109mm depth experimental flow condition

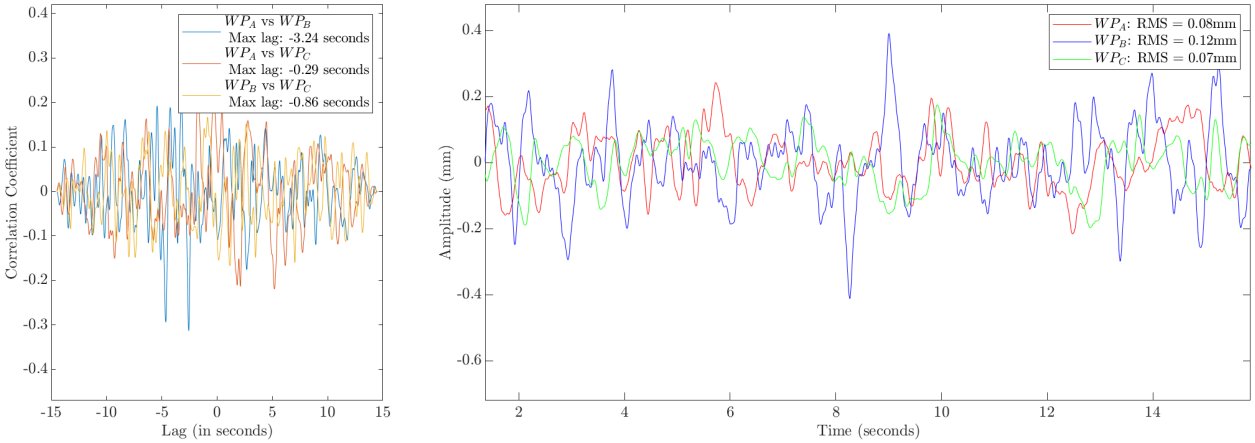

(b) 129mm depth experimental flow condition

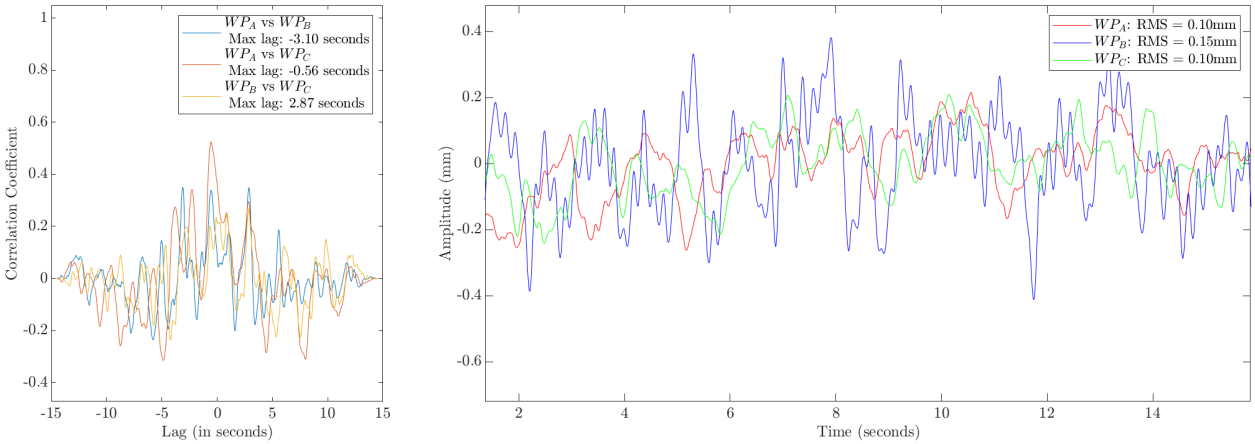

(c) 149mm depth experimental flow condition

Figure 8.5: Cross correlation (left), and raw signal (right) between the three wave probes at depths 109mm, 129mm and 149mm. There is a high correlation between wave probe A and C for the 149mm depth flow condition and this is also reflected in the raw signals. 149mm is the flow depth that generated the most free-surface turbulence so it is expected the different signals would have the strongest relationship.

8.1.1 Comparing the Wave Probe and the Kinect Sensor Data

Figure show the amplitude of the wave probe and the Kinect sensors together. Because the wave probe operated at 100 Hz compared to the Kinect sensors which only took images at 30 fps, the wave probe data was downsampled from 100 Hz to 30 Hz using the 'resample' function in order to compare them.

The first observation that can be made is the wave probes detected free-surface appears to fluctuate much less than the Kinect sensors. All three sensors detected higher amplitudes with higher flow depths suggesting that they are at least somewhat sensitive to changes in amplitude. The first generation Kinect performed more poorly with much larger flucuations/noise.

As discussed by Peakall and Warburton (1996), surface tension plays a significant role in free surface flows with a Weber number of below 11. The 49mm depth flow condition has a Weber number o 3.96 and is clearly under the influence of surface tension in addition to gravitational effects. This can be observed in the very low free-surface amplitudes detected.

Figure 8.7a to 8.7f show the frequency spectrum of the Kinect and the wave probes together. It can be seen that the Kinect 1 and the Kinect 2 sensor both contain very similar frequency components. As mentioned in the literature review, the Kinect 1 sensor uses a structured light technique whereas the Kinect 2 uses a time of flight technique. Despite the differences in remote sensing measurement technique, both appear to detect very similar frequency components whilst the magnitudes detected by the wave probe appear significantly smaller (possibly due to the separation between wave probe wires.

A cross correlation between the three sets of data was conducted and is presented in Figure 8.8. It can be seen that the Kinect 1 and 2 sensors both show a very good correlation although sometimes with a small lag for several deeper depths. Strangely, this is not reflected in all flows. In the 69mm, 89mm and 149mm cases, the lag is up to 300 frames which correspond to approximately 10 seconds. This could be an issue with the computer managing the Kinect sensors starting the recording slightly later (the code is sequential). The correlation between

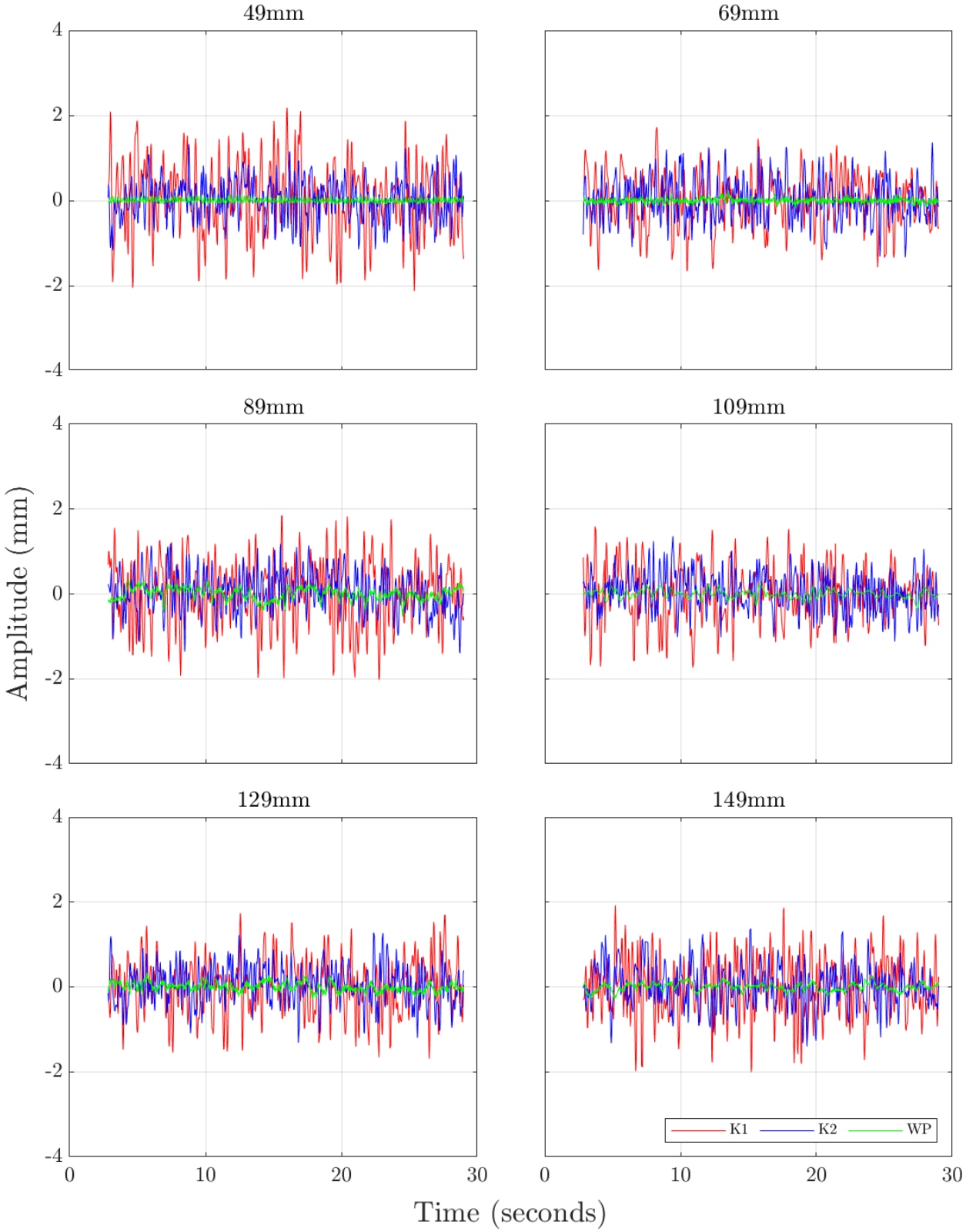

Figure 8.6: Time series comparison of the free-surface detected signal amplitude between the Kinect infrared sensors and the conductance wave probe. The wave probe signal has been downsampled from 100Hz to 30Hz. The wave probe signals are consistently lower in amplitude than the Kinect infrared sensors. The Kinect infrared sensors measure similar free-surface fluctuations for all depths.

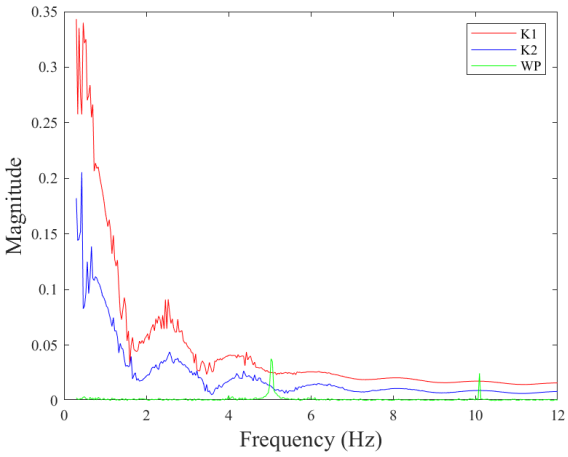

(a) 49mm depth flow condition

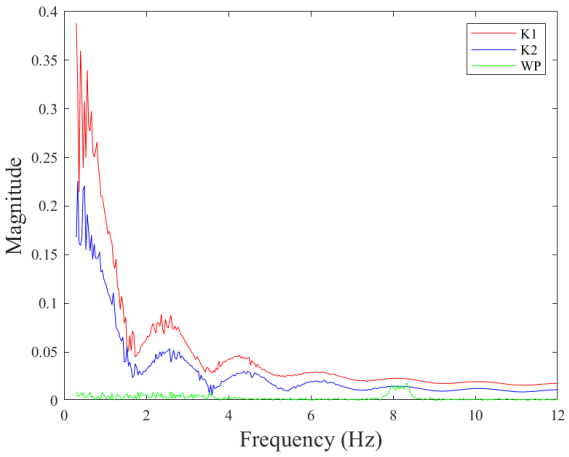

(b) 69mm depth flow condition

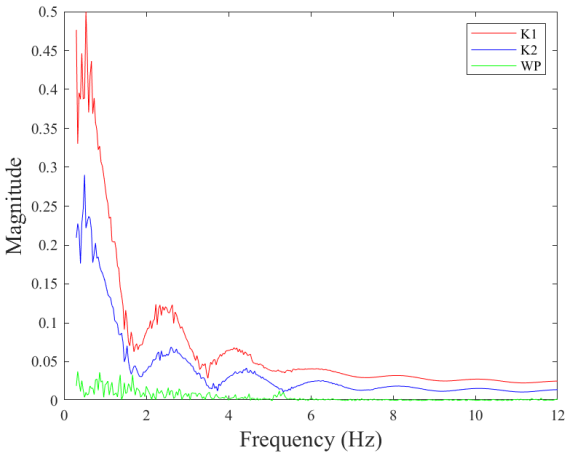

(c) 89mm depth flow condition

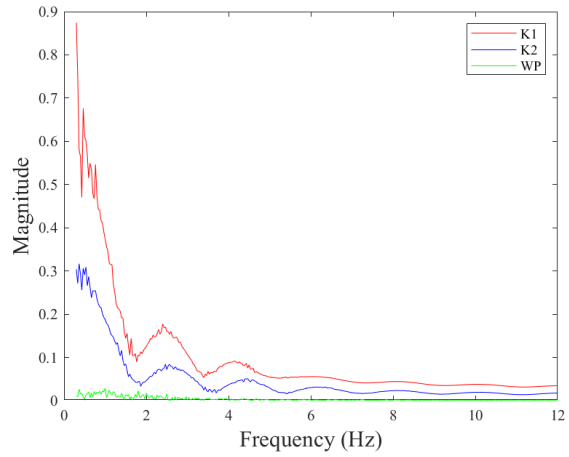

(d) 109mm depth flow condition

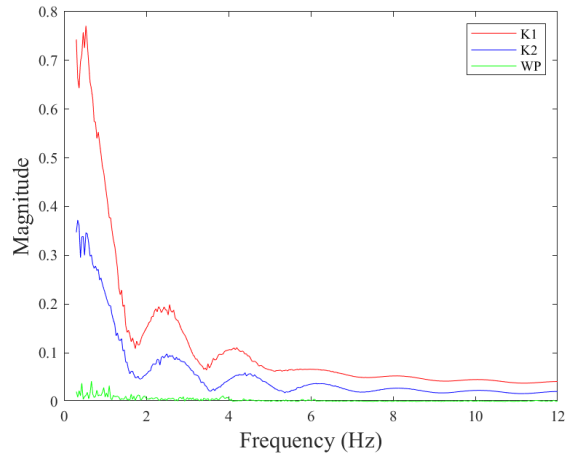

(e) 129mm depth flow condition

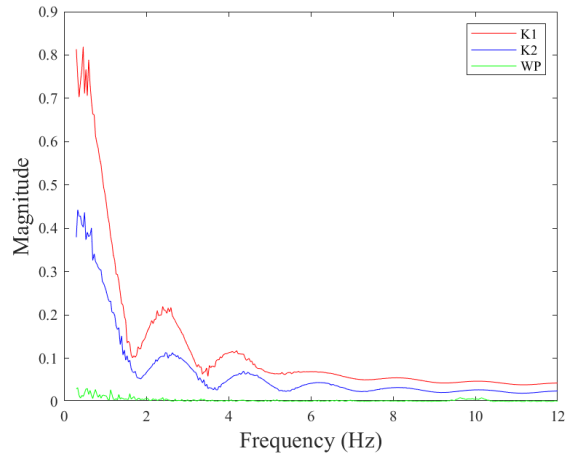

(f) 149mm depth flow condition

Figure 8.7: A comparison of the frequency spectrum between the Kinect infrared sensors and the conductance wave probe. K1 uses a structured light technique, K2 uses a Time-of-Flight technique and WP is conductance wave probe B. Both Kinect sensors reported localised peaks in the frequencies of 1 Hz, 2.8 Hz and 4.5 Hz.

the Kinect and the wave probes is the lowest for the most shallow depth. This is likely due to the inability of the Kinect abd wave probes to measurement small fluctuations.

Figure 8.9 compares the free-surface fluctuations using a probability density function. Besides the 129mm case, the Kinect 1 consistently detects a wider range of fluctuation and appears to have some skew. Meanwhile the wave probe has a much higher kurtosis with the majority of fluctuations only between -0.5mm and 0.5mm. As the probability density function clearly demonstrates, the majority of fluctuations detected by the wave probes are smaller than 0.2mm and even if the maximum amplitudes were affected, this did not affect the bulk of the data.

Some conclusions can be drawn from the comparison between the Kinect and the wave probe sensors. The wave probe sensing technique is conductance-based and well established. However, in this instance, it was affected by the analogue to digital conversion process which introduced significant stepping of the signal. This was filtered using a low-pass Butterworth filter. The filtered signal was more reasonable (albeit missing some higher amplitude fluctuations). This could be responsible for the sharp peak of the wave probe data in comparison to the Kinect sensors on the probability density function figures. The Kinect 1 sensor consistently sensed a wider range of fluctuations across all depths, the Kinect 2 sensor shows a similar range of free-surface fluctuations and shows more promise compared to the Kinect 1 sensor. Referring back to the colourant concentration and settling tests from section 5.1, the Kinect 1 sensor also performed poorly with detected depths up to 4mm away from the real depth. Given that the steady turbulent flows that were subsequently tested had surface fluctuations less than 4mm, it is unsurprising to find that it could not accurately detect the free-surface dynamics. This is supported by Combes et al. (2011) who did a series of similar tests as shown in Figure 8.10. Combes et al. (2011) achieved calibration in the form of a tangent law:

$$z = a\tan(br + c) + d), \tag{8.1.1}$$

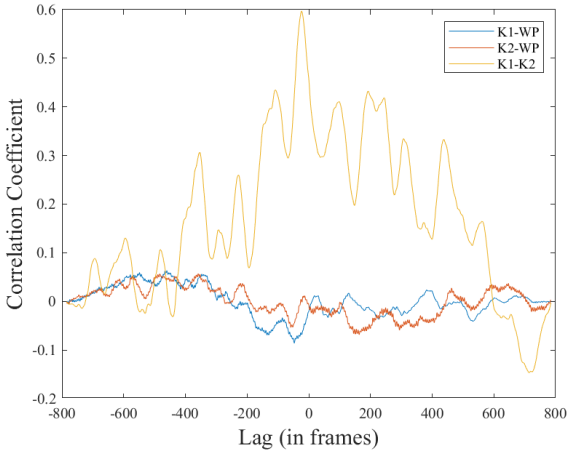

(a) 49mm depth flow condition

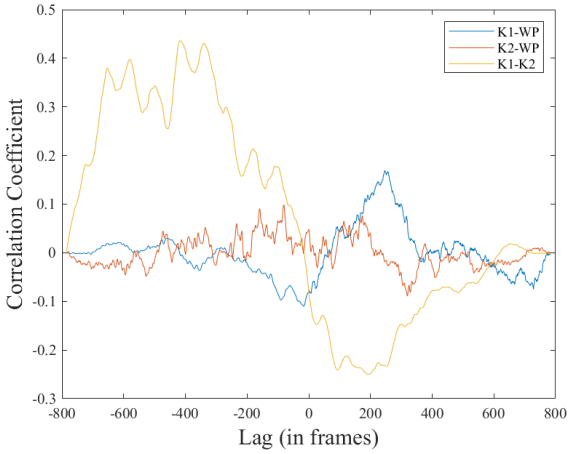

(b) 69mm depth flow condition

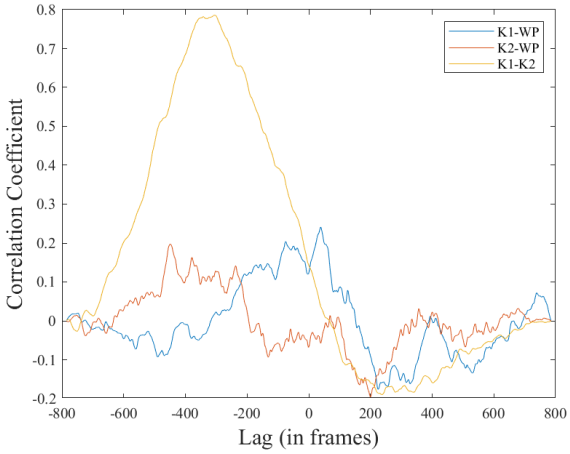

(c) 89mm depth flow condition

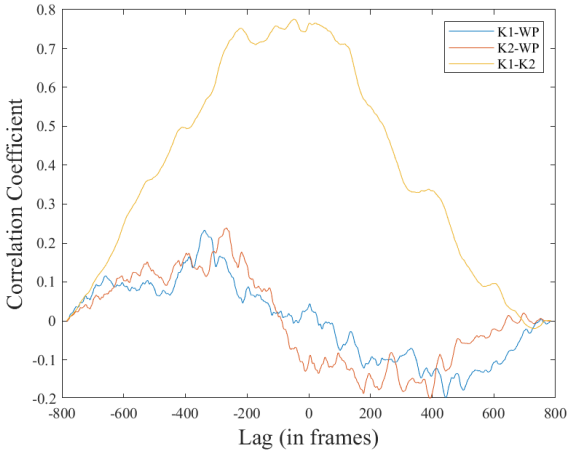

(d) 109mm depth flow condition

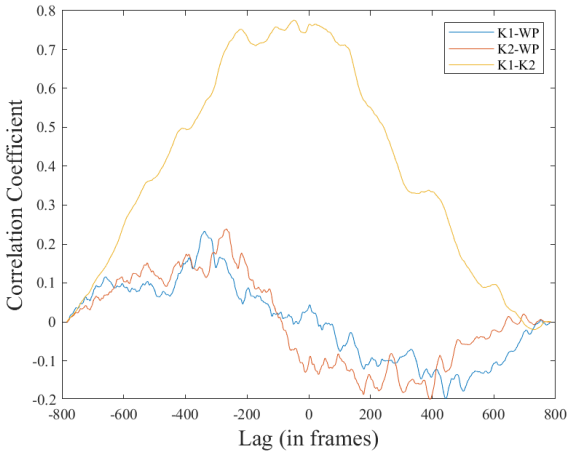

(e) 129mm depth flow condition

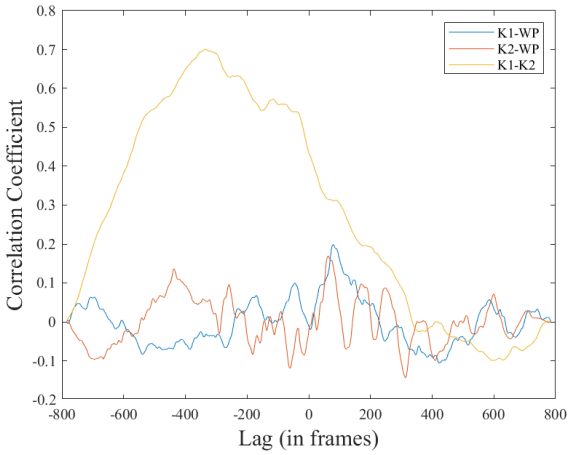

(f) 149mm depth flow condition

Figure 8.8: Cross correlation comparison with Kinect infrared and conductance wave probe sensors. K1 is Kinect version 1, K2 is Kinect version 2 and WP is conductance wave probe. A high correlation is observed between the two generations of Kinect sensors despite their differences in sensing technology. A lag of around 200 frames (6.6 seconds) appears consistently across all the flow conditions suggesting that the synchronous trigger did not result in measurements that were made entirely concurrently.

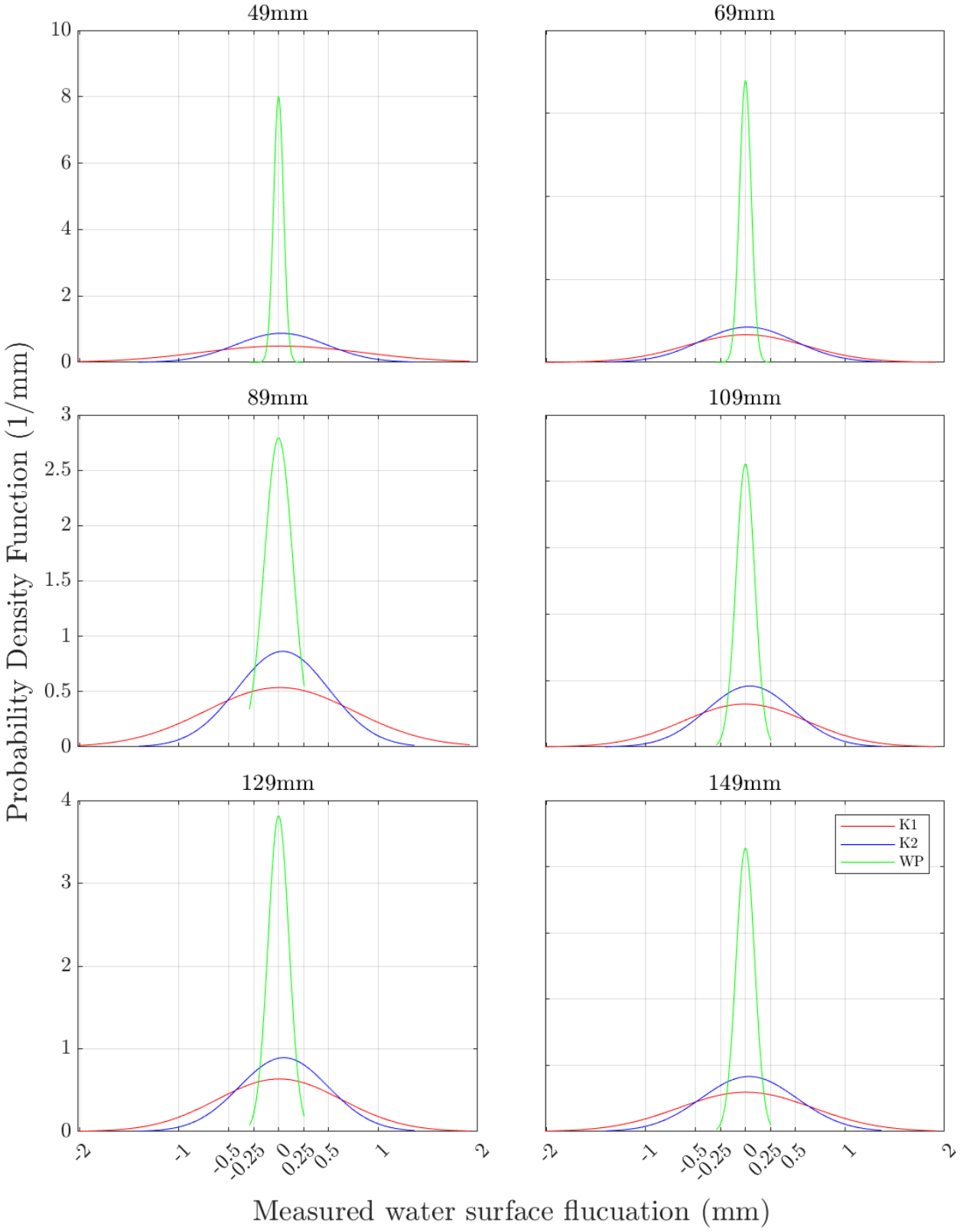

Figure 8.9: Comparison of free-surface fluctuation through a probability density function. K1 is Kinect version 1, K2 is Kinect version 2 and WP is conductance wave probe. The wave probe data detects free-surface fluctuations that are half the size compared to the Kinect sensors. The Kinect version 1 sensor also detects free-surface fluctuations with more amplitude than the Kinect version 2 sensor.

where z is the real distance between the camera and the calibration object, r is the raw sensor output and a, b, c, and d are variables to be estimated. This study used a linear first order polynomial between the bed and the flow. Given that the distance, D between the camera and the bed was fixed at 1.5m, the distance z between the camera and the free-surface is given as:

$$z = D - d \tag{8.1.2}$$

Making the equivalent formula using Combes et al. (2011) notation:

$$z = D - (er + f), \tag{8.1.3}$$

where e and f are the first order polynomial constants. Whilst the difference is notable, the range of Kinect measurements taken in this study varied from 49mm to 249mm, a range of 200mm. This is in contrast to the range tested by Combes et al. (2011). In their study, the distance varied from 700mm to 1900mm, a range of 1200mm (sub-figure A in Figure 8.10). The range measured in this study is only 16.6% compared to their study, taking 16.6% of from any part of their tangential function would result in an almost linear relationship. Furthermore, in Figure 8.10 sub figure C) from Combes et al. (2011) states that the Kinect sensor was 745mm away from the waves, much closer than the present study, this may explain the improvement in vertical resolution. In this present study, the Kinect sensors were placed further away in accordance to the advice from the suppliers (Microsoft) who indicated a minimum of 1.4m. This is likely due to the limited field of view at close distances making it unsuitable for the Kinect's original intended purpose (sensing people in a room). The clear trend from Combes et al. (2011) shows that the sensitivity of the sensor decreases with distance which explains why the present study was unable to reach the same depth resolution when detecting free-surface fluctuation. This is also backed up with studies from Zennaro et al. (2015) who found the accuracy decreased in a quadratic manner.

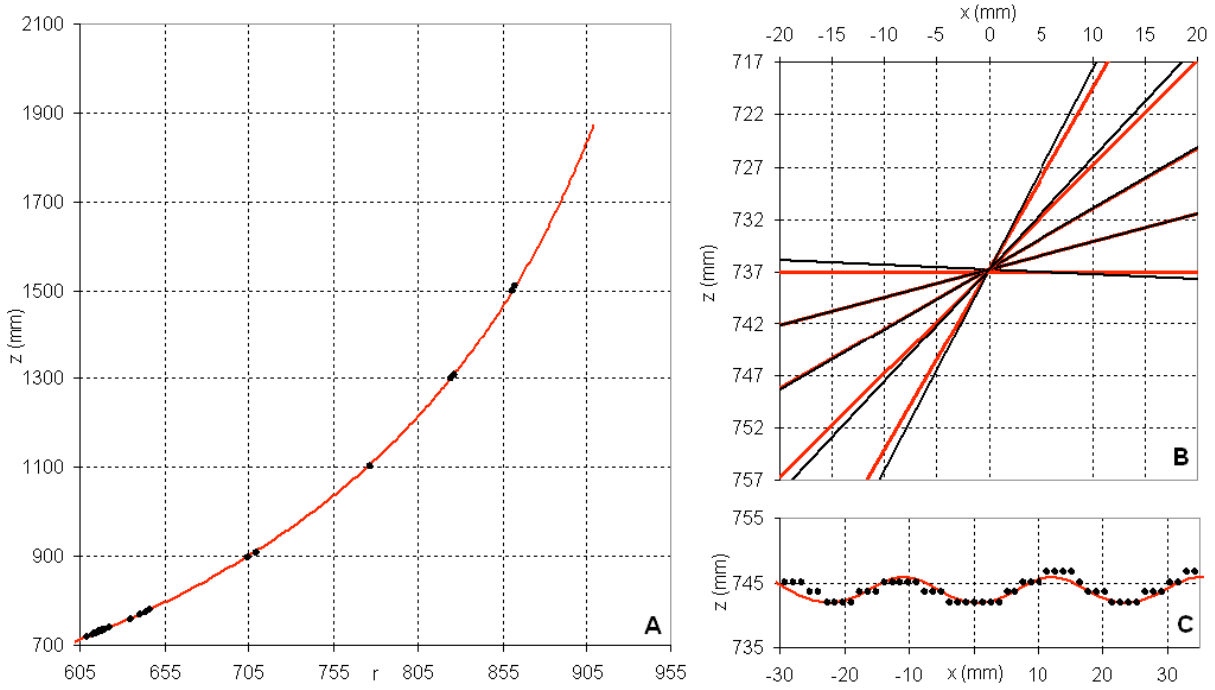

Figure 8.10: Kinect 1 results from Combes et al. (2011) 'A: true distance z as a function of the Kinect raw data. Black dots are the measured points and the red curve is the fitted tangent calibration law. B: estimation of slopes from 3 points, red lines indicate actual slopes and black ones indicate estimated slopes. C: estimation of a sinusoidal surface, the red curves indicate the actual sinusoid and the black dots indicate the z estimated from Kinect data.'

8.2 Flow analysis

8.2.1 Visualisation of Turbulent Structures Within the Flow

8.2.1.1 U-level

To visualise structures within the flow, U-level analysis can be used (Krogstad et al., 1992; Luchik and Tiederman, 1987; Nichols, 2015). When the streamwise velocity fluctuation magnitude exceeds the velocity standard deviation by a certain margin ('activation threshold', an event is deemed to have been triggered (event = 1). This event continues until the fluctuation drops below a 'deactviation' threshold (event = 0).

An event is deemed to be occurring if the instantaneous streamwise fluctuation rises above 30% of the standard deviation. An event in progress is deemed to have stopped if it falls below 25% of the standard deviation (Nichols, 2015).

At each spatial location in the PIV vector field, the variation of the streamwise fluctuation over time can be extracted and assessed for 'events' crossing the threshold. At each timestep, the PIV vector field can be translated into an 'event field' where the cells with an event occurring (events = 1) are marked to show the size and shape of potential coherent structures. A snapshot of the U-level flow sequence can be seen in Figure 8.11.

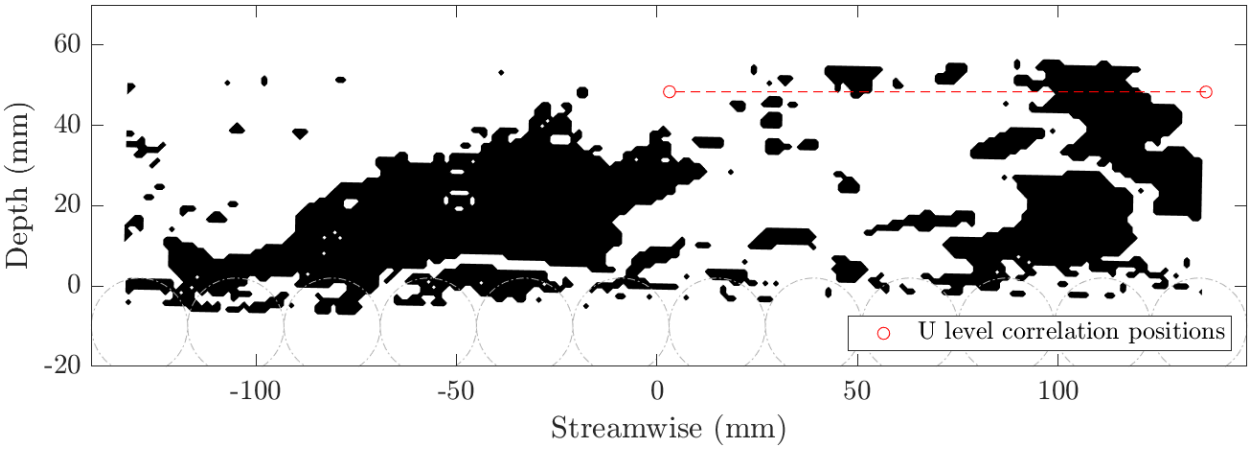

Figure 8.11: Snapshot of U-level event field at 53.99 seconds (49mm depth flow condition). The dark patches represent identified U-level events believed to be coherent structures in the 2D plane at the centerline of the flume. The red circles mark the spatial location where the signal is extracted for further correlation analysis (see Figure 8.13 and 8.14).

It can be observed from Figure 8.11 that large structures exist throughout the flow up to the free-surface. By repeating this analysis for each snapshot, a video of the structures moving through the flow over time was created. For U-level analysis on other flow depth conditions, videos of the U-level flow animation can be found here: www.youtube.com/playlist?list=PLBxWPtPkf1M_xS8FwEPETqtEwUqMgSVla. For printed copies, readers can use the QR code in Figure 8.12.

Figure 8.12: QR code to access video of the flow with turbulent structures identified using U-level.

From the video, the structures move in the same direction as the flow. By calculating the correlation between the coordinates at the upstream and downstream end of a large feature, the speed of the coherent structure can be calculated. This assumes minimal deformation in the coherent structure as it moves across the two reference points. The calculation is achieved by isolating the event data at two points at a known distance apart (see Figure 8.11) and extracting their event 'on/off' signal (Figure 8.13) and carrying out correlation analysis.

The velocity calculated are shown in Figure 8.14. A comparison their advection speed can be made to the near free-surface streamwise PIV velocity profiles from Figure 7.13. Table 8.1), shows the results of this comparison. With the exception of the lowest flow depth and

the unreliable flow condition at 149mm, it is clear that the coherent structures near the free-surface appear to travel within 1% of the bulk velocity. However, the coherent structure identification with the U-level approach is hindered somewhat by the large areas that are identified; it is not possible to separate smaller eddies from larger truly coherent structures. For this, a Proper Orthogonal Decomposition (POD) technique is utilised.

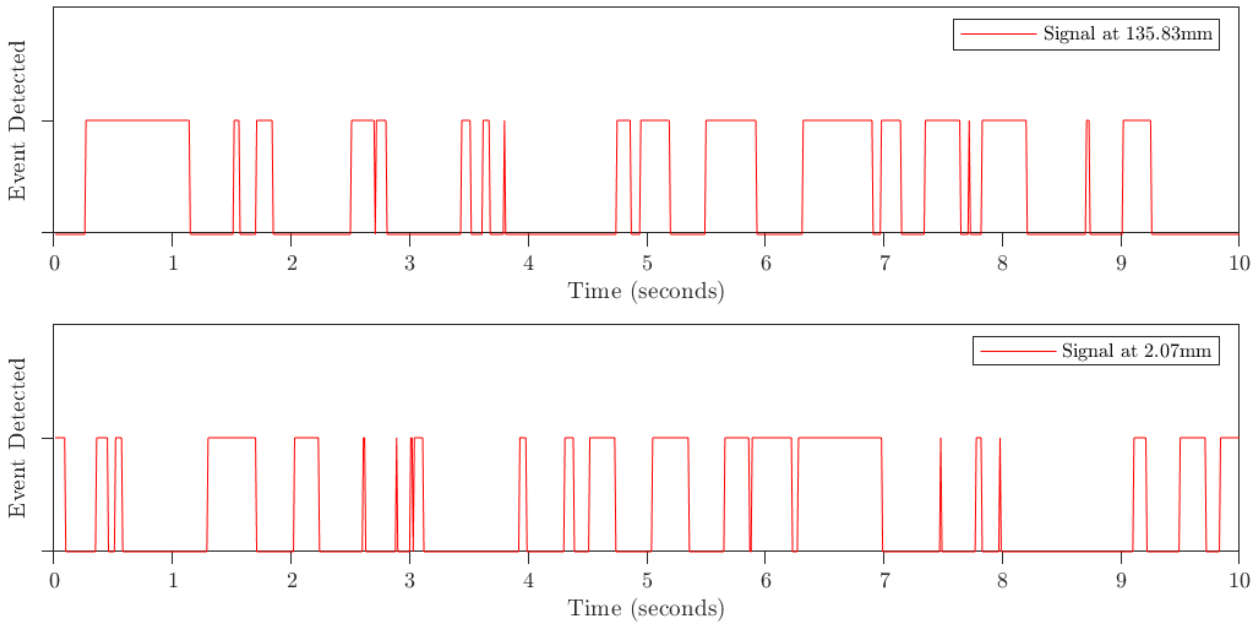

Figure 8.13: Extracted U-level event signals from the 49mm depth flow condition. An event is deemed to be occurring if the instantaneous streamwise fluctuation rises above 30% of the standard deviation. An event in progress is deemed to have stopped if it falls below 25% of the standard deviation Luchik and Tiederman, 1987.

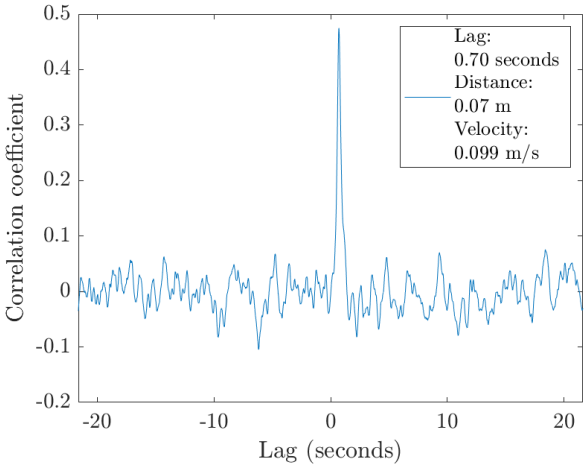

(a) 49mm depth flow condition

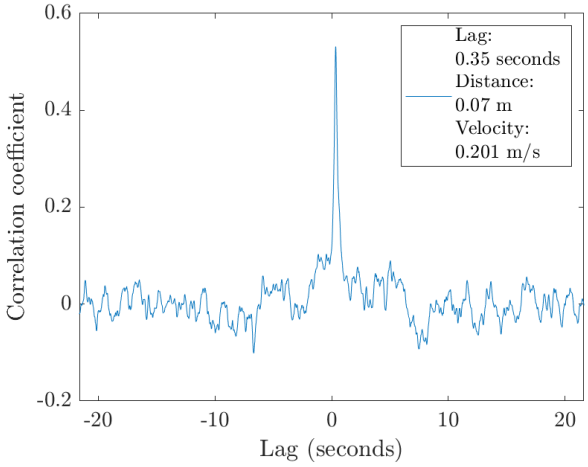

(b) 69mm depth flow condition

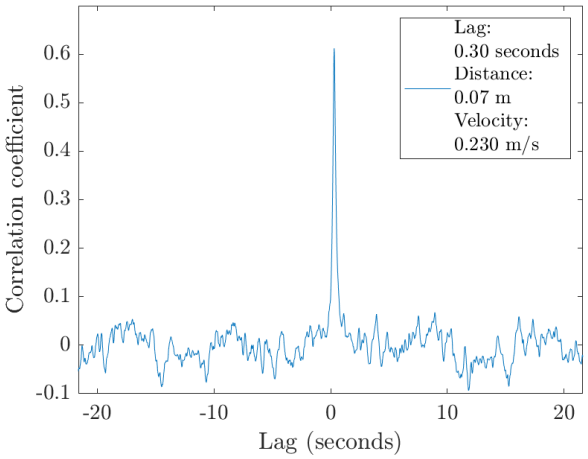

(c) 89mm depth flow condition

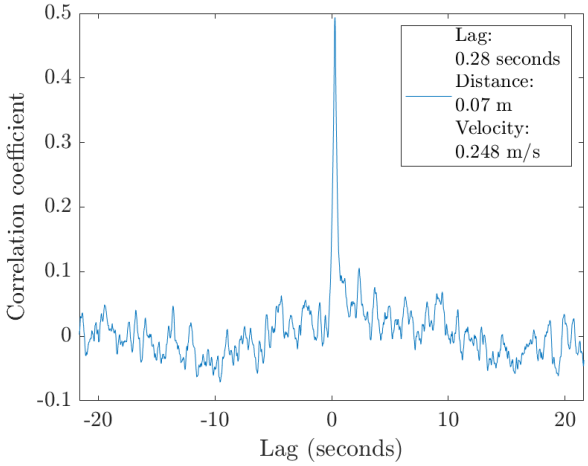

(d) 109mm depth flow condition

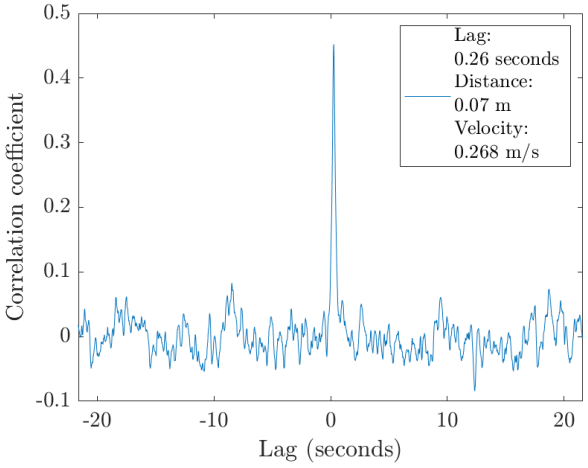

(e) 129mm depth flow condition

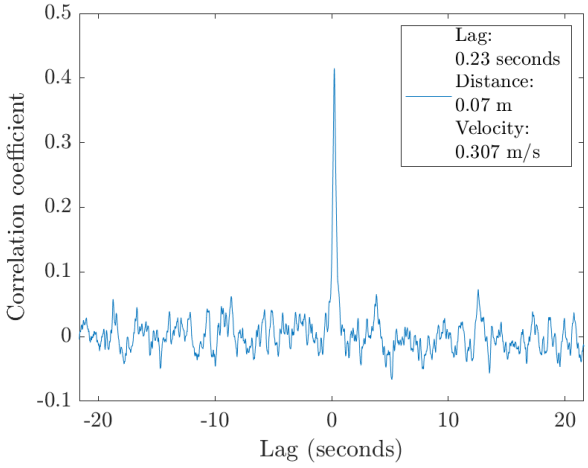

(f) 149mm depth flow condition

Figure 8.14: Cross correlation of two U-level event signals sampled at x = 74.13mm and 4.62mm from the centerline (of the PIV image).

Table 8.1: Comparison of U-level structure speed and PIV free-surface velocity. Besides the lowest depth and the 149mm flow condition that is known to be faulty, all other flow conditions show a match to within ± 1%.

Depth (mm)	U-level turbulent structure speed (m/s)	PIV near free-surface velocity (m/s)	% Difference
49	0.0999	0.102	2.1%
69	0.201	0.201	0.0%
89	0.23	0.231	0.4%
109	0.248	0.249	0.4%
129	0.268	0.266	0.8%
149	0.307	0.297	3.4%

8.2.2 Proper Orthogonal Decomposition (POD)

Since a large range of turbulence scales exists within the flow, the large scales often obscure the detection of smaller turbulent structures. Proper Orthogonal Decomposition (also known as Singular Value Decomposition) was deployed to identify different elements of the flow and remove the parts with the lowest energy (Berkooz et al., 1993; Sirovich, 1987). POD (or SVD) filters/decomposes input data into "modes" which contain different energies. The original signal is 100% energy so the sum total of all modes should add up to 100%.

The velocity field U, V, and W are decomposed separately using the snapshot method. For each direction (U, V, W), the flow field data is re-arranged from a (X, Y, Z, T) matrix into a 2D matrix with each column representing a single timestep containing all the velocity information. A total of 15,000 timesteps were used. POD is then applied to this transformed PIV dataset to obtain the basis functions.

Using the PIV data from the 49mm flow depth condition, Figure 8.15 shows the distribution of energy within each POD mode. It can be observed that the majority of the energy is captured within the first 10 modes and contributions beyond the first 50 modes represent minor effects. This is similar to other studies which deployed snapshot POD on smooth and rough channel flows (Sen et al., 2007).

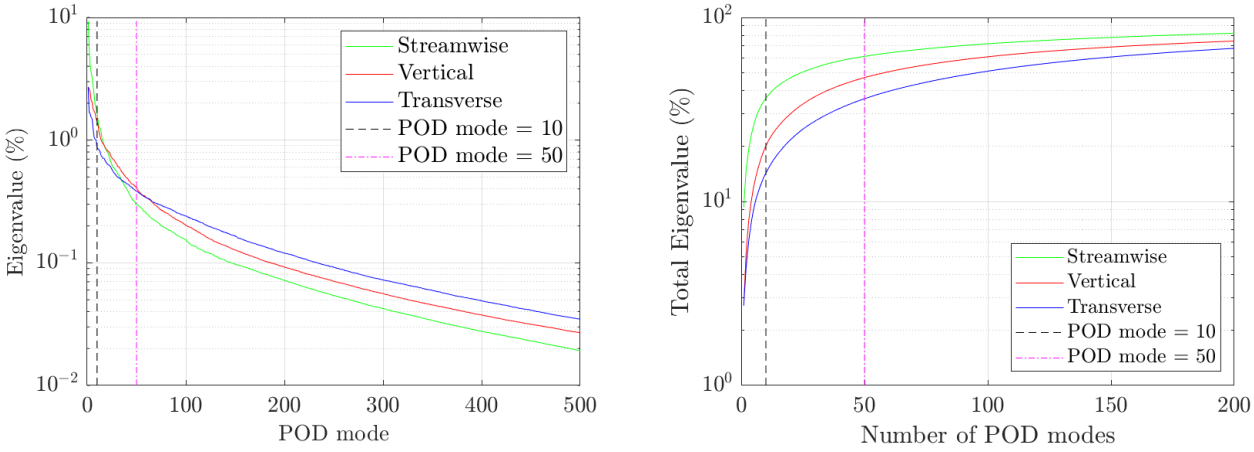

Figure 8.15: Percentage of energy captured decomposed over different modes using POD for the 49mm depth experimental flow condition in each direction. As the POD mode number increases, the energy contained in each mode decreases.

Mode 1 contains the most energy whilst mode 4 contains about half the energy. Figure 8.17

to 8.19 shows the Eigenfunctions for mode 1 to mode 10 in each direction. It is clear that mode 1 captures large structures that dominate the full depth of the flow whilst the other modes contain coherent structures of smaller and smaller size.

In the vertical direction (Figure 8.18), more distinct patterns are visible. Increasing modes show more regions of high and low intensity.

In the transverse direction (Figure 8.19), although some patches are still present, they are much more universal and surprisingly similar to the U-level identified structures. This is logical since the flow condition is shallow with no expectations of persistent transverse re-circulation zones. Higher POD modes do not seem to yield notable changes in the size or shapes of the features. However, it should be noted that the POD analysis using the transverse direction has more limitations compared with the other directions. This is because the PIV camera itself is pointed in the transverse direction so only very limited transverse velocity is detected (through the stereo vision and two level calibration plate). This is one reason why 3D CFD simulation is an important tool.

Figure 8.20 to 8.21 show the eigenfunction for the 129mm flow depth condition. In the vertical direction, Comparing the 129mm flow condition in Figure 8.21 to the 49mm flow condition in Figure 8.18, the periodic intensity is again evident.

To reconstruct the velocity field from a particular POD mode, the relevant POD modes are selected and the transformation reversed from the 2D matrix back onto (X, Y, Z, T) form. Based on the POD energy distribution shown in Figure 8.15, the velocity field for the 49mm flow depth condition was reconstructed using modes 1 to 10 (to capture large energetic structures) and 11 to 50 (to capture smaller remaining eddies).

Figure 8.22 shows an instantaneous snapshot of the velocity field recreated using POD modes 1 to 10 and 11 to 50. Arrows represent the filtered streamwise and bed-normal contributions whilst the contours are coloured based on the magnitude of the vectors. In the upper plot at the bed, the vector arrows clearly indicate the flow moving over the spheres. On the fourth sphere from the left, an in-sweep event is occurring possibly triggered by the ejection event

occurring on the fifth sphere. Above these events are smaller structures which are pushed up towards the free-surface. At the right hand side is a turbulent structure spanning almost the full depth of the flow. These are similar to the bursting events described by Komori et al. (1989) and Adrian et al. (2000).

Figure 8.22 lower shows the same time step but the velocity fluctuations are reconstructed using only POD modes 11 to 50. This removes a lot of the large energy structures. It can be observed that the remaining structures are much smaller and also reveals a structure interacting with the surface on the left hand side.

Figure 8.23 to Figure 8.25 show the reconstructed velocity fields for the 69mm, 89mm, 109mm, 129mm and 149mm flow depth conditions. These are again split using POD modes 1 to 10 and POD modes 11 to 50. As with the other flow depths, the coherent structures identified with POD modes 11 to 50 are much smaller than POD modes 1 to 10. To investigate the overall turbulent movement and behaviour of these structures, a more generalised approach with more statistical robustness is needed. Thus, the flow data at three different depth locations are extracted for further analysis. These locations are selected to be near the free-surface, within the flow and near the bed. The locations can be seen in Figures 8.22 to 8.25 marked with a red cross.

Animated versions of the flows shown in Figures 8.22 to 8.25 can be found as videos here: www.youtube.com/playlist?list=PLBxWPtPkf1M_tPaJw0owYpgw9tXewveCT. Readers can also use Figure 8.16's QR code.

Figure 8.16: QR code for video of the turbulent flows structures found with POD.

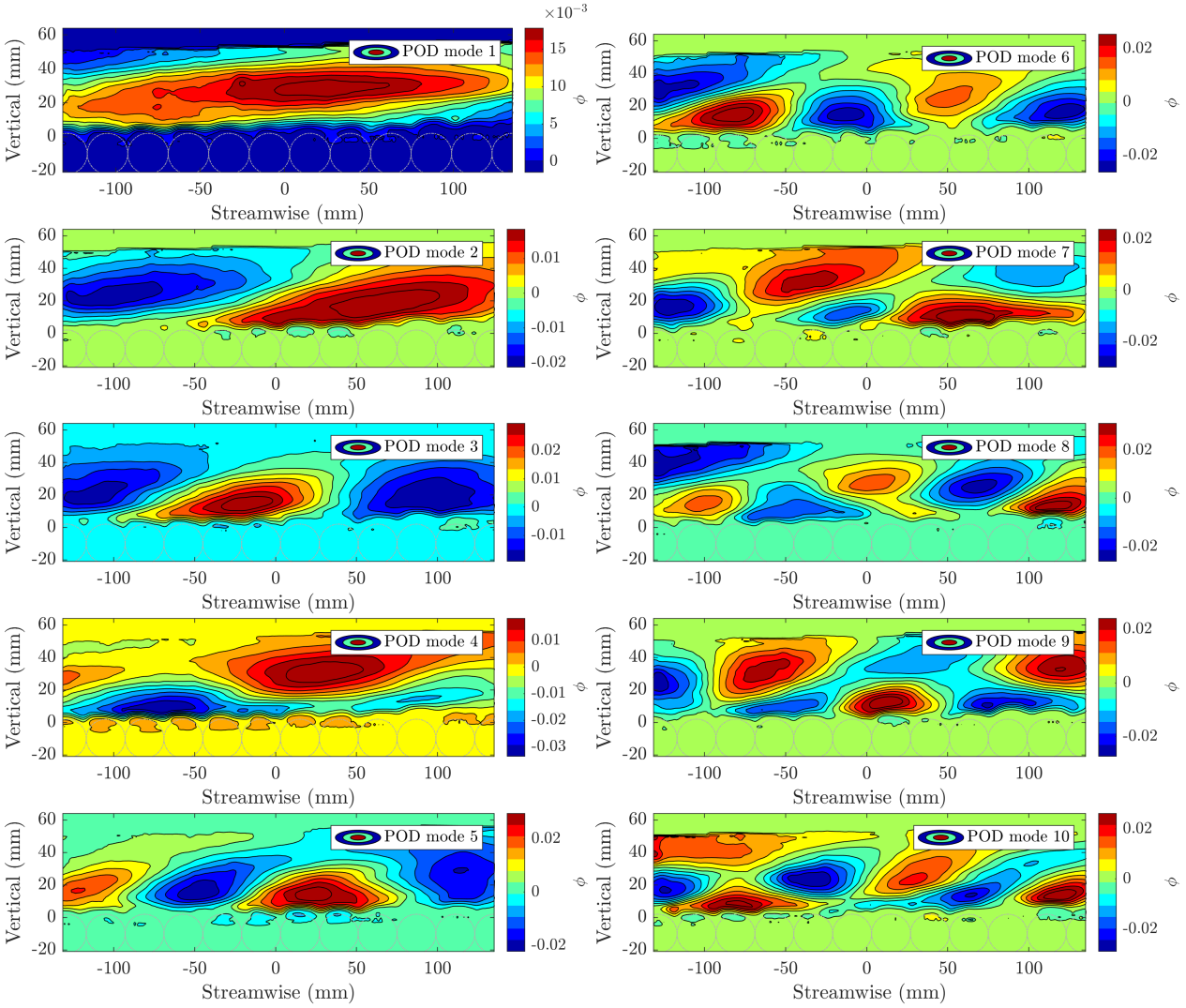

Figure 8.17: Contour map of the Eigenfunction, ϕ from POD of the 49mm flow condition using streamwise velocity fluctuation (U'). It can be seen that the first mode contains large scale features whilst the subsequent modes contain smaller and smaller features.

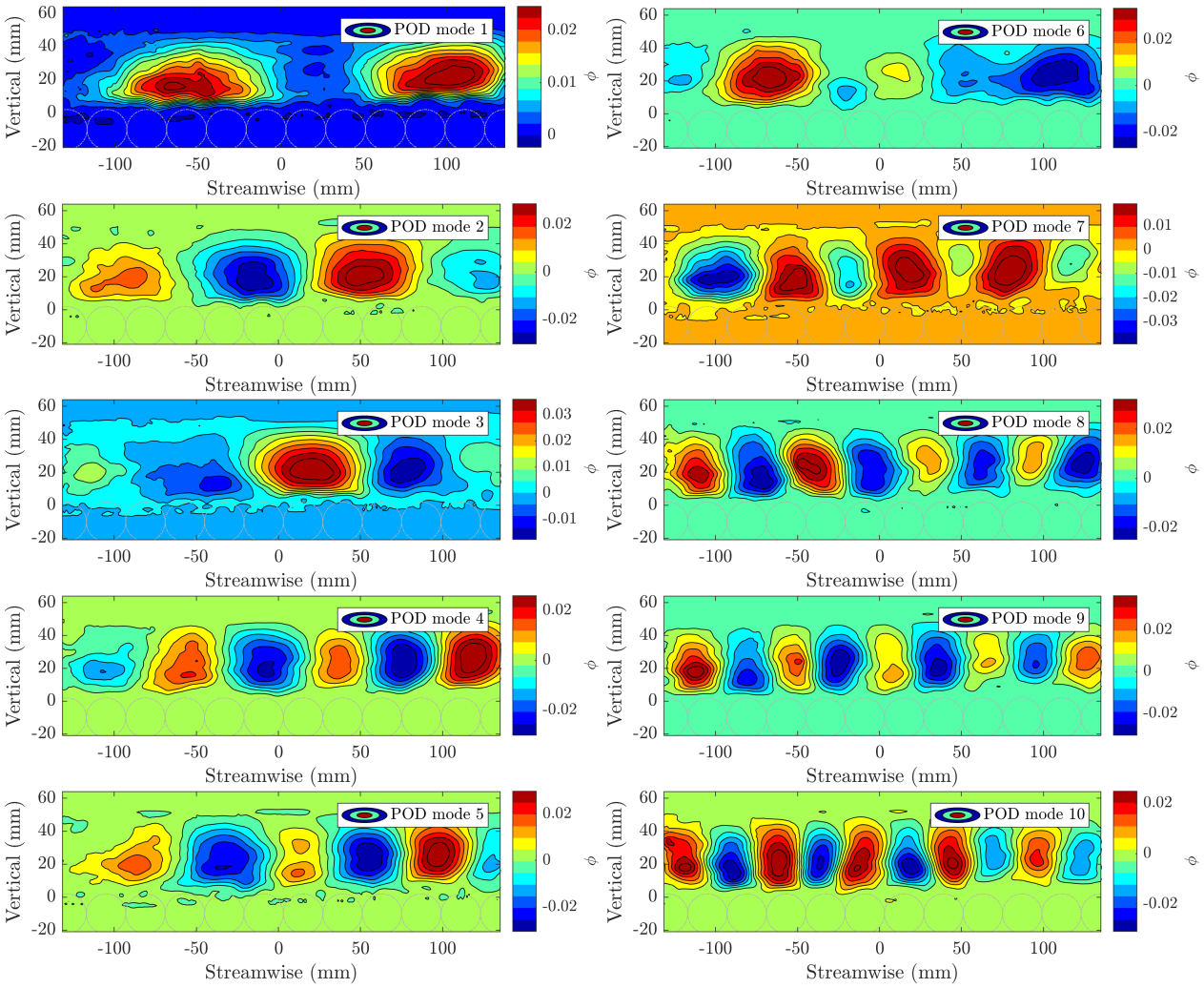

Figure 8.18: Contour map of the Eigenfunction, ϕ from POD of the 49mm flow condition using vertical velocity fluctuation (V'). Repeated patterns of high and low intensity can be observed in all modes with the higher modes containing more oscillations.

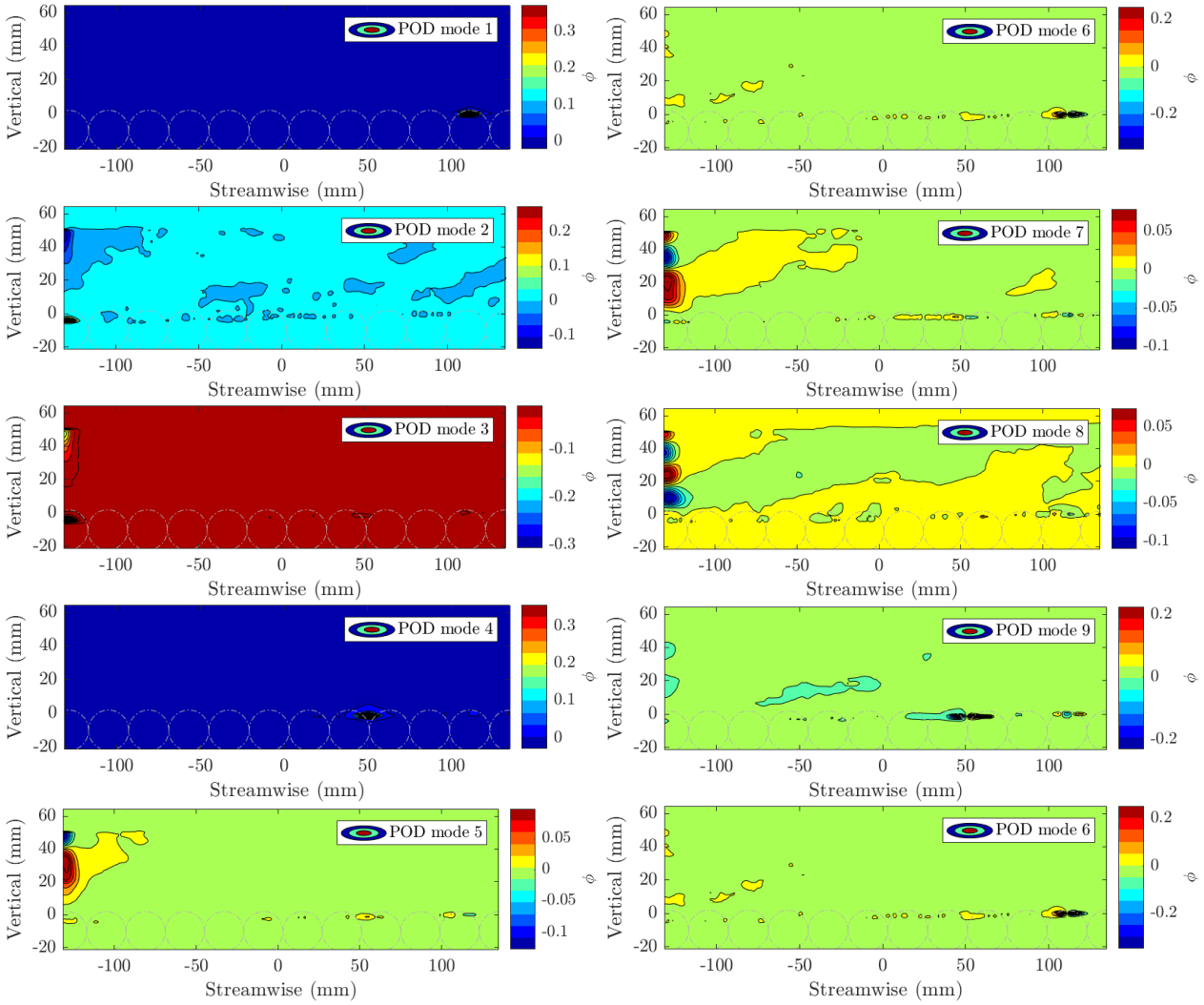

Figure 8.19: Contour map of the Eigenfunction, ϕ from POD of the 49mm flow condition using transverse velocity fluctuation (W'). Small areas distort the colourbar scale resulting in most of the contour map being in the orange to red region.

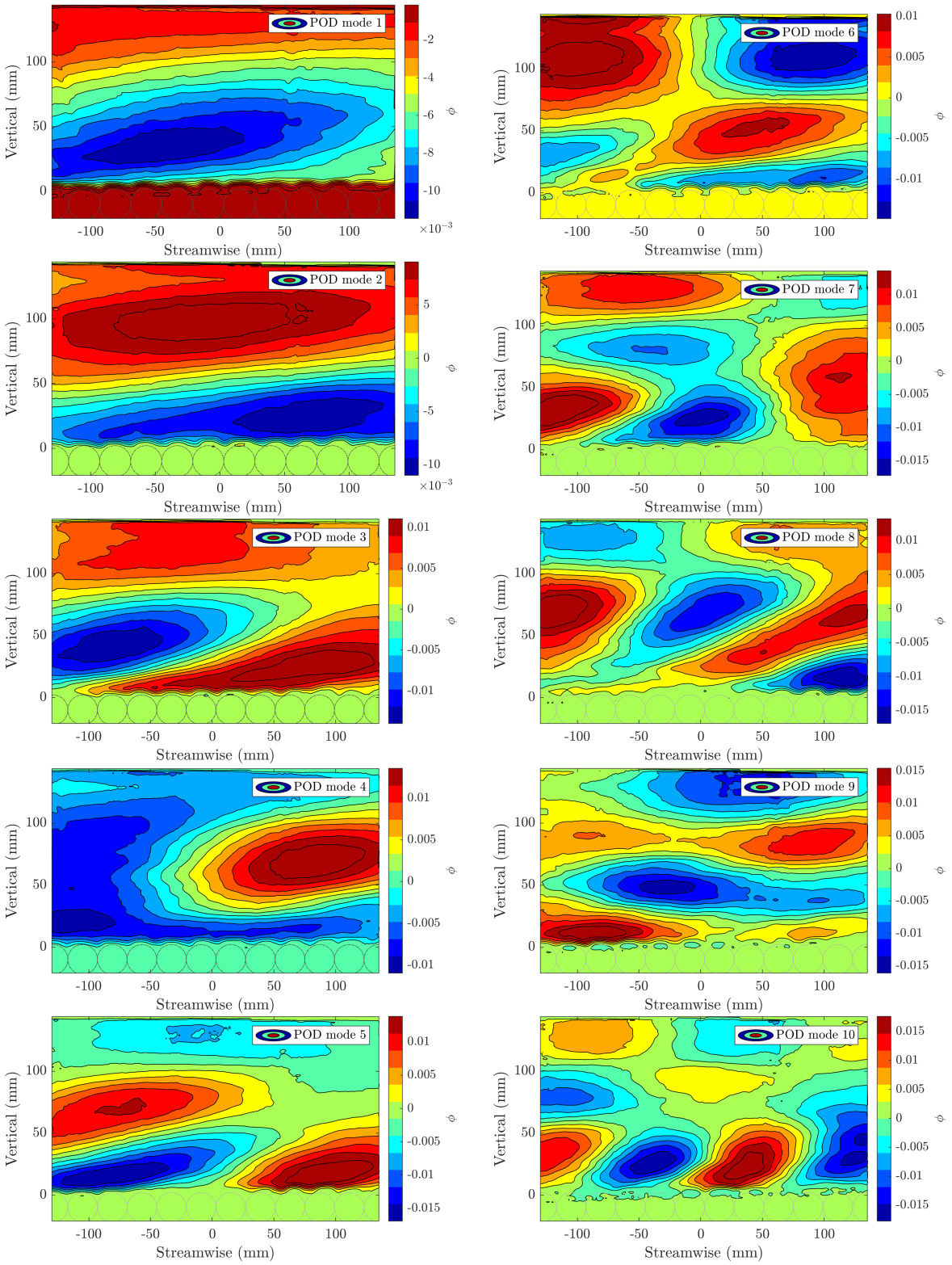

Figure 8.20: Contour map of the Eigenfunction, ϕ from POD of the 129mm flow condition using streamwise velocity fluctuation (U'). It can be seen that the first mode contains large scale features whilst the subsequent modes contain smaller and smaller features.

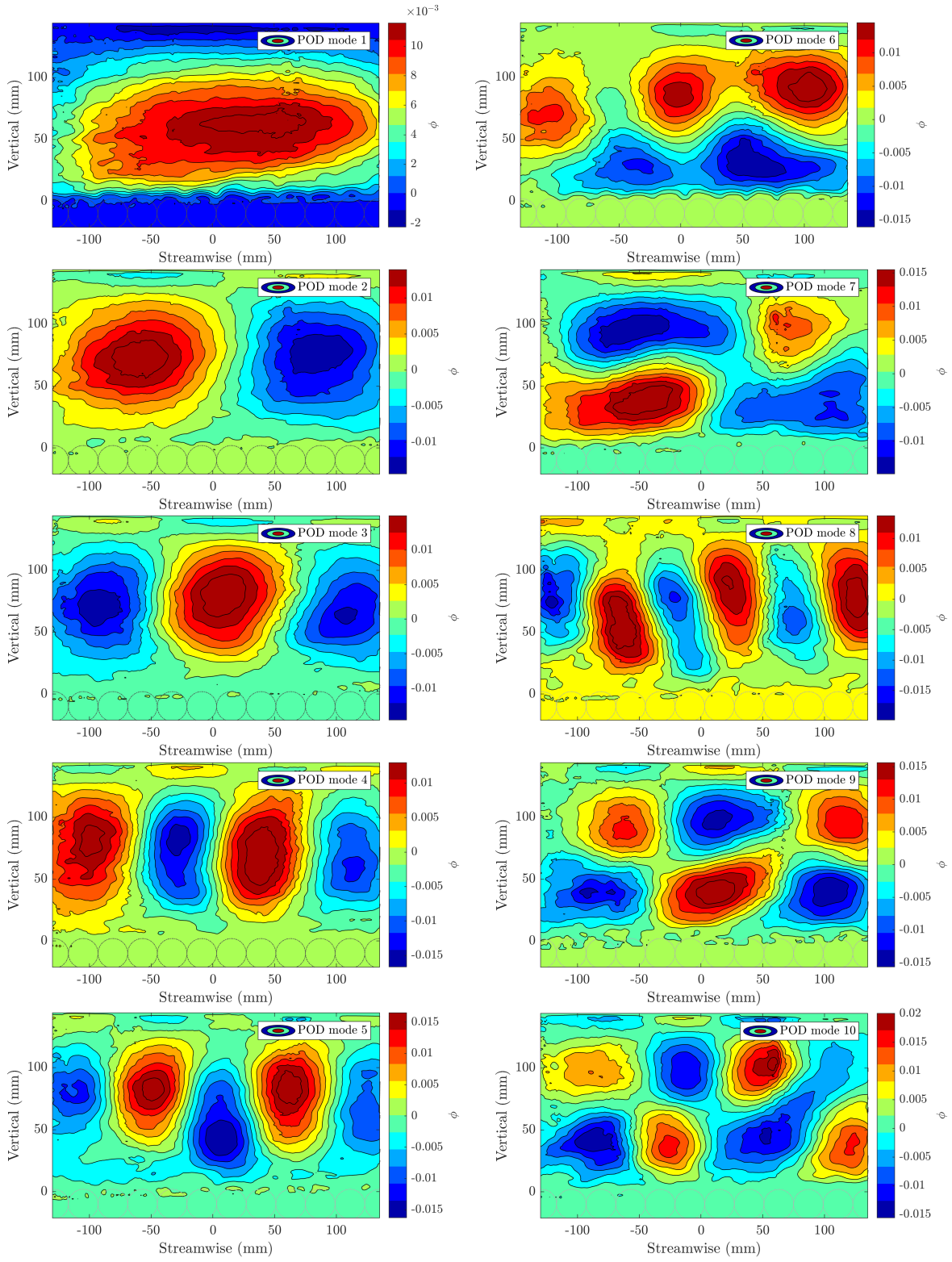

Figure 8.21: Contour map of the Eigenfunction, ϕ from POD of the 129mm flow condition using vertical velocity fluctuation (V'). Repeated patterns of high and low intensity can be observed in all modes with the higher modes containing more oscillations.

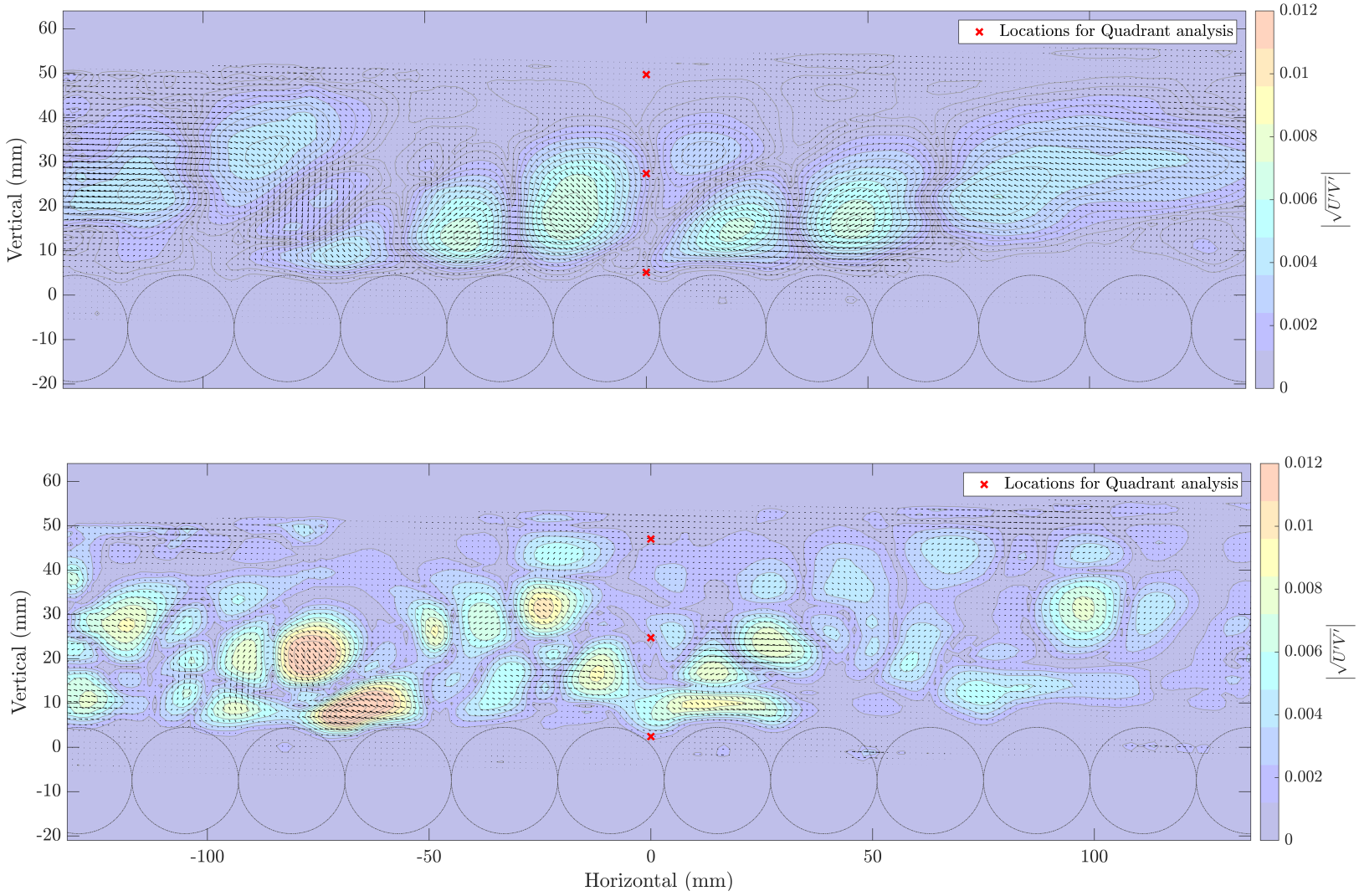

Figure 8.22: Contour map with vectors to indicate the instantaneous velocity fluctuation using the experimental PIV data at 108 seconds. The velocity data from the 49mm depth experimental flow condition was reconstructed using the POD modes 1 to 10 (upper) and 11 to 50 (lower). The colourbar represents $\sqrt{|U'V'|}$. Red crosses represent locations for Quadrant analysis. Some smaller, delicate interactions between the flow and the free-surface can be distinguished.

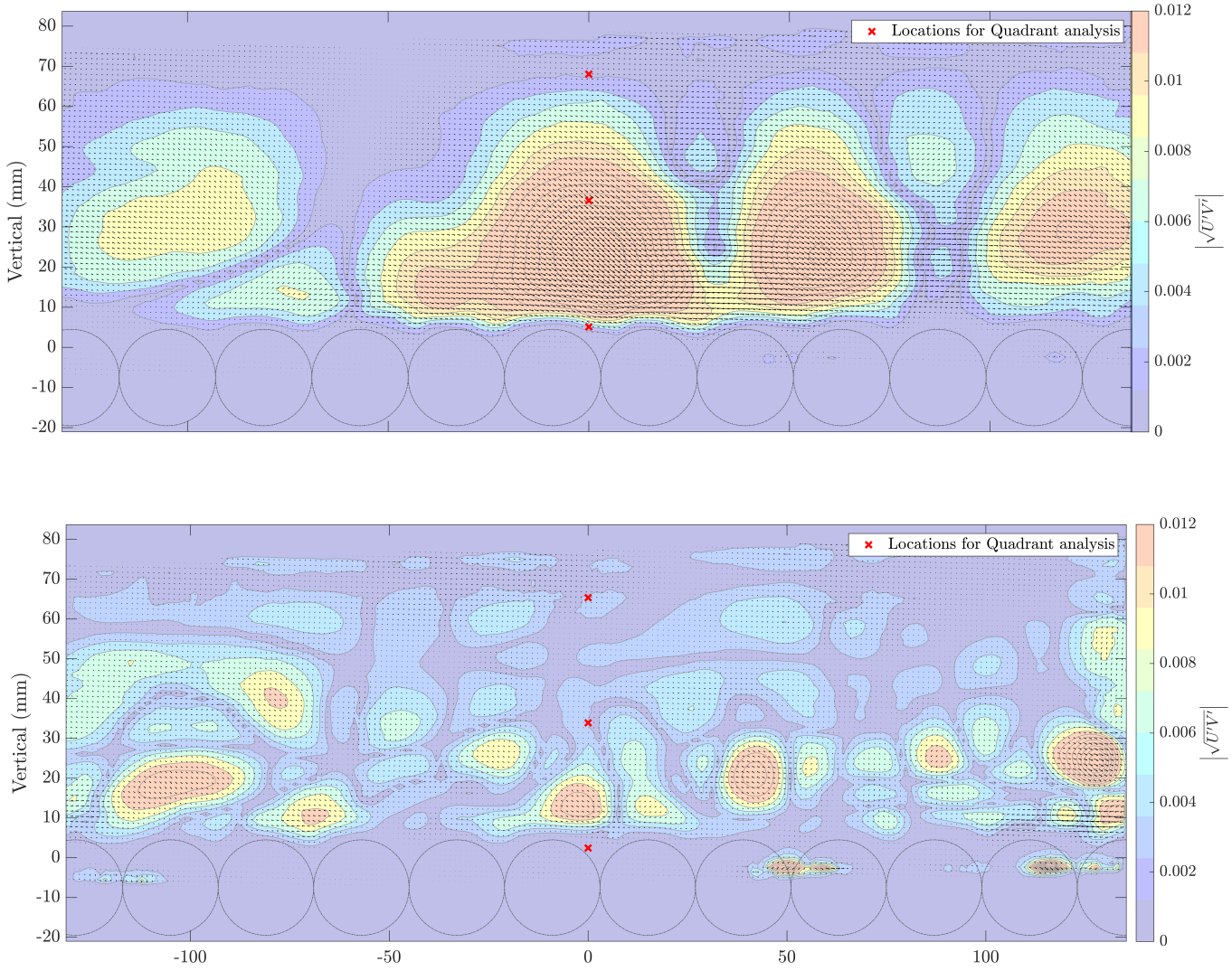

Figure 8.23: Contour map with vectors to indicate the instantaneous velocity fluctuation using the experimental PIV data at 108 seconds. The velocity data from the 69mm depth experimental flow condition was reconstructed using the POD modes 1 to 10 (upper) and 11 to 50 (lower). The colourbar represents $\sqrt{|U'V'|}$. Red crosses represent locations for Quadrant analysis. Some smaller, delicate interactions between the flow and the free-surface can be distinguished.

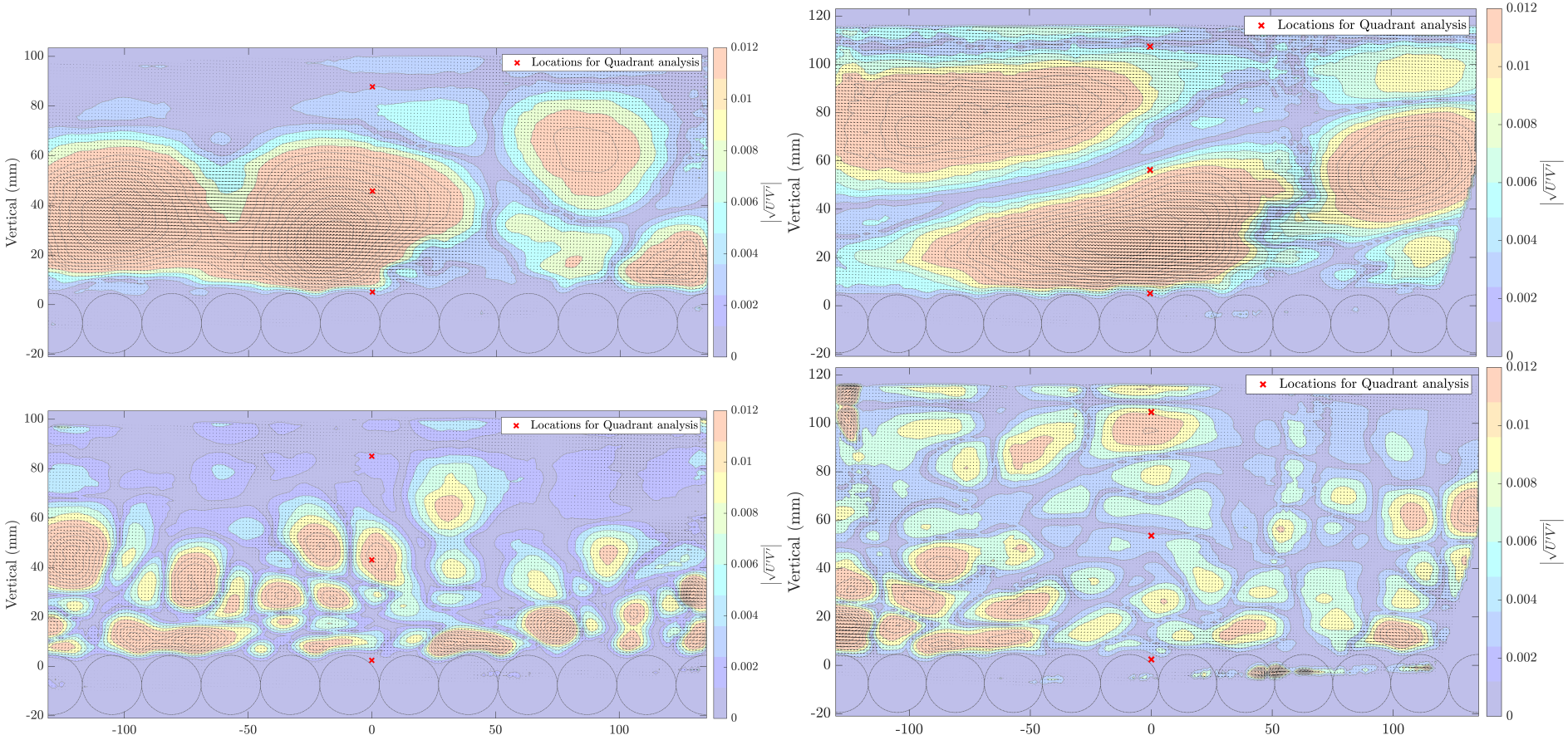

Figure 8.24: Contour map with vectors to indicate the instantaneous velocity fluctuation using the experimental PIV data at 108 seconds. The velocity data from the 89mm (left) and 109mm (right) depth experimental flow condition was reconstructed using the POD modes 1 to 10 (upper) and 11 to 50 (lower). The colourbar represents $\sqrt{|U'V'|}$. Red crosses represent locations for Quadrant analysis. Some smaller, delicate interactions between the flow and the free-surface can be distinguished.

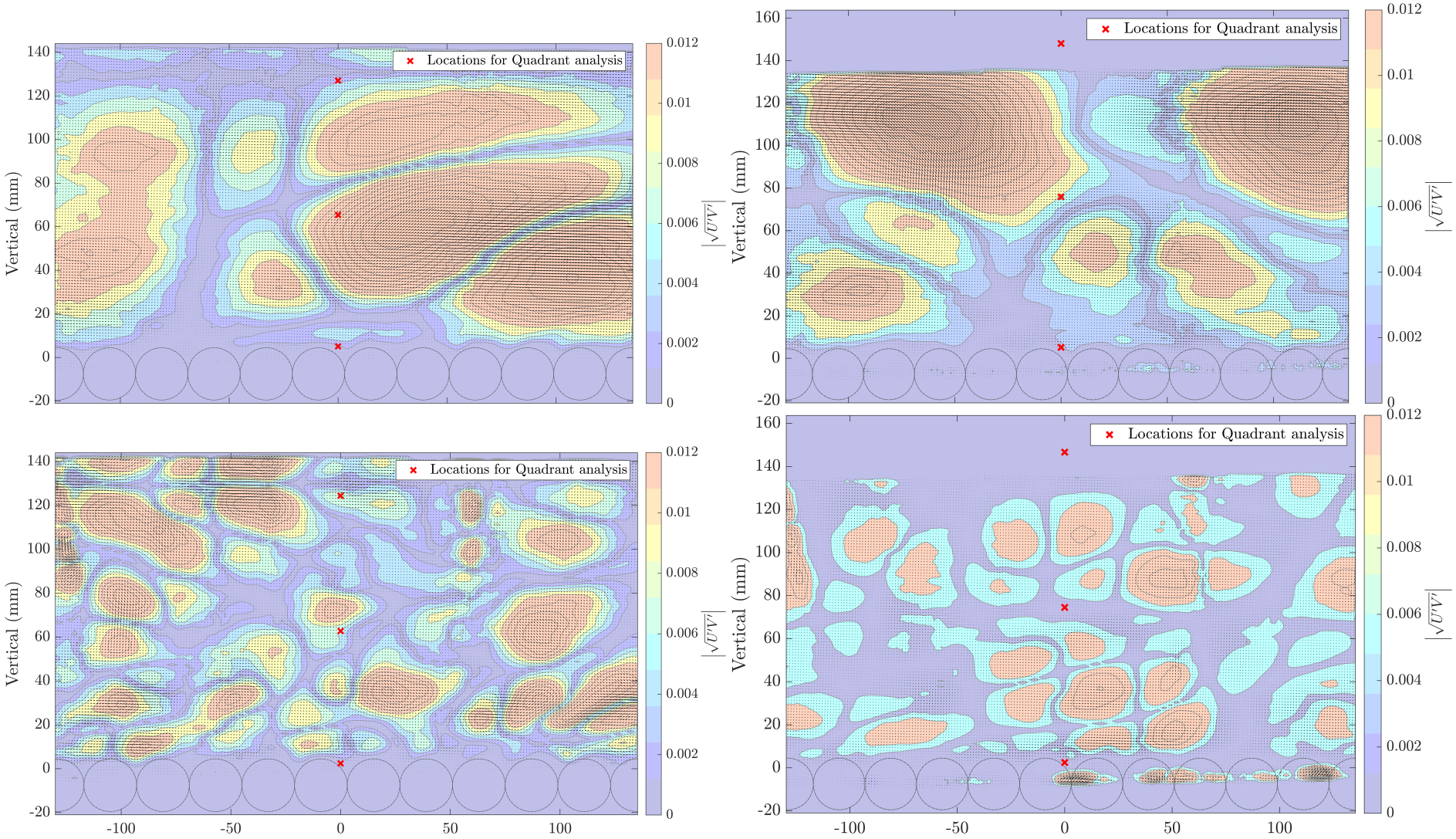

Figure 8.25: Contour map with vectors to indicate the instantaneous velocity fluctuation using the experimental PIV data at 108 seconds. The velocity data from the 129mm (left) and 149mm (right) depth experimental flow condition was reconstructed using the POD modes 1 to 10 (upper) and 11 to 50 (lower). The colourbar represents $\sqrt{|U'V'|}$. Red crosses represent locations for Quadrant analysis (see Section 8.2.3). Some smaller, delicate interactions between the flow and the free-surface can be distinguished by reconstructing with higher POD modes.

8.2.3 Quadrant Analysis

Quadrant analysis plots the velocity fluctuation over time in the streamwise direction against those the bed-normal direction (Grass, 1971; Wallace, 2016). As both streamwise and bed-normal velocity can be positive or negative, this leads to the creation of four 'Quadrants'. Each of these quadrants represents a particular type of physical behaviour in the flow (see Figure 8.26).

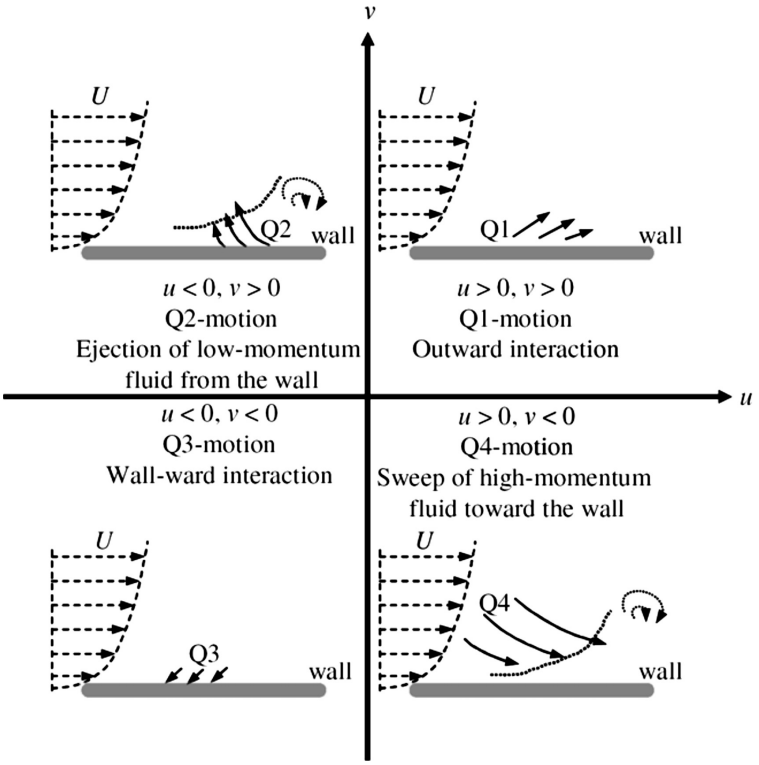

Figure 8.26: Illustration of Quadrant analysis used to study the behaviour of flows near features of interest. The streamwise velocity of a point is plotted on the x-axis whilst the vertical velocity is represented on the y-axis. Each quadrant corresponds to a different type of movement and represents different type of motion.

Figure 8.27 shows the quadrant analysis using velocity fluctuations reconstructed from the PIV POD modes 1 to 10. The exact locations are shown in Figure 8.22 to 8.25 by the red crosses. This reflects the energy contained in the large energetic structures. It can be seen that near the bed, the structures are mainly in Q2 and Q4. This supports previous research on the mechanism around ejection of structures from the bed towards the free-surface. As a result of the Q2 events, high momentum fluid must replace the fluid that has been ejected. This appears as Q4 events and were visually demonstrated in Figure 8.22 and 8.25.

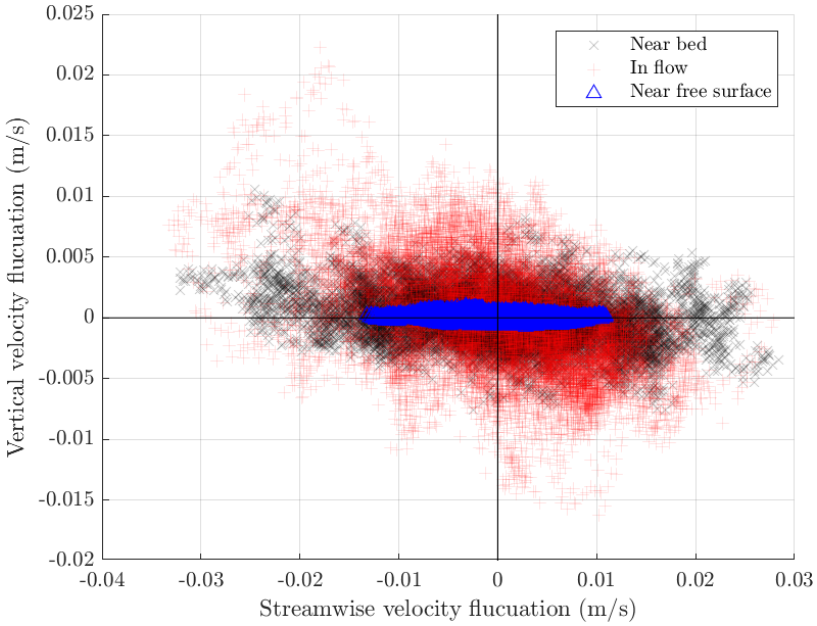

Figure 8.27: Quadrant analysis of the points marked on Figure 8.22 for the experimental 49mm flow condition using POD modes 1 to 10.

As the structures move away from the bed, the vertical fluctuations get larger before being reduced near the free-surface. This supports the theory that splat events occur as the vertical fluctuations reduce whilst the streamwise velocity fluctuation is high (Nagaosa and Handler, 2003).

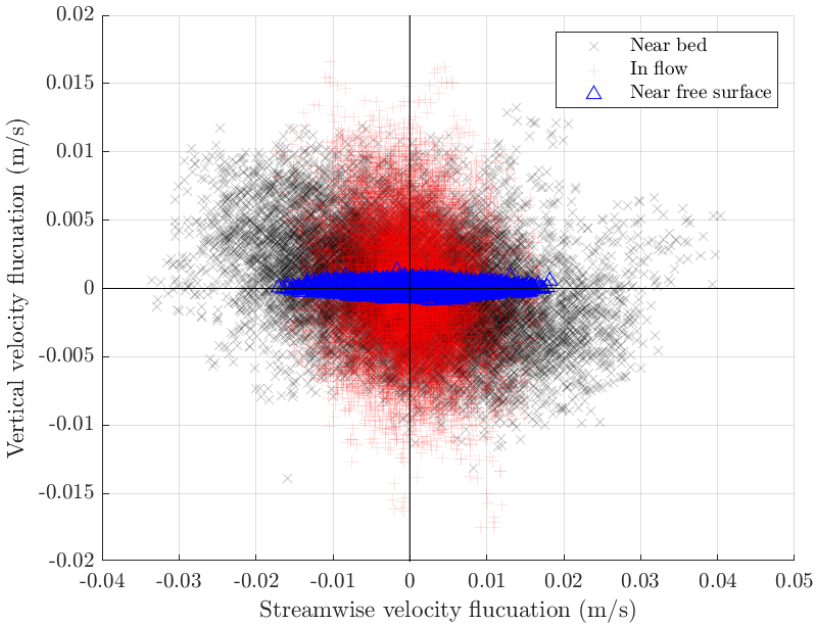

Figure 8.28: Quadrant analysis of the points marked on Figure 8.22 for the experimental 49mm flow condition using POD modes 11 to 50.

Figure 8.28 shows the quadrant analysis created using POD modes 11 to 50. It can be seen that near the bed, the Q2 and Q4 events are much less prevalent. There is also less variation as the structures move towards the free-surface. This would suggest that the smaller eddies reconstructed using the later POD modes are much more universal meaning they do not only simply exist at the bed, or in a special time or place. Instead, these eddies are present everywhere due to their size and minimal effect within the turbulence cascade. Near the free-surface, the vertical velocity fluctuation is once again attenuated in stark comparison to the streamwise fluctuation within the flow.

Looking at both figures 8.27 and 8.28 together, the flow appears the most turbulent at the bed (high u' and v'), followed by strong mixing in the flow (medium u' and v') whilst the free-surface is attenuated in both POD modes 1 to 10 and 11 to 50.

The quadrant analysis has shown that the presence of a rigid lid would suggest an incorrect distribution of the vertical energy as the structures hit the free-surface. With a rigid lid, the vertical velocity becomes zero whilst in real free-surfaces, a small fluctuation ($\pm$ 0.002 m/s) still exists which causes small deformations of the free-surface.

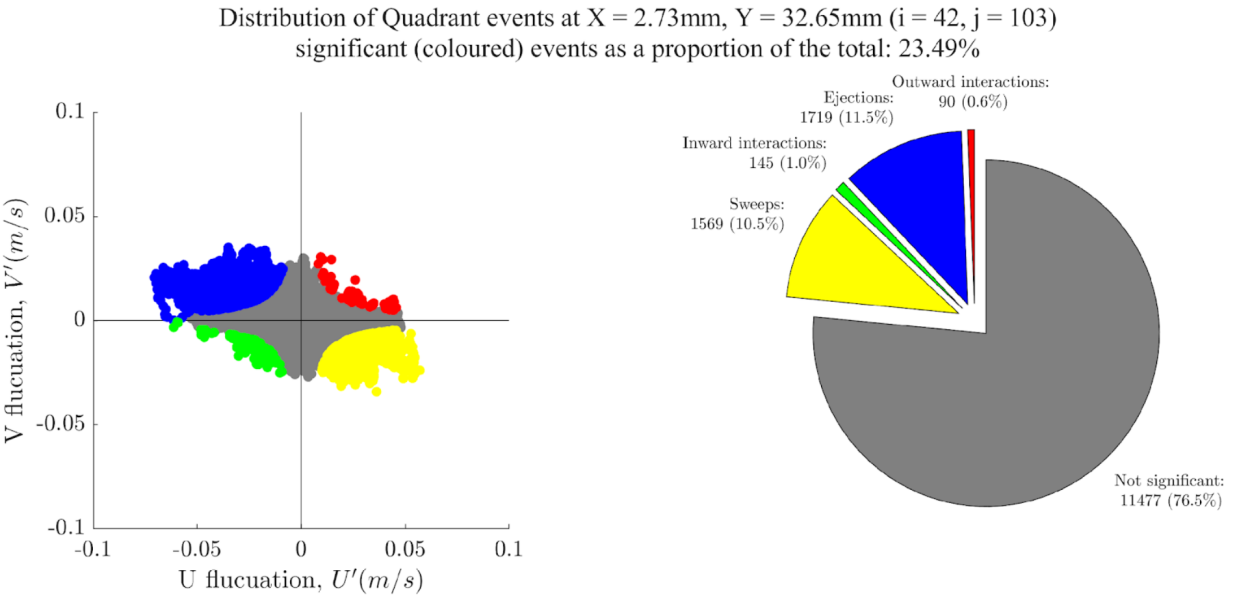

Figure 8.29: Quadrant analysis of PIV data with colours for each Quadrant.

Unlike previous studies, quadrant analysis can be taken one step further. By repeating the analysis for each point location and then mapping the type of significant event (if any)

in each quadrant back into the time domain (Figure 8.29), the real-time movement and type of behaviour of each structure can be identified visually (see Figure 8.30). When this is carried out for each time step, a video of how the behaviour changes over time can be created (see Figure 8.31 for the QR code or visit: www.youtube.com/playlist?list=PLBxWPtPkf1M8hGh0xKEWmlShaaN1kk30G).

The video animation is able to clearly show the formation and development of turbulent structures over time as they are generated by shear flow across the base of the bed. These rise over time as the flow progresses and induce an inrush behind them to fill in the space.

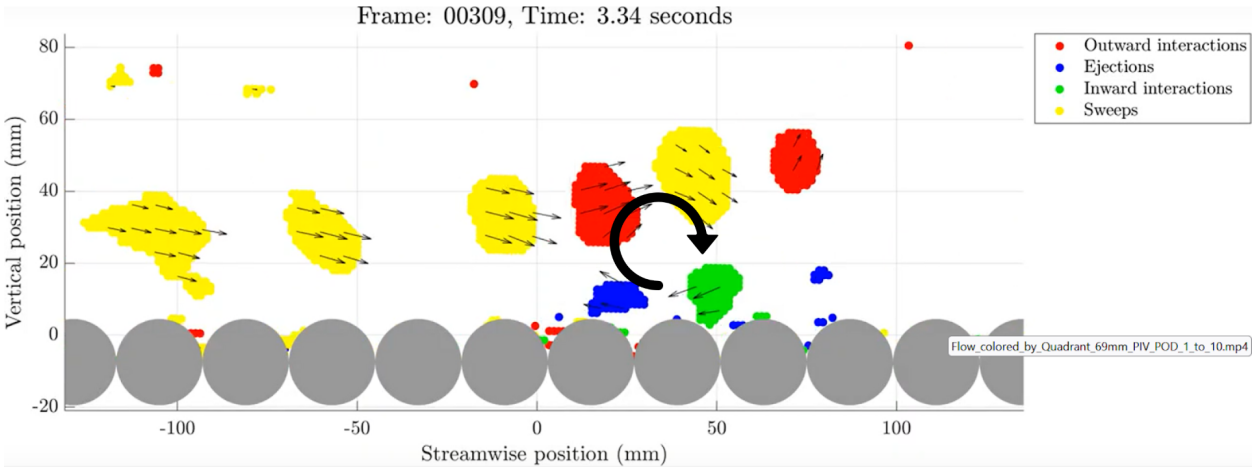

Figure 8.30: Identification of transient turbulent structures' behaviour using quadrant analysis in the time domain.

The next section will analyse the CFD data more closely by applying POD. As it has been shown that Quadrant analysis can give more useful information about a turbulent structure's movement and behaviour (when compared to U-level), Quadrant analysis will be tested on the CFD data. Additional techniques utilising the full 3D flow field will also be applied to investigate how the rigid lid influences the shape and movement of these turbulent structures near the free-surface.

Figure 8.31: QR code to access video of the identification of turbulent structures using reverse Quadrant analysis. 69mm flow depth condition with POD filter from modes 1 to 10. Data from experimental PIV.

8.2.4 Turbulent Structures in CFD simulations

POD was applied to the CFD data using the same snapshot approach as with the PIV. The CFD data from the 49mm flow condition were extracted using the *internalProbes* (aka *internalCloud*) function. The spatial resolution and coordinates used to extract the data were the same as the PIV to allow for a better comparison.

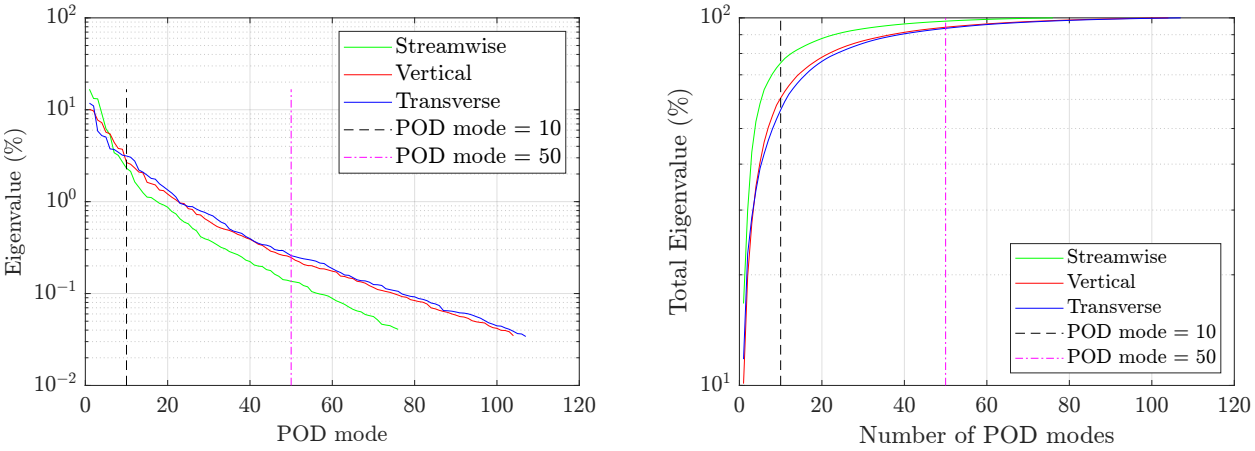

Figure 8.32: Percentage energy (%) captured decomposed over different modes using POD for the 49mm flow depth CFD simulation in each direction. As the POD mode number increases, the energy contained in each mode decreases.

Figures 8.33, 8.34 and 8.35 show the Eigenfunctions of the first four POD modes using the CFD velocity fluctuations in the respective streamwise, vertical and transverse directions.

In the vertical direction (Figure 8.34), similar to the PIV, the CFD also shows regions of alternating intensities. This reinforces the PIV data and suggests that there are universal mechanics governing regions of upwards and downwards motions in a cyclic manner. Combined with the knowledge that the free-surface also moves up and down, this could be definitive visual evidence that the free-surface motion is strongly linked to vertical movement of flow underneath.

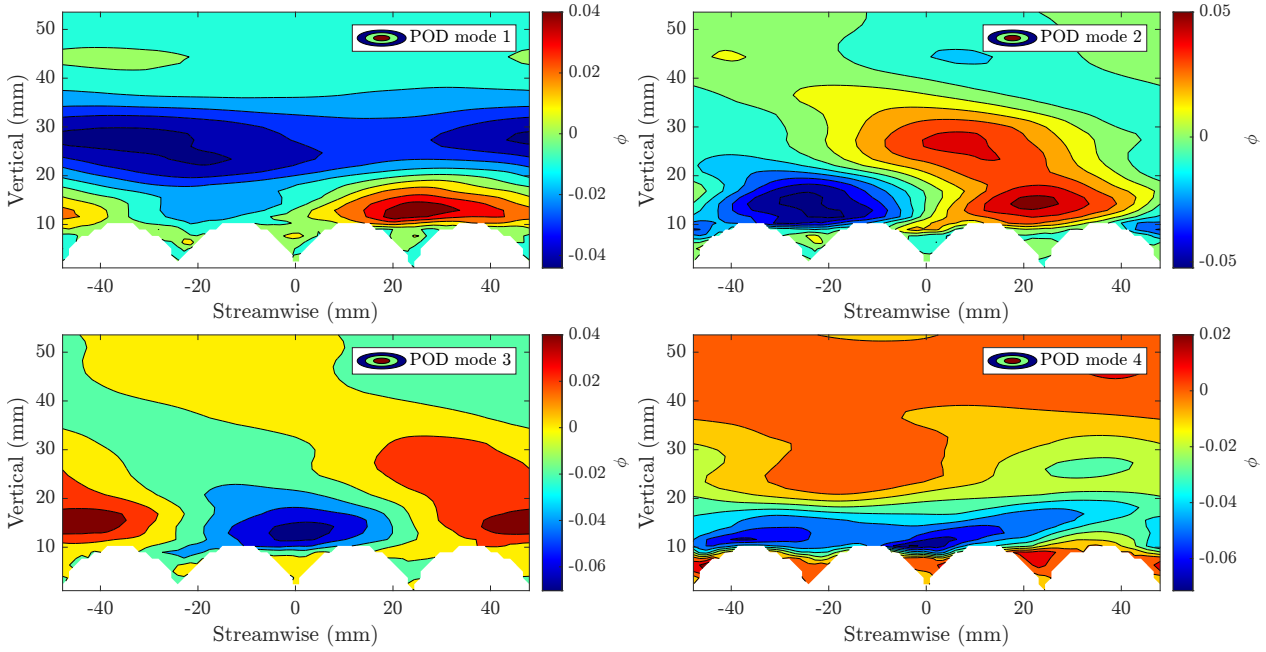

Figure 8.33: Eigenfunction of POD from the CFD simulation of the 49mm flow condition using streamwise velocity fluctuation (U').

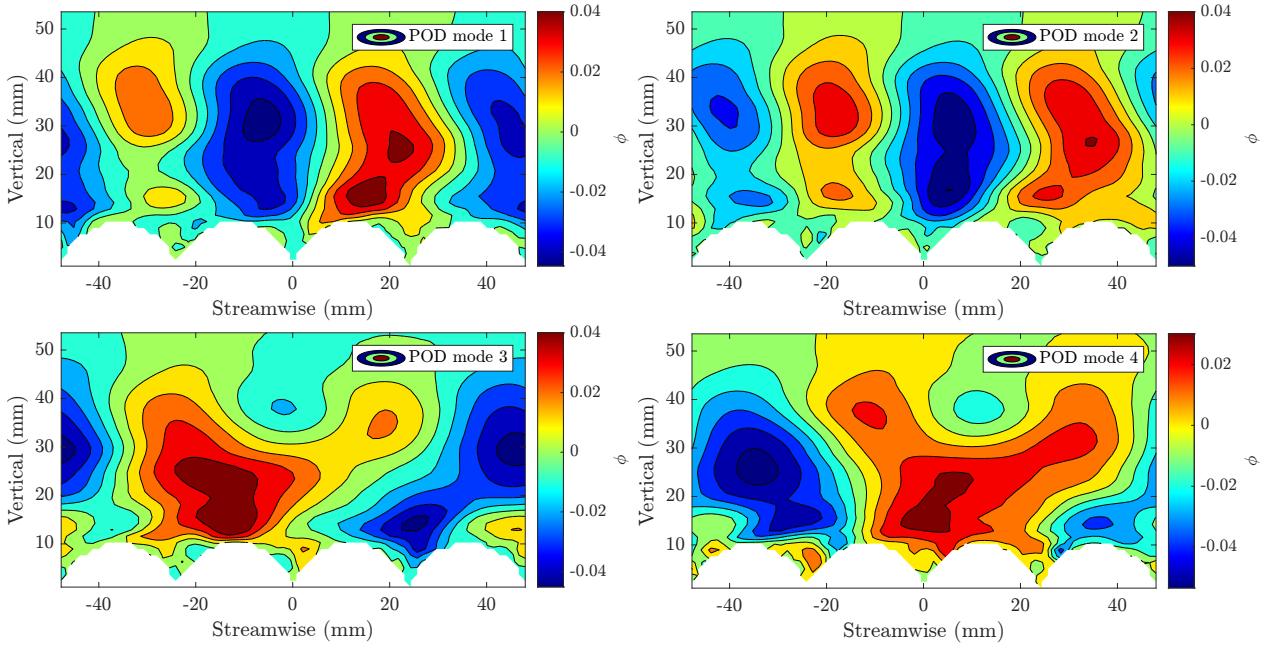

Figure 8.34: Eigenfunction of POD from the CFD simulation of the 49mm flow condition using vertical velocity fluctuation (V').

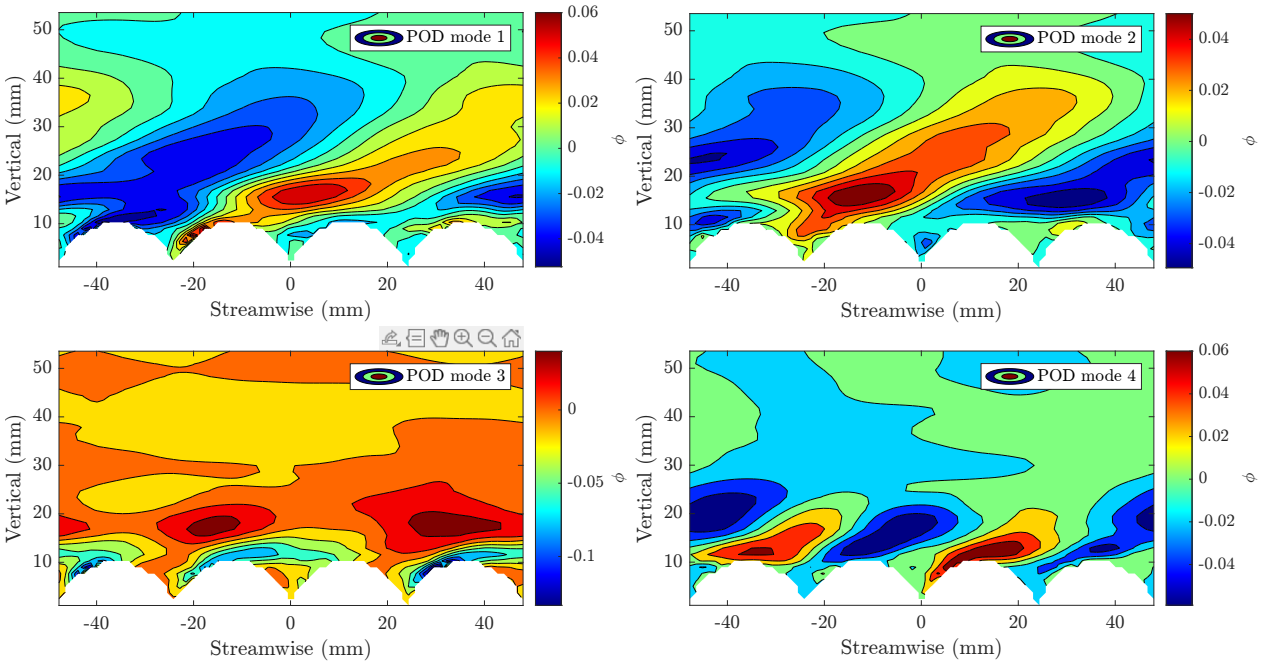

Figure 8.35: Eigenfunction of POD from the CFD simulation of the 49mm flow condition using transverse velocity fluctuation (W').

To study the behaviour of the flow over time, quadrant analysis is carried out at a single point location in the flow. Figures 8.36 and 8.37 show the extracted signal used for quadrant analysis.

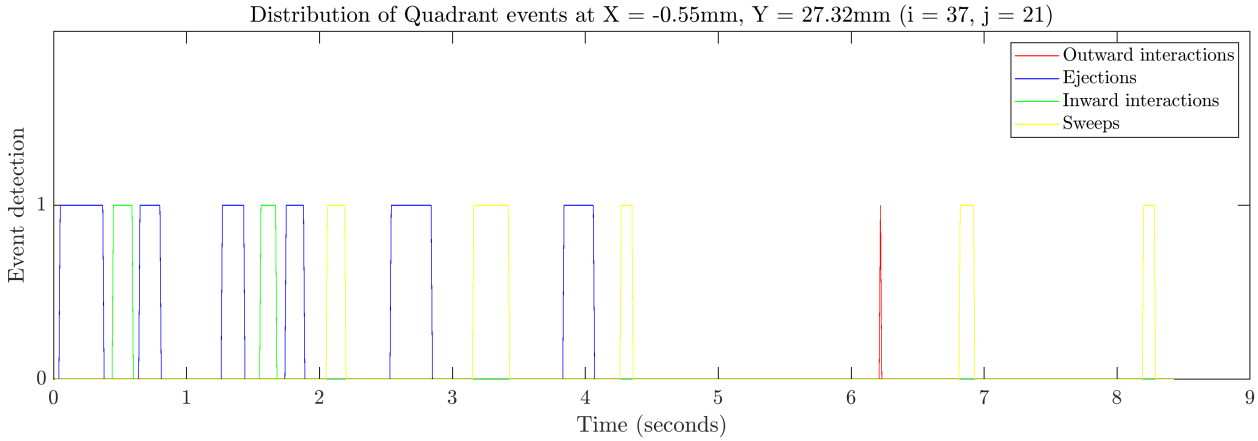

Figure 8.36: Extracted signal used in quadrant analysis for CFD 49mm flow depth condition filtered using POD modes 1 to 10.

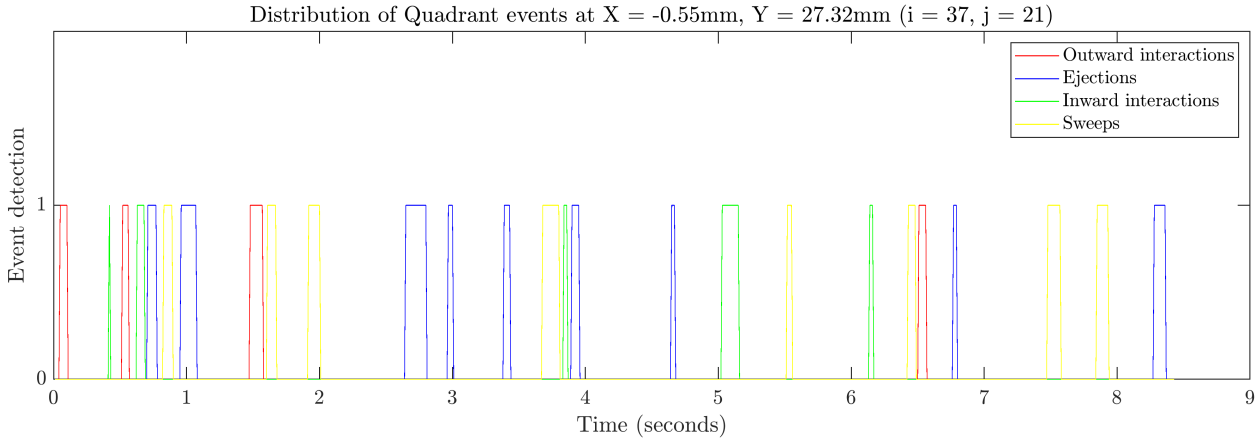

Figure 8.37: Extracted signal used in quadrant analysis for CFD 49mm flow depth condition filtered using POD modes 11 to 50.

Meanwhile, quadrant analysis on the large scales (POD modes 1 to 10) show that most of the significant events are ejection based. This is in contrast to the smaller scales (POD modes 11 to 50) which show more universal distribution of the significant events. It's important to note that the patterns shown in the quadrant analysis distribution here looks fairly distinct suggesting that there may not be sufficient simulation data to correctly generate a reasonable hole size for identifying events of significance.

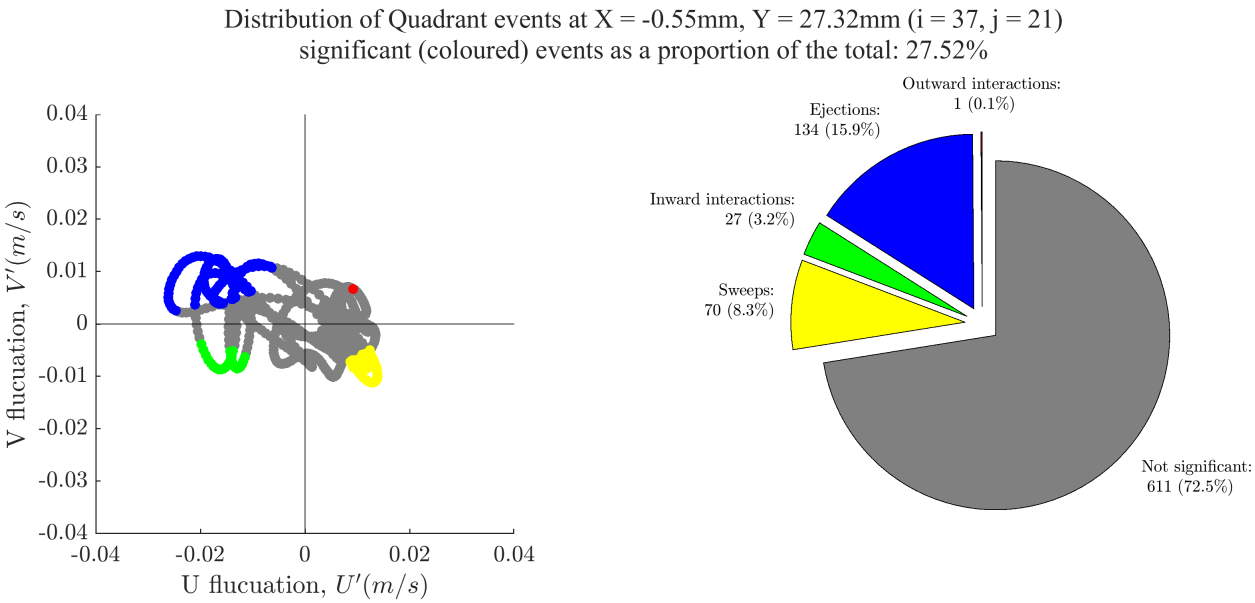

Figure 8.38: Quadrant analysis for CFD 49mm flow depth condition filtered using POD modes 1 to 10.

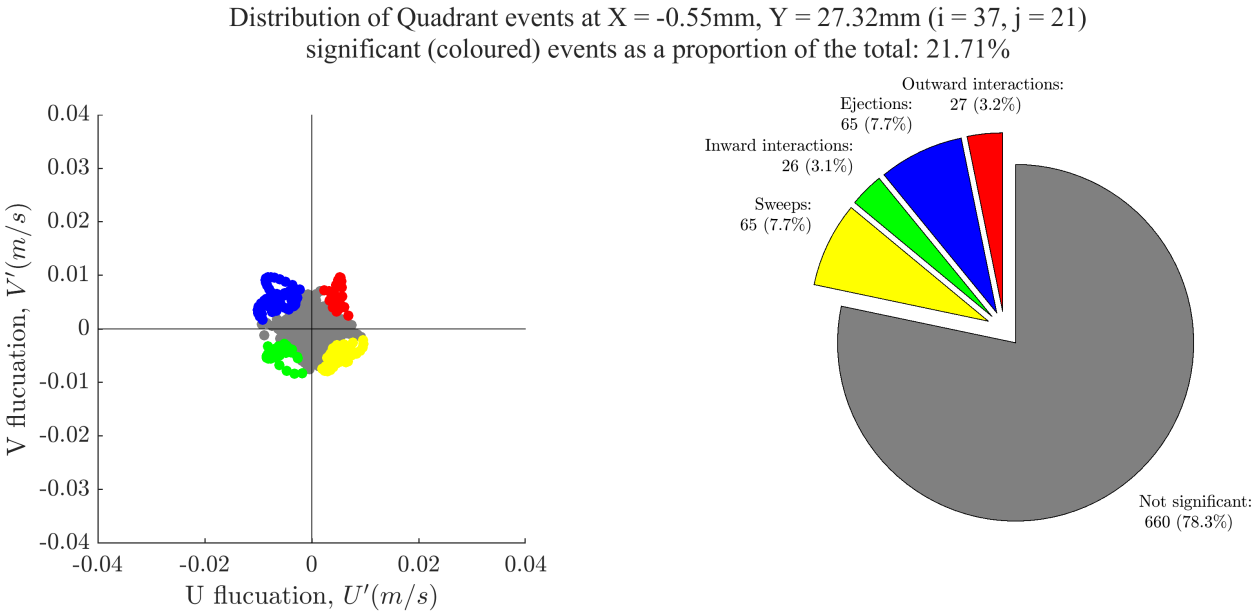

Figure 8.39: Quadrant analysis for CFD 49mm flow depth condition filtered using POD modes 11 to 50.

One benefit of quadrant analysis is that it only requires vector data in 2 directions (streamwise and vertical). This reduces the computational load. However, where transverse data is also available (e.g. CFD), then other techniques can take advantage of this additional information. The following section will use such techniques to investigate in more detail.

8.2.5 Coherent Structures Vortex Identification

Time series analysis was conducted by visual observation of flow snapshots and identifying the movement of coherent structures. This was achieved using vortex identification methods known as Q-criterion and Lambda-2.

Proposed by Hunt et al. (1988), Q-criterion is a variable that describes the main motion pattern of a fluid element. This is built on the gradient of velocity, L defined in equation 8.2.1:

$$L = \nabla \mathbf{V} = \begin{bmatrix} \frac{\partial u}{\partial x} & \frac{\partial u}{\partial y} & \frac{\partial u}{\partial z} \\ \frac{\partial v}{\partial x} & \frac{\partial v}{\partial y} & \frac{\partial v}{\partial z} \\ \frac{\partial w}{\partial x} & \frac{\partial w}{\partial y} & \frac{\partial w}{\partial z} \end{bmatrix} \tag{8.2.1}$$

where L can be decomposed into:

$$L = \frac{1}{2}L + \frac{1}{2}L + \frac{1}{2}L - \frac{1}{2}L, \tag{8.2.2}$$

or in factorised form:

$$L = \frac{1}{2}(L + L^T) + \frac{1}{2}(L - L^T) \tag{8.2.3}$$

From this, the strain rate tensor and vorticity tensor can be defined. A strain rate tensor which has symmetric properties. This describes the rate of stretching and shearing.

$$S = \frac{1}{2}(L + L^T) \tag{8.2.4}$$

A vorticity tensor which has skew-symmetric properties. This describes the rate of rotation.

$$\Omega = \frac{1}{2}(L - L^T) \tag{8.2.5}$$

Q is then defined as the second invariant of the velocity gradient tensor:

$$Q = \frac{1}{2}(||\Omega||^2 = ||S||^2) \tag{8.2.6}$$

Values of $Q > 0$ indicate areas of higher vorticity than strain rate in the flow whilst values of $Q < 0$ indicate areas of higher strain rate than vorticity in the flow In essence, for $Q > 0$, the rotation motion dominates, whilst for $Q < 0$, the deformation motion dominates. The vortex flow has the character of $Q > 0$, but not all regions with $Q > 0$ are necessarily vortex flow regions. Previous studies such as Jeong and Hussain (1995), Miura and Kida (1997), Nagaosa and Handler (2003) and Tanaka and Kida (1998) have demonstrated that a manual selection of a non-zero threshold can enable visualisation of more distinct features and structures in flow. The same approach is utilised here with different thresholds tested to assess the type and number of structures identified.

Testing the Q-criterion vortex identification method with the simulation of flow over a hemispherical boulder (from Section 6.3.3 and 7.3.3.2), the visualisation of the turbulent structures are clearly visible, being generated by the boulder protruding into the flow (Figure 8.40). This largely matches the findings discussed in section 7.3.3.1 and also the horseshoe vorticies found by Stoesser (2014).

A video animation of Figure 8.40 can be found at: https://www.youtube.com/playlist?list=PLBxWPtPkf1M9cDcX8rau391mJ_oJGKijh. A QR code for the same link is available in Figure 8.41.

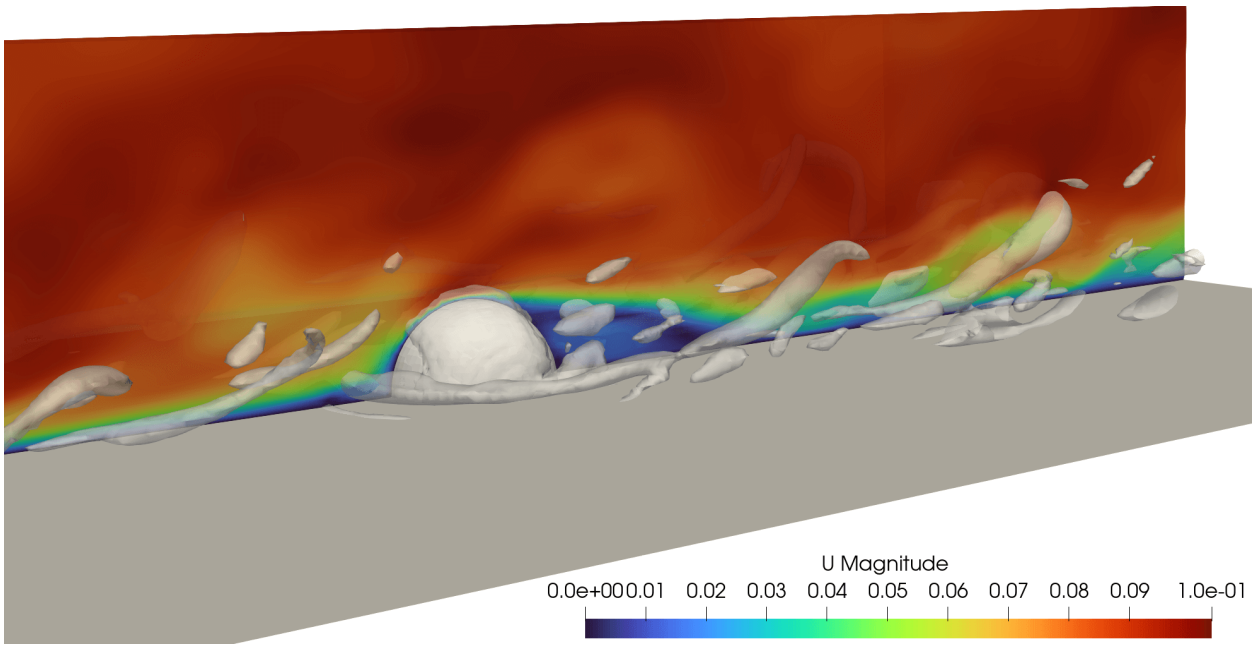

Figure 8.40: Centerlince slice of the velocity field with detected turbulent structures from LES simulation of flow over a hemi-sphere at 49mm depth. Structures were identified using a Q criterion threshold of 10.

Figure 8.41: QR code to access video of detected turbulent structures of flow over a hemi-sphere at 49mm flow depth.

8.2.6 Vortex Identification for Flow Over Rough Bed

To assess the validity of the rigid lid approximation, the 49mm flow depth LES simulation is used for closer analysis. This flow condition has the lowest relative submergence and is the shallowest flow. In Figure 8.42A, using a Q-criterion threshold of 40, it can be seen that numerous vortex-like structures are present within the flow. A similar analysis was carried out using the lambda-2 vortex detection method. The same time step is shown in Figure 8.42B. This method was proposed by Jeong and Hussain (1995) and is essentially a vortex core line detection algorithm which defines a vortex in terms of eigenvalues of the symmetric tensor.

With the lambda-2 method, the three eigenvalues from equation 8.2.6 are calculated for each point in the computational domain as λ_1,λ_2 and λ_3 where $\lambda_1 \geq \lambda_2 \geq \lambda_3$.

If $\lambda_2 < 0$, then a particle in the velocity field is defined as being within a vortex.

It captures the pressure minimum in a plane perpendicular to the vortex axis at high Reynolds numbers. Furthermore, unlike a pressure-minimum criterion, the lambda-2 method claims to accurately define vortex cores at low Reynolds numbers. This is important for the current application as the flow is not highly turbulent. Seddighi et al. (2015) were able to use the lambda-2 method for identifying vortices in channel flows with regular pyramidal roughness elements.

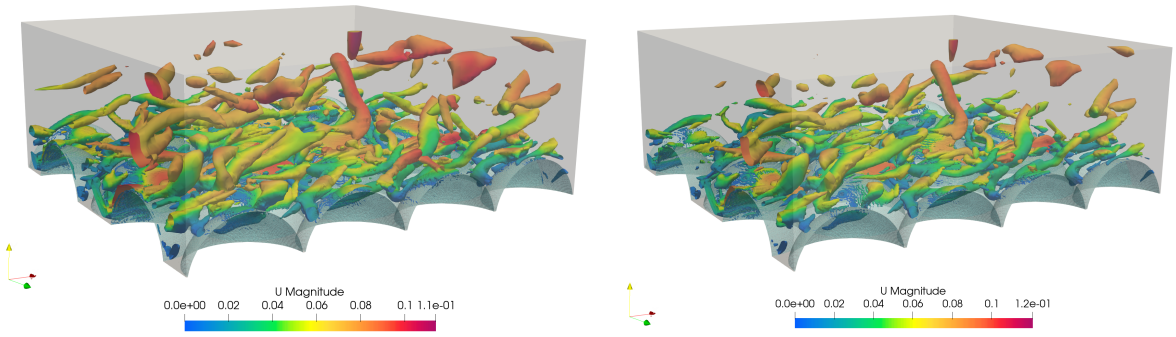

(a) Q-criterion method with threshold = 40 (b) lambda-2 method with a threshold = 50

Figure 8.42: Comparison of two different vortex detection methods using instantaneous snapshot of velocity data at 89.54 seconds in the simulation. The shape and the size of the detected structures are similar suggesting that both methods are equally valid (Cho et al., 2022).

In both figures, it can be observed that the vortices identified are similar in number, scale and shape. For both methods, the threshold value has been selected to identify vortices near the bed. Lowering the Q-criterion threshold enables more of the flow to be identified as a vortex.

A frame by frame analysis using a lower Q-criterion is shown in Figure 8.44. Time steps of 0.1 seconds are shown from 36.1 seconds to 36.4. It can be seen that the vortices appear to be rising from the bed whilst being deformed in the streamwise direction by the bulk flow (enclosed within the dashed blue lines). From 36.1 to 36.3 seconds, the effect of the turbulent structure hitting the rigid lid water surface can also be observed. These coherent structures appear to hit the underside of the water surface before being propagated in the streamwise direction with the bulk flow. With the rigid lid, it appears that they are then attached under the lid until the structure gets dissipated. A video animation of the flows are available at: www.youtube.com/playlist?list=PLBxWPtPkf1M93vaHBshL5BAjEEsgkuCOR. Alternatively, the reader can also use the QR code in Figure 8.43.

Figure 8.43: QR code to access video of the flow simulated using LES.

Assessing this further, Figure 8.45 shows the simulation domain with a top view using lambda-2 with threshold = 10. A horizontal flat plane is taken 2.5mm below the free-surface with the colours representing the velocity in the vertical direction. It can be observed that the presence of turbulent structures often coincides with the green coloured regions. This

suggests that turbulent structures move with a different vertical velocity to the bulk flow and will hit the free-surface (given the proximity of the horizontal plane with the free-surface).

By studying the creation and movement of turbulent structures using different Q-criterion thresholds, it is clear that the turbulent structures that are generated at the bed do occasionally grow to enough magnitude to break through the near surface water layer and impinge on the water surface above. Since a rigid lid has very different properties to a flexible lid, it can be said that the rigidity of the lid will lead to an unrealistic response of the turbulent structure as it impacts the free-surface. The impingement of the turbulent structures on a free-surface would be expected to generate at least some upwards deformation of the free-surface shortly followed by a downwards deformation due to the gravitational force and surface tension pulling the flexible lid back downwards. The fluctuation of the free-surface would likely transmit some force or pressure onto the coherent structure possibly causing it to re-enter the central part of the flow and possibly triggering new bursts at the bed to restart the cycle again.

Conceptually, if the flow is visualised 'upside-down' such that the free-surface becomes the 'bed', then should be clear that the underside of the water-air interface is also dynamically 'rough'. When the bulk flow attempts to move past this turbulent rough movement, it is inevitable that the bulk flow is affected by the underside of the free-surface. In wave propagation theory, a wave is referred to as 'smooth' if its wavelength is considered 'long' with respect to the turbulence length scales. However, if the length scale of the wave is similar to eddy length scales, from the perspective of the flow, the surface appears very rough. In the framework proposed by Brocchini and Peregrine (2001), they suggest that these specific shallow flow conditions create small surface fluctuations. Based on the Reynolds' number, empirical turbulent sub-layer studies and analysis conducted in the present study, it is clear that the dominant turbulent scales are also of similar scale to the free-surface fluctuation. Therefore, the use of a rigid lid will certainly have a noticeable effect on the re-distribution of turbulent energies from coherent structures as they impinge on the free-surface.

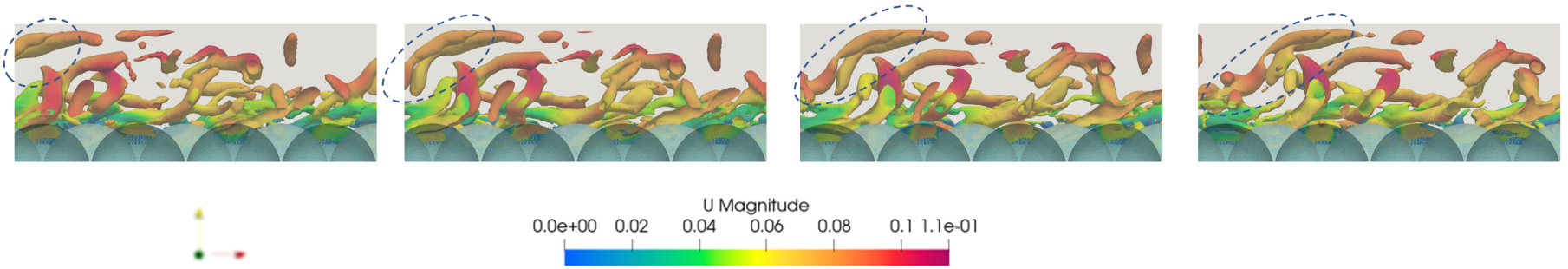

Figure 8.44: CFD simulation of open channel periodic flow over a rough bed of spherical caps using WALE (Wall Adapting Local Eddy) turbulence modelling (Cho et al., 2022). Snapshots taken at 0.1 second intervals with coherent structures identified using Q-criteron = 20. The colourbar shows the streamwise velocity, U. Dashed ellipses highlight a structure that is being stretched and advected by the flow.

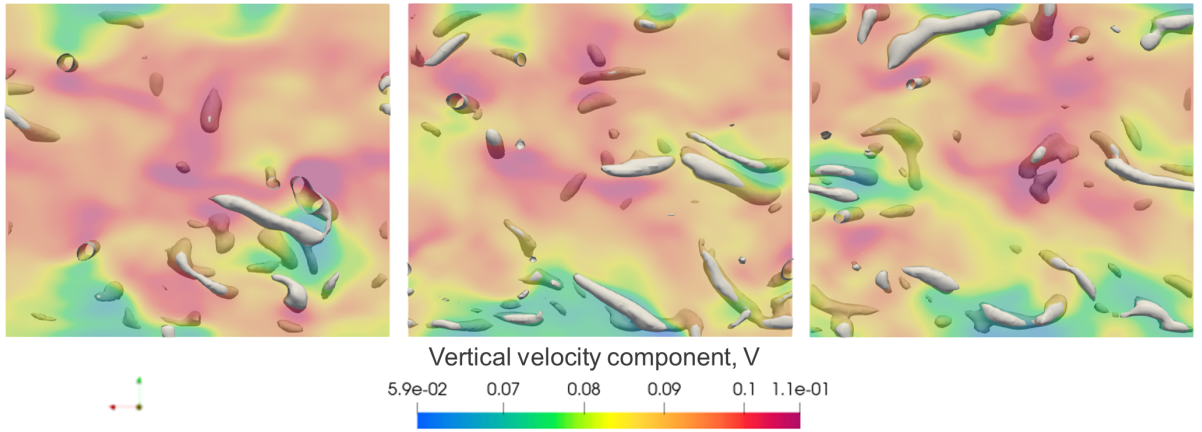

Figure 8.45: Coherent structures identification using the Lambda method (Jeong and Hussain, 1995). Threshold limit = 10. Selected frames at 23.68, 36.0 and 36.9 seconds from left to right. Coloured by vertical velocity. Horizontal plane taken 2.5mm below the free-surface. Areas of vertical velocity appear to correlate with the presence of local turbulent structures (Cho et al., 2022).

8.2.7 Assessment of the rigid lid approximation

Figure 8.46 shows a comparison between the time-averaged velocity profiles from the CFD simulation against PIV and ADV measurements. Figure 8.47 shows a similar comparison for turbulence intensity (calculated using Equation 2.3.4).

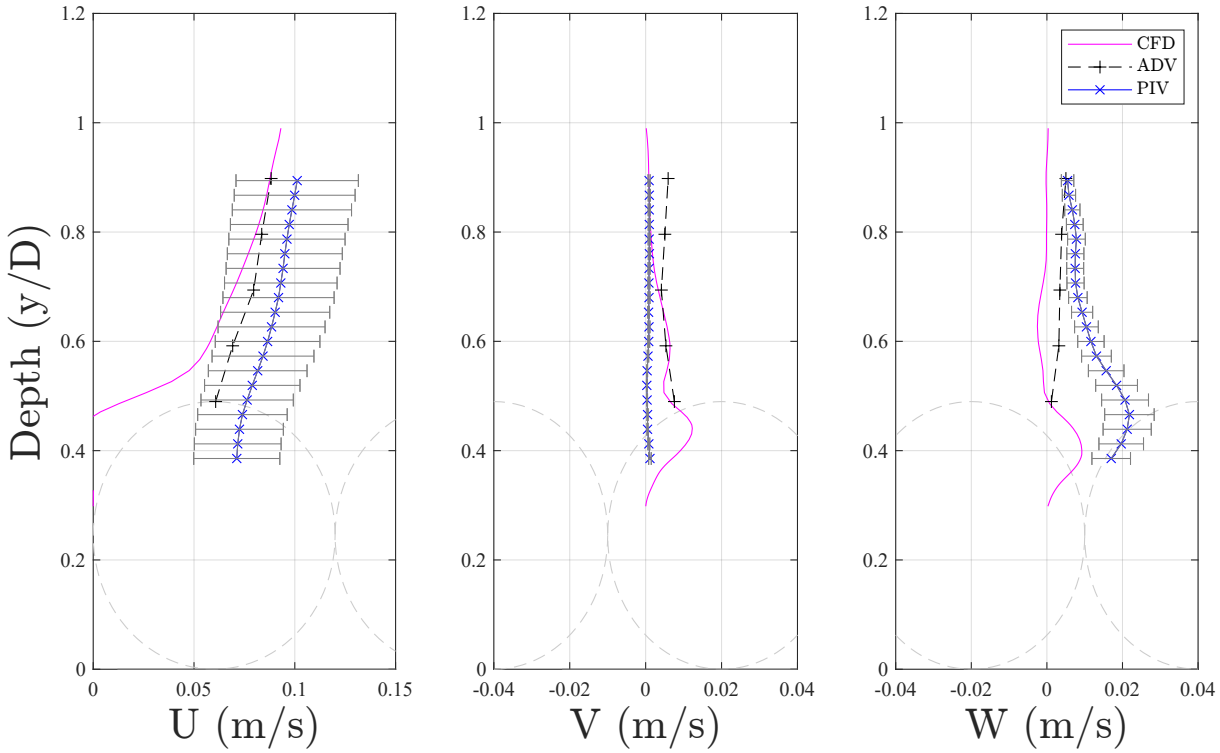

Figure 8.46: Comparison of mean velocity profile (Cho et al., 2022). Rough bed has been added to illustrate the relative level and scale of the bed elements. U, V and W are the velocities in the streamwise, vertical and transverse direction.

Between the spherical caps, the turbulence from the CFD appears to be very large. This cannot be validated using the experimental data because the PIV and ADV are only able to provide reliable data above the spheres. The PIV cameras do not have line of sight to see deep in between the spheres and the ADV probe and its sampling volume is too large to fit in between the spheres.

It should be noted that the position of the bed (d_2) in the CFD domain is a virtual plane, with the actual bed (from the experiments) located at the bottom of the spheres (which is outside the computational domain and not modelled). The flat virtual plane uses a slip condition whilst the spherical tops uses a no-slip boundary condition. This complex dual

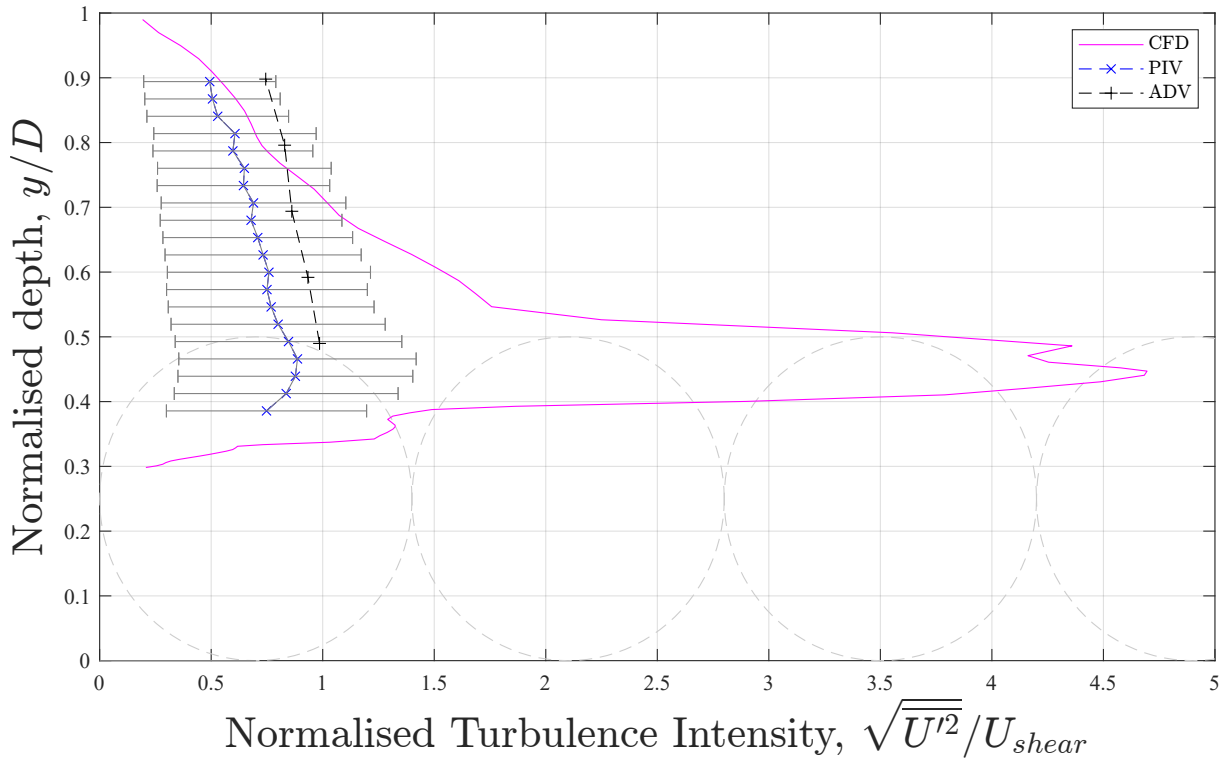

Figure 8.47: Comparison of turbulence intensity profile (Cho et al., 2022). The dashed grey circles representing the rough bed have been added to illustrate the relative level and scale of the bed elements. The experimental instruments (PIV and ADV) are quite similar however the profile for the CFD simulation shows large turbulence intensity near the bed.

boundary setup prevents an improper turbulent boundary layer from forming further away from the real bed.

Figure 8.48 shows a comparison of the Reynolds' shear stress from the CFD, PIV and ADV (calculated using Equations 2.3.5 to 2.3.7). Whilst the CFD and the experimental tests follow similar trends, the Reynolds shear stresses near the rigid lid free-surface are subdued. The rigid lid imposes zero vertical fluctuation as a boundary, therefore, the vertical velocity fluctuation at the rigid lid will always be zero. Referring back to the mean velocity profile in Figure 8.46, this can also be observed as the CFD vertical velocity profile (middle pane), ends with zero velocity at the free-surface.

Since the equation for RS_{uv} includes the term V', it is a mathematical inevitability that RS_{uv} near the free-surface is reduced to zero (see Equation 2.3.5). This effect is evident in Figure 8.48 especially in the region of normalised depth from 0.7 to 1. The CFD and experimental profiles can be seen diverging which sugests that the Reynolds' stress in this region

is inaccurate. This would affect wider turbulent structure interactions with the free-surface. In turn, this would also would also likely affect the sediment transportation mechanism since the free-surface region moves the fastest and a lack of proper turbulence in this region may prevent sediment from properly entering/remaining in this region of fast moving flow.

The following section attempts to artificially re-create a free-surface based on the vorticity of the flow underneath the rigid lid.

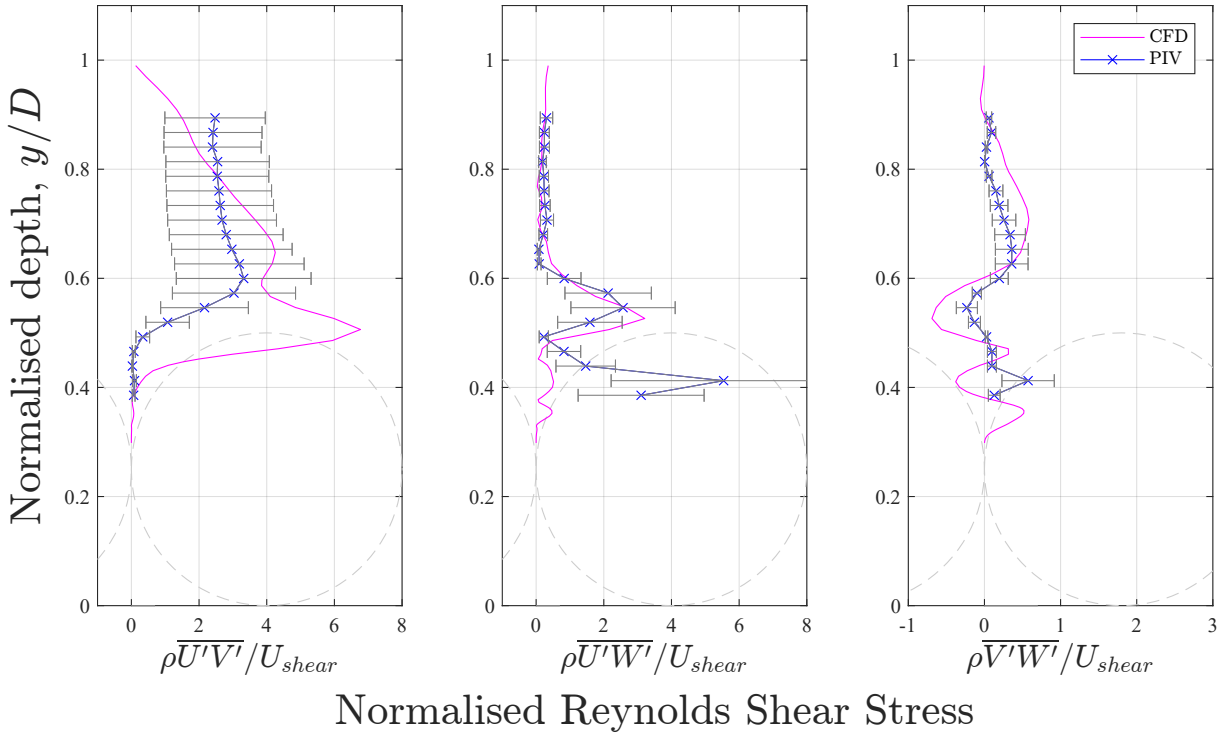

Figure 8.48: Comparison of Reynolds stress profile (Cho et al., 2022). The dashed grey circles representing the rough bed have been added to illustrate the bed.

8.2.7.1 Pseudo Free-surface Re-construction with Vorticity Near Rigid Lid

Since it was now clear that turbulent structures are impacting the rigid lid, an attempt to reconstruct the free-surface was made using the vorticity field.

This was first tested on the simulation flow over a hemi-spherical boulder at 172.19 seconds. Figure 8.49 shows the instantaneous reconstruction of the free-surface. Using ParaView post-processing software, the *warp by vector* function was applied to vorticity field which deformed the upper boundary based on the values at the rigid lid. It can be seen that there are more high amplitude fluctuations at the centerline than towards the transverse sides of the domain. This makes sense as the boulder on the bed is in the centerline and the turbulent structures generated tend to rise vertically. There are no boulders at the sides of the domain so the fluctuations are likely due to the fluctuations at the centerline travelling and dissipating into smaller fluctuations towards the sides.

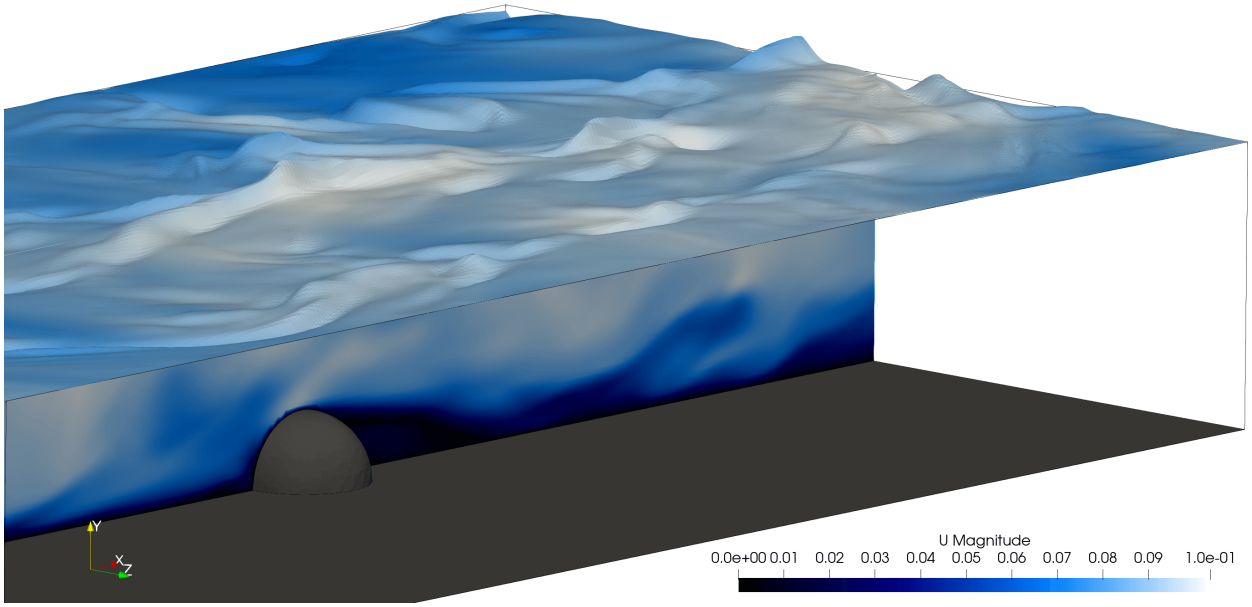

Figure 8.49: Pseudo free-surface elevation reconstructed using vorticity vectors with the 'warp by vector' function from LES simulation of flow over a hemi-sphere at 49mm depth (data used taken at 172.19 seconds into the simulation).

Unlike experiments, CFD time steps can be saved and restarted to obtain the same results. These time step files can also be used in a different simulation with no loss in accuracy. The next section will present the results of flow over a rough bed with free-surface modelling.

8.2.7.2 Flow over rough bed with free-surface

To investigate further the nature of turbulent structures deforming the free-surface, the simulation with a free-surface was analysed. Figure 8.50 shows the results from a flexible free-surface LES simulation initiated using the LES rigid lid simulation after it had stabilised. The turbulent structures identified by Q-criterion are shown along with the deformation of the free-surface. The main flow and turbulent structures are coloured by the magnitude of the velocity and the free-surface itself is coloured according to the scale of its deformation. Besides the usual signs of a clear ejection of structures towards the free-surface, several other important events can be seen near the free-surface.

Firstly, a large structure (labelled A) impacting the free-surface is immediately visible underneath the free-surface. It is clear that this coincides with the free-surface being deformed suggesting that structures hitting the free-surface do cause a localised upwards displacement. Secondly, a structure (labelled B) is seen pointing and moving away from the free-surface just beneath a localised indentation (or dimple) in the free-surface. This suggests that the free-surface causes the structures to to rebound back down into the flow, perhaps in response to the surface oscillating due to surface tension and gravity as surmised by Nichols and Rubinato (2016).

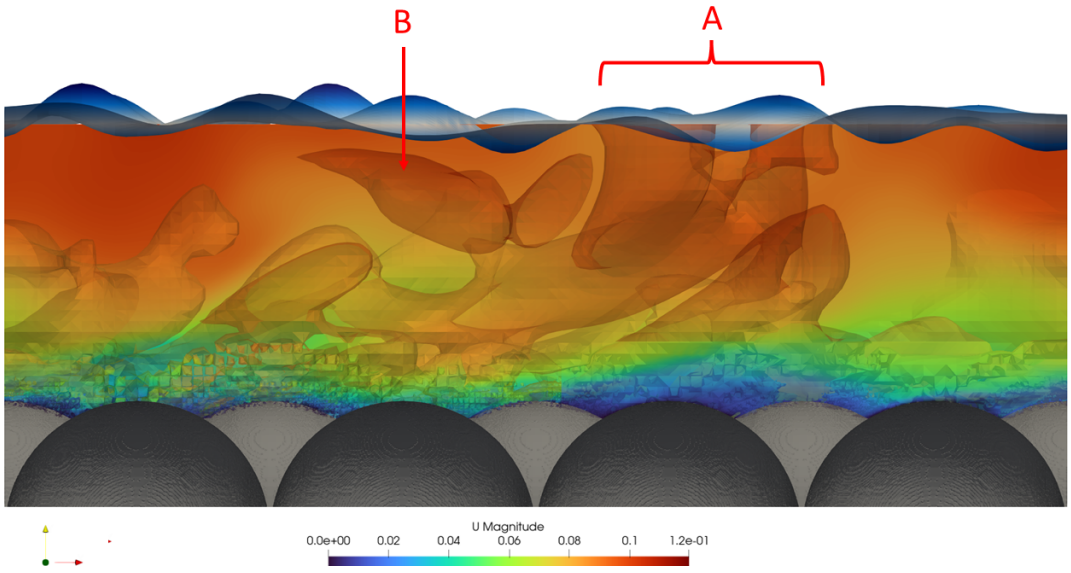

Figure 8.50: Free-surface using wave height field from *potentialFreeSurfaceFoam*. Structures in region A hit the free-surface and cause a surface deformation. Structure B is pushed into the flow by the surface moving downwards.

A similar investigation was conducted with the vorticity field creating a pseudo free-surface in the same way as section 8.2.7.1. This helps to check whether the structures in close proximity to the surface really cause any effect. If they do, then the reconstructed free-surface should have similar characteristics. In Figure 8.51, it can be observed that the high free-surface deformation that is detected from the flexible lid simulation also occurs at the same location when re-constructed using the vorticity the field (it also coincides with the large free-surface deformations). This makes sense as the identification of the structures was done using Q-criterion which itself is based on vorticity. However, the free-surface constructed using vorticity is not exactly the same shape as the flexible lid simulation. This suggests that not all upwards free-surface deformations originate from a turbulent structure impacting the free-surface.

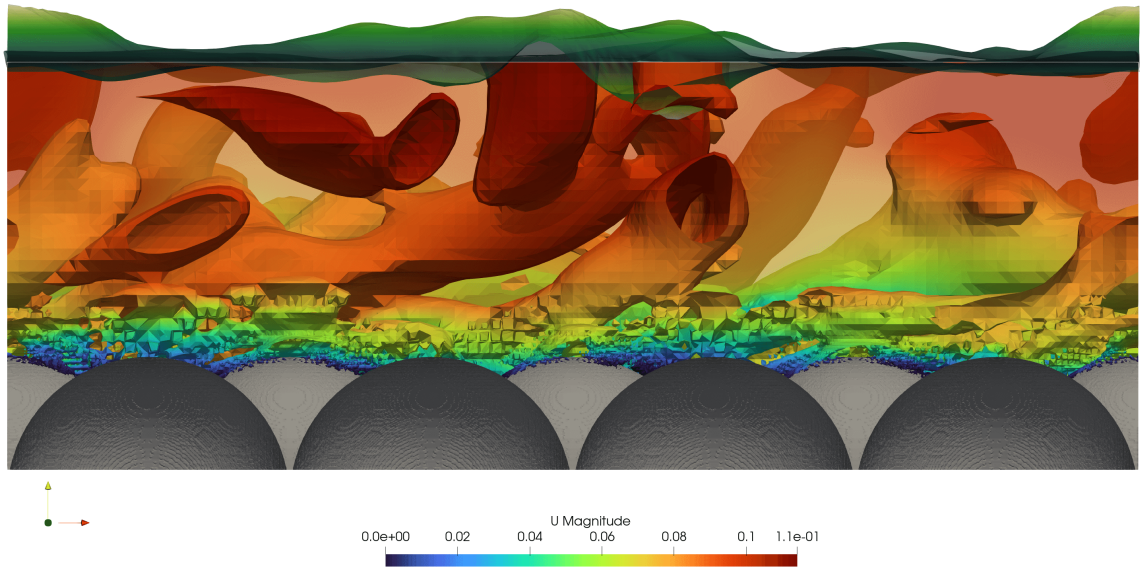

Figure 8.51: An artificial pseudo free-surface visualisation generated using *potentialFreeSurfaceFoam* (vorticity). This is not dissimilar to the shapes created using the zeta function and suggests that the vorticity immediately below the free-surface has a big effect on the free-surface behaviour.

Instead, several physical effects are happening sequentially. Here are several facts: 1) the free-surface has surface tension and is subject to gravity. Conservation of mass in open channel flows dictates that what goes up must come down. 2) Movement contains momentum and the pushing of the turbulent structure back into the flow followed by a downwards deflection of the free-surface suggests that the free-surface will not just return directly to its

nominal position before the impact. Instead, it clearly goes below the normal position as demonstrated in Figure 8.49. Nichols (2014) suggested that the movement of the free-surface deflections resembles that of a decaying simple harmonic motion. Thus, it is likely that the smaller upwards deflections are the 'after effects' of a prior impact and the energy is being dissipated through surface oscillations. Imagine a small object falling under gravity onto a flat stationary pool of water, at the location where the object makes contact, the water surface is forced down by the impact before rebounding upwards. It then oscillates until the energy is completely dissipated. The same effect is likely occurring here but in the opposite direction (since the turbulent structures are ejected from the bed and impact the free-surface from underneath instead of from above). As the flow is stabilised and the bed is periodic, it is likely that these free-surface effects are the origins of capillary waves (Zhang, 2002).

Shen et al. (1999) simulated 2D flow with DNS and found that a blockage layer exists near the free-surface resulting in only the most energetic structures from impacting the free-surface. If true, then from a statistical perspective, only the largest surface deformations are from the impact of turbulent structures whilst smaller deformations are the after-effects. Based on the frequency of large deformation events on the free-surface, the number of large turbulent structures can be estimated. From Kolmogorov's energy cascade, an estimate of the smaller eddies which must therefore be underneath the free-surface can also be deduced and an understanding of the turbulent mixing, particulate suspension and sediment transportation can be predicted.

To study this further, the free-surface from the experimental tests were analysed more closely by applying statistical tools to the Kinect infrared sensors' and wave probes' data.

8.2.8 Analysing Free-surface and Sub-surface Relationship

To investigate the relationship between the free-surface and the overall flow conditions, the experimental free-surface fluctuations from the wave probes are plotted against different flow parameters. For each of the six experimental flow conditions, the free-surface fluctuations are represented by their peak-to-peak and root-mean-squared values. Figure 8.52 and Figure 8.53 show the wave probe fluctuations against the flow depth and bulk flow velocity. At the lower flow depth conditions of 49mm and 69mm, the free-surface amplitude increases consistently. However, for the deeper flow depth conditions, the free-surface amplitude does not clearly increase with depth or flow velocity. To study this further, a comparison is made using dimensionless numbers.

Based on Weber number (see eq. 2.6.1) in Figure 8.56, it almost appears as if two different sets of flows are being observed, one set with particularly low free-surface fluctuations perhaps where surface tension is significantly reducing the amplitude and one set with higher consistent free-surface fluctuations. Comparing across the three wave probes, the measurement of the free-surface is quite similar for wave probes A and C. Wave probe B appears to behave differently at the deeper flow conditions from 89mm to 149mm.

Figure 8.54 uses Manning's number (the effect of the rough bed on the flow, see eq. 2.1.1). The relative roughness of the bed on the flow diminishes with deeper flow conditions. Hence, the Manning's number is highest for the lowest flow depth as the effect of the rough bed on the flow is the strongest. Although the Manning's number remains similar for the 69mm and 89mm flow conditions, the wave probe fluctuations increase in size from 0.2mm to 0.4mm, likely driven by the increased flow rate.

This is similar when looking at the variation of the Reynolds' number see (eq. 2.2.9) with free-surface fluctuation (Figure 8.55). As the overall flow turbulence increases, the free-surface wave amplitudes increase.

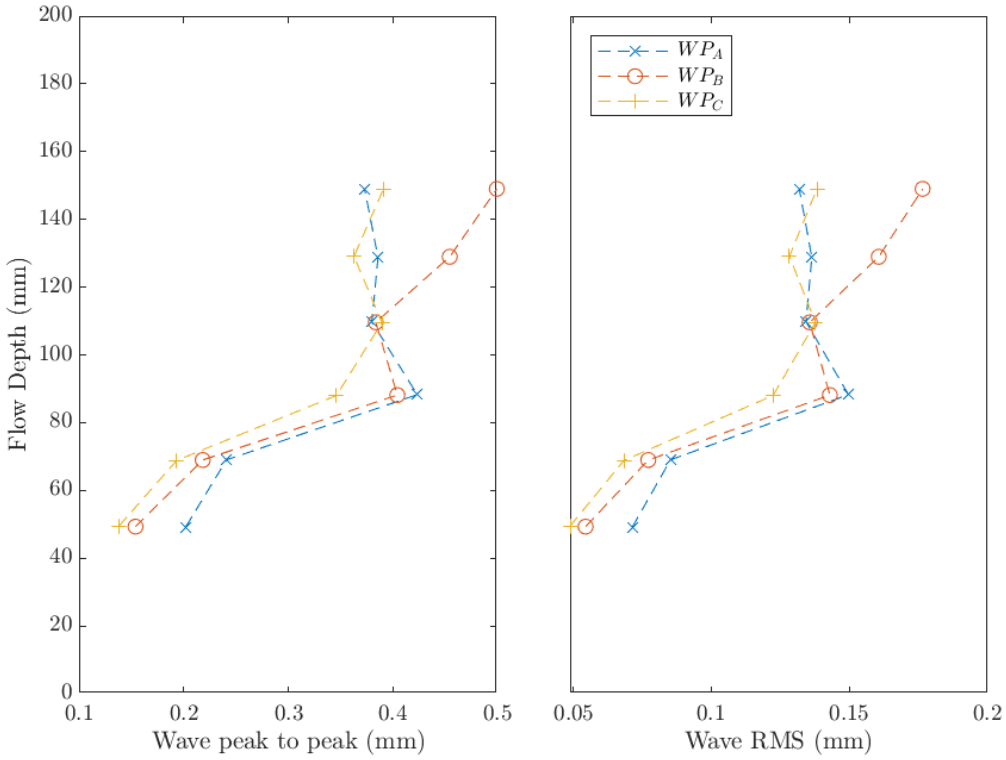

Figure 8.52: Wave Probe Fluctuation vs Flow depth. Note how overall, the flow depth increases as the wave fluctuations increase.

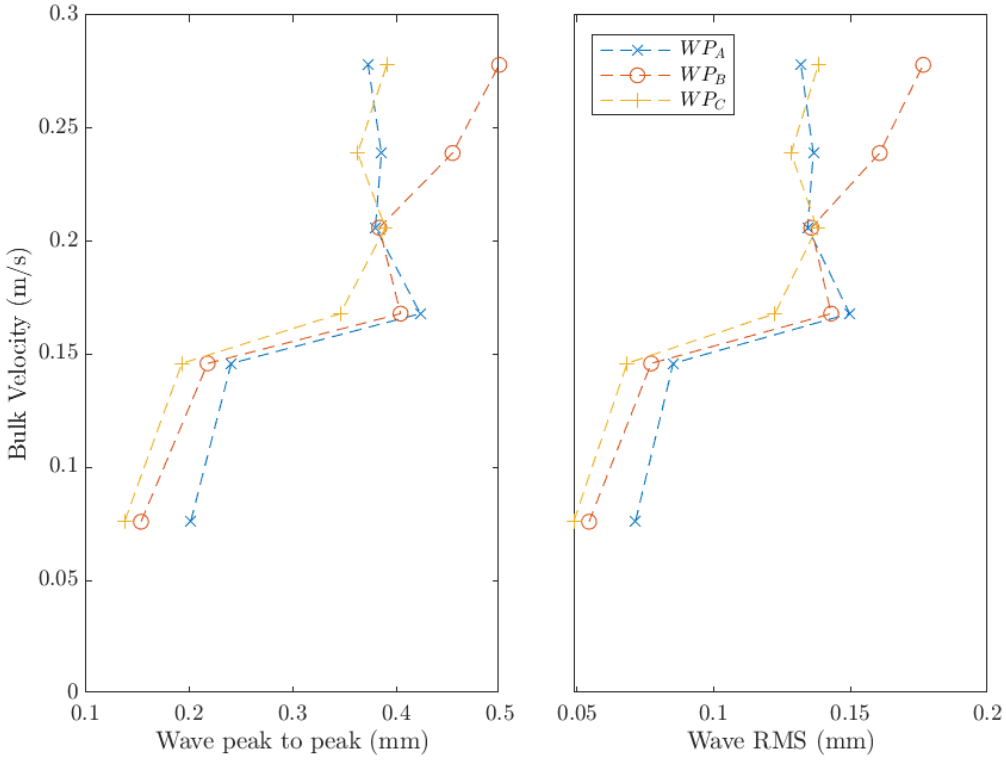

Figure 8.53: Wave Probe Fluctuation vs Mean flow velocity as calculated using the bulk flow rate.

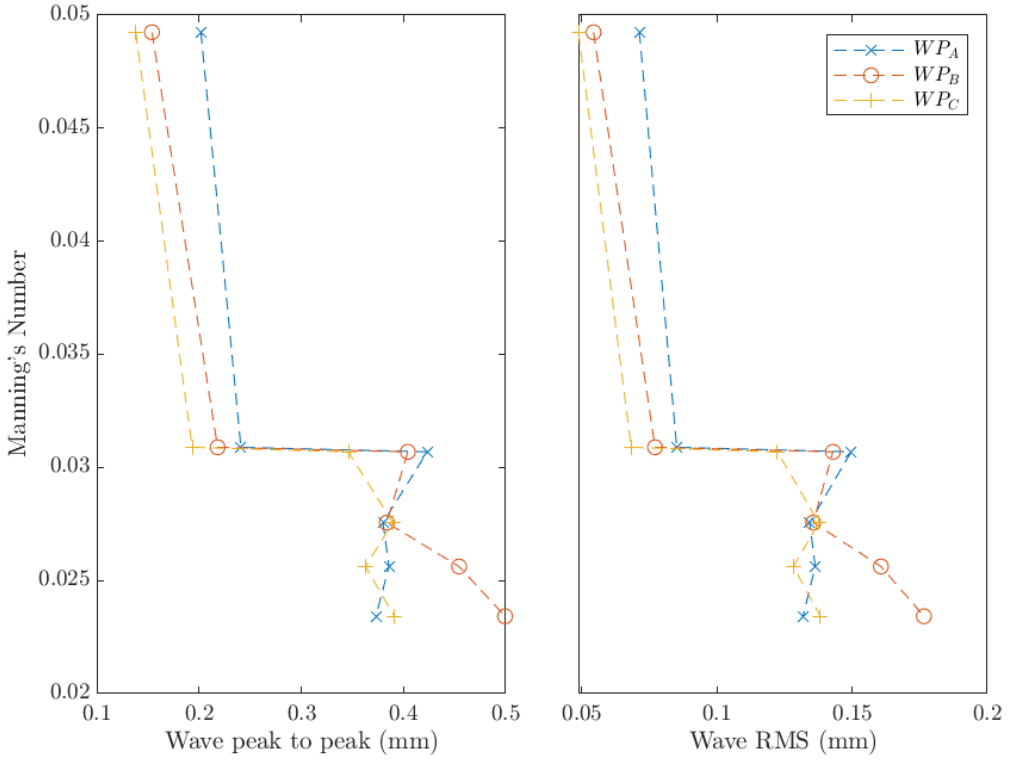

Figure 8.54: Wave Probe Fluctuation vs Manning's number (see eq. 2.1.1).

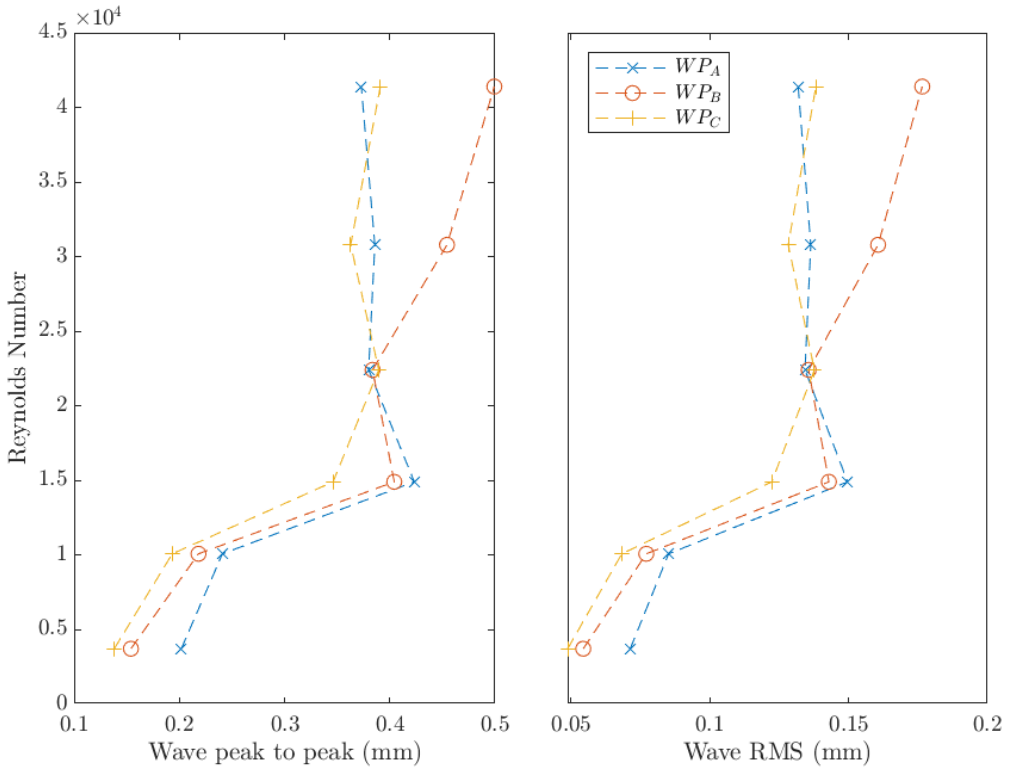

Figure 8.55: Wave Probe Fluctuation vs Reynolds' number (see eq. 2.2.9).

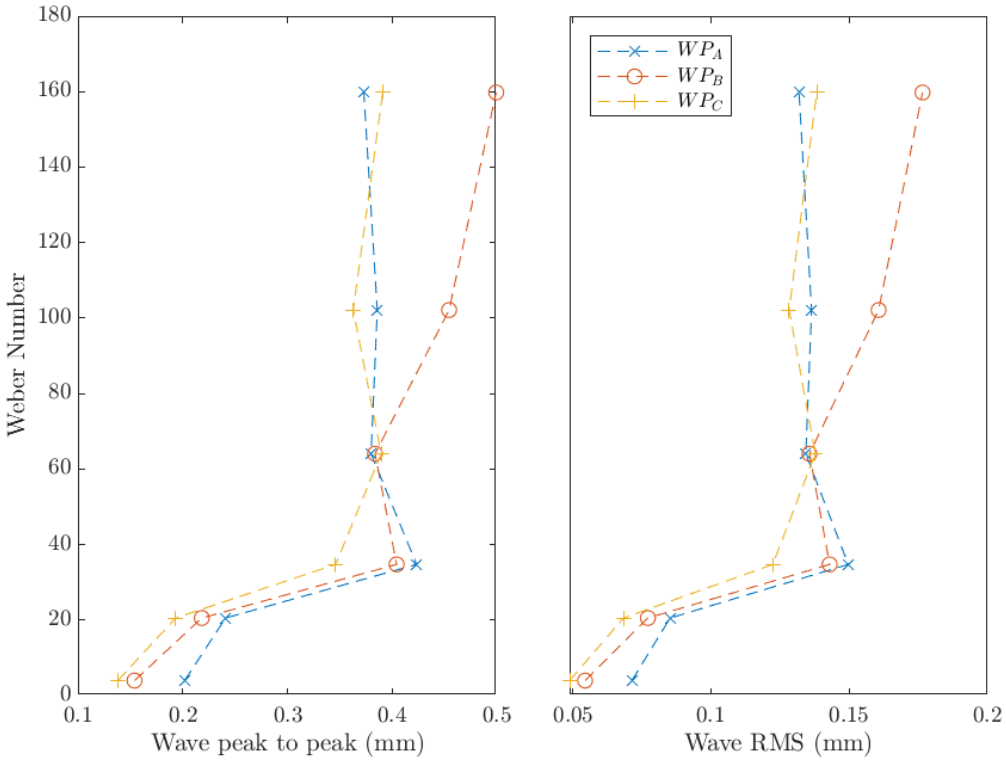

Figure 8.56: Wave Probe Fluctuation vs Weber number (see eq. 2.6.1).

8.3 Summary

A set of experimental shallow flow conditions were designed and tested to generate a novel dataset. These all focus specifically on a single gradient with varying flow rate (and hence flow depth). This simulates a real-life an open channel cunnette in a fixed outdoor location with different upstream rainfall that drives a variation in discharge rate, flow depth and relative submergence. These conditions generated a range of free-surface features <1mm in height.

U-level analysis was carried out to identify coherent structures within the flow. At any point within the flow, any instantaneous velocity fluctuations can be compared against a threshold related to the standard deviation of the velocity signal. Any part which exceeds a 'Starting threshold' would begin a turbulent 'event'. Once the fluctuation magnitude falls below the ending threshold (again, relative to the standard deviation), that specific event would be classified as finished. This time-series analysis process was repeated for every spatial point within the flow field to identify events passing through space over time. Based on this, a 2D image of the flow could be generated showing a snapshot of the turbulent structures which exists at that moment. As there were 15,000 frames of PIV vector fields, 15,000 frames of turbulent U-level events could be created and merged into an animation recreating the movement of turbulent events occurring during the experimental tests. Based on this, virtual probes were placed at two streamwise locations within the flow, both just beneath the free-surface to extract the turbulent event signals. A cross correlation was carried out using the entire time series to determine the rate at which these structures moved when near the free-surface. This was repeated for all flow conditions and the results compared with the PIV streamwise velocity profiles. With the exception of the lowest flow depth (49mm) and the flow condition with experimental errors (149mm), it was found that the turbulent features moved at the same speed (to within 1%) of the local bulk flow. This supports the findings of Fujita (2011) and Nichols and Rubinato (2016). Of interest is that this relationship appears to breakdown in the shallowest flow condition where the bulk flow is the slowest. This could be due to the shear from the bed having a more significant influence on the free surface due

to their very close proximity. To explore this further, Proper Orthogonal Decomposition was applied to the PIV velocity fluctuation data.

A review of the turbulence energy distribution stored across the POD modes indicated that a large proportion of the turbulence energy are contained in the first 10 modes, whilst modes 11 to 50 are able to capture the majority of any remaining energy. The decomposition was able to separate smaller eddies from the larger ones revealing a fascinating interaction of the turbulence cascade which was previously obscured due to the convolution between the small and large eddies. Whereas the U-level analysis was only able to give binary true-false black/white representation of a turbulent structure, the reconstructed velocity field using different POD modes now have scalar values assigned. Since each mode is properly orthogonal, there are no overlaps from one mode to the next. Animation of the reconstructed velocity field using the higher modes reveals small turbulence structures growing from the bed, detaching and being advected whilst the first modes show large structures being propagated at the same rate as the bulk velocity. Furthermore, a deeper look at the vertical POD modes indicates the existence of periodic structures across all modes. These decrease in size and may be partially responsible for the vertical movement of the free-surface. Since the combination of every POD mode in the vertical direction will return over 99% of the original velocity field, the consistent variation in free-surface fluctuation amplitude seems highly linked to the existence of these periodic features below the free-surface.

To quantify this in a more mathematical sense, the first 10 POD modes were used to recreate a velocity field containing the large high energy eddies whilst modes 11 to 50 were used to create another velocity field with only the smaller low energy eddies. At three defined locations within the flow (near the bed, in the center of the flow and near the free-surface), the velocity fluctuation was extracted for quadrant analysis. The quadrant plot of the high energy velocity field showed that the ejection and sweep quadrants were the strongest in the middle depth of the flow whereas for the low energy velocity field, the strongest ejection and sweep quadrants were near the bed locations. One likely explanation supported by the visualisation techniques is that the ejection events from the smaller eddies (in POD modes 11 to 50) at the bed, gain energy (to enter POD modes 1 to 10) and physically grow into

larger into the middle of the flow depth. Near the free-surface, all POD modes indicate a significant contraction of the vertical velocity fluctuation (due to the free surface). However, it is important to note that the vertical velocity does not fall to zero (unlike in a rigid lid assumption).

This brings about a transition to a discussion on the assessment on whether a rigid lid used in CFD simulation is suitable.

The final representative CFD simulations were developed with a two stage approach whereby a coarse mesh was created for an initial RANS simulation to develop flow statistics before being mapped onto a finer second stage mesh with LES to develop transient turbulent structures. Both the resulting time-averaged velocity profiles and the turbulent intensities from the simulation correlate well with experimental results. However, Reynolds' shear stresses associated with the vertical velocity fluctuation were artificially reduced to zero near the rigid lid. This is due to the boundary condition forcing zero vertical velocity at the rigid lid resulting in no vertical fluctuations. This was shown to affect the flow from a normalised depth of 1 (at the free-surface) to 0.7 (30% below the free-surface).

It was visually proven in both CFD simulations and experimental tests that turbulent structures that are generated at the bed can impinge on the free-surface/rigid lid. For rigid lids, once the turbulent structure impacts, the structure is then pinned at the lid and dragged along by the bulk flow until the structure dissipates. If the lid were to be flexible and representative of a real free-surface, the response of the turbulent structures are certainly expected to be different.

By studying the creation and movement of turbulent structures using different Q-criterion thresholds, it is clear that the turbulent structures that are generated at the bed do occasionally grow to enough magnitude to break through the near surface water layer and impinge on the water surface above. Since a rigid lid has very different properties to a flexible lid, it can be said that the rigidity of the lid will lead to an unrealistic response of the turbulent structure as it impacts the free-surface. The impingement of the turbulent structures on a free-surface would be expected to generate at least some upwards deformation of the

free-surface shortly followed by a downwards deformation due to the gravitational force and surface tension pulling the flexible lid back downwards. The fluctuation of the free-surface would likely transmit some force or pressure onto the coherent structure possibly causing it to re-enter the central part of the flow and possibly triggering new bursts at the bed to restart the cycle again. Therefore, whilst the turbulence energy generation and dissipation may appear to be mostly normal deeper inside the flow; near the free surface, the lack of vertical motion forces poor Reynolds shear stresses which has a negative influence on the abillity of the simulation to accurately represent the rest of the flow depth. This is particularly true for shallow flows with large obstacles or high flow rates because they cause larger turbulent structures and have a smaller distance to the free-surface.

The final chapter will highlight the key results presented in the context of the research question and outline the work that could be explored further in the future.

Chapter 9

Conclusion

9.1 Summary of work

This research included experimental and numerical investigation of free surface flows. Experimentally, four different types of sensing techniques were calibrated and tested.

To measure the free surface, a traditional conductance wave probe and two different types of 3D infra-red sensors from Microsoft's Kinect gaming series were used. To determine the distance from the Kinect sensors to the object, the two infra-red sensors used an infra-red speckle pattern and time-of-flight technique respectively. To prevent infra-red light from penetrating the free-surface and ensure it was reflected back to the sensors, a white TiO_2 colourant was mixed into the water to make it opaque. The required concentration and the time taken for the colourant to settle and affect the measurement was determined through testing. For milk, the minimum concentration was 4%. For TiO_2, the minimum concentration was 0.01%. With TiO_2, it was discovered that after 20 minutes the perceived depth may drop by up to 4mm (with milk, for Kinect generation 2, the drop was less than 0.4mm). However, the milk will go stale within several days so its use in large scale applications are limited.

The resolution capability of the Kinect sensors was explored by deploying the sensors to

measure gravity waves. To measure the velocity within the flow, stereo planar Particle Imaging Velocimetry (PIV) and Acoustic Doppler Velocimetry (ADV) was used. The stereo PIV was calibrated and set up in a novel configuration with the laser plane being projected up from beneath the flume bed. It was demonstrated that water-filled hollow glass spheres can allow the PIV laser plane through the sphere bed with some static refraction of the laser plane which can be corrected easily. The ADV data was post-processed with de-spiking. Six experimental flow conditions were designed to give a range of relative submergence and turbulence conditions representative of typical real-life shallow water open channel flows. Each condition was repeated twice, one with seeding particles for stereo PIV measurements and one was with TiO_2 for Kinect 3D infra-red measurements. For all flow conditions, the ADV was used at several different streamwise positions to monitor the stabilisation of the velocity profile upstream of the main PIV (and Kinect) detection zone. After measuring the free-surface with the Kinect, conductance probes were subsequently used to measure the free-surface fluctuation at three point source locations within the Kinect infra-red sensors' field of view. These allowed the different free-surface measurements to be compared.

In total, over 10TB of high-quality experimental data has been generated and validated. This forms a new data set for benchmark comparison against future work. This is accessible via Zenodo at https://zenodo.org/records/8151332.

In computational modelling, it was demonstrated that it is not currently possible to fully simulate an open channel, rough bed, free-surface flow in a 10m long flume with a 0.5m width at shallow flow depths. This is because the resolution of mesh required both at the bed and at the free-surface creates a computational problem that is beyond the capability of modern computers to solve in a reasonable time. Instead, periodic boundaries must be used in the streamwise direction to minimise the mesh size required. The domain size was chosen based on the size of the largest eddy (normally approximately the same size as the depth of flow). 11 periodic flow simulations were carried out. These were based on three different flow depths which corresponded to three experimental flow conditions (49mm, 69mm, 109mm). Three smooth bed simulations were used to test the periodic boundary conditions and establish a mean velocity and turbulence profile. This used RANS modelling and an artificial roughness

factor. The transition from RANS to LES was tested using two simulations of flow over a spherical boulder (The first one with RANS and then using the results to initialise a second simulation using LES). This also enabled the optimal mesh over a single hemi-sphere to be identified to inform the mesh for the full bed of spherical tops. Finally, six rough bed simulations using a rigid lid approximation were created. These were was based on the same three 49mm,69mm and 109mm experimental flow conditions, using RANS first to generate average flow statistics before transitioning to an LES simulation to resolve transient turbulent structures. A rough bed with a flexible lid was also tested using *potentialFreeSurfaceFoam*. In total, it is estimated that over 500,000 CPU hours have been consumed in periodic flow simulations.

9.2 Key contributions

Four main key novel contributions were achieved in this PhD programme.

1. Novelty in PIV plane setup

   Traditional planar PIV of open channel flows attempts to illuminate the flow particles by shining a laser from above the water surface down into the flow. However, the fluctuating nature of the free-surface causes almost random fluctuations in the illumination intensity. This is hard to correct in imaging and negatively impacts the accuracy of the vector calculation. In this study, the laser plane is instead projected upwards from beneath the bed into the flow . Where the laser hits the bed of spheres, hollow transparent spheres are used so that the laser is able to pass through. Water fills the hollow structure reducing refraction effects. As the spheres are closely packed in a hexagonal pattern, they remain stationary relative to the fluctuating free-surface. Thus, the illumination remains fixed and any irregularities in light intensity can be easily corrected using a sliding background prior to the vector calculation. This work is currently in the process of being submitted to the Journal of Flow Measurement and Instrumentation (see Figure 9.1).

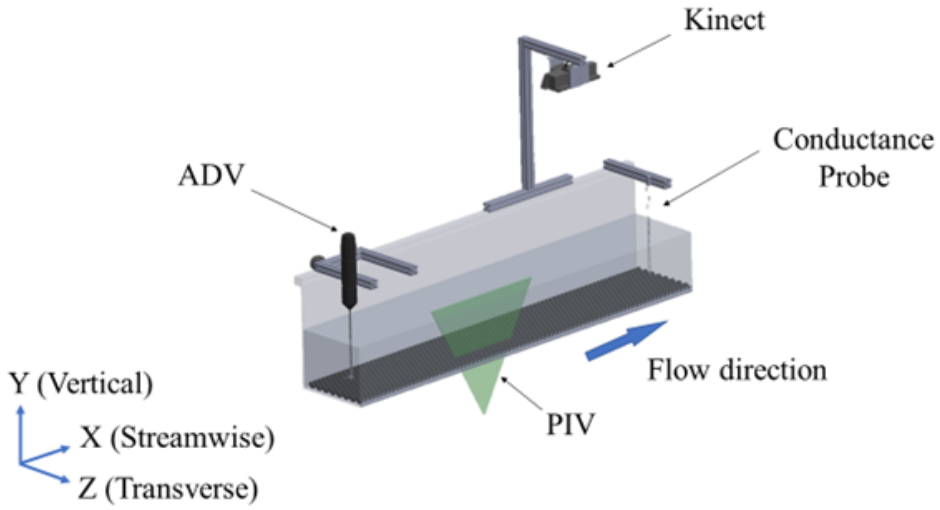

Figure 9.1: PIV laser of flow over bed of hollow transparent spheres.

2. Novelty in Free-surface sensing

   Traditional free-surface sensors are only able to measure in 1D (e.g. conductance probe) or 2D (e.g. LIF). Two 3D infrared sensors from the gaming industry was tested, with their performance carefully analysed and findings published in the Sensors journal. Primarily it was discovered that such sensors are able to confidently detect dynamic free-surfaces with vertical features larger than about 1cm. Below this size, features are more difficult to extract and various sources of noise affect the accuracy of the measurement. The capability of such low-cost, off the shelf components demonstrates how technology transfer from other applications can generate new data and methods for measuring open channel flows (see Figure 9.2).

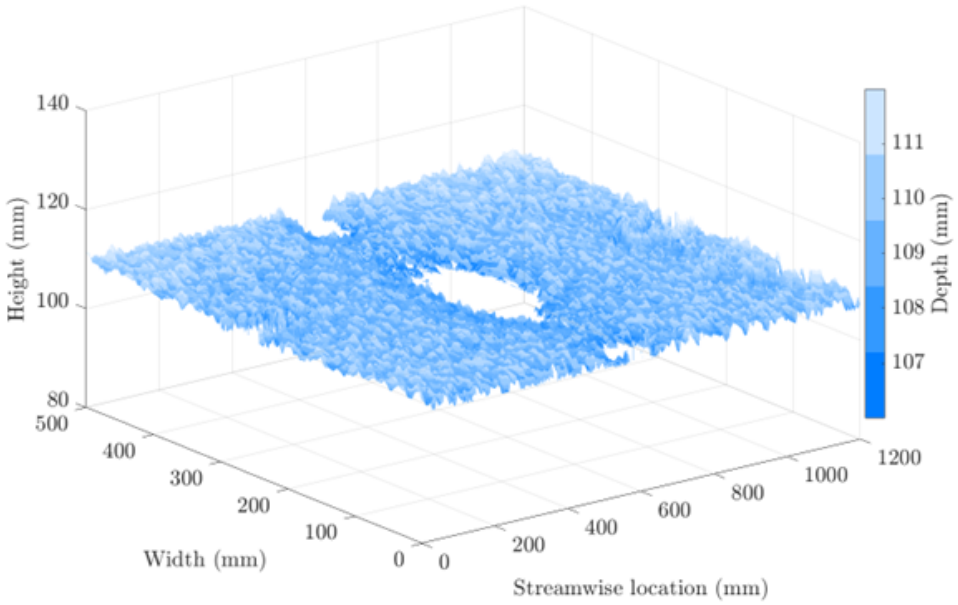

Figure 9.2: Novel 3D infrared sensor testing (video here: https://www.youtube.com/playlist?list=PLBxWPtPkf1M_8a_3Y1E4TTlvL-ZCYGaF_).

3. Novelty in Turbulent structure identification

   Turbulent structure identification methods such as U-level rely on only the streamwise velocity fluctuation to give a binary decision on whether a turbulent structure is present in a particular spatial location at a specific time. This is achieved by comparing a location's instantaneous streamwise velocity deviation from the time-averaged mean, with its standard deviation. On the other hand, Quadrant analysis was originally intended to look at the general "time-processed" behaviour of flow at different locations. In this study, the general behaviour aspect is reversed to enable identification of transient structures. This utilises both streamwise and vertical fluctuations, increasing the relevance of the data when compared to 1D approaches such as U-level. When compared to established methods Q-criterion and Lambda-2, it can be observed that the structures identified are similar in shape and size. Unlike Q-criterion and Lambda-2, this Quadrant analysis identification method can use 2D data instead of 3D making it mathematically simpler and less computationally intensive. This work is currently in the process of being submitted to the Journal of Hydraulic Research (see Figure 9.3).

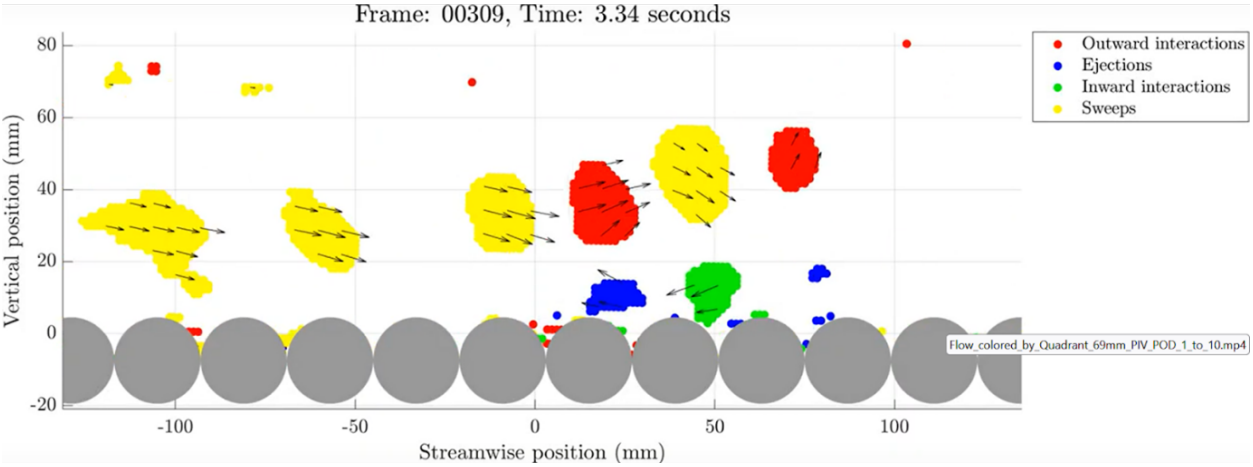

Figure 9.3: New Turbulent Structure Identification method.

4. Novelty in CFD simulation

   OpenFOAM is one of the most popular open-source CFD software packages. However, within its example codes, there are no turbulent open channel periodic flows. This study produced such an example which is validated against experimental results and published in the Water journal. Users are able to easily adapt this with their own bed geometry (as an .stl file) and flow conditions for a turbulent open channel simulation. The scripts and all settings are shared using github and can be accessed freely (see Figure 9.4).

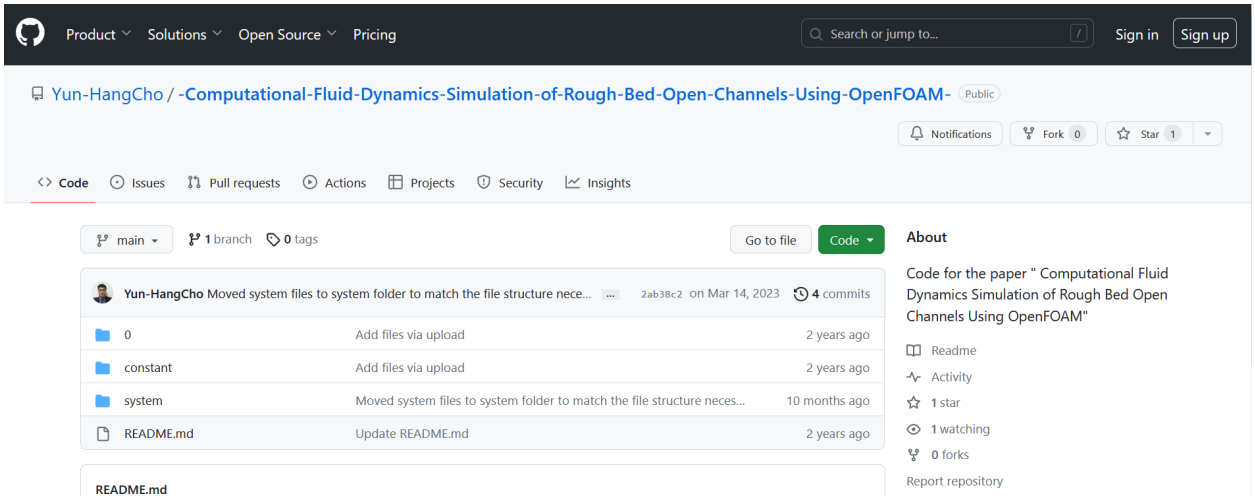

Figure 9.4: New OpenFOAM contribution (available on github at: github.com/Yun-HangCho).

9.3 Comparison with research questions

In response to the two main research questions posed in this thesis:

- Does a rigid lid boundary in shallow rough bed open channel simulations affect the accuracy of the flow characteristics for flows with small free-surface fluctuations?

Yes, the rigid lid free-surface approximation has been shown to affect the accuracy of turbulence and Reynolds' shear stress. This rigid lid approximation assumes that because the vertical fluctuation at the free-surface is <1mm, it can be assumed to be zero. This is unrealistic as it effectively removes all Reynolds' shear stress with a vertical component (i.e. the streamwise-vertical and the transverse-vertical shear stresses). In addition, by removing the vertical component, the turbulent structures cannot be properly resolved and modelled near the free-surface. This is despite a very fine, scale-resolving Wall Adapting Large Eddy model being used.

- Can low-cost, off-the-shelf 3D infrared sensors be used in measuring smaller turbulent free-surfaces? What are the challenges?

Not at the moment. The sensors tested were two Kinect infrared 3D sensor from the gaming industry. Although it was able to accurately detect the shape of large scale features, the distances measured were affected by noise. This noise obscured much of the smaller scale features. Placing the sensors closer to the surface is one way to improve the resolution but doing so will reduce the available field of view. In order to prevent the light rays from penetrating the free-surface of the flow and detecting the distance of other objects (such as the flow bed), the flow needed to be coloured white. This is normally only practical in laboratory environments.

9.4 Implications

The rigid lid assumption has been used for many studies as an acceptable approximation. It has now been shown that this is not realistic, especially for flows with low-depth (high relative submergence and Manning's number). The inaccurate turbulence modelling near the free-surface is likely to impact proper modelling of turbulence-driven processes such as sediment transportation and pollutant mixing.

Poor modelling of sediment transportation can cause severe issues. For example, during periods of high rainfall, the increased flows normally lead to more sediment transportation in channels. The prediction of where the sediment may be deposited helps to identify key areas inside the water infrastructure network that are likely to become blocked. This can inform mitigation efforts (e.g. to widen a channel or install sensors at a particular location). Poor modelling will lead to incorrect identification of at-risk regions, reducing the effect of these mitigation efforts. Poor modelling of pollutant mixing significantly impacts understand of how different types of pollutants are spread throughout the water network. For example, in the event of a combined sewage discharge into a clean river, there will be a reduced understanding of how the sewage will mix and dissipate into the river. Predictions of water quality at different points in time or space may be adversely affected.

9.5 Future work

To rule out any potential source of error from the use of the OpenFOAM and/or turbulence modelling, future work could also simulate the same flow conditions using different software. For example, the same flow conditions were simulated in collaboration with colleagues at UCL using their Hydro3D software. For these simulations, an Immersed Boundary Method (IBM) was used with a free-surface modelling technique known as the Level Set Method (LSM). The only similarities are in the flow conditions and in the use of an LES WALE turbulence modelling method.

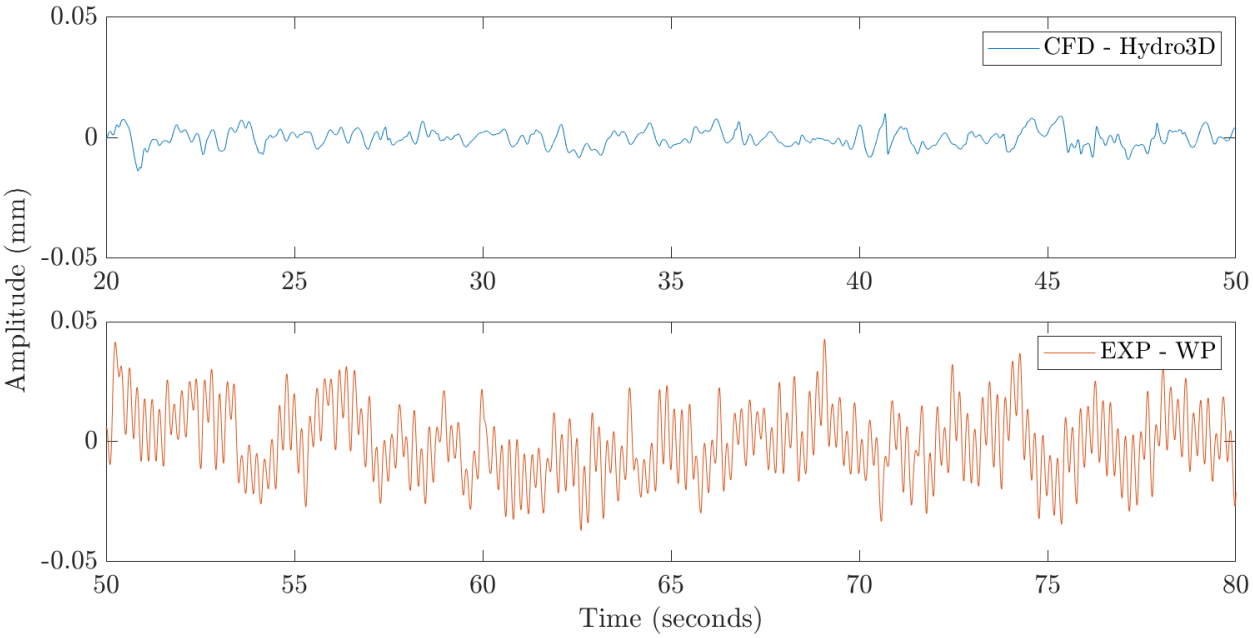

Figure 9.5: Free-surface amplitude comparison between the Hydro3D free-surface simulation at 49mm flow depth and the experimental data collected using the wave probe. 'zphi' is the free-surface fluctuation term from Hydro3D.

Figure 9.5 shows the free-surface positions extracted from the UCL Hydro3D CFD simulation and the experimental wave probe data presented earlier in this thesis. The standard deviation of the experimental wave probe fluctuation was 0.0144mm whilst the standard deviation of the CFD simulation was 0.0041mm. This is over half as small.

Figure 9.6 shows a distribution of the vertical fluctuations which indicates that the simulated free-surface is of a smaller magnitude than the experimental ones ($\pm$0.04 mm from the

experiment and ±0.02 mm). This suggests that historical use of the rigid lid maybe due to simulated free-surface being smaller in amplitude than expected.

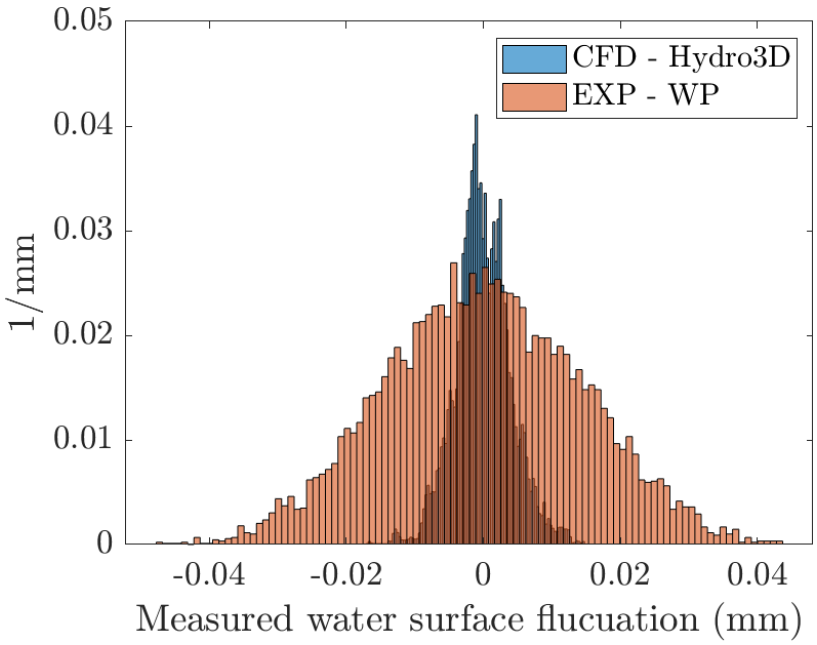

Figure 9.6: Histogram comparison between the Hydro3D free-surface simulation at 49mm flow depth (labelled 'CFD - Hydro3D') and the experimental data collected using the wave probe (labelled 'EXP - WP').

To better compare the decay and distribution of the free-surface fluctuations, the signals were normalised against the maximum amplitudes and compared using the power spectrum (see Figure 9.7). The results show that the distribution and decay of the power is quite similar between the experiments and the Hydro 3D simulation suggesting that the modelling and decay of the fluctuations in the simulation is working properly. Therefore, future work should investigate the sub-surface turbulence and the free-surface fluctuation generation mechanism rather than excessive attenuation of the existing fluctuations.

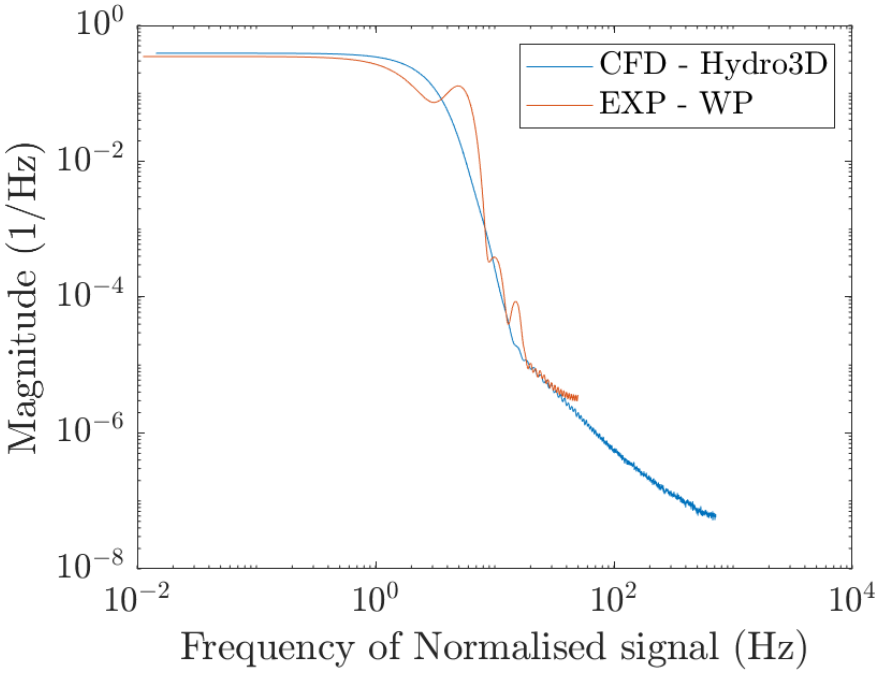

Figure 9.7: Power spectrum comparison between the Hydro3D free-surface simulation at 49mm flow depth and the experimental data collected using the wave probe. The signals have been normalised by the maximum amplitude.

References

Adrian, R. J., C. D. Meinhart and C. D. Tomkins (Nov. 2000). 'Vortex organization in the outer region of the turbulent boundary layer'. In: *Journal of Fluid Mechanics* 422. Copyright: Copyright 2018 Elsevier B.V., All rights reserved., pp. 1–54. ISSN: 0022-1120. DOI: 10.1017/S0022112000001580.

ADS (2020). URL: https://www.adsenv.com/.

Alfonsi, G., D. Ferraro, A. Lauria and R. Gaudio (Aug. 2019). 'Large-eddy simulation of turbulent natural-bed flow'. In: *Physics of Fluids* 31 (8), p. 085105. ISSN: 1070-6631. DOI: 10.1063/1.5116522. URL: http://aip.scitation.org/doi/10.1063/1.5116522.

Ambrosino, F. and A. Funel (2006). 'OpenFOAM and Fluent Features in CFD Simulations on CRESCO High Power Computing System'. In: *Final Workshop of Grid Projects*. DOI: https://doi.org/10.1016/j.jweia.2012.02.023. URL: https://www.sciencedirect.com/science/article/pii/S0167610512000475.

Ariza, Cristian, Cintia Casado, Ruo Qian Wang, Eric Adams and Javier Marugán (July 2018). 'Comparative Evaluation of OpenFOAM® and ANSYS® Fluent for the Modeling of Annular Reactors'. In: *Chemical Engineering and Technology* 41 (7), pp. 1473–1483. ISSN: 15214125. DOI: 10.1002/ceat.201700455.

Bayon, Arnau and P. López-Jiménez (Mar. 2015). 'Numerical analysis of hydraulic jumps using OpenFOAM'. In: *Journal of Hydroinformatics* 17, pp. 662–678. DOI: 10.2166/hydro.2015041.

Bayon, Arnau, Francisco Valles-Morán and P. López-Jiménez (July 2015). 'Numerical analysis and validation of South Valencia Sewage Collection System Diversion'. In: 36th IAHR World CongressAt: The Hague (Holland).

Belytschko, T., Y. Krongauz, D. Organ, M. Fleming and P. Krysl (Dec. 1996). 'Meshless methods: An overview and recent developments'. In: *Computer Methods in Applied Mechanics and Engineering* 139 (1-4), pp. 3–47. ISSN: 0045-7825. DOI: 10.1016/S0045-7825(96)01078-X.

Berkooz, G, P Holmes and J L Lumley (1993). 'The Proper Orthogonal Decomposition in the Analysis of Turbulent Flows'. In: *Annual Review of Fluid Mechanics* 25.1, pp. 539–575. DOI: 10.1146/annurev.fl.25.010193.002543. URL: https://doi.org/10.1146/annurev.fl.25.010193.002543.

Best, Jim (2005). 'The fluid dynamics of river dunes: A review and some future research directions'. In: *Journal of Geophysical Research: Earth Surface* 110.F4. DOI: https://doi.org/10.1029/2004JF000218. URL: https://agupubs.onlinelibrary.wiley.com/doi/abs/10.1029/2004JF000218.

Bhaganagar, Kiran (2008). 'Direct numerical simulation of unsteady flow in channel with rough walls'. In: *Physics of Fluids* 20.10, p. 101508. DOI: 10.1063/1.3005859. URL: https://doi.org/10.1063/1.3005859.

Bomminayuni, Sandeep and Thorsten Stoesser (July 2011). 'Turbulence Statistics in an Open-Channel Flow over a Rough Bed'. In: *Journal of Hydraulic Engineering* 137 (11), pp. 1347–1358. ISSN: 0733-9429. DOI: 10.1061/(ASCE)HY.1943-7900.0000454. URL: https://ascelibrary.org/doi/abs/10.1061/%5C%28ASCE%5C%29HY.1943-7900.0000454%20https://ascelibrary.org/doi/10.1061/%5C%28ASCE%5C%29HY.1943-7900.0000454.

Boulos, M.N., B. Resch, J.G. Crowley, D.N. Breselin, G. Sohn, R. Burtner and E.a Jezierski (2011). 'Crowdsourcing, citizen sensing and sensor web technologies for public and environmental health surveillance and crisis management: trends, OGC standards and application examples'. In: *International Journal Health Geographics*. DOI: doi:https://doi.org/10.1186/1476-072X-10-67.

Boussinesq, Joseph (1842-1929). Auteur du texte (1877). 'Essai sur la théorie des eaux courantes / par J. Boussinesq'. In: URL: https://gallica.bnf.fr/ark:/12148/bpt6k56673076.

Brocchini, M. and D. H. Peregrine (2001). 'The dynamics of strong turbulence at free surfaces. Part 1. Description'. In: *Journal of Fluid Mechanics* 449, pp. 225–254. ISSN: 00221120. DOI: 10.1017/S0022112001006012.

Brown, Claire, Matt Walpole, Lucy Simpson and Megan Tierney (2011). *UK National Ecosystem Assessment (2011) The UK National Ecosystem Assessment: Technical Report.* URL: http://uknea.unep-wcmc.org/Resources/tabid/82/Default.aspx.

Brown, G.L. and A. Roshko (1974). 'On density effects and large structure in turbulent mixing layers'. In: *Journal of Fluid Mechanics* 64.4, pp. 775–816.

Cea, L., J. Puertas and L. Pena (Mar. 2007). 'Velocity measurements on highly turbulent free surface flow using ADV'. In: *Experiments in Fluids* 42 (3), pp. 333–348. ISSN: 07234864. DOI: 10.1007/s00348-006-0237-3.

CFD support (2020). *Laminar vs. Turbulent Flow.* URL: https://www.cfdsupport.com/OpenFOAM-Training-by-CFD-Support/node334.html.

CFD-Wiki (2022). *Turbulence intensity.* URL: https://www.cfd-online.com/Wiki/Turbulence_intensity (visited on 09/10/2022).

Chadwick, A. and J. Morfett (2002). *Hydraulics in Civil and Environmental Engineering.* CRC Press. DOI: https://doi.org/10.4324/9780203027776.

Cho, Y.-H., M. Rubinato and A. Nichols (2017). *Sensing of surface water patterns using Kinect. IAHR World Congress.* KL, Malaysia.

Cho, Yun Hang, My Ha Dao and Andrew Nichols (Oct. 2022). 'Computational fluid dynamics simulation of rough bed open channels using openFOAM'. In: *Frontiers in Environmental Science* 10, p. 1906. ISSN: 2296665X. DOI: 10.3389/FENVS.2022.981680/BIBTEX.

Churchill Controls (2011). 'Wave Monitor Manual'. In: pp. 1–19. URL: https://www.churchill-controls.co.uk/all-products/level-measurement/wave-monitor/.

Clark, Shawn P. and Nicholas Kehler (Oct. 2011). 'Turbulent flow characteristics in circular corrugated culverts at mild slopes'. In: *Journal of Hydraulic Research* 49 (5), pp. 676–684. ISSN: 00221686. DOI: 10.1080/00221686.2011.596399.

Colebrook, C F (1939). 'Turbulent Flow in Pipes, with Particular Reference to the Transition Region Between the Smooth and Rough Pipe Laws.' In: *Journal of the Institution of*

Civil Engineers 11.4, pp. 133–156. DOI: 10.1680/ijoti.1939.13150. URL: https://doi.org/10.1680/ijoti.1939.13150.

Colombini, M. and G. Parker (1995). 'Longitudinal streaks'. In: *Journal of Fluid Mechanics* 304, pp. 161–183.

Combes, Benoit, A. Guibert, Etienne Mémin and Dominique Heitz (Nov. 2011). 'Free-surface flows from Kinect: Feasibility and limits'. In: *FVR2011*. Poitiers, France, 4 p. URL: https://hal.archives-ouvertes.fr/hal-00676338.

Combés, Benoit, Dominique Heitz, Anthony Guibert and Etienne Mémin (2015). 'A particle filter to reconstruct a free-surface flow from a depth camera'. In: *Fluid Dynamics Research* 47.5, p. 51404. ISSN: 01695983. DOI: 10.1088/0169-5983/47/5/051404. eprint: 1601.00507. URL: http://dx.doi.org/10.1088/0169-5983/47/5/051404.

COMSOL (2015). *Diffusion Equation: Fick's Laws of Diffusion*. URL: https://uk.comsol.com/multiphysics/diffusion-equation.

Corti, A., S. Giancola, G. Maineteti and R. Sala (2016). 'A metrological characterization of the Kinect V2 time-of-flight camera'. In: *Robotics and Autonomous Systems* 75, pp. 584–594.

Daly, Bart J (1969). 'A technique for including surface tension effects in hydrodynamic calculations'. In: *Journal of Computational Physics* 4.1, pp. 97–117. ISSN: 0021-9991. DOI: https://doi.org/10.1016/0021-9991(69)90042-4. URL: https://www.sciencedirect.com/science/article/pii/0021999169900424.

Dancey, C. L., M. Balakrishnan, P. Diplas and A. N. Papanicolaou (2000). 'The spatial inhomogeneity of turbulence above a fully rough, packed bed in open channel flow'. In: *Experiments in Fluids 2000 29:4* 29 (4), pp. 402–410. ISSN: 1432-1114. DOI: 10.1007/S003489900107. URL: https://link.springer.com/article/10.1007/s003489900107.

Dantec Dynamics (2017). *Hot wire and hot film probes*. URL: https://www.dantecdynamics.com/hot-wire-and-hot-film-probes..

Danz, Adam (2020). *quiverRotate*. URL: https://uk.mathworks.com/matlabcentral/fileexchange/75055-quiverrotate.

Defina, Andrea (1996). *Transverse spacing of low-speed streaks in a channel flow over a rough bed*. Ed. by Stuart McLelland Sean J. Bennett James L. Best. 1st ed. Vol. 1. J. Wiley & Sons, pp. 87–99. ISBN: 0-471-95723-2.

Deshpande, Suraj S., Lakshman Anumolu and Mario F. Trujillo (Jan. 2012). 'Evaluating the performance of the two-phase flow solver interFoam'. In: *Computational Science and Discovery* 5 (1), p. 14016. ISSN: 17494680. DOI: 10.1088/1749-4699/5/1/014016. URL: www.iop.org/journals/csd.

Dey, Subhasish (2014). 'Turbulence in Open-Channel Flows'. In: *Fluvial Hydrodynamics: Hydrodynamic and Sediment Transport Phenomena*. Berlin, Heidelberg: Springer Berlin Heidelberg, pp. 95–187. ISBN: 978-3-642-19062-9. DOI: 10.1007/978-3-642-19062-9_3. URL: https://doi.org/10.1007/978-3-642-19062-9_3.

Dey, Subhasish and Ratul Das (2012). 'Gravel-Bed Hydrodynamics: Double-Averaging Approach'. In: *Journal of Hydraulic Engineering* 138.8, pp. 707–725. DOI: 10.1061/(ASCE)HY.1943-7900.0000554. URL: https://ascelibrary.org/doi/abs/10.1061/%5C%28ASCE%5C%29HY.1943-7900.0000554.

Dolcetti, G. (2016a). *Remote monitoring of shallow turbulent flows*. Sheffield: University of Sheffield.

Dolcetti, G., K.V. Horoshenkov, A. Krynkin and S. Tait (2016). 'Frequency-wavenumber spectrum of the free surface of shallow turbulent flows over a rough boundary'. In: *Physics of Fluids* 28.10.

Dolcetti, Giulio (2016b). *Remote monitoring of shallow turbulent flows based on the Doppler spectra of airborne ultrasound*. URL: https://etheses.whiterose.ac.uk/16006/1/Thesis_final_corrections_Dolcetti.pdf.

Ducros, F., Nicoud Franck and Thierry Poinsot (Jan. 1998). 'Wall-Adapting Local Eddy-Viscosity Models for Simulations in Complex Geometries'. In: *Numerical Methods for Fluid Dynamics VI*.

European Commission (2000). *Establishing a framework for Community action in the field of water policy*. Tech. rep. Brussels: EU Publications Office.

Evonik Industries (2018). *VESTOSINT® Polyamide 12 Powders*. URL: https://www.vestosint.com/en.

Falco, R. E. (1977). 'Coherent motions in the outer region of turbulent boundary layers'. In: *The Physics of Fluids* 20.10, S124–S132. DOI: 10.1063/1.861721. URL: https://aip.scitation.org/doi/abs/10.1063/1.861721.

Fasso, C. (1987). *Birth of Hydraulics During the Renaissance Period. Hydrualics and Hydraulic Research: A Historical Overview*.

Feinberg, Milo, Pal Schmitt, James Donegan and Jarlath McEntee (Sept. 2019). 'An efficient numerical framework for the assessment of free surface effects on crossflow tidal turbines'. English. In: *European Wave and Tidal Energy Conference (EWTEC 2019): Proceedings*. European Wave and Tidal Energy Conference, EWTEC ; Conference date: 01-09-2019 Through 06-09-2019. URL: https://ewtec.org/conferences/ewtec-2019/.

Ferziger, J.H. (2002). *Computational Methods for Fluid Dynamics*.

Fowler, H. J. and C. G. Kilsby (2003). 'A regional frequency analysis of United Kingdom extreme rainfall from 1961 to 2000'. In: *International Journal of Climatology* 23.11, pp. 1313–1334. DOI: https://doi.org/10.1002/joc.943. URL: https://rmets.onlinelibrary.wiley.com/doi/abs/10.1002/joc.943.

Fujita, I.F. (2011). *Advection features of water surface profile in turbulent open-channel flow with hemisphere roughness elements*. Vis Mec Proc(4), 1.

Gakhar, Saksham, Jeffrey R. Koseff and Nicholas T. Ouellette (2020). 'On the surface expression of bottom features in free-surface flow'. In: *Journal of Fluid Mechanics* 900. ISSN: 14697645. DOI: 10.1017/jfm.2020.548.

Garcia Novo, Patxi, Yusaku Kyozuka and Maria Jose Ginzo Villamayor (2019). 'Evaluation of turbulence-related high-frequency tidal current velocity fluctuation'. In: *Renewable Energy* 139.C, pp. 313–325. DOI: 10.1016/j.renene.2019.02.. URL: https://ideas.repec.org/a/eee/renene/v139y2019icp313-325.html.

Goring, Derek G. and Vladimir I. Nikora (2002). 'Despiking Acoustic Doppler Velocimeter Data'. In: *Journal of Hydraulic Engineering* 128.1, pp. 117–126. DOI: 10.1061/(ASCE)

0733-9429(2002)128:1(117). URL: https://ascelibrary.org/doi/abs/10.1061/%5C%28ASCE%5C%290733-9429%5C%282002%5C%29128%5C%3A1%5C%28117%5C%29.

Grass, A. J. (1971). 'Structural features of turbulent flow over smooth and rough boundaries'. In: *Journal of Fluid Mechanics* 50.2, pp. 233–255. DOI: 10.1017/S0022112071002556.

Grass, A. J., R. J. Stuart, M. Mansour-Tehrani, J. D. A. Walker and F. T. Smith (1991). 'Vortical structures and coherent motion in turbulent flow over smooth and rough boundaries'. In: *Philosophical Transactions of the Royal Society of London. Series A: Physical and Engineering Sciences* 336.1640, pp. 35–65. DOI: 10.1098/rsta.1991.0065. URL: https://royalsocietypublishing.org/doi/abs/10.1098/rsta.1991.0065.

Guardian (July 2022). *China floods leave at least 12 dead, with thousands evacuated — China — The Guardian*. URL: https://www.theguardian.com/world/2022/jul/18/china-floods-sichuan-gansu-province-dead-thousands-evacuated.

Guide, OpenFOAM User (2022). 'OpenFOAM User Guide: k-omega-SST Delayed Eddy Simulation (DES)'. In: URL: https://www.openfoam.com/documentation/guides/latest/doc/guide-turbulence-des-k-omega-sst-des.html.

Gulliver, J.S. and M.J. Halverson (1987). 'Measurements of large streamwise vortices in an open-channel flow'. In: *Water Resource Research* 23.1, pp. 115–123.

Handler, Robert A. and Qi Zhang (2013). 'Direct numerical simulations of a sheared interface at low wind speeds with applications to infrared remote sensing'. In: *IEEE Journal of Selected Topics in Applied Earth Observations and Remote Sensing* 6.3, pp. 1086–1091. ISSN: 19391404. DOI: 10.1109/JSTARS.2013.2241736.

Hansard, M.L. (2012). 'Time of Flight Cameras'. In: *Principles, Methods, and Applications. In SpringerBriefs in Computer Science (p.* Springer, p. 95.

Hänsch, Susann, Dirk Lucas, Thomas Höhne, Eckhard Krepper and Gustavo Montoya (2013). 'Comparative simulations of free surface flows using vof-methods and a new approach for multi-scale interfacial structures'. In: vol. 1 C. ISBN: 9780791855560. DOI: 10.1115/FEDSM2013-16104.

Harlow, F. and J. Welch (1965). 'Numerical Calculation of Time-Dependent Viscous Incompressible Flow of Fluid with Free Surface'. In: *The Physics of Fluids* 8.

Hart, John (2016). 'Comparison of Turbulence Modeling Approaches to the Simulation of a Dimpled Sphere'. In: *Procedia Engineering* 147. The Engineering of SPORT 11, pp. 68–73. ISSN: 1877-7058. DOI: https://doi.org/10.1016/j.proeng.2016.06.191. URL: https://www.sciencedirect.com/science/article/pii/S1877705816306385.

Hedlund, André (2014). 'Evaluation of RANS turbulence models for the simulation of channel flow'. PhD thesis. URL: http://urn.kb.se/resolve?urn=urn:nbn:se:uu:diva-238649.

Heinz, S. (2020). 'A review of hybrid RANS-LES methods for turbulent flows: Concepts and applications'. In: *Progress in Aerospace Sciences* 114, p. 100597.

Higuera, Pablo, Javier L. Lara and Inigo J. Losada (Jan. 2013). 'Simulating coastal engineering processes with OpenFOAM®'. In: *Coastal Engineering* 71, pp. 119–134. ISSN: 03783839. DOI: 10.1016/j.coastaleng.2012.06.002.

Hirt, C. and B. Nichols (1979). 'Volume of Fluid (VOF) Method for the dynamics of free boundaries'. In: *Journal of Computational Physics* 39, pp. 201–225.

Holzmann, Tobias (Nov. 2019). *Mathematics, Numerics, Derivations and OpenFOAM®*. Holzmann CFD.

Home, D., M. F. Lightstone and M. S. Hamed (2009). 'Validation of DES-SST Based Turbulence Model for a Fully Developed Turbulent Channel Flow Problem'. In: *Numerical Heat Transfer, Part A: Applications* 55.4, pp. 337–361. DOI: 10.1080/10407780902720841. URL: https://doi.org/10.1080/10407780902720841.

Horoshenkov, K. V., A Nichols, S. J. Tait and G A Maximov (2013a). 'The pattern of surface waves in a shallow free-surface flow'. In: *Journal of Geophysical Research: Earth Surface*.

— (2013b). 'The pattern of surface waves in shallow free surface flow'. In: *Journal of Geophysical Research: Earth Surface* 118, pp. 1864–1876.

Hughes, Roger L. (2010). 'A mathematical determination of von Karman's constant, K'. In: *http://dx.doi.org/10.1080/00221686.2007.9521792* 45 (4), pp. 563–566. ISSN: 00221686. DOI: 10.1080/00221686.2007.9521792. URL: https://www.tandfonline.com/doi/abs/10.1080/00221686.2007.9521792.

Hujaleh, A. (2016). *Remote Sensing of Flow Processes to Quantify Rates of Mixing*. Sheffield: University of Sheffield.

Hunt, JCR., AA. Wray and P. Moin (1988). 'Eddies stream, and convergence zones in turbulent flows'. In: *Proceedings of the 1988 Summer Program*. URL: https://ntrs.nasa.gov/citations/19890015184.

Hyun, B. S., R. Balachandar, K. Yu and V. C. Patel (Sept. 2003). 'Assessment of PIV to measure mean velocity and turbulence in open-channel flow'. In: *Experiments in Fluids* 35 (3), pp. 262–267. ISSN: 07234864. DOI: 10.1007/s00348-003-0652-7. URL: https://link.springer.com/article/10.1007/s00348-003-0652-7.

Jee, S. and K. Shariff (2014). 'Detached-eddy simulation based on the v2-f model'. In: *International Journal of Heat and Fluid Flow* 46, pp. 84–101.

Jeong, Jinhee and Fazle Hussain (1995). 'On the identification of a vortex'. In: *Journal of Fluid Mechanics* 285, pp. 69–94. DOI: 10.1017/S0022112095000462.

Kadivar, Mohammadreza, David Tormey and Gerard McGranaghan (May 2021). 'A review on turbulent flow over rough surfaces: Fundamentals and theories'. In: *International Journal of Thermofluids* 10. DOI: 10.1016/J.IJFT.2021.100077.

Kazemi, Ehsan, Andrew Nichols, Simon Tait and Songdong Shao (2017). 'SPH modelling of depth-limited turbulent open channel flows over rough boundaries'. In: *International Journal for Numerical Methods in Fluids* 83.1, pp. 3–27. ISSN: 10970363. DOI: 10.1002/fld.4248.

Keylock, Chris, R.J. Hardy, Daniel Parsons, R.I. Ferguson, Stuart Lane and Keith Richards (Aug. 2005). 'The theoretical foundations and potential for large-eddy simulation (LES) in fluvial geomorphic and sedimentological research'. In: *Earth-Science Reviews* 71, pp. 271–304. DOI: 10.1016/j.earscirev.2005.03.001.

Kline, S.J., W.C. Reynolds, F.A. Schraub and P.W. Runstadler (1967). 'The structure of turbulent boundary layers'. In: *Journal of Fluid Mechanics* 30.4, pp. 741–773.

Kolmogorov, A.N. (1941). 'The Local Structure of Turbulence in Incompressible Viscous Fluid for Very Large Reynolds''. In: *Numbers. Doklady Akademiia Nauk SSSR* 30, pp. 301–305.

Komori, Satoru, Yasuhiro Murakami and Hiromasa Ueda (1989). 'The Relationship between Surface-Renewal and Bursting Motions in an Open-Channel Flow'. In: *Journal of Fluid Mechanics* 203.103, pp. 103–123. ISSN: 14697645. DOI: 10.1017/S0022112089001394.

Kompenhans, J., M. Raffel, L. Dieterle, T. Dewhirst, H. Vollmers, K. Ehrenfried, C. Willert, K. Pengel, C. Kähler, A. Schröder and O. Ronneberger (2000). 'Particle Image Velocimetry in Aerodynamics: Technology and Applications in Wind Tunnels'. In: *Journal of Visualization* 2 (3-4), pp. 229–244. ISSN: 13438875. DOI: 10.1007/BF03181440. URL: https://link.springer.com/article/10.1007/BF03181440.

Korachi, Issam al, M. Benelmostafa, Najim Salhi, M. Boulerhcha and J.D. Chaabane (Jan. 2012). 'Application for wale model in numerical simulations of shallow water turbulents flows'. In: *Physical and Chemical News* 66, pp. 49–55.

Krogstad, P. A., R. A. Antonia and L. W.B. Browne (1992). 'Comparison between rough- and smooth-wall turbulent boundary layers'. In: *Journal of Fluid Mechanics* 245, pp. 599–617. ISSN: 1469-7645. DOI: 10.1017/S0022112092000594. URL: https://www.cambridge.org/core/journals/journal-of-fluid-mechanics/article/abs/comparison-between-rough-and-smoothwall-turbulent-boundary-layers/227C483011F779BC3BE385DCF7FCA

Kumar, S., R. Gupta and S. Banerjee (1998). 'An experimental investigation of the characteristics of free-surface turbulence in channel flow'. In: *Physics of Fluids* 10.2, pp. 437–456. DOI: 10.1063/1.869573. URL: https://doi.org/10.1063/1.869573.

Lamb, Horace (1993). *Hydrodynamics*. New York : Cambridge University Press.

Launder, B.E. and B.I. Sharma (1974). 'Application of the energy-dissipation model of turbulence to the calculation of flow near a spinning disc'. In: *Letters in Heat and Mass Transfer* 1.2, pp. 131–137. ISSN: 0094-4548. DOI: https://doi.org/10.1016/0094-4548(74)90150-7. URL: https://www.sciencedirect.com/science/article/pii/0094454874901507.

LaVision (2018). *LaVision - Downloads - Manuals*. URL: https://www.lavision.de/en/downloads/manuals/.

— (2022). *Cameras for PIV*. URL: https://www.lavision.de/en/products/cameras/cameras-for-piv/.

Leonardi, S., P. Orlandi, R. J. Smalley, L. Djenidi and R. A. Antonia (2003). 'Direct numerical simulations of turbulent channel flow with transverse square bars on one wall'. In: *Journal of Fluid Mechanics* 491, pp. 229–238. DOI: 10.1017/S0022112003005500.

Lien, Kim, Jason Monty, Michelle Chong and Andrew Ooi (Jan. 2004). 'The Entrance Length for Fully Developed Turbulent Channel Flow'. In: *15th Australasian Fluid Mechanics Conference*.

Lommer, M. (2002). 'Using Laser-Induced Flourescece in the study of surface water turbulence'. In: *Journal of Florensic Science. Boston*.

Lu, Louise and Volker Sick (2013). 'High-speed particle image velocimetry near surfaces'. In: *Journal of visualized experiments : JoVE* (76). ISSN: 1940-087X. DOI: 10.3791/50559. URL: https://pubmed.ncbi.nlm.nih.gov/23851899/.

Luchik, T. S. and W. G. Tiederman (1987). 'Timescale and structure of ejections and bursts in turbulent channel flows'. In: *Journal of Fluid Mechanics* 174, pp. 529–552. ISSN: 1469-7645. DOI: 10.1017/S0022112087000235. URL: https://www.cambridge.org/core/journals/journal-of-fluid-mechanics/article/abs/timescale-and-structure-of-ejections-and-bursts-in-turbulent-channel-flows/003AE029BFD5ECB6314EE87813659504.

Manes, Costantino, Dubravka Pokrajac, Ian McEwan and Vladimir Nikora (Dec. 2009). 'Turbulence structure of open channel flows over permeable and impermeable beds: A comparative study'. In: *Physics of Fluids* 21 (12), p. 125109. ISSN: 1070-6631. DOI: 10.1063/1.3276292. URL: https://aip.scitation.org/doi/abs/10.1063/1.3276292.

Manning, Robert (1895). 'On the flow of water in open channels and pipes.' In: *Journal of the Institution of Civil Engineers* XXIV.4, pp. 179–207. URL: https://www.worldcat.org/title/on-the-flow-of-water-in-open-channels-and-pipes/oclc/81979335.

Mansilla, Caterina Torres (2018). 'Numerical Modelling of Hydraulic Free Surface Flows and Scale Effects Associated with Physical Modelling'.

Martínez-Aranda, Sergio, Javier Pato, Daniel Caviedes-Voullième, I. García-Palacín and Pilar Garcia-Navarro (Aug. 2018). 'Towards transient experimental water surfaces: A new

benchmark dataset for 2D shallow water solvers'. In: *Advances in Water Resources* 121. DOI: 10.1016/j.advwatres.2018.08.013.

Menter, F. (1993). 'Zonal Two Equation k-w Turbulence Models For Aerodynamic Flows'. In: *23rd Fluid Dynamics, Plasmadynamics, and Lasers Conference*. DOI: 10.2514/6.1993-2906. URL: https://arc.aiaa.org/doi/abs/10.2514/6.1993-2906.

Microsoft (2014). *Kinect hardware: Kinect hardware key features and benefits. Microsoft Developer Website*.

Miura, Hideaki and Shigeo Kida (1997). 'Identification of Tubular Vortices in Turbulence'. In: *Journal of the Physical Society of Japan* 66.5, pp. 1331–1334. DOI: 10.1143/JPSJ.66.1331. URL: https://doi.org/10.1143/JPSJ.66.1331.

Miyake, Yutaka, Koichi Tsujimoto and Naonori Nagai (Jan. 2002). 'Numerical simulation of channel flow with a rib-roughened wall'. In: *Journal of Turbulence* 3, N35. DOI: 10.1088/1468-5248/3/1/035.

Monaghan, J. J. (Feb. 1994). 'Simulating Free Surface Flows with SPH'. In: *Journal of Computational Physics* 110 (2), pp. 399–406. ISSN: 0021-9991. DOI: 10.1006/JCPH.1994.1034.

Montecchia, Matteo, Geert Brethouwer, Stefan Wallin, Arne V. Johansson and Thilo Knacke (Dec. 2019). 'Improving LES with OpenFOAM by minimising numerical dissipation and use of explicit algebraic SGS stress model'. In: *Journal of Turbulence* 20 (11-12), pp. 697–722. ISSN: 1468-5248. DOI: 10.1080/14685248.2019.1706740. URL: https://www.tandfonline.com/doi/full/10.1080/14685248.2019.1706740.

Morgan, Gerald (2013). *Application of the Interfoam VoF Code to Coastal Wave/Structure Interaction*. URL: https://researchportal.bath.ac.uk/en/studentTheses/application-of-the-interfoam-vof-code-to-coastal-wavestructure-in.

Mori, Nobuhito, Takuma Suzuki and Shohachi Kakuno (2007). 'Noise of Acoustic Doppler Velocimeter Data in Bubbly Flows'. In: *Journal of Engineering Mechanics* 133.1, pp. 122–125. DOI: 10.1061/(ASCE)0733-9399(2007)133:1(122). URL: https://ascelibrary.org/doi/abs/10.1061/%28ASCE%290733-9399%282007%29133%3A1%28122%29.

Moura Paredes, Guilherme (2012). 'Application of dynamic meshes to potentialFreeSurfaceFoam to solve for 6DOF floating body motions'. In: URL: https://vbn.aau.dk/en/publications/application-of-dynamic-meshes-to-potentialfreesurfacefoam-to-solv.

Muraro, Fabio, Giulio Dolcetti, Andrew Nichols, Simon J. Tait and Kirill V. Horoshenkov (Jan. 2021). 'Free-surface behaviour of shallow turbulent flows'. In: *Journal of Hydraulic Research* 59 (1), pp. 1–20. ISSN: 0022-1686. DOI: 10.1080/00221686.2020.1870007. URL: https://www.tandfonline.com/doi/full/10.1080/00221686.2020.1870007.

Nagaosa, R. and R.A. Handler (2003). 'Statistical analysis of coherent vortices near a free surface in fully developed turbulence'. In: *Physical Fluids* 15.2, pp. 375–394.

Nagaosa, Ryuichi (1999). 'Direct numerical simulation of vortex structures and turbulent scalar transfer across a free surface in a fully developed turbulence'. In: *Physics of Fluids* 11.6, pp. 1581–1595. DOI: 10.1063/1.870020. URL: https://doi.org/10.1063/1.870020.

Nagib, H. M. and Y. G. Guezennec (1986). 'On the structure of turbulent boundary layers.' In: 30.

National Climate Change Secretariat (2012). *Climate Change & Singapore: Challenges. Opportunities. Partnerships*, pp. 1–140. ISBN: 9789810724924. URL: papers2://publication/uuid/1DCC6A06-6AD9-4EAB-9A3D-BBDD9A056CA7.

Nezu, I. and H. Nakagawa (1991). *Turbulence in Open-Channel Flows*. Kyoto: CRC Press.

Nezu, Iehisa (June 1977). *Turbulence structure in a open channel flow*. Kyoto, Japan: Kyoto University.

— (2005). 'Open-Channel Flow Turbulence and Its Research Prospect in the 21st Century'. In: *Journal of Hydraulic Engineering* 131.4, pp. 229–246. DOI: 10.1061/(ASCE)0733-9429(2005)131:4(229).

Nezu, Iehisa and Wolfgang Rodi (1986). 'Open-channel Flow Measurements with a Laser Doppler Anemometer'. In: *Journal of Hydraulic Engineering* 112.5, pp. 335–355. DOI: 10.1061/(ASCE)0733-9429(1986)112:5(335). URL: https://ascelibrary.org/doi/

abs/10.1061/%5C%28ASCE%5C%290733-9429%5C%281986%5C%29112%5C%3A5%5C%28335%5C%29.

Nezu, Iehisa and Michio Sanjou (2011). 'PIV and PTV measurements in hydro-sciences with focus on turbulent open-channel flows'. In: *Journal of Hydro-environment Research* 5.4. IMAGE VELOCIMETRY, pp. 215–230. ISSN: 1570-6443. DOI: https://doi.org/10.1016/j.jher.2011.05.004. URL: https://www.sciencedirect.com/science/article/pii/S1570644311000554.

Nguyen, Van Thinh (2015). '3D numerical simulation of free surface flows over hydraulic structures in natural channels and rivers'. In: *Applied Mathematical Modelling* 39.20, pp. 6285–6306. ISSN: 0307-904X. DOI: https://doi.org/10.1016/j.apm.2015.01.046. URL: https://www.sciencedirect.com/science/article/pii/S0307904X15000499.

Nichols, A., M. Rubinato, YH. Cho and J. Wu (June 2020). 'Optimal use of titanium dioxide colourant to enable water surfaces to be measured by kinect sensors'. In: *f* 20 (12), pp. 1–17. ISSN: 14248220. DOI: 10.3390/s20123507.

Nichols, Andrew (2015). *Free surface dynamics in shallow turbulent flows*. Sheffield: University of Sheffield.

Nichols, Andrew, K. V. Horoshenkov and S. J. Tait (2014). 'Shallow gravel-bed river flows: The behaviour of the free surface and the flow information contained within'. In: *Proceedings of the International Conference on Fluvial Hydraulics, RIVER FLOW 2014*, pp. 301–309. DOI: 10.1201/b17133-46.

Nichols, Andrew and Matteo Rubinato (2016). 'Remote sensing of environmental processes via low-cost 3D free-surface mapping'. In: *4th IHAR Europe Congress, Liege, Belgium, 27-29 July 2016*.

Nichols, Andrew, Simon J. Tait, Kirill V. Horoshenkov and Simon J. Shepherd (2016). 'A model of the free surface dynamics of shallow turbulent flows'. In: *Journal of Hydraulic Research* 54.5, pp. 516–526. ISSN: 00221686.

Nichols, B.D. and C.W. Hirt (1973). 'Calculating three-dimensional free surface flows in the vicinity of submerged and exposed structures'. In: *Journal of Computational Physics* 12.2, pp. 234–246. ISSN: 0021-9991. DOI: https://doi.org/10.1016/S0021-

9991(73)80013-0. URL: https://www.sciencedirect.com/science/article/pii/S0021999173800130.

Nicoud, F. and F. Ducros (1999). 'Subgrid-Scale Stress Modelling Based on the Square of the Velocity Gradient Tensor'. In: *Flow, Turbulence and Combustion 1999 62:3* 62 (3), pp. 183–200. ISSN: 1573-1987. DOI: 10.1023/A:1009995426001. URL: https://link.springer.com/article/10.1023/A:1009995426001.

Nikuradse, Joann (1933). 'Stromungsgesetze in Rauhem Rohren. (Laws of Turbulent Pipe Flow in Smooth Pipes.)' In: *VDI-Forschungsheft:* URL: https://boulderschool.yale.edu/sites/default/files/files/Nikuradse%5C%20Laws%5C%20of%5C%20Flow%5C%20in%5C%20Rough%5C%20Pipes%5C%201933.pdf.

Nortek (2017). 'Quick Guide – Vectrino – Nortek Support Center'. In: URL: https://support.nortekgroup.com/hc/en-us/articles/360029839231-Quick-Guide-Vectrino.

— (2018). 'The comprehensive manual for velocimeters'. In: ISSN: 0196-6553.

OpenFOAM (2016). *section 4.3. Mesh generation with the blockMesh utility.* URL: https://www.openfoam.com/documentation/user-guide/4-mesh-generation-and-conversion/4.3-mesh-generation-with-the-blockmesh-utility.

— (July 2017). *OpenFOAM 5.0 Released — OpenFOAM Foundation — OpenFOAM.* URL: https://openfoam.org/release/5-0/.

— (2022). *OpenFOAM: User Guide: Residuals.* URL: https://www.openfoam.com/documentation/guides/latest/doc/guide-solvers-residuals.html.

Osborn, Timothy J. and Mike Hulme (July 2002). 'Evidence for trends in heavy rainfall events over the UK'. In: *Philosophical transactions. Series A, Mathematical, physical, and engineering sciences* 360 (1796), pp. 1313–1325. ISSN: 1364-503X. DOI: 10.1098/RSTA.2002.1002. URL: https://pubmed.ncbi.nlm.nih.gov/12809141/.

Ouriemi, Malika, Pascale Aussillous, Yannick Peysson and Élisabeth Guazzelli (June 2007). 'Determination of the critical Shields number for particle erosion in laminar flow'. In: *Physics of Fluids - PHYS FLUIDS* 19. DOI: 10.1063/1.2747677.

Patel, S. and Y. Chauhan (2014). 'Heart attack detection and medical attention using motion sensing device'. In: *International Journal Scientific Research Publications* 4.1, pp. 1–4.

Patterson, M Ashton (Apr. 1958). 'Turbulence Spectrum Studies in the Sea with Hot Wires - [PDF Document]'. In: *Limnology and Oceanography* 3 (2), pp. 171–180. URL: https://fdocuments.in/document/turbulence-spectrum-studies-in-the-sea-with-hot-wires.html.

Peakall, J. and J. Warburton (1996). 'Surface tension in small hydraulic river models - the significance of the Weber number'. In: *Journal of Hydrology (New Zealand)* 35.2, pp. 199–212. ISSN: 00221708, 24633933. URL: http://www.jstor.org/stable/43944772.

Presse, Agence France (July 2022). *After the floods: Germany's Ahr valley then and now – in pictures — Germany — The Guardian*. URL: https://www.theguardian.com/world/2022/jul/13/floods-then-and-now-photographs-germany-ahr-valley-flooding-disaster-july-2021.

Reynolds, Osborne (1883). 'XXIX. An experimental investigation of the circumstances which determine whether the motion of water shall be direct or sinuous, and of the law of resistance in parallel channels'. In: *Philosophical Transactions of the Royal Society of London* 174, pp. 935–982. DOI: 10.1098/rstl.1883.0029. URL: https://royalsocietypublishing.org/doi/abs/10.1098/rstl.1883.0029.

Rezaeiravesh, S. and M. Liefvendahl (May 2018). 'Effect of grid resolution on large eddy simulation of wall-bounded turbulence'. In: *Physics of Fluids* 30 (5), p. 055106. ISSN: 10897666. DOI: 10.1063/1.5025131. URL: http://aip.scitation.org/doi/10.1063/1.5025131.

Rogati, Monica (June 2017). *The AI Hierarchy of Needs — Hacker Noon*. URL: https://hackernoon.com/the-ai-hierarchy-of-needs-18f111fcc007 (visited on 30/09/2020).

Roy, A., T. Buffin-Belanger and H.a Lamarre (2004). 'ize, shape and dynamics of large scale turbulent flow structures in a gravel bed river'. In: *Journalof Fluid Mechanics* 500, pp. 1–27.

Ruonan, Bai, Cao Liekai, Wang Xingkui and Li Danxun (2016). 'Comparison of ADV and PIV Measurements in Open Channel Flows'. In: *Procedia Engineering* 154. 12th Interna-

tional Conference on Hydroinformatics (HIC 2016) - Smart Water for the Future, pp. 995–1001. ISSN: 1877-7058. DOI: https://doi.org/10.1016/j.proeng.2016.07.588. URL: https://www.sciencedirect.com/science/article/pii/S1877705816319774.

Sarbolandi, Hamed, Damien Lefloch and Andreas Kolb (2015). 'Kinect range sensing: Structured-light versus Time-of-Flight Kinect'. In: *Computer Vision and Image Understanding* 139, pp. 1–20. ISSN: 1090235X. DOI: 10.1016/j.cviu.2015.05.006. eprint: 1505.05459. URL: http://dx.doi.org/10.1016/j.cviu.2015.05.006.

Savelsberg, Ralph and Willem Van De Water (2009). 'Experiments on free-surface turbulence'. In: *Journal of Fluid* 619, pp. 95–125.

Savelsberg, Ralph and Willem van de Water (Jan. 2008). 'Turbulence of a Free Surface'. In: *Phys. Rev. Lett.* 100 (3), p. 034501. DOI: 10.1103/PhysRevLett.100.034501. URL: https://link.aps.org/doi/10.1103/PhysRevLett.100.034501.

Savory, E. and N. Toy (1986a). *Experiments in Fluids The flow regime in the turbulent near wake of a hemisphere **, pp. 181–188.

— (1986b). 'Hemisphere and hemisphere-cylinders in turbulent boundary layers'. In: *Journal of Wind Engineering and Industrial Aerodynamics* 23. Special Issue 6th Colloquium on Industrial Aerodynamics Building Aerodynamics, pp. 345–364. ISSN: 0167-6105. DOI: https://doi.org/10.1016/0167-6105(86)90054-1. URL: https://www.sciencedirect.com/science/article/pii/0167610586900541.

Schlichting, Hermann and Klaus Gersten (Oct. 2016). *Boundary-Layer Theory*. Springer Berlin Heidelberg, pp. 1–799. ISBN: 9783662529195. DOI: 10.1007/978-3-662-52919-5.

Schmitt, Pál, Christian Windt, Josh Davidson, John V. Ringwood and Trevor Whittaker (Sept. 2020). 'Beyond VoF: alternative OpenFOAM solvers for numerical wave tanks'. English. In: *Journal of Ocean Engineering and Marine Energy*. ISSN: 2198-6444. DOI: 10.1007/s40722-020-00173-9.

Schulze, Lydia ; and Carsten Thorenz (2014). *The Multiphase Capabilities of the CFD Toolbox OpenFOAM for Hydraulic Engineering Applications Zur Verfügung gestellt in Kooperation mit/Provided in Cooperation with: Kuratorium für Forschung im Küsteningenieurwesen (KFKI)*, pp. 1007–1016. URL: https://hdl.handle.net/20.500.11970/99530.

Seddighi, M., S. He, D. Pokrajac, T. O'Donoghue and A. E. Vardy (2015). 'Turbulence in a transient channel flow with a wall of pyramid roughness'. In: *Journal of Fluid Mechanics* 781, pp. 226–260. DOI: 10.1017/jfm.2015.488.

Sen, M., Kiran Bhaganagar and V.Juttijudata (2007). 'Application of proper orthogonal decomposition (POD) to investigate a turbulent boundary layer in a channel with rough walls'. In: *Journal of Turbulence* 8, N41. DOI: 10.1080/14685240701615960. URL: https://doi.org/10.1080/14685240701615960.

Sethian, J. A. and Peter Smereka (2003). 'LEVEL SET METHODS FOR FLUID INTERFACES'. In: *Annual Review of Fluid Mechanics* 35.1, pp. 341–372. DOI: 10.1146/annurev.fluid.35.101101.161105. URL: https://doi.org/10.1146/annurev.fluid.35.101101.161105.

Shahriari, Shervin, Josef Schneider and Gerald Zenz (Aug. 2020). 'Selected applications of an open-source three-dimensional computational fluid dynamic code in hydraulic engineering'. In: *Österreichische Wasser- und Abfallwirtschaft* 72.7, pp. 291–307. ISSN: 1613-7566. DOI: 10.1007/s00506-020-00676-7. URL: https://doi.org/10.1007/s00506-020-00676-7.

Shen, Lian, Xiang Zhang, Dick K. P. Yue and George S. Triantafyllou (1999). 'The surface layer for free-surface turbulent flows'. In: *Journal of Fluid Mechanics* 386, pp. 167–212. DOI: 10.1017/S0022112099004590.

Shuard, Adrian M., Hisham B. Mahmud and Andrew J. King (Apr. 2016). 'Comparison of two-phase pipe flow in openFOAM with a mechanistic model'. In: vol. 121. Institute of Physics Publishing. DOI: 10.1088/1757-899X/121/1/012018.

Singh, K. M., N. D. Sandham and J. J. R. Williams (2007). 'Numerical Simulation of Flow over a Rough Bed'. In: *Journal of Hydraulic Engineering* 133.4, pp. 386–398. DOI: 10.1061/(ASCE)0733-9429(2007)133:4(386). URL: https://ascelibrary.org/doi/abs/10.1061/%5C%28ASCE%5C%290733-9429%5C%282007%5C%29133%5C%3A4%5C%28386%5C%29.

Sirovich, L. (1987). 'Turbulence and the dynamics of coherent structures, Part I: Coherent structures'. In: *Quarterly of Applied Mathematics* 45, p. 561.

Smith, Barton L. and Douglas R. Neal (2016). 'Particle Image Velocimetry'. In: ed. by Richard W. Johnson. 2nd ed. Routledge.

Smith, W. A. M. Nimmo, S. A. Thorpe and A. Graham (1999). 'Surface effects of bottom-generated turbulence in a shallow tidal sea.' In: 400, pp. 251–254.

Spalart, P. R., W.-H. Jou, M. Strelets, S. R. Allmaras, C. Liu, L. Sakell and Z. Liu (1997). 'Comments on the Feasibility of LES for Wings, and on a Hybrid RANS/LES Approach, International conference; 1st, Advances in DNS/LES: Direct numerical simulation and large eddy simulation'. In: *Advances in DNS/LES: Direct numerical simulation and large eddy simulation, International conference; 1st, Advances in DNS/LES: Direct numerical simulation and large eddy simulation.* Greyden Press; pp. 137–148. ISBN: 1570743657. URL: https://www.tib.eu/de/suchen/id/BLCP%3ACN032430355.

Stauffer, Beat and Dorothee Spuhler (1991). *Open Channels and Drains — SSWM.* URL: https://sswm.info/sswm-university-course/module-2-centralised-and-decentralised-systems-water-and-sanitation/further/open-channels-and-drains.

Stoesser, Thorsten (2014). 'Large-eddy simulation in hydraulics: Quo Vadis?' In: *Journal of Hydraulics Research* 52 (4), pp. 441–452. DOI: 10.1080/00221686.2014.944227. URL: https://www.tandfonline.com/doi/abs/10.1080/00221686.2014.944227.

Stoesser, Thorsten, Fabrice Mathey, Jochen Fröhlich and Wolfgang Rodi (Jan. 2003). 'LES OF FLOW OVER MULTIPLE CUBES'. In: *ERCOFTAC Bulletin.*

Stoesser, Thorsten and Wolfgang Rodi (Jan. 2007). 'Large Eddy Simulation of Open-Channel Flow Over Spheres'. In: *High Performance Computing in Science and Engineering '06.* Springer Berlin Heidelberg. Chap. 4, pp. 321–330. ISBN: 978-3-540-36165-7. DOI: 10.1007/978-3-540-36183-1_23.

Strelets, M. (2001). 'Detached eddy simulation of massively separated flows'. In: *39th Aerospace Sciences Meeting and Exhibit.* DOI: 10.2514/6.2001-879. URL: https://arc.aiaa.org/doi/abs/10.2514/6.2001-879.

Tamburrino, Aldo and John S. Gulliver (1999). 'Grosses structures en écoulement turbulent en canal à surface libre'. In: *Journal of Hydraulic Research* 37.3, pp. 363–380. ISSN: 00221686. DOI: 10.1080/00221686.1999.9628253.

Tan, Hugh and C. Yeo (Jan. 2009). 'The Potential of Native Woody Plants for Enhancing the Urban Waterways and Water Bodies Environment in Singapore'. In.

Tanaka, Mitsuru and Shigeo Kida (June 1998). 'Characterization of vortex tubes and sheets'. In: *Physics of Fluids A: Fluid Dynamics* 5 (9), p. 2079. ISSN: 0899-8213. DOI: 10.1063/1.858546. URL: https://aip.scitation.org/doi/abs/10.1063/1.858546.

Taylor, G.I. (1935). 'Statistical Theory of Turbulence'. In: *The Royal Society* 151.873, pp. 444–454.

Teixeira, M.A. (2006). 'On the initiation of surface waves by turbulent shear flow'. In: *Dynamics of Atmospheres and Oceans* 41.1, pp. 1–27.

Teuber, Katharina, Tabea Broecker, Arnau Bayón, Gunnar Nützmann and Reinhard Hinkelmann (2019). 'CFD-modelling of free surface flows in closed conduits'. In: *Progress in Computational Fluid Dynamics, An International Journal* 19 (6), p. 368. ISSN: 1468-4349. DOI: 10.1504/pcfd.2019.103266.

Thakkar, M., A. Busse and N. Sandham (2017). 'Direct numerical simulation of turbulent channel flow over a surrogate for Nikuradse-type roughness'. In: *Journal of Fluid Mechanics* 837.

Thorenz, Carsten and Jann Strybny (July 2012). *On the numerical modelling of filling-emptying system for locks*. URL: https://henry.baw.de/ere/20.500.11970/106397?locale-attribute=en.

Tudor, Sarah (June 2022). *Sewage pollution in England's waters*. URL: https://lordslibrary.parliament.uk/sewage-pollution-in-englands-waters/.

UK Government (2008). *Climate Change Act 2008*. URL: https://www.legislation.gov.uk/ukpga/2008/27/contents.

Ulanowski, Joseph Z. and Nobuhito Mori (2014). *Despiking*. URL: https://uk.mathworks.com/matlabcentral/fileexchange/15361-despiking.

Versteeg, H.a (2007). *An Introduction fo Computational Fluid Dynamics: The Finite Folyme Method Approach*.

Vinci, Leonardo da (1517). *A deluge*. URL: https://www.rct.uk/collection/912380/a-deluge.

Wacławczyk, Marta and Martin Oberlack (Oct. 2011). 'Closure proposals for the tracking of turbulence-agitated gas–liquid interfaces in stratified flows'. In: *International Journal of Multiphase Flow* 37 (8), pp. 967–976. ISSN: 0301-9322. DOI: 10.1016/J.IJMULTIPHASEFLOW.2011.05.006.

Wallace, James M (2016). 'Quadrant Analysis in Turbulence Research: History and Evolution'. In: *Annu. Rev. Fluid Mech* 48, pp. 131–158. DOI: 10.1146/annurev-fluid-122414-034550. URL: www.annualreviews.org.

Wasenmüller, Oliver and Didier Stricker (2017). 'Comparison of kinect v1 and v2 depth images in terms of accuracy and precision'. In: *Lecture Notes in Computer Science (including subseries Lecture Notes in Artificial Intelligence and Lecture Notes in Bioinformatics)* 10117 LNCS, pp. 34–45. ISSN: 16113349. DOI: 10.1007/978-3-319-54427-4_3.

Welahettige, Prasanna and Knut Vaagsaether (Dec. 2018). 'Comparison of OpenFOAM and ANSYS Fluent'. In: vol. 142. Linköping University Electronic Press, pp. 1005–1012. DOI: 10.3384/ecp171421005.

Welch, Peter D. (1967). 'The Use of Fast Fourier Transform for the Estimation of Power Spectra: A Method Based on Time Averaging Over Short, Modified Periodograms'. In: *IEEE Transactions on Audio and Electroacoustics* 15 (2), pp. 70–73. ISSN: 00189278. DOI: 10.1109/TAU.1967.1161901.

Wilcox, David C (2008). 'Formulation of the k-! Turbulence Model Revisited'. In: DOI: 10.2514/1.36541.

— (1988). 'Reassessment of the scale-determining equation for advanced turbulence models'. In: *AIAA Journal* 26.11, pp. 1299–1310. DOI: 10.2514/3.10041. URL: https://doi.org/10.2514/3.10041.

Xie, Zhihua, Binliang Lin, Roger A. Falconer, Andrew Nichols, Simon J. Tait and Kirill V. Horoshenkov (2021). 'Large-eddy simulation of turbulent free surface flow over

a gravel bed'. In: *https://doi.org/10.1080/00221686.2021.1908437* 60 (2), pp. 205–219. ISSN: 00221686. DOI: 10.1080/00221686.2021.1908437. URL: https://www.tandfonline.com/doi/abs/10.1080/00221686.2021.1908437.

Yakhot, V., S. A. Orszag, S. Thangam, T. B. Gatski and C. G. Speziale (July 1992). 'Development of turbulence models for shear flows by a double expansion technique'. In: *Physics of Fluids A* 4 (7), pp. 1510–1520. ISSN: 08998213. DOI: 10.1063/1.858424. URL: http://aip.scitation.org/doi/10.1063/1.858424.

Yalin, M. Selim (1992). 'CHAPTER 2 - TURBULENCE'. In: *River Mechanics*. Ed. by M. Selim Yalin. Oxford: Pergamon, pp. 29–62. ISBN: 978-0-08-040190-4. DOI: https://doi.org/10.1016/B978-0-08-040190-4.50007-1. URL: https://www.sciencedirect.com/science/article/pii/B9780080401904500071.

Yeh, Y. and H. Z. Cummins (May 1964). 'LOCALIZED FLUID FLOW MEASUREMENTS WITH AN He–Ne LASER SPECTROMETER'. In: *Applied Physics Letters* 4 (10), pp. 176–178. ISSN: 0003-6951. DOI: 10.1063/1.1753925. URL: /aip/apl/article/4/10/176/46492/LOCALIZED-FLUID-FLOW-MEASUREMENTS-WITH-AN-He-Ne.

Yeoh, Guan Heng, Jiyuan Tu, Guan Heng Yeoh and Jiyuan Tu (2019). 'Chapter 6 – Free Surface Flows'. In: *Computational Techniques for Multiphase Flows*, pp. 415–462.

Yu, Ignatius T.S., Yuguo Li, Tze Wai Wong, Wilson Tam, Andy T. Chan, Joseph H.W. Lee, Dennis Y.C. Leung and Tommy Ho (2004). 'Evidence of Airborne Transmission of the Severe Acute Respiratory Syndrome Virus'. In: *New England Journal of Medicine* 350.17, pp. 1731–1739. ISSN: 00284793. DOI: 10.1056/NEJMoa032867.

Zennaro, Simone, Matteo Munaro, Simone Milani, Pietro Zanuttigh, Andrea Bernardi, Stefano Ghidoni and Emanuele Menegatti (July 2015). 'Performance evaluation of the 1st and 2nd generation Kinect for multimedia applications'. In: DOI: 10.1109/ICME.2015.7177380.

Zhang, Xin (2002). 'Enhanced dissipation of short gravity and gravity capillary waves due to parasitic capillaries'. In: *Physics of Fluids* 14.11, pp. L81–L84. DOI: 10.1063/1.1519260. URL: https://doi.org/10.1063/1.1519260.

Zhou, Lixing (2018). 'Chapter 5 - Modeling of Single-Phase Turbulence'. In: *Theory and Modeling of Dispersed Multiphase Turbulent Reacting Flows*. Ed. by Lixing Zhou. Butterworth-

Heinemann, pp. 89–120. ISBN: 978-0-12-813465-8. DOI: https://doi.org/10.1016/B978-0-12-813465-8.00005-3. URL: https://www.sciencedirect.com/science/article/pii/B9780128134658000053.

Appendix A

Appendix

A.1 Source code

All the code used to generate the mesh, run the simulation are located at:

https://github.com/Yun-HangCho/PhD-OpenFOAM-Open-Channel-Flows-scripts

A.2 Contact details

If there are any questions, please reach out on linkedin:

https://www.linkedin.com/in/yh-cho/

Alternatively, contact me at: yun-hang@hotmail.com

Github: https://github.com/Yun-HangCho

Videos of turbulent structures:

https://drive.google.com/drive/folders/1nTB1WTwMfGGDGXY2mi6dWRsQgMosjm2k?usp=sharing.